

Copyright Warning & Restrictions

The copyright law of the United States (Title 17, United States Code) governs the making of photocopies or other reproductions of copyrighted material.

Under certain conditions specified in the law, libraries and archives are authorized to furnish a photocopy or other reproduction. One of these specified conditions is that the photocopy or reproduction is not to be “used for any purpose other than private study, scholarship, or research.” If a user makes a request for, or later uses, a photocopy or reproduction for purposes in excess of “fair use” that user may be liable for copyright infringement,

This institution reserves the right to refuse to accept a copying order if, in its judgment, fulfillment of the order would involve violation of copyright law.

Please Note: The author retains the copyright while the New Jersey Institute of Technology reserves the right to distribute this thesis or dissertation

Printing note: If you do not wish to print this page, then select “Pages from: first page # to: last page #” on the print dialog screen

The Van Houten library has removed some of the personal information and all signatures from the approval page and biographical sketches of theses and dissertations in order to protect the identity of NJIT graduates and faculty.

ABSTRACT

THE AGING AND IMPACTS OF ATMOSPHERIC SOOT: CLOSING THE GAP BETWEEN EXPERIMENTS AND MODELS

by
Ogochukwu Yvonne Enekwizu

The main goal of this dissertation is to generate data and parameterizations to accurately represent soot aerosols in atmospheric models. Soot from incomplete combustion of fossil fuels and biomass burning is a major air pollutant and a significant contributor to climate warming. The environmental impacts of soot are strongly dependent on the particle morphology and mixing state, which evolve continuously during atmospheric transport via a process known as aging. To make predictions of soot impacts on the environment, most atmospheric models adopt simplifications of particle structure and mixing state, which lead to substantial uncertainties. Using an experimentally constrained modeling approach, this dissertation aims to improve the predictive capabilities of atmospheric models regarding the impacts of soot. Accordingly, the study objectives are to: (1) conduct experiments and simulations to investigate how soot properties evolve during aging; (2) develop physical parameterizations between soot particle properties and aging environment using established relationships; (3) incorporate the parameterizations in a particle-resolved aerosol model.

Experiments to investigate morphological changes are conducted by exposing airborne aggregates of well-defined mass, size, and composition to vapors of chemicals condensable at atmospheric conditions. The underlying mechanisms that lead to structural change are then identified and applied in theoretical calculations for soot aging. Optical experiments are conducted to measure light absorption and scattering by soot and

compared against literature reported values to resolve differences. Additionally, rigorous optical calculations are performed with morphological data from aging experiments to investigate the contributions of morphology and mixing state to parameters of interest in atmospheric models.

This work has developed a novel analytical framework for predicting the morphological mixing state and extent of restructuring of soot aggregates during atmospheric aging. The framework is validated by experimental measurements for a wide range of condensing vapors in realistic multicomponent systems, and is based on a single dimensionless parameter χ . The χ -parameter is controlled by coating material properties of vapor supersaturation and wettability for a specified soot monomer diameter. In the course of this study, the roles of vapor condensation and coating evaporation on aggregate restructuring are also found to be influenced by coating wettability. Based on rigorous optical calculations, the differences in measured and modeled optical properties of soot are resolved by varying monomer size and introducing necking material, between monomers. Additionally, the effect of the morphological mixing state on soot optical properties is found to depend strongly on the compactness of the aggregate. A simplified representation of χ -framework is incorporated into the particle resolved aerosol model, PartMC-MOSAIC and successfully tested on soot particles in an idealized urban air parcel. This demonstrates the suitability of this approach in facilitating accurate predictions of morphology-dependent soot properties in PartMC-MOSAIC.

Overall, the findings of this dissertation represent a significant advancement in understanding the processes governing the transformations and environmental impacts of soot that will benefit the atmospheric experimental and modeling research communities.

**THE AGING AND IMPACTS OF ATMOSPHERIC SOOT: CLOSING THE
GAP BETWEEN EXPERIMENTS AND MODELS**

**by
Ogochukwu Yvonne Enekwizu**

**A Dissertation
Submitted to the Faculty of
New Jersey Institute of Technology
in Partial Fulfillment of the Requirements for the Degree of
Doctor of Philosophy in Chemical Engineering**

**Otto H. York Department of
Chemical and Materials Engineering**

December 2020

Copyright © 2020 by Ogochukwu Yvonne Enekwizu

ALL RIGHTS RESERVED

APPROVAL PAGE

**THE AGING AND IMPACTS OF ATMOSPHERIC SOOT: CLOSING THE
GAP BETWEEN EXPERIMENTS AND MODELS**

Ogochukwu Yvonne Enekwizu

Dr. Alexei F. Khalizov, Dissertation Advisor Date
Associate Professor of Chemistry and Environmental Sciences, NJIT

Dr. Edward L. Dreizin, Committee Member Date
Distinguished Professor of Chemical and Materials Engineering, NJIT

Dr. Ecevit A. Bilgili, Committee Member Date
Associate Professor of Chemical and Materials Engineering, NJIT

Dr. Gennady Y. Gor, Committee Member Date
Assistant Professor of Chemical and Materials Engineering, NJIT

Dr. V. Faye McNeill, Committee Member Date
Professor of Chemical Engineering, Columbia University, NY

BIOGRAPHICAL SKETCH

Author: Ogochukwu Yvonne Enekwizu

Degree: Doctor of Philosophy

Date: December 2020

Undergraduate and Graduate Education:

- Doctor of Philosophy in Chemical Engineering, New Jersey Institute of Technology, Newark, NJ, 2020
- Master of Science in Chemical Engineering, University of Houston, Houston, TX, 2013
- Bachelor of Engineering in Chemical Engineering, Nnamdi Azikiwe University, Awka, Nigeria, 2009

Major: Chemical Engineering

Presentations and Publications:

Publications:

Enekwizu, O.Y., Hasani, A., McGuinness, M., Khalizov, A.F. (Submitted to Environmental Science and Technology). Vapor Condensation and Coating Evaporation are Both Responsible for Soot Aggregate Restructuring.

Enekwizu, O.Y., Singh, D., Khalizov, A.F. (2020). Absorption and Scattering of Light by Soot Aggregates with Uniform and Pendular Ring Coatings. *Journal of Aerosol Science*, 147, 105583.

Chen, C., Enekwizu, O.Y., Ma, X., Jiang, Y., Zheng, J., Khalizov, A.F., Ma, Y. (2020). Effect of Organic Coatings Derived from the OH-Initiated Oxidation of Amines on Soot Morphology and Cloud Activation. *Atmospheric Research*, 239, 10495.

Chen, C., Enekwizu, O.Y., Fan, X., Dobrzanski, C.D., Ivanova, E.V., Ma, Y., Gor, G.Y., Khalizov, A.F. (2018). Single Parameter for Predicting the Morphology of Atmospheric Black Carbon. *Environmental Science & Technology*, 52(24), 14169-14179.

Chen, C., Enekwizu, O.Y., Ma, Y., Zakharov, D., Khalizov, A.F. (2017). The Impact of Sampling Medium and Environment on Particle Morphology. *Atmosphere*, 8(9), 162.

Presentations:

Enekwizu, O.Y., Singh, D., Khalizov, A.F. Tracking the Evolution in Soot Aggregate Optical Properties Concurrently with its Morphology. Presented virtually at the American Physical Society (APS) Mid-Atlantic Section Meeting, December 2020.

Enekwizu, O.Y., Singh, D., Khalizov, A.F. Tracking the Evolution in Soot Aggregate Optical Properties Concurrently with its Morphology. Presented virtually at the American Geophysical Union (AGU) Annual Fall Meeting, December 2020.

Enekwizu, O.Y., Hasani, A., McGuinness, M., Khalizov, A.F. Is it Condensation or Evaporation that Drives Aggregate Restructuring? Presented virtually at the Society of Women Engineers (SWE) Annual Conference, November 2020.

Enekwizu, O.Y., Singh, D., M., Khalizov, A.F. An Algorithm for Soot Aggregate Restructuring. Presented virtually at the American Association for Aerosol Research (AAAR) Annual Conference, October 2020.

Enekwizu, O.Y., Singh, D., Khalizov, A.F. Tracking the Evolution in Soot Aggregate Optical Properties Concurrently with its Morphology. Presented virtually at the American Association for Aerosol Research (AAAR) Annual Conference, October 2020.

Enekwizu, O.Y., Chen, C., Fan, X., Dobrzanski, C.D., Ivanova, E.V., Ma, Y., Gor, G.Y., Khalizov, A.F. Vapor Supersaturation Controls the Properties and Impacts of Atmospheric Soot. Presented virtually at the Society of Women Engineers (SWE) Local Conference, May 2020.

Enekwizu, O.Y., Singh, D., McGuinness, M., Khalizov, A.F. The Dependence of the Optical Properties of Soot Aggregates on their Morphological Mixing State. Presented at the American Geophysical Union (AGU) Annual Fall Meeting, San Francisco, CA, December 2019.

Enekwizu, O.Y., Hasani, A., McGuinness, M., Khalizov, A.F. Quantifying the Thickness of Volatile Particle Coatings. Presented at the American Association for Aerosol Research (AAAR) Annual Conference, Portland, OR, October 2019.

Enekwizu, O.Y., Singh, D., McGuinness, M., Khalizov, A.F. The Dependence of the Optical Properties of Soot Aggregates on their Morphological Mixing State. Presented at the American Association for Aerosol Research (AAAR) Annual Conference, Portland, OR, October 2019.

Enekwizu, O.Y., Chen, C., Fan, X., Dobrzanski, C.D., Ivanova, E.V., Ma, Y., Gor, G.Y., Khalizov, A.F. Vapor Supersaturation Controls the Properties and Impacts of Atmospheric Soot. Presented at the New Jersey Water Environment Association (NJWEA) Annual Conference, Atlantic City, NJ, May 2019.

- Enekwizu, O.Y., Chen, C., Fan, X., Dobrzanski, C.D., Ivanova, E.V., Ma, Y., Gor, G.Y., Khalizov, A.F. Condensation Induced Restructuring of Atmospheric Soot Aggregates. Presented at the Dana Knox Research Showcase, New Jersey Institute of Technology (NJIT), Newark, NJ, April 2019.
- Enekwizu, O.Y., Chen, C., Fan, X., Dobrzanski, C.D., Ivanova, E.V., Ma, Y., Gor, G.Y., Khalizov, A.F. Condensation Induced Restructuring of Atmospheric Soot Aggregates. Presented at the Annual Northeast Regional Meeting on Kinetics and Dynamics, Hartford, CT, January 2019.
- Enekwizu, O.Y., Chen, C., Fan, X., Dobrzanski, C.D., Ivanova, E.V., Ma, Y., Gor, G.Y., Khalizov, A.F. Vapor Supersaturation Controls the Properties and Impacts of Atmospheric Soot. Presented at the American Geophysical Union (AGU) Annual Fall Meeting, Washington, DC, December 2018.
- Enekwizu, O.Y., Chen, C., Fan, X., Dobrzanski, C.D., Ivanova, E.V., Ma, Y., Gor, G.Y., Khalizov, A.F. Vapor Supersaturation Controls the Properties and Impacts of Atmospheric Soot. Presented at the National Society of Black Physicists (NSBP) Conference, Columbus, OH, November 2018.
- Enekwizu, O.Y., Chen, C., Fan, X., Dobrzanski, C.D., Ivanova, E.V., Ma, Y., Gor, G.Y., Khalizov, A.F. Vapor Supersaturation Controls the Properties and Impacts of Atmospheric Soot. Presented at the American Institute of Chemical Engineers (AIChE) Annual Conference, Pittsburgh, PA, October 2018.
- Enekwizu, O.Y., Chen, C., Dobrzanski, C.D., Gor, G.Y., Khalizov, A.F. Development of a Saturation Ratio Model for Controlling the Mixing State of Soot. Presented at the New Jersey Water Environment Association (NJWEA) Annual Conference, Atlantic City, NJ, May 2018.
- Enekwizu, O.Y., Chen, C., Dobrzanski, C.D., Gor, G.Y., Khalizov, A.F. A Condensation Model for Prediction of the Mixing State of Soot Aerosol. Presented at the Dana Knox Research Showcase, New Jersey Institute of Technology (NJIT), Newark, NJ, April 2018.
- Enekwizu, O.Y., Chen, C., Dobrzanski, C.D., Gor, G.Y., Khalizov, A.F. A Condensation Model for Prediction of the Mixing State of Soot Aerosol. Presented at the Annual Northeast Regional Meeting on Kinetics and Dynamics, Boston, MA, January 2018.
- Enekwizu, O.Y., Chen, C., Dobrzanski, C.D., Gor, G.Y., Khalizov, A.F. Development of a Saturation Ratio Model for Controlling the Mixing State of Soot. Presented at the GEM American Society of Engineering Education (ASEE) Research Showcase, Washington, DC, January 2018.

Enekwizu, O.Y., Chen, C., Ma, Y., Zakharov, D., Khalizov, A.F. The Impact of Sampling Medium and Environment on Nanoparticle Morphology. American Physical Society (APS) Mid-Atlantic Section Meeting, Newark, NJ, November 2017.

To my parents:

Emmanuel Chukwunyelu Enekwizu (Daddy) and Ozoemena Edna Enekwizu (Mummy)
Thank you for your prayers, unconditional love and constant support throughout this
journey.

To my siblings:

Adaobi Enekwizu (Dr. Wiggy) and Obinna Anadu (Tobaski)
For hugs, love, food and always accommodating me whenever I needed a reprieve from
being a grad student. I am so grateful.

Chigozie Enekwizu (Goz) and Adannia Enekwizu (Ada)

For your consistent support, warmth and kindness. You've always been there for me.

Emeka Enekwizu (Mita) and Chinwe Enekwizu (Chinny)

For always believing in me, calming my fears and constantly cheering me on. Thank you!

To my nieces and nephews:

Chinedum, Chinemelum, Chidubem, Nesochi, Kene and Netochi

For the hugs, smiles, kisses, and excitement on seeing me. For playing quietly and putting
up with your Aunty's incessant studying.

ACKNOWLEDGMENT

I'm grateful to God for the completion of this dissertation. His grace and provision have sustained me through this PhD journey, and I have been blessed with the wisdom, drive and focus to pursue my research.

My heartfelt gratitude goes to Dr. Alexei Khalizov for his guidance, apparently inexhaustible patience, constant support, and mentorship as my dissertation advisor. He has honed me into the researcher I am today. I would like to thank him for giving me countless opportunities to excel in my research, for teaching me to stay curious, for inspiring creativity in me, for his constructive critique and humor. He has done everything in his power to guide me towards a successful career. I am forever indebted to him and hope he is proud of me and the work we have accomplished.

Special thanks go to Dr. Gennady Gor who was my first contact with NJIT. I am especially grateful for his recommendation to join Dr. Khalizov's research group. I am also glad I took his molecular modeling class because it helped me learn how to program in Python, despite my initial aversion to programming. My research has benefited immensely from collaborations with him and I am thankful for his encouragement and advice over the years. I would also like to thank my committee members Dr. Edward Dreizin, Dr. Ecevit Bilgili and Dr. Faye McNeill for sharing their time and expertise in the completion of my research.

I am grateful to the National Science Foundation (NSF) for financial support (AGS-1463702) over the duration of my study as well as the Air and Waste Management Association (A&WMA), the Society of Women Engineers (SWE), and the New Jersey Water and Environmental Association (NJWEA) for grants and financial scholarships.

Many thanks to Dr. Nicole Riemer for patiently teaching me how to use her PartMC-MOSAIC code and willingness to write recommendation letters for me. I am also grateful to Dr. Liu for assistance with using T-matrix codes for my research. Special thanks also goes to the NJIT ARCS staff (Gedaliah Wolosh and Kevin Walsh) for the vital computational support.

I would like to thank the very diverse (both in culture and mindset) members of the Atmospheric Chemistry group who have always cheered me on. We have shared both triumphs and failures and have sat patiently through countless presentation rehearsals and (never-ending) meetings. It has been a pleasure working with Dr. Chong Qiu, Na Mao, Ali Hasani, Mary McGuinness, and Egor Demidov. I am especially grateful to my mentee and resident computing whiz, Divjyot Singh without whom most of my computational work would not have been completed. He is going to make a great grad student (no pressure).

My gratitude also goes to my friends at NJIT: Lydia Rodrigues, Apurva Limaye, Anh Tong, Marwa Choudhury, Chadakarn Sirasitthichoke, Ella Ivanova, Pham Dung, and Vishnu Deep. Thank you for sharing research ideas, formatting tips, and encouragement over numerous cups of bobba tea. I am especially thankful to my sisters from Houston: Tochi Amadi, Ngozi Onwuama, Prisca Tihfon, Eposi Tihfon, Mercede Barnes, Chinyere Eigege, Tawana Robinson, Sujeeta Menon, Kemi Ogundipe, Nicky Pizana, Rashida Moore, Preethi Chinta, Tamara Ita, Vickie Glen, Heather Chappelle, Anna Li, Kelley Lou and Lakresha Norton (who we lost two years ago). Though I was out of sight, I was never out of their minds. I appreciate the prayers, care packages, surprise visits and impromptu trips. I am also grateful to my lifelong besties Ogochukwu Udokwelu, Ruth Umeadi, Jane Igbadumhe, Ogochukwu Ugeh and Chuka Ononiwu for their unwavering support and care.

Finally, I am indebted to my family, the Enekwizus for their unconditional love and support. Thank you for motivating me to pursue my dreams, for cheering me on when I wanted to give up, and for telling off the haters who thought I'd never make it. You all inspire me to be the best I can be. I hope I have made you all proud.

TABLE OF CONTENTS

Chapter	Page
1 INTRODUCTION	1
1.1 Background and Significance	1
1.1.1 Atmospheric Soot	3
1.1.2 Morphology	5
1.1.3 Mixing State	7
1.1.4 Atmospheric Aging	9
1.1.5 Optical Properties	12
1.1.6 Aerosol Models	18
1.2 Research Objectives	19
1.3 Organization of Dissertation	20
2 METHODOLOGY	22
2.1 Laboratory Studies	22
2.1.1 Flow Reactor Experiments	23
2.1.2 Electron Microscopy and Image Processing	27
2.1.3 Data Analysis	28
2.2 Computational Studies	31
2.2.1 Numerical Generation of Aggregates	31
2.2.2 Multiple Sphere T-Matrix (MSTM)	33
2.2.3 Discrete Dipole Approximation (DDA)	34
3 SINGLE PARAMETER REPRESENTATION OF THE MIXING STATE AND MORPHOLOGY OF SOOT	36

TABLE OF CONTENTS
(Continued)

Chapter	Page
3.1 Introduction	36
3.1.1 Morphological Changes in Coated Soot Aggregates	37
3.1.2 Trends between Soot Morphology and Coating Material Properties	42
3.1.3 Two Distinct Morphological Mixing States	44
3.1.4 Model for Competitive Condensation on Soot Aggregates	47
3.1.5 Study Objectives	53
3.2 Modeling of Vapor Supersaturation in Condenser	53
3.3 Results and Discussion	55
3.3.1 Vapor Supersaturation Profiles	55
3.3.2 Mechanism Leading to Two Distinct Morphological Mixing States	59
3.4 Conclusions	66
4 IS IT CONDENSATION OR EVAPORATION THAT DRIVES AGGREGATE RESTRUCTURING?	68
4.1 Introduction	68
4.2 Particle Growth Measurements	69
4.2.1 Electrostatic Particle Classifier	71
4.3 Results and Discussion	75
4.3.1 Three Distinct Regions in Vapor Supersaturation for Aggregate Restructuring	75
4.3.2 Vapor Supersaturation Required to Fully Encapsulate a Soot Aggregate.	83
4.3.3 Dependence of Aggregate Restructuring on Coating Volatility	84

TABLE OF CONTENTS
(Continued)

Chapter	Page
4.4 Conclusions	87
5 VALIDATION OF CHI MODEL WITH MULTICOMPONENT SYSTEM	90
5.1 Introduction	90
5.2 Chamber Experiments	92
5.3 Results and Discussion	93
5.3.1 Fresh Soot Measurements	93
5.3.2 Soot Aging with Low Initial Amine Concentration	94
5.3.3 Soot Aging with High Initial Amine Concentration	99
5.3.4 CCN Activity of Aged Soot	103
5.4 Conclusions	107
6 AN ALGORITHM FOR SOOT AGGREGATE RESTRUCTURING	109
6.1 Introduction	109
6.1.1 The Schnitzler Model	111
6.1.2 Study Objectives	114
6.2 Modeling Aggregate Restructuring with the Morse Potential	114
6.3 Results and Discussion	116
6.4 Conclusions	121
7 EXPERIMENTAL MEASUREMENTS OF LIGHT ABSORPTION AND SCATTERING BY SOOT	123
7.1 Introduction	123

TABLE OF CONTENTS
(Continued)

Chapter	Page
7.2 Eliminating the Effects of Multiple Charging	125
7.2.1 Experimental Re-Classification	126
7.2.2 Mathematical Adjustment	127
7.3 Results and Discussion	129
7.3.1 Calibration Measurements	129
7.3.2 MAC Determination via Re-Classification	130
7.3.3 MAC Determination via Data Reprocessing	132
7.4 Conclusions	136
8 OPTICAL SIMULATIONS OF LIGHT ABSORPTION AND SCATTERING BY SOOT	137
8.1 Introduction	137
8.1.1 Study Objectives	140
8.2 Numerical Simulation of Bare and Coated Soot Aggregates	141
8.3 Optical Models	144
8.4 Reconciling the Measured and Modeled Optical Properties of Fresh Soot	148
8.5 Optical Predictions for Coated Fractal Aggregates	152
8.5.1 Dependence of Soot Optical Properties on the Coating Distribution	152
8.5.2 Sensitivity to Monomer Radius and Wavelength	161
8.6 Optical Predictions for Coated Compact Aggregates	163
8.7 Conclusions	169

TABLE OF CONTENTS
(Continued)

Chapter	Page
9 NOVEL PARAMETERIZATIONS FOR PARTICLE RESOLVED AEROSOL MODELS	172
9.1 Introduction	172
9.2 A Restructuring Framework for PartMC-MOSAIC	175
9.3 Results and Discussion	178
9.4 Conclusions	179
10 CONCLUSIONS AND FUTURE WORK	180
10.1 Conclusions	180
10.2 Directions for Future Study	183
APPENDIX A AEROSOL INSTRUMENTATION	185
A.1 Differential Mobility Analyzer (DMA)	185
A.2 Aerosol Particle Mass Analyzer (APM)	187
A.3 Condensation Particle Counter (CPC)	188
A.4 Cavity Attenuated Phase Shift Single Scattering Albedo (CAPS PM _{SSA}) Monitor	189
APPENDIX B MEASUREMENTS OF COATED PARTICLE MOBILITY DIAMETER DURING VAPOR CONDENSATION AND COATING EVAPORATION EXPERIMENTS.....	192
B.1 Coated Particle Mobility Diameter Curves for DA and TEGMBE	192
B.2 TEG Evaporation During Transit	193
B.3 Comparing the <i>Gfd</i> Curves of TEG and OA	194
APPENDIX C MEASURED MASS-MOBILITY AND OPTICAL DATA	196

TABLE OF CONTENTS
(Continued)

Chapter	Page
C.1 Optical Data for Re-Classification Method	196
C.2 Optical and Mass-Mobility Data for Mathematical Adjustment Method	197
APPENDIX D COATING VOLUME CONVERSIONS FOR COATED SOOT AGGREGATES	198
D.1 Conversion of Coating Volume to Monomer Coating Thickness	199
D.2 Conversion of Coating Volume to Necking Parameter	200
D.3 Modified Approach for Conversion of Coating Volume to t and α	202
D.4 Conversion of Coating Volume to Shell Thickness for Core-Shell Model	203
D.5 Conversion of Coating Volume to Monomer Coating Thickness for RDG-Mie Model	203
APPENDIX E SIMULATED OPTICAL PROPERTIES FOR BARE AND COATED SOOT	205
E.1 Optical Model Comparisons for Bare Soot	205
E.2 Configuration Averaging of Bare and Coated Soot	206
E.3 Sensitivity of Optical Properties of Coated Fractal Soot to Variations in Monomer Radius and Incident Wavelength	207
E.1 Optical Data for Coated Fractal and Compact Soot	207
APPENDIX F PYTHON AND FORTRAN CODES FOR IMPLEMENTING AGGREGATE RESTRUCTURING	210
F.1 Python Code for Aggregate Restructuring	210
F.2 Fortran Code for Particle Collapse Module (pmc_collapse).....	212
REFERENCES	218

LIST OF TABLES

Table	Page
3.1 Properties of Coating Materials	38
3.2 Morphological Changes in Thinly Coated Soot Aggregates ($13 \pm 2\%$ coating fraction) Based on Convexity Determined from Scanning Electron Microscopy Images	42
5.1 Comparison of the Effects of Organic Coatings from the Photooxidation of Different Precursors on the Mass Growth Factor (G_{fm}) and Size Growth Factor (G_{fd}) of Soot Particles	97
6.1 Simulation Parameters for Restructuring Algorithm	117
7.1 Fractional Contributions of Modes in a Size Distribution	132
8.1 Soot Refractive Indices	146
8.2 Dependence of Particle Mobility Diameter, Gyration Radius and Aggregate Size on Monomer Size Variation.....	149
C.1 Measured Optical Cross-Sections for Re-Classification	196
C.2 Measured Optical Cross-Sections for Data Processing	197
C.3 Mass-Mobility Measurements	197
E.1 Radiative Properties of Uncoated Soot Aggregates Calculated Using Different Optical Models. Fractal Dimension D_f is Fixed at 1.78, Scaling Prefactor k_o is Equal to 1.3, Monomer Radius R_s is Equal to 14 nm, and the Incident Wavelength λ is Fixed at 530 nm	205
E.2 Ensemble Averaged Cross-sections and Relative Standard Deviations (RSD) from Mean for 5 Realizations of Uniformly and Capillary Coated Fractal Aggregates ($N_s = 20$, $D_f = 1.78$, $k_o = 1.3$, $R_s = 14$ nm, $\lambda = 530$ nm)	206
E.3 Optical Cross-sections of Uniformly Coated Fractal Aggregates Made of Monomers with Different Radii ($N_s = 20$, $D_f = 1.78$, $k_o = 1.3$, $\lambda = 530$ nm)	207
E.4 Optical Cross-sections for Uniformly Coated Fractal Aggregates at Various Wavelengths ($N_s = 20$, $D_f = 1.78$, $k_o = 1.3$, $r_m = 14$ nm)	207

LIST OF FIGURES

Figure	Page
1.1 The impacts of atmospheric aerosols	2
1.2 Schematic of soot nanoparticle formation from polycyclic aromatic hydrocarbon (PAH) molecules	4
1.3 SEM micrographs of 240 nm initial mobility diameter soot aggregates in: (a) fractal configuration (before coating) (b) compact configuration (after coating). A volume equivalent spherical approximation is shown in (c)	6
1.4 Common representations of mixing state: (a) external mixture (b) well-mixed internal mixture (c) core-shell mixture. Both (b) and (c) are internal mixtures	8
1.5 Single-particle extinction (Q_{ext}), absorption (Q_{abs}), and scattering (Q_{sca}) efficiencies of an absorbing sphere ($m = 1.73 + 0.6i$)	13
2.1 The aerosol system comprised of the generation, coating/processing, and measurement modules. DMA is the differential mobility analyzer, APM is the aerosol particle mass analyzer, and CPC is the condensation particle counter	23
2.2 Coating chamber made of Pyrex glass (46 cm length and 2 cm inside diameter) containing coating liquid	25
2.3 Experimental setup for light scattering and extinction measurements. CAPS PM _{SSA} is the cavity attenuated phase shift single scattering albedo monitor	27
2.4 Calculation of convexity: (a) original SEM image, (b) 2D projected area of aggregate (c) convex polygon around aggregate image	28
2.5 An aggregate of 20 monomers with fractal dimension $D_f = 1.78$ and prefactor $k_o = 1.3$ generated by (a) particle-cluster aggregation and (b) cluster-cluster aggregation.....	33
3.1 Mobility diameter change (Gfd) as a function of mass change (Gfm) for soot aggregates coated with (a) TEG, (b) TEGMBE, (c) DA, (d) TDA, (e) BEHP, (f) BEHA, (g) DOS, (h) OA and (i) SA. Squares (green) and triangles (orange) represent aggregates with initial mobility diameters of 240 nm and 350 nm respectively. Solid and dashed lines correspond to coated and coated-denuded soot respectively. See Table 3.1 for acronyms	39

LIST OF FIGURES
(Continued)

Figure	Page
<p>3.2 Morphological changes in soot aggregates that were exposed to condensable vapors of different chemicals and then denuded. (a) Mass-mobility relationship showing the dependence of mobility diameter change (Gfd) on mass change (Gfm) and coating mass fraction (f_m). (b-e), Scanning electron microscopy images of soot aggregates, where (b) is an uncoated aggregate, (c) is a coated aggregate with 10% mass fraction DA, (d) is a coated aggregate with 13% OA, and (e) is a coated aggregate with 43% OA. Initial mobility diameter is 240 nm in (a) and 350 nm in (b-e). See Table 3.1 for acronyms.....</p>	41
<p>3.3 Dependence of convexity (top panel) and mobility diameter change, Gfd (bottom panel) on the surface tension (a, c), and saturation vapor pressure at 25 °C (b, d) of the coating material. The initial mobility diameter of soot aggregates is 350 nm and the coating mass fraction is $13 \pm 2\%$. The dashed line represents uncoated soot (convexity = 0.54, $Gfd = 1$). See Table 3.1 for acronyms</p>	43
<p>3.4 Two models representing the morphological mixing state of coated soot aggregates. (a) A coating layer with effective thickness ΔR_s is distributed uniformly over monomer spheres. (b) Pendular rings of radius r_m are formed by capillary condensation at the junctions between monomer spheres. R_m is the radius of curvature of the meniscus. The extent to which the gap is filled by condensate is described in terms of the angle θ. (c) A thickly coated aggregate with $r_m \sim \Delta R_s$</p>	45
<p>3.5 Mobility diameter change (Gfd) as a function of pendular ring thickness (r_m, blue, low supersaturation) and effective coating thickness (ΔR_s, red, high supersaturation) for soot aggregates that were coated and then denuded. The range of ΔR_s and r_m corresponding to nearly complete restructuring of soot is indicated by the vertical green band. See Table 3.1 for acronyms</p>	47
<p>3.6 Saturation ratio ($\zeta+1$) calculated for OA (a), and TEG (b) vapor condensation on PSL aerosol in the coating reactor. T_C is the centerline temperature and T_W is the wall temperature, both experimentally measured. See Table 3.1 for acronyms</p>	56
<p>3.7 Particle diameter (D_p) calculated for OA (a), and TEG (b) vapor condensation on PSL aerosol in the coating reactor. T_C is the centerline temperature and T_W is the wall temperature, both experimentally measured. Experimentally measured values (red dots) were 126 and 108 nm, respectively. See Table 3.1 for acronyms</p>	57

LIST OF FIGURES
(Continued)

Figure	Page
3.8 Mobility diameter change (<i>Gfd</i>) of soot aggregates with increasing saturator temperature, measured by tandem differential mobility analysis (DMA-DMA) and electrostatic particle classification (DMA-EPC) methods. Particle size measurements were conducted at a distance of 3.5 m and 0.04 m for DMA-DMA and DMA-EPC, respectively. The initial mobility diameter of soot is 240 nm and the coating material is triethylene glycol (TEG)	59
3.9 Time variation in the calculated ratio of the condensate amount in the gap and on the sphere for different χ . The monomer diameter is 28 nm. As χ increases, condensation in the gap becomes more competitive. The amount of condensate in the gap becomes equal to the amount of condensate on the sphere at $\chi \sim 0.65$	61
3.10 Calculated competition between the uniform vapor condensation over the entire aggregate (sphere) and capillary condensation in junctions (gap): (a) DA ($\zeta = 0.36$, $\chi = 1.042$) and (b), OA ($\zeta = 20.5$, $\chi = 0.029$). Reduced amount of condensate equaling 1.0 corresponds to half of the volume of the monomer sphere. The monomer sphere diameter is 28 nm. See Table 3.1 for acronyms	62
3.11 Extent of restructuring (<i>Gfd</i>) as a function of the dimensionless parameter χ . The monomer sphere diameter is 28 nm. See Table 3.1 for acronyms	63
3.12 Calculated competition between the uniform vapor condensation over the entire aggregate surface (sphere) and capillary condensation in junctions (gap) for different monomer diameters: (a), 7 nm ($\chi = 0.590$), (b), 28 nm ($\chi = 0.147$), and (c), 45 nm ($\chi = 0.092$). Reduced amount of condensate equaling 1.0 corresponds to half of the volume of the monomer sphere. The condensing vapor is oleic acid, OA ($\zeta = 4.0$)	65
4.1 Schematic of the system for aerosol generation, processing and measurement. The electrostatic particle classifier (EPC), shown on the right, is sufficiently compact to be placed at any location after the saturator exit. DMA is the differential mobility analyzer, APM is the aerosol mass analyzer and CPC is the condensation particle counter	70
4.2 Schematic of the electrostatic particle classifier. The high voltage collector rod is coaxial with the stainless-steel tube which is grounded. The red arrows indicate the aerosol flow path	71

LIST OF FIGURES
(Continued)

Figure	Page
4.3 Calibration of the electrostatic particle classifier: (a) collection efficiency as a function of applied voltage for different particle diameters, (b) voltage-size dependence for a 50% collection efficiency. The error bars are smaller than the symbols used for the data points	74
4.4 Evolution in particle growth factor (Gfd) of soot aggregates with increasing saturator temperature, measured by tandem differential mobility analysis (DMA-DMA) and electrostatic particle classification (DMA-EPC) methods. The initial mobility diameter of soot is 240 nm and the coating material is triethylene glycol (TEG). The dashed lines highlight the different regions of vapor supersaturation. Inset shows an expanded view of Gfd at low saturator temperatures. The green circle represents PSL with a 150 nm initial mobility diameter.....	76
4.5 Modeled (line) and measured (squares) profiles of particle diameter as a function of distance from the exit of the saturator during soot aging with triethylene glycol (TEG). The blue solid line in the experimental data is provided to guide the eye. The dashed blue lines represent the final compact soot morphology while the dashed green lines represent uncoated PSL. The saturator temperature is 50°C and the initial (uncoated) particle mobility diameter is 240 nm	78
4.6 Measured diameter of soot and PSL particles exposed to TEG vapor produced at different saturator chamber temperatures. The electrostatic particle classifier (EPC) was placed at a distance of 0.04 m from the exit of the saturator chamber. The initial mobility diameters of PSL and soot particles are 150 and 240 nm, respectively	83
4.7 Dependence of soot aggregate restructuring on coating volatility at near saturated ($\zeta \leq 0$) and mildly supersaturated ($\zeta < 0.07$) conditions. The electrostatic particle classifier (EPC) was placed at 0.04 m from the exit of the saturator. Initial aggregate mobility diameter is 240 nm. See Table 3.1 for acronyms	85
5.1 Multimodal distribution of mobility-classified fresh soot aerosol showing the existence of multiply charged particles. Recharging processes are indicated above the corresponding size modes	93
5.2 Evolution in (a) mass growth factor (Gfm), (b) diameter growth factor (Gfd), (c) effective density (ρ_{eff}), and (d) shape factor (χ_{shape}) of soot particles upon photochemical aging in the presence of 15 ppb amines with 150 nm initial diameter	94

LIST OF FIGURES
(Continued)

Figure	Page
5.3 Evolution in (a) mass growth factor (G_{fm}), (b) diameter growth factor (G_{fd}), (c) effective density (ρ_{eff}), and (d) shape factor (χ_{shape}) of soot particles upon photochemical aging in the presence of H_2O_2 with 150 nm initial diameter	96
5.4 Evolution in G_{fd} of soot particles upon photochemical aging and coating removal process in the presence of 15 ppb amines	98
5.5 Evolution in (a) mass growth factor (G_{fm}), (b) diameter growth factor (G_{fd}), (c) effective density (ρ_{eff}), and (d) shape factor (χ_{shape}) of soot particles upon photochemical aging in the presence of 100 ppb amines with 150 nm initial diameter	100
5.6 Evolution in G_{fd} of soot particles upon photochemical aging and coating removal process in the presence of 100 ppb amines	102
5.7 CCN/CN (activation ratio) evolution during the aging process, (a-c) are for 15 ppb initial amine concentration, (d-f) are for 100 ppb initial amine concentration; (a, d) represent $\zeta = 0.23\%$, (b, e) represent $\zeta = 0.42\%$, (c, f) represent $\zeta = 0.81\%$.	104
5.8 CCN/CN (activation ratio) evolution of 150 nm soot particles at three water vapor supersaturations (SS) during photochemical aging in the presence of H_2O_2	106
6.1 Illustration of the (a) capillary, and (b) bridging forces used in the Schnitzler model	113
6.2 The Morse potential (red line), force (blue line) and harmonic potential (red dashes)	115
6.3 Sample illustration of convergence criteria for aggregate restructuring: (a) root mean square displacement (RMSD), (b) root mean square force (RMSF), (c) maximum displacement, and (d) maximum force	118
6.4 Evolution in the Morse energy (a) and fractal dimension (b) of an aggregate of 20 monomers during a restructuring run	118
6.5 Evolution of particle morphology (D_f) with time of an initially fractal aggregate comprising (a) 20 monomers, and (b) 120 monomers. The monomers in the aggregate are colored for better visualization	119

LIST OF FIGURES
(Continued)

Figure	Page
6.6 Experimental (left) and modeled (right) restructuring of soot aggregates. Particle structure before aging is shown at the top and the final partially compacted structure after aging is given at the bottom	120
6.7 Levels of structural collapse for an ensemble of 10 different aggregates. Each aggregate configuration is comprised of 20 monomers with initial fractal parameters of 1.78 and 1.3 for D_f and k_o , respectively	120
6.8 Different realizations of aggregates with the same initial fractal parameters ($N_s = 20$, $D_f = 1.78$, $k_o = 1.3$, $R_s = 14$ nm)	121
7.1 Size dependence of the aerosol charging probability. The values above curves indicate the number of particle charges. Adapted from Wiedensohler, (1988)	125
7.2 (a) Aerosol size distribution, (b) Multi-modal distribution of a recharged soot aerosol showing the existence of multiply charged particles. Recharging processes are indicated above the corresponding size modes	126
7.3 Extinction and scattering coefficients as a function of number concentration for 240 nm PSL spheres used the calibration of CAPS-SSA monitor. The dashed line represents a 1:1 correlation	130
7.4 (a) Mass absorption cross-section (MAC), and (b) single scattering albedo (SSA) of uncoated soot as a function of particle size. Values for MAC and SSA were obtained with and without experimental reclassification of the soot aerosol. The standard MAC value of $7.5 \text{ m}^2/\text{g}$ is also shown. Error bands are indicated for each measurement	131
7.5 (a) Mass absorption cross-section (MAC), and (b) single scattering albedo (SSA) of uncoated soot as a function of particle size. Values for MAC and SSA were obtained with and without mathematical correction for the contribution of multiply charged particles. The standard MAC value of $7.5 \text{ m}^2/\text{g}$ is also shown. Error bands are indicated for each measurement	133
7.6 Mass absorption cross-section (MAC) of uncoated soot obtained via experimental recharging (grey squares), mathematical correction of peak mode contributions (orange circles), linear (green triangles), and quadratic (cyan diamonds) on particle size. The green band represents the range for the standard MAC value of $7.5 \text{ m}^2/\text{g}$	134

LIST OF FIGURES
(Continued)

Figure	Page
7.7 An SEM micrograph of mobility classified fresh soot showing the existence of long, linear chain aggregates that are likely to bias optical measurements. Initial mobility diameter of soot is 240 nm	135
8.1 Monomer-monomer contacts observed in soot aggregates: (a) point-touch, (b) overlap, and (c) necking	139
8.2 Dipole representation of a bare (a, d), uniformly coated (b, e), and pendular ring coated (c, f) soot aggregate of 20 monomers. The blue colored dipoles are the graphitic monomers and the red colored dipoles are the coating material. <i>CVF</i> for the coated aggregates in this case is 0.27.....	144
8.3 Approximate models for mixing state representation: (a) volume equivalent core-shell model, (b) RDG-Mie model. Blue represents soot and red is represents the coating	147
8.4 Calculated (a) mass absorption cross-section (MAC) and (b) single scattering albedo (SSA) as a function of aggregate mobility diameter for fixed and variable monomer radius. The fractal dimension, D_f is 1.78, structure factor k_o is 1.3, and the incident wavelength λ is 530 nm	150
8.5 Calculated (a) mass absorption cross-section (MAC) and (b) single scattering albedo (SSA) as a function of necking fraction for fresh soot. Necks are comprised of lightly absorbing brown carbon (1.65+0.003i), strongly absorbing brown carbon (1.65+0.03i) and graphitic carbon (1.73+0.6i). D_f is 1.78, k_o is 1.3, monomer radius R_s is 14 nm, and the incident wavelength λ is 530 nm	151
8.6 Cross-sections for light absorption and scattering by coated fractal aggregates comprising 5 monomers (a, b), 40 monomers (c, d) and 120 monomers (e, f) at various coating volume fractions, <i>CVF</i> ($D_f = 1.78$, $k_o = 1.3$, $R_s = 14$ nm, $\lambda = 530$ nm)	153
8.7 Absorption (a) and scattering (b) cross-section ratio, $R_{P/U}$ of pendular ring coated aggregates to uniformly coated aggregates for different coating volume fractions ($N_s = 5, 40$ and 120 , $D_f = 1.78$, $k_o = 1.3$, $R_s = 14$ nm, $\lambda = 530$ nm). The dashed line shows when the optical properties for the two coating distributions are the same (i.e., $R_{P/U} = 1$)	154

LIST OF FIGURES
(Continued)

Figure	Page
8.8 2D representation of a pendular ring coated aggregate showing coating spill from monomer junctions to aggregate surface as the coating volume fraction increases; the <i>CVF</i> is 0.27 for (a), 0.5 for (b) and 0.8 for (c)	155
8.9 Dependence of single scattering albedo (SSA) for coated fractal aggregates comprising (a) 5 monomers, (b) 40 monomers, and (c) 120 monomers on the coating volume fraction ($D_f = 1.78$, $k_o = 1.3$, $R_s = 14$ nm, $\lambda = 530$ nm)	156
8.10 Dependence of asymmetry parameter, $\langle g \rangle$ for coated fractal aggregates comprising (a) 5 monomers, (b) 40 monomers, and (c) 120 monomers on the coating volume fractions ($D_f = 1.78$, $k_o = 1.3$, $R_s = 14$ nm, $\lambda = 530$ nm). The dashed line represents the asymmetry parameter for uncoated soot	158
8.11 Dependence of calculated (a) absorption and (b) scattering cross-section ratio $R_{P/U}$ (pendular ring coated aggregates to uniformly coated aggregates) on the monomer radius, using $CVF = 0.08, 0.7$, $N_s = 40$, $D_f = 1.78$, $k_o = 1.3$, and $\lambda = 530$ nm. The dashed line corresponds to $R_{P/U} = 1$	162
8.12 Dependence of calculated (a) absorption and (b) scattering cross-section ratio $R_{P/U}$ (pendular ring coated aggregates to uniformly coated aggregates) on the incident wavelengths, using $CVF = 0.08, 0.7$, $N_s = 40$, $D_f = 1.78$, $k_o = 1.3$, and $R_s = 14$ nm. The dashed line corresponds to $R_{P/U} = 1$	163
8.13 Dependence of calculated (a) absorption cross-section, (b) scattering cross-section, (c) single scattering albedo (SSA), and (d) asymmetry parameter $\langle g \rangle$ on aggregate fractal dimension for $N_s = 40$ monomers ($k_o = 1.3$, $R_s = 14$ nm, $\lambda = 530$ nm)	165
8.14 Cross-sections for light absorption and scattering by coated fractal (a, c) and compact (b, d) aggregates comprising 40 monomers at various coating volume fractions, CVF . ($k_o = 1.3$, $R_s = 14$ nm, $\lambda = 530$ nm)	166
8.15 Absorption (a) and scattering (b) cross-section ratio, $R_{P/U}$ of pendular ring coated aggregates to uniformly coated aggregates as a function of coating volume fraction for different fractal dimensions, D_f ($N_s = 40$, $k_o = 1.3$, $R_s = 14$ nm, $\lambda = 530$ nm). The dashed line shows when the optical properties for the two coating distributions are the same (i.e., $R_{P/U} = 1$)	167

LIST OF FIGURES
(Continued)

Figure	Page
8.16 Dependence of asymmetry parameter, $\langle g \rangle$ for coated fractal (a, b) and compact (c, d) aggregates comprising 40 monomers on the coating volume fraction ($k_o = 1.3$, $R_s = 14$ nm, $\lambda = 530$ nm). The dashed line represents the asymmetry parameter for uncoated soot corresponding to the aggregate fractal dimension, D_f .	168
9.1 (a) Modal aerosol models represent aerosol size distribution as a sum of nodes. (b) Sectional models store the number or mass of aerosol per bin. Both models cannot accurately represent aerosol mixing state. A particle-resolved model (c) such as PartMC can easily store complex mixing states that represent diversity in particle composition	173
9.2 Schematic illustrating the overall approach for integrating the restructuring module (pmc_collapse) in PartMC-MOSAIC	177
9.3 Particle structure evolution for soot containing particles in an idealized urban plume scenario	178
A.1 Schematic of a differential mobility analyzer (DMA)	187
A.2 Schematic of an aerosol particle mass analyzer (APM)	188
A.3 Schematic of a condensation particle counter (CPC)	189
A.4 Schematic of the cavity attenuated phase shift single scattering albedo (CAPS PM _{SSA}) monitor	190
B.1 Change in mobility diameter, Gfd of soot aggregates as a function of saturator temperature for (a) DA, and (b) TEGMBE determined via tandem mobility (DMA-DMA) and electrostatic classification (DMA-EPC) methods. Initial mobility diameter of soot is 240 nm	193
B.2 Dependence of aggregate restructuring and growth on (a) the saturator temperature and (b) saturation vapor pressure of the coating at the experiment temperature. The coatings used are oleic acid (OA) and triethylene glycol (TEG). The initial mobility diameter of the soot aggregates is 240 nm. The solid lines are for coated soot and the dashed lines are for coated-denuded soot measurements.	194

LIST OF FIGURES
(Continued)

Figure	Page
D.1 Models for mixing state representation: (a) uniform distribution of coating material over soot monomers with effective coating thickness t (DDA Uniform), (b) pendular ring distribution at junctions between monomer spheres (DDA ring), (c) volume equivalent core-shell model with coating thickness t_{shell} (d) RDG-Mie model with coating thickness t_{mon_shell}	198
D.2 Monomer coating thickness as a function of coating volume fraction (CVF). The red circles represent estimates of t for $CVF = 0.7$ ($N_s = 40$, $D_f = 1.78$, $k_o = 1.3$, $R_s = 14$ nm)	200
D.3 Relationship between necking parameter and coating volume in monomer junction for a coated dimer	201
D.4 Monomer coating thickness (a) and necking parameter (b) as a function of coating volume thickness. The blue dots represent calculated estimates of CVF based on predefined t and α values ($N_s = 40$, $D_f = 1.78$, $k_o = 1.3$, $R_s = 14$ nm)	202
E.1 Cross-sections for light absorption and scattering by coated fractal (a, c) and partially compact (b, d) aggregates comprising 40 monomers at various coating volume fractions, CVF . ($k_o = 1.3$, $R_s = 14$ nm, $\lambda = 530$ nm)	208
E.2 Dependence of single scattering albedo (SSA) for coated fractal (a, b) and compact (c, d) aggregates comprising 40 monomers on the coating volume fraction ($D_f = 1.78$, $k_o = 1.3$, $R_s = 14$ nm, $\lambda = 530$ nm)	209

CHAPTER 1

INTRODUCTION

Aerosols are minute particles suspended in air that play an important role in the Earth's atmospheric system. This dissertation focuses on atmospheric soot (or black carbon, BC), a primary aerosol of anthropogenic origin, to elucidate mechanisms that relate the morphology of soot nanoparticles to light absorption and the ability to form cloud droplets. These mechanisms are governed by physical parameters derived from the processes associated with atmospheric aging. A novel parameterization for predicting the morphological mixing state of soot is proposed and discussed. Adopting a similar framework to connect the optical properties of soot to morphology via experimental and computational studies has major implications on the representation of soot aerosols in atmospheric models.

1.1 Background and Significance

Atmospheric aerosols have a significant impact on global climate, air quality, and human health (Figure 1.1). Aerosols can influence climate directly by altering the Earth's radiative balance through the scattering or absorption of solar radiation (Haywood & Boucher, 2000; Seinfeld & Pandis, 2006), and indirectly by changing cloud formation and precipitation as cloud and ice condensation nuclei (Lohmann & Feichter, 2005). When high concentrations of aerosols are present in the air, they can serve as sites for various chemical reactions (Finlayson-Pitts & Pitts, 2000) and have been linked to respiratory and cardiovascular diseases (Pöschl, 2005) and poor visibility (Watson, 2002).

Particulate matter in the atmosphere arises from natural sources and anthropogenic activities. Primary aerosols like mineral dust, sea salt, fly ash, pollen, and soot are emitted directly as particles while secondary aerosols like sulfuric acid particles are formed from gas-to-particle conversion in the atmosphere through the processes of nucleation and condensation of gaseous precursors (Seinfeld & Pandis, 2006), as shown in Figure 1.1.

The main parameters that govern the impacts of atmospheric aerosols are their concentration, size, shape, and chemical composition. Particle shapes can range from a few nanometers (ultrafine) to tens of microns (coarse) in diameter while typical atmospheric concentrations span from 10^2 (clean) to 10^5 (polluted) particles per cm^3 of air. Particle structures exist in varying degrees of complexity, ranging from simple cubic (sodium chloride), spherical (sulfuric acid, pollen) or hexagonal prism (ammonium sulfate) through irregular (fly ash), or fractal-like (soot).

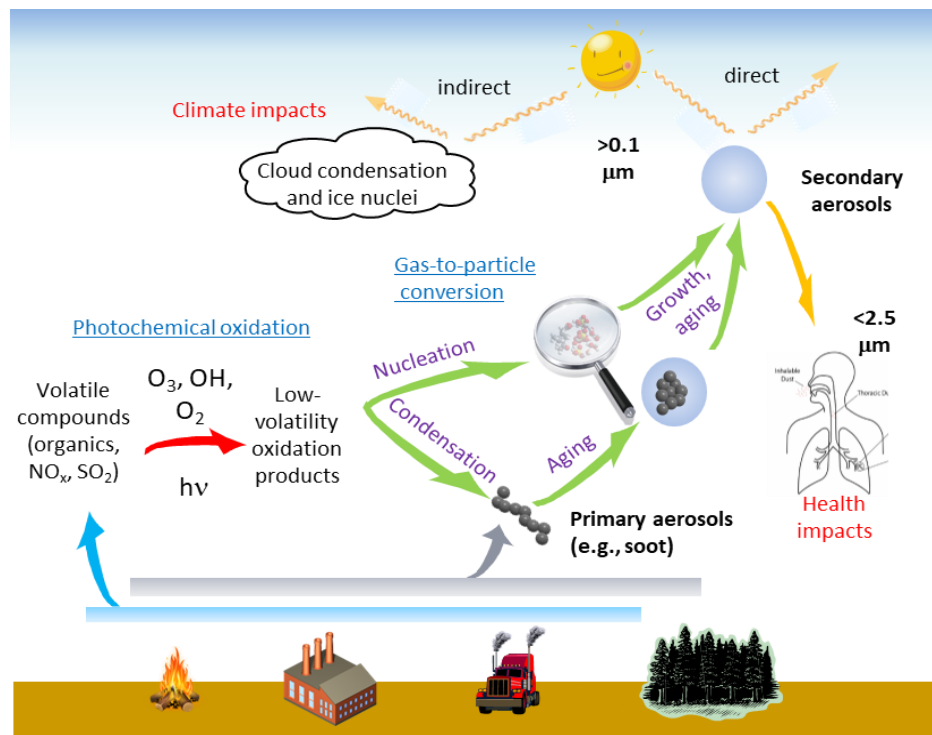


Figure 1.1 The impacts of atmospheric aerosols.

1.1.1 Atmospheric Soot

Soot derived from the incomplete combustion of fossil fuels and biomass burning is a well-known atmospheric pollutant that contributes significantly to the perturbation of the Earth's radiative balance. Internal combustion engines, industrial power plants and residential heating are the main sources of atmospheric soot particles. An efficient light absorber, not only is soot second to CO₂ as a global climate warming agent (Bond, *et al.*, 2013), but its high concentrations in megacities give rise to regional hotspots (Ramanathan & Carmichael, 2008). By warming the atmosphere and cooling the surface, soot creates a temperature inversion that reduces vertical air mixing and exacerbates pollution (Jacobson, 2012). Fractal soot with its high surface area also plays an important role in atmospheric chemistry, e.g., serving as a site for converting NO₂ to HONO (Khalizov, *et al.*, 2010) and reacting with O₃ (Kamm, *et al.*, 1999). Like other atmospheric aerosols, soot affects cloud and ice formation processes, and, consequently, precipitation patterns. Long-range transport in the Northern Hemisphere delivers soot to polar regions, where it is a major component of the Arctic haze; when deposited on the surface of snow and ice, soot accelerates snow melting (Hansen & Nazarenko, 2004).

The extent of the above environmental impacts is strongly dependent on the mixing with other pollutants and morphology of soot particles, which vary with source and combustion conditions (Ramana, *et al.*, 2010). Most atmospheric models assume soot particles to be spheres, which exist separately from other particulate matter constituents. More advanced models treat soot as a core embedded in a shell made of other materials. Soot, however, has a more complex structure, forming from gaseous polycyclic aromatic hydrocarbons (PAH) under oxygen-starved conditions (see Figure 1.2). The PAH

molecules cluster into carbon nanoparticles via a process known as soot inception. The carbon nanoparticles then grow and coagulate to form larger fractal-like structures. Only after significant aging, when gaseous species condense on the fractal aggregates forming a coating layer, does structural collapse to a close-packed arrangement occur.

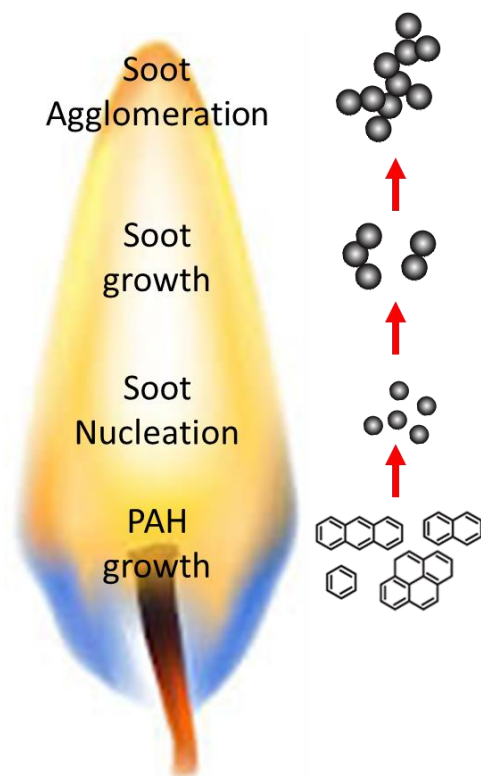


Figure 1.2 Schematic of soot nanoparticle formation from polycyclic aromatic hydrocarbon (PAH) molecules.

Accurate estimations of the impacts of atmospheric soot rely on the fidelity of the models used to represent its geometry and composition (Bond, *et al.*, 2013). However, even for well-aged soot the assumption of a core-shell configuration has been shown to be inaccurate (Cappa, *et al.*, 2012) resulting in substantial uncertainty in the contribution of soot aerosols to climate changes. The source of this uncertainty stems from a poor understanding of the evolution in the properties of soot during atmospheric aging. To

address this shortcoming, the relationship between soot morphology, mixing state, and optical properties during atmospheric aging must be understood. These concepts are described in further detail in the subsections below.

1.1.2 Morphology

Traditionally, the most commonly used aerosol property is the particle size. It is often assumed that the shape of atmospheric aerosols is spherical, which is a valid assumption for most applications of interest so that the size can be represented by the geometric particle diameter. The non-sphericity of atmospheric particles becomes important in dealing with aerosols like soot. Atmospheric soot particles are complex chain aggregates of graphitic monomer spheres whose diameters range from 10 – 60 nm (Adachi, *et al.*, 2007; Wentzel, *et al.*, 2003). Thus, soot aggregates are described by several parameters, including equivalent diameter (by volume, mass, or mobility), monomer diameter, dynamic shape factor, effective density, and fractal dimension (D_f) (DeCarlo, *et al.*, 2004). The latter parameter, defined by the power law (Sorensen, 2011) in Equation (1.1), is commonly used for soot morphology characterization,

$$N_s = k_o \left(\frac{R_g}{R_s} \right)^{D_f} \quad (1.1)$$

where N_s is the number of monomers in the aggregate, k_o is the prefactor (structural coefficient), R_s is the monomer radius, and the aggregate radius of gyration, R_g is given by

$$R_g = \sqrt{\frac{1}{N_s} \sum_{i=1}^{N_s} (\mathbf{r}_i - \mathbf{r}_0)^2} \quad (1.2)$$

Here \mathbf{r}_i denotes the position vector of the i th monomer, and \mathbf{r}_o is the position of the aggregate's center of mass. In this idealized description, all monomers are homogeneous spheres with the same monomer radius R_s , and neighboring monomers are in point touch with each other. An important consequence of Equation (1.1) in describing soot morphology is that it ensures that the self-similarity of the aggregates is preserved on different length scales (i.e., Equation 1.1 applies to the aggregate as a whole and also to any sufficiently large parts of the aggregate). The monomers may be arranged in an open fractal (Figure 1.3a, $D_f < 2$) or densely packed (Figure 1.3b, $D_f \sim 3$) configuration, subject to fuel source and combustion conditions.

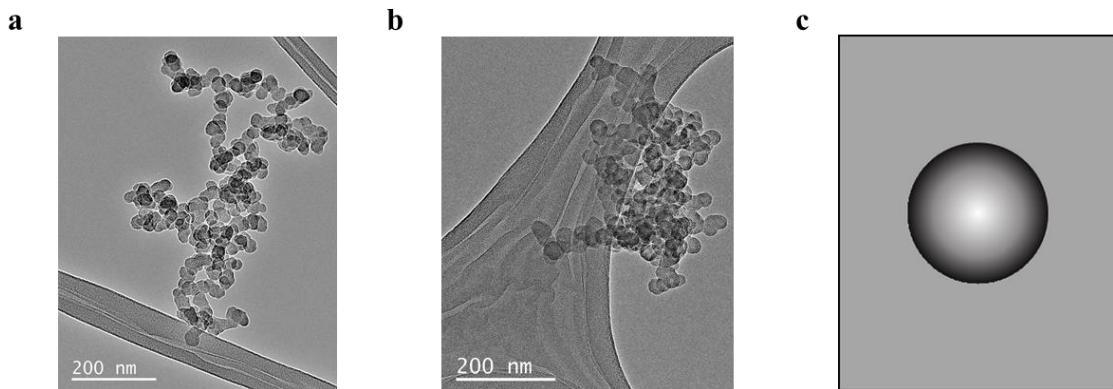


Figure 1.3 SEM micrographs of 240 nm initial mobility diameter soot aggregates in: (a) fractal configuration (before coating) (b) compact configuration (after coating). A volume equivalent spherical approximation is shown in (c).

Depending on their fractal dimension, soot aggregates exhibit varying radiative properties (Liu, *et al.*, 2008) and atmospheric lifetimes (Adachi, *et al.*, 2007). For instance, fractal aggregates have longer atmospheric lifetimes because they experience larger drag than compact particles of equivalent mass (Colbeck, *et al.*, 1997). Also, fractal aggregates absorb solar radiation more effectively than compact particles, producing a greater optical attenuation and radiative heating for a given atmospheric mass loading (Kahnert, 2010b).

Thus, the commonly adopted approximation of soot particles as volume equivalent spheres in atmospheric models (Figure 1.2c) can be quite erroneous, even for compact aggregates especially as N_s increases. Moderately sized compact aggregates have been shown to absorb more solar radiation due to increased interactions between the monomers that make up the aggregate compared to their volume equivalent representation (Liu, *et al.*, 2008).

In the atmosphere, soot aggregates rarely retain their fractal morphology for very long. Their large surface-to-volume ratio promotes gas-surface interactions, such as surface oxidation (Khalizov, *et al.*, 2010; Nienow & Roberts, 2006) and vapor condensation of inorganic or organic compounds (Adachi & Buseck, 2008; Zhang, *et al.*, 2008) which increase the hygroscopicity of soot (Browne, *et al.*, 2015). These processes of surface oxidation, vapor condensation and water absorption change the mixing state of soot and induces morphological transformations of fractal soot to partially compact or fully compact configurations.

1.1.3 Mixing State

Ambient aerosols are often complex mixtures of both organic and inorganic components (Wang, *et al.*, 2010a). Two major representations of aerosols exist in atmospheric models: externally mixed (where individual species are present in different particles) and internally mixed (several species are mixed homogeneously within the same particle). These two representations can be considered as the two extreme scenarios of the generally more complex mixing state of ambient aerosols which vary widely depending on geographical location and source.

Biomass burning soot, which originates from wood combustion and wildfire events, is heavily coated with organic material and is accompanied by the release of brown carbon

(or tar balls) (China, *et al.*, 2013). Diesel engine soot is generated with a thin adsorbed layer of polycyclic aromatic hydrocarbons (PAH), lubricating oil, and sulfuric acid produced during combustion (Olfert, *et al.*, 2007), forming an internally mixed heterogeneous structure. When released into the atmosphere, these soot particles often exist as external mixtures (Jacobson, 2000) with other non-light absorbing aerosols (Figure 1.4a). As the soot particles age, they develop heavy coats and grow due to coagulation, gas phase oxidation reactions and condensation on the particle surfaces. This conversion process transforms fresh fractal forms of soot into internal mixtures of soot with sulfate, nitrate, ammonium, organics, and water (Moffet & Prather, 2009). In atmospheric models, such internal mixtures have either been represented as a well-mixed homogeneous particle (Figure 1.4b) or as a compact soot core embedded in a shell made of other materials as shown in Figure 1.4c (Jacobson, 2000). The well-mixed model has been shown to be unrealistic because the major constituent of soot particles, elemental carbon, is a solid material that does not mix with other chemicals on a molecular level (Jacobson, 2012).

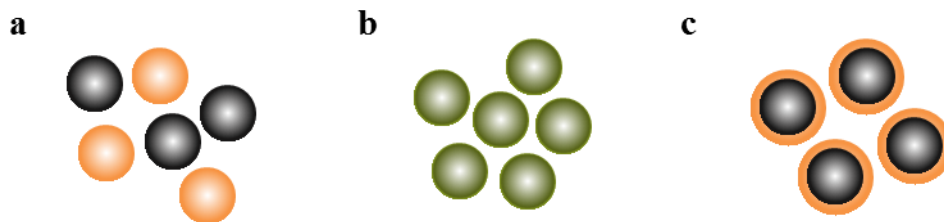


Figure 1.4 Common representations of mixing state: (a) external mixture (b) well-mixed internal mixture (c) core-shell mixture. Both (b) and (c) are internal mixtures.

Some studies have shown that the mixing of soot with other substances can occur within a few hours (Moffet & Prather, 2009; Moteki, *et al.*, 2007), but the extent of internal mixing in the atmosphere is highly variable. Global climate models usually assume that soot mixes with other substances within 5 days of emission (Jacobson, 2001b). Within this

relatively short duration, the morphology of soot in the mixture may remain unaltered or change considerably and that has significant impact on its optical properties (Jacobson, 2000; Moteki, *et al.*, 2007).

1.1.4 Atmospheric Aging

Freshly emitted soot particles are generally hydrophobic but may take up water because of water-soluble compounds (such as sulfuric acid) whose precursors may be present in the fuels (Weingartner, *et al.*, 1997). During transport in the atmosphere, the hydrophilicity of soot can increase due to surface oxidation, condensation of semi-volatile vapors, coagulation with other aerosol particles, and cloud processing. Collectively, these processes which are referred to as aging, change the mixing state of soot. The aging time scale of soot (i.e., the time required for fresh hydrophobic soot to be converted to hydrophilic soot) is an important parameter in global climate models. Sufficiently aged particles may become cloud condensation nuclei (CCN) or ice nuclei (IN), thus affecting the global transport of soot.

Surface oxidation: Oxidation by atmospheric OH, O₃, SO₂, NO_x, and HNO₃ leads to the formation of polar surface groups that can allow the initially hydrophobic soot to become hydrophilic (Zuberi, *et al.*, 2005). These surface groups may also present sites for molecular adsorption and other heterogeneous chemistry, such as the dark (Khalizov, *et al.*, 2010) or photoactivated (Monge, *et al.*, 2010) reaction of soot with NO₂ and/or H₂O that results in the formation of HONO, an important source of OH radicals.

Vapor condensation: The vapor condensation of organic and inorganic compounds of low volatility is a major path toward the formation of mixed or coated soot. Heavily coated soot

is often represented as a spherical soot-core and coating-shell configuration, which may not always be realistic. Not always do aged soot aggregates collapse into compact structures or become located at the center of the host material (Adachi, *et al.*, 2010). Indeed, studies suggest that vapor condensation on soot aggregates is initiated in the interstitial regions between monomers because of the inverse Kelvin effect (Crouzet & Marlow, 1995). Further growth may occur preferentially between monomers leading to the formation of a pendular ring of condensate which increases in volume till the entire aggregate is enclosed by the coating. Parts of the aggregate with larger void spaces may support quicker growth, resulting in an off-center location of the soot particle within the coating host. Such off-center configurations have been observed in field studies (Adachi & Buseck, 2008; Adachi, *et al.*, 2010; Wentzel, *et al.*, 2003).

Heterocoagulation: Coagulation of emitted soot with other particulates (sea spray, ammonium sulfate) present in the atmosphere results in the formation of internal-external mixtures (IEM) of decreasing hydrophobic content with increasing distance from the emission source (Jacobson & Seinfeld, 2004). Coagulation of soot with sulfate or nitrate aerosols increases its water affinity whereas collisions with hydrophobic primary organic aerosols may diminish water adsorption until the surface of mixed particles is functionalized via surface oxidation reactions. A study on the day and night aging timescales of atmospheric soot revealed coagulation to be the dominant aging mechanism for soot at nighttime (Riemer, *et al.*, 2004). Model simulations on a global scale also indicate that coagulation accounts for about 50% of the increased particle size of mixed soot aggregates following their emissions while the rest may be attributed to surface oxidation and condensation processes (Jacobson, 2001a).

Cloud processing: The process of forming a stable liquid droplet or ice particle is called activation. This process may occur homogeneously when gas molecules aggregate to form clusters that change phase to liquid or solid. However, nucleation of water droplets in particle-free air requires unrealistically high supersaturations (up to 400%). In the real atmosphere, cloud droplets form when water nucleates heterogeneously on aerosol particles at supersaturations as low as 0.1 – 0.3%. Aerosol particles that can potentially form cloud drops are known as cloud condensation nuclei (CCN) and can indirectly influence rainfall patterns.

The ability of a particle to act as CCN at a given water saturation (S_w) depends on the soluble particle fraction it has, which is a function of its size and composition (Dusek, *et al.*, 2006a). This relationship is described by the Kohler equation (Seinfeld & Pandis, 2006):

$$\ln(S_w) = \frac{4M_w\gamma_w}{RT\rho_w D_p} - \frac{6n_s M_w}{\pi\rho_w D_p^3} = \frac{A}{D_p} - \frac{B}{D_p^3} \quad (1.3)$$

where M_w , ρ_w are the molecular weight and density of the water, γ_w is the surface tension of the air-water interface, n_s is the number of moles of the soluble species, R is the gas constant, T is the temperature and D_p is the particle diameter. Equation (1.3) describes the water supersaturation required to maintain the stability of a droplet. The A term accounts for the Kelvin effect which tends to increase the saturation vapor pressure while B accounts for the solubility of the particle which decreases the saturation vapor pressure. For spherical particles, the critical supersaturation decreases with increasing diameter.

Fresh soot aggregates are poor CCN due to the large critical supersaturations associated with the small diameter and hydrophobic nature of the monomer spheres

(Dusek, *et al.*, 2006b). The accumulation of hygroscopic material during aging increases the size and hydrophilicity of soot particles thus making them more effective CCN (Zuberi, *et al.*, 2005). In contrast, the acquisition of non-polar PAHs can inhibit water absorption or adsorption (Bigg, 1986; Prenni Anthony, *et al.*, 2007). Aggregates with increased hydrophilicity can also serve as ice nuclei (IN) when immersed in a supercooled droplet (DeMott, *et al.*, 1999). As CCN and IN, soot particles have the propensity to affect the formation of warm and cold clouds, thereby impacting cloud reflectivity, lifetime and precipitation, which in turn affects the hydrological cycle, and, consequently surface temperature (Bond, *et al.*, 2013; Jacobson, 2012). The dissipation of clouds during evaporation could also cause further particle collapse or aggregation into larger clusters which would significantly alter soot morphology.

The combined processes of atmospheric aging may lead to mixing states and structural transformations far more complicated than the ones currently used in atmospheric models. Aged soot particles may be embedded in organic and inorganic material (Adachi & Buseck, 2008), partially coated (China, *et al.*, 2015), or thinly coated (Khalizov, *et al.*, 2009b). Dissimilar restructuring behavior observed for soot particles coated by similar organic compounds (Chen, *et al.*, 2016) raises the question of the distribution of condensed material on the aggregate surface and how it relates to structural change. Thus, knowledge of the mixing state of soot is key to understanding its restructuring mechanism and associated impacts.

1.1.5 Optical Properties

Atmospheric aerosols directly influence climate processes through the scattering and absorption of incident solar (short wave) radiation, and via the absorption of surface-

emitted thermal (infrared) radiation. The intensity of light, as it passes through aerosol, decreases because of scattering and absorption, which together represent light extinction. The ratio of scattering to extinction is defined as the single scattering albedo (SSA) and represents the fraction of light extinction that can be attributed to scattering. Particles with SSA near unity tend to scatter light and cool the atmosphere, whereas particles with lower values of SSA absorb light and produce a warming effect. Absorbing aerosols are also defined in terms of a mass absorption cross-section (MAC) which relates the absorptive efficiency of a particle per unit mass.

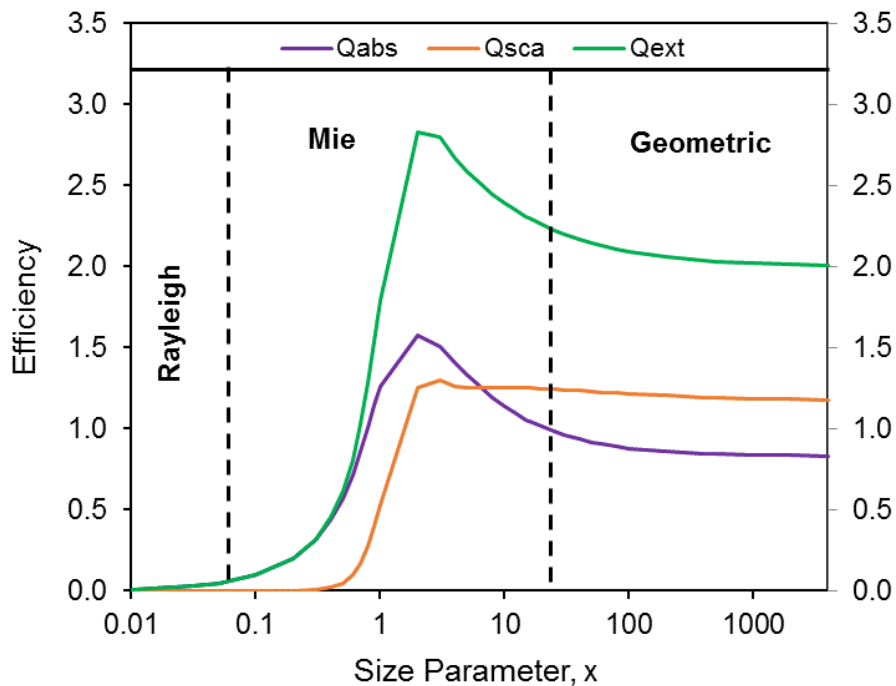


Figure 1.5 Single-particle extinction (Q_{ext}), absorption (Q_{abs}), and scattering (Q_{sca}) efficiencies of an absorbing sphere ($m = 1.73 + 0.6i$).

For a given wavelength of light, the magnitude of scattering and absorption depends on particle size, shape, and refractive index (Seinfeld & Pandis, 2006). This is conveniently illustrated with the aid of the size parameter, x :

$$x = \frac{2\pi R_s}{\lambda} \quad (1.4)$$

where λ is the light wavelength. Particles smaller than the light wavelength ($x \ll 1$) are in the Rayleigh regime, particles which are comparable in size with the wavelength ($x \sim 1$) are in the Mie regime, while particles much larger than wavelength ($x \gg 1$) are in the geometric regime (see Figure 1.5).

Scattering and absorption can easily be estimated using Lorentz-Mie theory for spherical, homogeneous particles (Bohren & Huffman, 1983). However, such predictions are not easily made for particles with a complex morphology like soot aggregates. One way of applying the Mie theory to soot is by using the volume-equivalent sphere approximation. This approximation tends to work well for small ($N_s < 10$) and compact aggregates but becomes unreliable for large and fractal aggregates that are not representative of compact spheres (Köylü, *et al.*, 1995). This is because a compact sphere of soot shields part of the light absorbing mass near its center from interacting with the incident light. By contrast, a fractal aggregate allows a larger part of its graphitic mass to come into contact with incident light, thus contributing to absorption of radiative energy. This is why the homogeneous sphere model underestimates absorption and over-predicts the SSA of bare soot aggregates. The Rayleigh-Debye-Gans (RDG) theory, which is considered the simplest method for predicting light absorption and scattering by aggregates, assumes that soot monomers are smaller than the incident wavelength, and that multiple electromagnetic interactions among the monomers are negligible (Sorensen, 2001). Thus, scattering and absorption by aggregates can be represented as functions of scattering and absorption of a single monomer sphere. While the first assumption in the RDG theory is often well satisfied by soot aggregates, the second is not. Early studies have shown that monomer interactions can

significantly affect calculated optical properties (Fuller, 1995; Mackowski, 1995). For instance, (Liu & Mishchenko, 2005) showed that accounting for monomer interactions enhanced soot absorption by as much as 25% and SSA by a factor of 10. With the steady advance of computational capacities, more rigorous numerically exact methods have become increasingly preferred. Methods such as the Multiple Sphere T-Matrix (MSTM) (Mishchenko, *et al.*, 1996) and Discrete Dipole Approximation (DDA) (Draine & Flatau, 1994) explicitly consider the fractal morphology of soot when calculating its optical properties. A significant complexity in using these theoretical models arises from the need to define a specific morphology or more often consider a range of morphologies; those are subject to variation during atmospheric aging.

Most atmospheric particles are efficient light scatterers with SSA values close to unity. In contrast, freshly emitted soot particles (black carbon) scatter weakly, but absorb strongly, with SSA as low as 0.15 (Saliba, *et al.*, 2016; Schnaiter, *et al.*, 2003). Such strong absorption results in the warming of the atmosphere. Multiple studies have shown that the internal mixing of soot leads to an enhancement in its ability to absorb and scatter solar radiation (Chylek & Wong, 1995; Jacobson, 2000; Khalizov, *et al.*, 2009a), significantly altering its climate effects. The physically unrealistic well-mixed model, which is commonly used to represent internally mixed soot in global climate models, can lead to the over-prediction of absorption by 100%. Radiative transfer models that assume the more realistic core-shell geometry estimate forcing due to internal mixtures of soot to be much lower (Jacobson, 2001a) with reported absorption enhancements of about 30% (Fuller, *et al.*, 1999; Schnaiter, *et al.*, 2003).

Laboratory measurements (Bueno, *et al.*, 2011; Shiraiwa, *et al.*, 2010) have shown that the core-shell model is likely to be representative of heavily aged or thickly coated soot particles, which tend to assume the core-and-shell morphology. However, Zeng, *et al.* (2019) showed that adopting a core-shell model underestimates the radiative forcing caused by hygroscopic growth of aged soot aggregates and overestimates the radiative forcing caused by internal mixing. On the other hand, thinly coated soot particles may retain their fractal configuration if the coating material is solid or highly viscous (Leung, *et al.*, 2017b). Explicit consideration of the fractal morphology of thinly coated soot aggregates via DDA calculations has yielded varying results with the prediction of significantly higher (Soewono & Rogak, 2013) and lower (Liu, *et al.*, 2016) light absorption values than the core-shell Mie model for a volume equivalent sphere. Both small (Cappa, *et al.*, 2012) and large (Liu, *et al.*, 2015) absorption enhancement factors have been reported in ambient measurements for heavily aged soot. Observations of lower absorption enhancement contrast with lab measurements, and was demonstrated in the study by Fierce, *et al.* (2016) to be the result of neglecting particle composition diversity. Their analysis showed that the thickest coatings are found on smaller soot particles, resulting in strong absorption enhancement. Larger soot particles end up with thin coatings, corresponding to a weak enhancement in light absorption. Since absorption is dominated by the larger, thinly coated soot particles under most atmospheric conditions, the average enhancement is also low. Thus, laboratory studies which assume a uniform coating thickness across the entire population of soot containing particles tend to overestimate absorption by as much as a factor of 2 (Fierce, *et al.*, 2016). Overestimation of absorption enhancement in laboratory and modeling studies may also be indicative of a deviation from the assumed core-shell

geometry of thickly coated soot particles. Sedlacek, *et al.* (2012) used a single particle soot photometer (SP2) to show the existence of these non-core shell soot containing particles and estimated that they constituted about 60% of the particle population in a plume from biomass burning. Calculations confirm that such off-center embedded soot aggregates show a lower enhancement (as much as 20%) in light absorption (Adachi, *et al.*, 2010; Fuller, *et al.*, 1999; Kahnert, *et al.*, 2012). However, it was estimated that concentric core-shell geometries will overestimate absorption by no more than 15% (Fuller, *et al.*, 1999).

The knowledge of the evolution in the optical properties of soot during atmospheric aging is crucial for the accurate quantification of the soot radiative properties. Results from previous studies show that it is necessary to account for the variations that arise due to changes in both particle mixing state and morphology. Discrepancies between several studies considering both modeled and measured optical properties for atmospheric soot, point to a need for measurements and modeling studies of well-characterized laboratory-based soot aggregates. Numerical methods for optical calculations must be employed as it is clear from the above cited and other studies (He, *et al.*, 2015; Kahnert, *et al.*, 2013; Kahnert, *et al.*, 2012; Luo, *et al.*, 2018) that the generally adopted core-shell model does not suffice as it neglects the possibilities of other mixing states and morphologies. From an atmospheric modeling perspective, it is imperative to identify the morphological and compositional features that have the strongest impact on optical properties, and those that only cause minor changes.

1.1.6 Aerosol Models

Atmospheric formation and removal of aerosols are governed by several complex processes such as nucleation, condensation, evaporation, coagulation, chemical transformations, partitioning, wet and dry deposition. Mathematical models are typically employed to predict the spatial and temporal distributions of aerosols or gaseous species in the atmosphere based on these individual processes, some of which are parameterized for more computational efficiency (Coakley, *et al.*, 1983; Nenes & Seinfeld, 2003). The most general form of an atmospheric aerosol model adopts a distribution-based approach, using several modes or bins to predict aerosol size and composition distribution as a function of location and time. The representation of soot particles in these aerosol models has proven to be challenging because of their non-uniform composition and constantly evolving physical properties during their atmospheric lifetime. Thus, simplifying assumptions of soot morphology and mixing state are made.

Some aerosol models have tried to improve on the previously described external and internal mixing simplifications applied to soot by adopting approaches where processes such as condensation of sulfuric acid on soot, chemical oxidation and/or coagulation between different particle classes are explicitly modeled to some extent (Stier, *et al.*, 2005; Wilson, *et al.*, 2001). However, these models represent the particle population as a bulk, and as such, neglect the diversity in particle composition within a size range. A more advanced particle-resolved aerosol model, PartMC-MOSAIC, overcame this limitation by explicitly tracking the composition of each individual particle in the aerosol population (Riemer, *et al.*, 2009; Zaveri, *et al.*, 2008). This approach has the obvious benefit of prediction accuracy down to the particle scale and thus can be used to connect microscale

processes with larger atmospheric models. However, the volume equivalent sphere approximation still applies for soot aggregates and as such, no morphological transformations of the aggregate backbone during aging events are considered. For accurate predictions of soot impacts, particle-resolved aerosol model capabilities need to be upscaled to include the restructuring of soot-containing particles in addition to predicting per particle composition. Thus, it is important to understand the restructuring mechanisms of soot and identify the key parameters that control them for incorporation in aerosol and larger scale atmospheric models.

1.2 Research Objectives

This dissertation uses a combination of laboratory and modeling techniques to identify and implement relationships that interconnect soot mixing state, morphology, optical properties and cloud forming ability as a function of changing environmental conditions. The following outstanding scientific questions will be addressed:

- What drives aggregate restructuring?
- How is the coating material distributed around the soot aggregate and how does its restructuring depend on the coating distribution?
- How do light absorption and scattering depend on morphology and the distribution of the coating material?
- How does the distribution of the coating material and morphology of the aggregate affect its ability to act as cloud condensation nuclei (CCN)?

Addressing the above questions require a fundamental knowledge of the morphology and mixing state of soot. Mass-mobility measurements along with scanning electron and transmission electron microscopies will be used to examine the structure and

composition of generated airborne aggregates. Specific tasks that will be performed include:

- (a) Conducting experiments and simulations to understand how soot morphological, optical and cloud nucleating properties respond to aging.
- (b) Developing predictive parameterizations from relationships established in experiments and simulations.
- (c) Implementing the parameterizations in a particle-resolved aerosol model.

The physical parameterizations developed for particle mixing state, morphology, and optical properties will improve predictions of the impacts of soot on radiative forcing.

1.3 Organization of Dissertation

The material presented in this report is organized into ten chapters. After this introductory chapter, Chapter 2 describes the experimental and computational techniques adopted in this study. Chapter 3 explains the development of a parameter for describing the mixing state and morphology of soot during atmospheric aging. The main properties that control aggregate restructuring are identified and the implications on the evaluation of soot impacts are discussed. Chapter 4 investigates the roles of vapor condensation and coating evaporation in aggregate restructuring as well as the importance of coating wettability. The results obtained in Chapters 3 and 4 are expanded upon in Chapter 5 for a more realistic aging environment consisting of multiple condensing vapors. The impacts of a multicomponent system of coatings on aggregate restructuring and CCN activation of soot are discussed. Chapter 6 outlines the development of an algorithm to simulate aggregate restructuring. Chapter 7 describes methods for obtaining accurate optical properties of bare soot via laboratory measurements. Chapter 8 details the optical calculations of numerically

simulated soot aggregates. The effects of morphology and coating distribution on the soot radiative properties are examined. The incorporation of the morphology and mixing state parameter into a particle-resolved aerosol, PartMC-MOSAIC is described in Chapter 9. Finally, conclusions and directions for future study are provided in Chapter 10.

CHAPTER 2

METHODOLOGY

To simulate the effects of aging on atmospheric soot, a combination of laboratory experimentation and computational modeling techniques were employed. In this chapter, a brief overview of laboratory approaches for soot aging studies is given and following this, detailed descriptions of the experimental setups used in this research study. Analysis procedures for characterizing soot properties (e.g., size, mass, composition, structure, optics etc.) are discussed as well as the main computational algorithms used to simulate soot optical properties.

2.1 Laboratory Studies

The vast majority of knowledge about soot aging, transformation and impacts during atmospheric transport is derived from laboratory investigations. Most of these studies make use of either aerosol flow reactors (Ghazi & Olfert, 2013; Khalizov, *et al.*, 2009a; Ma, *et al.*, 2013a; Slowik, *et al.*, 2007) or large volume environmental chambers (smog chambers) (Khalizov, *et al.*, 2013; Schnitzler, *et al.*, 2014; Wittbom, *et al.*, 2014) in combination with mass-mobility instrumentation. Chamber experiments are generally carried out in batch mode and are designed to mimic atmospheric conditions as closely as possible. As with the real atmosphere, there are several complicating factors associated with chamber studies such as the interaction of soot aggregates with complex vapor mixtures whose compositions and properties are unknown (Lee, *et al.*, 2004; Qiu, *et al.*, 2012). Flow reactor experiments, on the other hand, are more often suited for understanding the effects of

individual gaseous species on soot properties. Though both experimental approaches were employed, flow reactor methods are of central interest to the studies presented in this dissertation.

2.1.1 Flow Reactor Experiments

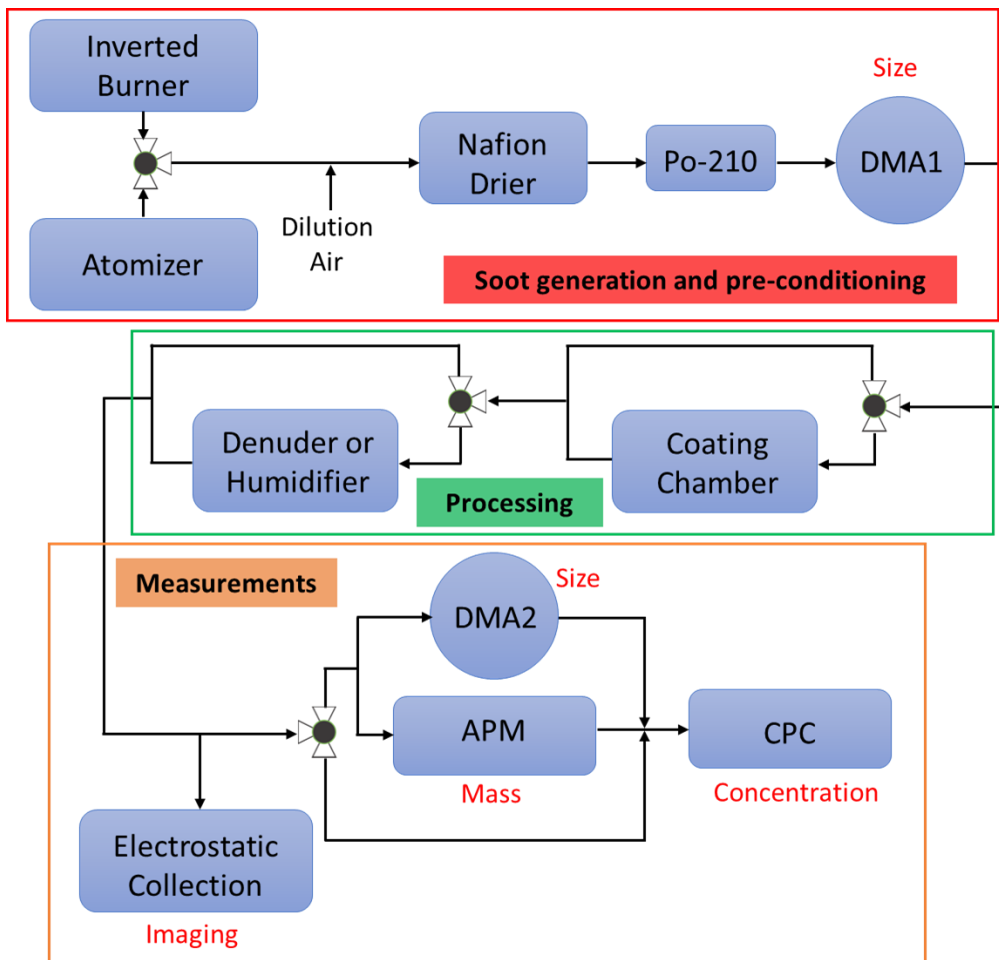


Figure 2.1 The aerosol system comprised of the generation, coating/processing, and measurement modules. DMA is the differential mobility analyzer, APM is the aerosol particle mass analyzer, and CPC is the condensation particle counter.

The experimental setup for the flow reactor system is comprised of 3 units for aerosol generation, processing and measurements (Figure 2.1). Detailed explanation of the instrumentation is provided in Appendix A.

Aerosol generation: Soot was generated by combustion of natural gas in air in an inverted diffusion burner (Coderre, *et al.*, 2011; Stipe, *et al.*, 2005). A global flame equivalence ratio ϕ of 0.5 was maintained, using 0.9 and 17.1 liters per minute (LPM) of natural gas and air, respectively (ϕ is the actual fuel–oxygen ratio divided by the stoichiometric fuel–oxygen ratio). The inverted burner employed in this study produced a very stable output in terms of the particle number size distribution, number density, and effective density. Soot was sampled from the burner exhaust with an ejector dilutor, using particle-free air pre-heated to 150 °C to prevent water condensation. Other aerosols were produced by nebulization of the corresponding aqueous solutions in a constant output atomizer (TSI 3076). In all cases, the generated aerosol flow was dried in a diffusion drier filled with silica gel and in a Nafion drier (Perma Pure, PD-07018T-24MSS), which were connected in series, resulting in a relative humidity (RH) below 5%, as measured by a Vaisala HMM100 sensor. Aerosol was brought to an equilibrium charge distribution in a bipolar diffusion charger (Po-210, 400 μ Ci, NRD Staticmaster) and size classified in a differential mobility analyzer (DMA, TSI 3081), which was operated at a 0.3 LPM sample flow and a sheath-to-sample flow ratio of 10, corresponding to a 10 – 700 nm mobility diameter range. In most experiments, after leaving the first DMA, soot aerosol was passed through a thermodenuder (TD1) to remove intrinsic organic carbon.

Aerosol processing: Size-classified particles were sent through a Pyrex glass chamber (Figure 2.2) partly filled with liquid coating material (~15 ml) and maintained at a constant

temperature by a heating tape connected to a PID controller. The chamber acted as a saturator, i.e., upon entering the chamber, aerosol flow became saturated with coating vapor. After leaving the chamber, the aerosol flow cooled down while traveling along the stainless-steel tubing, resulting in a supersaturated vapor condensing on the particles and on the tubing wall. When required, the coating was removed from the particles by sending the aerosol flow through a thermal denuder (TD2) maintained at 300°C or humidified by sending the aerosol flow through a Nafion humidifier. In some experiments, particles were collected on silicon wafer chips (Ted Pella, 16008) or lacey grids (Ted Pella, 01883) for scanning electron microscopy (SEM) imaging, using a custom-built electrostatic sampler (Dixkens & Fissan, 1999).

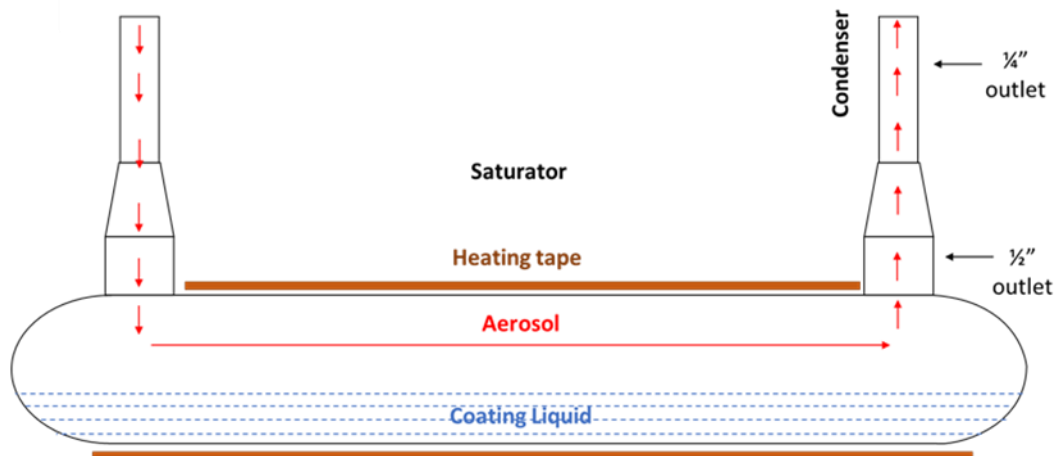


Figure 2.2 Coating chamber made of Pyrex glass (46 cm length and 2 cm inside diameter) containing coating liquid.

Mass-mobility measurements: Particle mobility diameter and absolute mass were measured using a system consisting of two DMAs (tandem DMA or TDMA), an aerosol particle mass analyzer (APM, Kanomax 3601), and a condensation particle counter (CPC, TSI 3772). The first DMA was maintained at a constant voltage to select particles of a specified

mobility diameter. The size-classified particles were coated or coated/denuded, as described above. To measure mobility diameter of processed particles, the aerosol flow was sent through the second DMA. To measure coated particle mass, aerosol flow was diverted to the APM. Voltage in the second DMA or APM was scanned and the resulting particle concentration at the exit of either was measured by the CPC to obtain mobility or mass distribution, respectively.

Optical measurements: In some experiments, a cavity attenuated phase shift single scattering albedo (CAPS-PM_{SSA}, Aerodyne) monitor was used to measure light scattering and extinction by soot aerosols at a wavelength of 530 nm. Absorption values were derived from the difference of measured scattering and extinction. For optical studies, aerosol generation and processing were performed as described above. However, the sheath and sample flow rates in both DMAs were maintained at 6.5 and 1.0 LPM respectively. In some experiments, a second bipolar charger was placed between the two DMAs to recharge the aerosol flow before size re-classification by DMA2. The purpose of this second charger was to help eliminate multiply charged particles that bias measurement accuracy. Upon exiting the dual DMA system, the aerosol flow of fresh or processed particles was further diluted to allow simultaneous measurements of optical properties and particle number concentrations at a 1.0 LPM sample flow. Aerosol number density was adjusted between 200 and 2000 particles cm⁻³ to maintain extinction and scattering coefficients in the range 1 – 50 Mm⁻¹. A schematic of the aerosol system with the integrated CAPS-PM_{SSA} and secondary charger is illustrated in Figure 2.3.

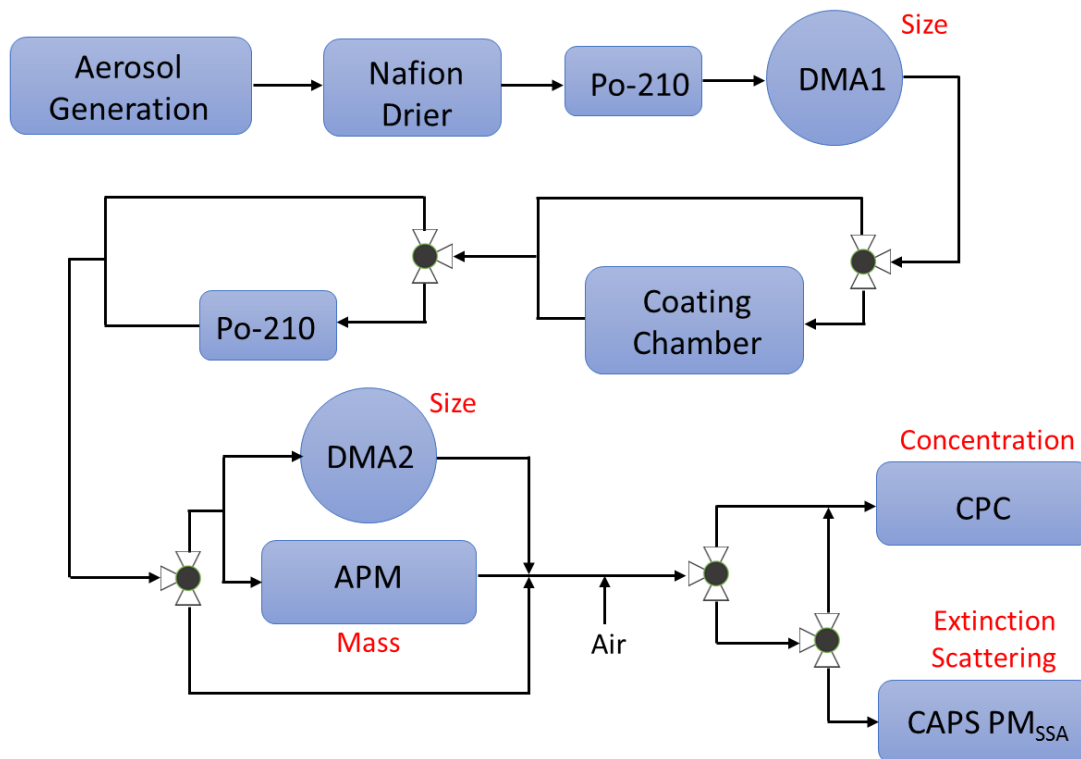


Figure 2.3 Experimental setup for light scattering and extinction measurements. CAPS PM_{SSA} is the cavity attenuated phase shift single scattering albedo monitor.

2.1.2 Electron Microscopy and Image Processing

Aerosol samples collected on silicon chips and lacey grids were imaged with a LEO 1530VP Field Emission Scanning Electron Microscope (FE-SEM), using a 5 kV accelerating voltage. A limited number of samples were studied by FEI Titan 80-300 ETEM located in the Center for Functional Nanomaterials at Brookhaven National Lab, using a 300 kV accelerating voltage. No metal or carbon film coating was applied to the particle samples before imaging. For each sample, at least 12 randomly selected individual aggregates were inspected at different magnifications. The SEM and ETEM micrographs were manually pre-processed using Adobe Photoshop to adjust contrast and/or gray level in order to separate particles from the substrate background. For soot aggregates on silicon, adjusting the levels was sufficient, but for soot aggregates on lacey grid samples a manually

drawn outline was required because the aggregates and lacey fibers had a comparable level of gray and/or contrast. The average monomer diameter was determined by measuring 10 – 15 monomers in each aggregate.

Processed images were used to measure particle dimensions and morphology. In the case of soot, the aggregate convexity was determined (Chakrabarty, *et al.*, 2006a; China, *et al.*, 2015). Convexity is the ratio of the aggregate projected area A_a over the area of the convex hull polygon $A_{polygon}$, as defined by Equation (2.1),

$$Convexity = \frac{A_a}{A_{polygon}} \quad (2.1)$$

where A_a and $A_{polygon}$ were determined from the images using MATLAB-based code written in-house (Figure 2.4). The convexity characterizes the compactness of soot aggregates, varying between 0 and 1, with the larger value corresponding to more compact aggregates.

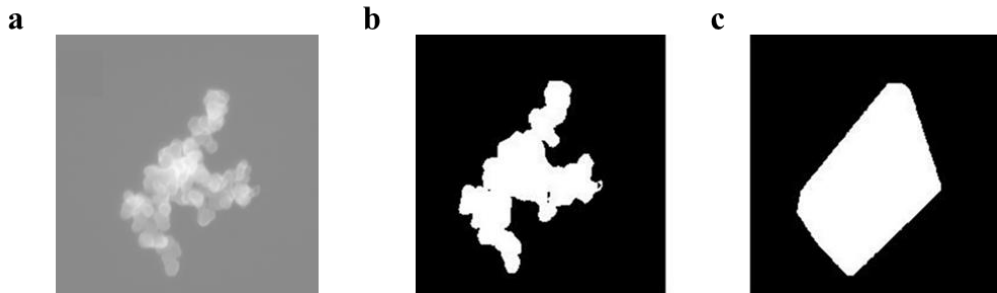


Figure 2.4 Calculation of convexity: (a) original SEM image, (b) 2D projected area of aggregate (c) convex polygon around aggregate image.

2.1.3 Data Analysis

Particle mass growth factor (G_{fm}) and diameter growth factor (G_{fd}) were used to characterize the change in particle mass and size, respectively during aging:

$$Gfm = \frac{m_{processed}}{m_{initial}} \quad (2.2)$$

$$Gfd = \frac{D_{processed}}{D_{initial}} \quad (2.3)$$

where $m_{initial}$ and $m_{processed}$ are particle mass and $D_{initial}$ and $D_{processed}$ are the mean particle mobility diameter before and after exposure to the condensing vapor. The precision of TDMA and APM measurements was better than 0.5% and 1%, respectively.

The effective particle density ρ_{eff} was calculated from particle mass ($m_{initial}$ or $m_{processed}$) and diameter ($D_{initial}$ or $D_{processed}$),

$$\rho_{eff} = \frac{6m}{\pi D^3} \quad (2.4)$$

Particle material density ρ_m , was calculated from the material density of soot ρ_{soot} , density of the coating material, $\rho_{coating}$ and mass fraction of the coating (f_m):

$$\rho_m = \frac{\rho_{coating}\rho_{soot}}{f_m\rho_{soot} + (1 - f_m)\rho_{coating}} \quad (2.5)$$

$$f_m = 1 - \frac{1}{Gfm} \quad (2.6)$$

The material density of soot was taken as 1.77 g cm^{-3} (Park, *et al.*, 2004). From the particle material density, the volume equivalent diameter D_{ve} (Equation 2.7), and shape factor χ_{shape} (Equation 2.8) before and during aging were derived as follows:

$$D_{ve} = \sqrt[3]{\frac{6m_{processed}}{\pi\rho_m}} \quad (2.7)$$

$$\chi_{shape} = \frac{D_{processed}}{C_{processed}} \times \frac{C_{ve}}{D_{ve}} \quad (2.8)$$

where $C_{processed}$ and C_{ve} are the Cunningham slip correction factors for $D_{processed}$ and D_{ve} , respectively (DeCarlo, *et al.*, 2004).

For optical measurements, aerosol extinction (C_{ext}), scattering (C_{sca}), and absorption (C_{abs}) cross-sections (in m^2) were calculated by normalizing the corresponding optical coefficients, σ_i over the measured particle number density, N :

$$C_i = \frac{\sigma_i}{N} \quad (2.9)$$

where i represents extinction, scattering or absorption. The single scattering albedo, SSA is derived from the ratio of scattering and extinction:

$$SSA = \frac{\sigma_{sca}}{\sigma_{ext}} \quad (2.10)$$

From these measurements, the relative enhancement of light absorption by soot aggregates as a function of morphology, mixing state, and coating thickness can be estimated. The mass absorption cross-section, MAC (in m^2/g) was determined using particle mass from mass-mobility measurements:

$$MAC = \frac{C_i}{m} \quad (2.11)$$

2.2 Computational Studies

Morphological information derived from experimental studies was used to simulate soot aggregates for the calculation of their optical properties via approximate and numerically exact methods. The numerical methods adopted in this study for simulating the optical properties of soot are the Multiple Sphere T-Matrix (MSTM) and Discrete Dipole Approximation (DDA). Results obtained from these methods were also compared against the commonly used Rayleigh-Debye-Gans (RDG) and Mie approximations for soot optical studies.

2.2.1 Numerical Generation of Aggregates

The numerical generation of soot aggregates was done using algorithms that imitate the formation of fractal geometries as described by the statistical scaling law in Equation (1.1). Such algorithms can be divided into particle-cluster aggregation (PCA) and cluster-cluster aggregation methods (CCA), depending on whether aggregation in the simulation occurs between isolated particles and clusters, or between clusters. Both methods were adopted in this work with the PCA algorithm used exclusively for the generation of fractal aggregates and the CCA algorithm for both fractal and compact morphologies.

Particle cluster aggregation (PCA) algorithm: In the PCA method, the aggregate is formed via iterative additions of single monomer spheres. The aggregate generation process begins with the random attachment of two monomers to form a cluster, after which further monomer additions to the cluster are considered successful if the monomers are in point touch (no overlap) and the calculated radius of gyration, R_g satisfies Equation (1.1) for preset values of fractal dimension D_f , and prefactor k_o . In this dissertation, the latter two were set to 1.78 and 1.3 (Sorensen, 2011), respectively, to represent fractal aggregates

formed via diffusion-limited cluster aggregation (DLCA) (Kolb, *et al.*, 1983; Meakin, 1983). The clustering is repeated until the aggregate attains the desired number of monomers, N_s , which was varied between 5 and 1000. The simulated aggregates are assumed to be monodisperse, with the monomer radius R_s set in the range of 5 to 30 nm, as is typical for laboratory generated and field collected soot aggregates (Adachi, *et al.*, 2007; Wentzel, *et al.*, 2003). The user-interactive FracMAP package (Chakrabarty, *et al.*, 2009) was used to generate aggregates via the PCA method.

Cluster-cluster aggregation (CCA) algorithm: The CCA method is based on a hierarchical scheme of aggregation of small sized clusters which obey Equation (1.1). In this dissertation, the CCA algorithm developed by Mackowski (1995) was used to generate both fractal ($D_f < 2.1$) and compact ($D_f > 2.1$) aggregates and is described here in brief. The aggregate generation process begins with a set of isolated spheres, $N_M \geq N_s$. A random pair is picked and joined at a random contact point leaving $N_M - 1$ particles. A new pair is selected from the set, and the pair is joined. The combination of a pair of clusters is constrained by the distance between the center of masses of the two clusters, which is such that Equation (1.1) still holds. The combining clusters are then rotated as solid bodies until they have at least one contact point and no overlapping. After performing the procedure for all clusters on one level, another level involving larger clusters begins and the procedure is repeated till an aggregate of N_s spheres has been formed.

Aggregates produced by the CCA algorithms are more representative of real soot particles formed via DLCA (Filippov, *et al.*, 2000). In contrast to the PCA generated structures, no central part or symmetry of the aggregate can be noticed (see Figure 2.5).

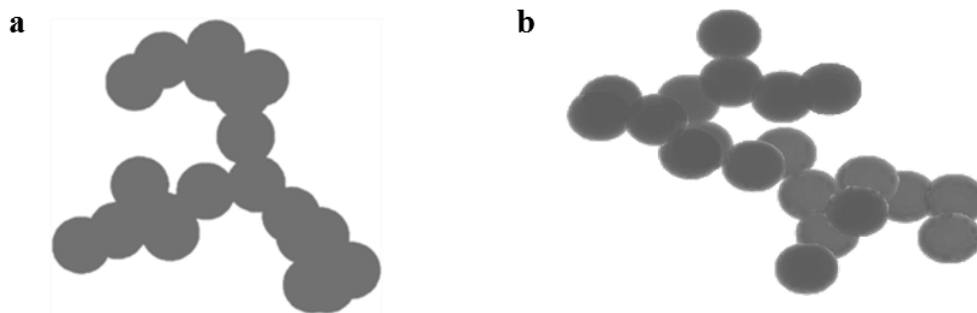


Figure 2.5 An aggregate of 20 monomers with fractal dimension $D_f = 1.78$ and prefactor $k_o = 1.3$ generated by (a) particle-cluster aggregation and (b) cluster-cluster aggregation.

2.2.2 Multiple Sphere T-Matrix (MSTM)

The MSTM method (Mackowski & Mishchenko, 2011) is a robust computational technique that can be applied to arbitrary configurations of spheres such as the monomers that comprise a soot aggregate. It is based on the superposition formulation for radiative interactions among monomer clusters in fixed and random orientations with respect to the incident electromagnetic (light) wave (Mishchenko, *et al.*, 1996). The monomers in the aggregate can be located internally or externally to each other and may have different dielectric properties. Using the MSTM method for calculating the optical properties of soot imposes two restrictions: (1) the monomers in the aggregate must be homogeneous spheres, (2) the monomers must not overlap i.e., the surfaces of any two spheres, whether internal or external, can only have one point of contact. An important advantage of the T-matrix method is that it allows one to perform analytical orientational averaging of optical cross-sections obtained for different realizations of the same aggregate (Khlebtsov, 1992; Mishchenko, 1991). Thus, its computational speed and accuracy in comparison to other numerically exact methods is high. The MSTM code is publicly available and recent versions have been tailored to run on parallel computing environments (Mackowski &

Mishchenko, 2011). For this work, the MSTM version 3.0 was used. The Fortran source files were compiled under Linux on NJIT's Kong cluster with the help of the Academic and Research Computing Systems (ARCS) department. With initial guidance from Dr. Li Liu (NASA Goddard Institute for Space Studies), a set of sensitivity runs were performed to select optimal values of parameters associated with the numerical solution and convergence of the output values. The output files generated by running the MSTM code contain optical parameters of interest such as extinction, absorption and scattering efficiencies (Q_{ext} , Q_{abs} , Q_{sca}) of the numerically simulated soot aggregates.

2.2.3 Discrete Dipole Approximation (DDA)

DDA (Draine & Flatau, 1994) is a versatile approach for modeling the optical properties of particles of arbitrary geometry and has been used in a large number of modeling studies for soot (Dong, *et al.*, 2015; Kahnert, *et al.*, 2013; Scarnato, *et al.*, 2013; Soewono & Rogak, 2013; Yon, *et al.*, 2015). Unlike MSTM, there are no restrictions in the DDA method to particle shape, thus it can accommodate overlaps between monomer spheres, necking in aggregates, and nonspherical monomers. However, it is more computationally intensive than MSTM because orientation averaging of the optical properties derived for simulated aggregates is performed numerically not analytically. In DDA, the particle shape is described as a collection of small cubical volumes (dipoles) that interact with electromagnetic waves and each other. To converge to an accurate solution, the interdipole separation, d , has to be chosen sufficiently small such that the quantity $|m|kd < 1$, where m is the complex refractive index and $k = 2\pi/\lambda$ is the wavenumber, with λ being the incident wavelength. This is to ensure that the dipole approximation holds (Yurkin & Kahnert, 2013) and that the geometry of the particle is well approximated by an array of dipoles

(Liu, *et al.*, 2018). Besides the particle geometry, the constraint on $|m|kd$ also depends on whether or not the aggregates are coated. Accuracy of the DDA results can be confirmed by checking convergence with decreasing d and by comparison with MSTM results for point touch cases. For this study, the Amsterdam DDA (ADDA) version 1.3 (Yurkin & Hoekstra, 2011), an open source C implementation of DDA, was used. The source codes were compiled under Linux on NJIT's Kong cluster with the help of ARCS. The output files generated by running the DDA algorithm contained orientation-averaged extinction, scattering and absorption cross-sections (C_{ext} , C_{sca} , C_{abs}). Another useful optical property derived from DDA simulations is the asymmetry parameter, $\langle g \rangle$ defined by:

$$\langle g \rangle = \frac{1}{2} \int_0^\pi F_{11}(\theta) \sin \theta \cos \theta d\theta \quad (2.12)$$

where $F_{11}(\theta)$ is the scattering phase function. The asymmetry parameter indicates if scattered light is preferentially in the forward direction ($\langle g \rangle \rightarrow 1$), isotropic ($\langle g \rangle = 0$), or scattered in the backward direction ($\langle g \rangle \rightarrow -1$).

CHAPTER 3

SINGLE PARAMETER REPRESENTATION OF THE MIXING STATE AND MORPHOLOGY OF ATMOSPHERIC SOOT¹

The mixing state assumptions typically employed in atmospheric models are not very representative of fresh or aged soot aggregates as evidenced by field observation studies (Adachi, *et al.*, 2010; Wentzel, *et al.*, 2003). Details such as the distribution of the coating material on the surface of individual soot aggregates and the structural rearrangement of the monomers in the aggregate, which may have significant impacts on predicted properties, are not properly portrayed. This is because the mechanisms behind the constantly evolving structure and composition of mixed soot aggregates during atmospheric aging are little understood. In this chapter, we propose a parameter for predicting the morphological mixing state of soot as a function of its aging environment.

3.1 Introduction

Aggregate restructuring that may arise from the condensation of organic or inorganic compounds during atmospheric aging is, theoretically, expected to depend on the properties of the condensing chemicals. Some solid polycyclic aromatic hydrocarbon (PAH) coatings have been suggested to anchor primary carbon spheres more firmly in place preventing rearrangement (Slowik, *et al.*, 2007), though recent observations indicate that PAH coatings can also induce significant restructuring, if they remain in subcooled liquid state

¹ The findings presented for this chapter have been published in the peer-review journal, Environmental Science & Technology under the reference listing: Chen, C.; Enekwizu, O. Y.; Fan, X.; Dobrzanski, C. D.; Ivanova, E. V.; Ma, Y.; Gor, G. Y.; Khalizov, A. F., Single Parameter for Predicting the Morphology of Atmospheric Black Carbon. *Environmental Science & Technology* **2018**, 52, (24), 14169-14179.

in thin films (Chen, *et al.*, 2016). On the contrary, the presence of liquid coatings always results in more compact configurations which have typically been attributed to the surface tension forces of the condensing material that act to minimize the surface area of the aggregate (Kütz & Schmidt-Ott, 1992; Mikhailov, *et al.*, 1998). These forces are believed to intensify as the thickness of the coating material grows (Ghazi & Olfert, 2013). While a recent study concluded that soot restructuring increases with increasing surface tension of the coating material (Schnitzler, *et al.*, 2017), there was a lack of proper particle characterization in terms of mass, shape factor and density before and after structural changes for this result to be definitive. Thus, it is quite possible that the observed structural change was due to different masses of condensate on the soot aggregates for the various chemicals used. There may very well be other factors that play a more important role such as coating viscosity, wettability, and distribution over the aggregate surface.

3.1.1 Morphological Changes in Coated Soot Aggregates

To test the hypothesis suggested by literature that restructuring is driven primarily by the surface tension and mass of the coating liquid for internally mixed soot aerosols, our research group conducted experiments (described in Chapter 2) where size-classified soot aggregates were exposed to vapors of nine condensable liquids with very different functionalities (Table 3.1). The surface tension for these liquids ranged from 23 – 73 mN m⁻¹. The coating mass was controlled through vapor supersaturation, which depended on the temperature of the liquid coating material in the saturator and aerosol cooling rate in the condenser, where most of the condensation took place. In response to an increase in vapor supersaturation, the size and mass of the soot particles changed due to vapor condensation, as shown in Figure 3.1 by the normalized particle diameter (Gfd) and mass

(*Gfm*). Soot aggregates of two initial mobility diameters (240 nm and 350 nm) were investigated. Additionally, coated particles were also thermodenuded (dashed lines) to discriminate the compaction of the soot backbone from the overall change in particle size.

Table 3.1 Properties of Coating Materials

Coating material	Acronym	Molar mass, gmol ⁻¹	Density, g cm ⁻³	Surface tension, mNm ⁻¹	Boiling point, °C	Vapor pressure, Pa ^{b,c}	Kelvin length, nm
Triethylene glycol	TEG	150.17	1.12	46.5	287	1.32×10 ⁻³	5.0
Triethylene glycol monobutyl ether	TEGMBE	206.28	0.99	31.4	278	2.50×10 ⁻³	5.3
Diethyl adipate	DA	202.25	1.01	32.7	245	5.80×10 ⁻²	5.3
Tetradecane	TDA	198.38	0.76	26.7	251	1.50×10 ⁻²	5.6
Diocetyl sebacate	DOS	426.67	0.91	31.1	436	2.22×10 ⁻⁸	11.7
Oleic acid	OA	282.46	0.90	32.8	360	5.46×10 ⁻⁷	8.3
Bis(2-ethylhexyl) adipate	BEHA	370.57	0.92	30.0	417	8.50×10 ⁻⁷	9.7
Bis(2-ethylhexyl) phthalate	BEHP	390.56	0.99	31.2	384	1.42×10 ⁻⁷	9.9
Sulfuric acid (H ₂ SO ₄ , 69 weight percent)	SA	98.08	1.60	73	165 ^a	2.9×10 ⁻⁹	3.6

^a Temperature at which the total pressure above sulfuric acid solution (mostly due to water vapor) reaches 101325 Pa. ^b Saturation vapor pressure at 25 °C. ^c References to surface tension and saturated vapor data sources: TEG (Daubert & Danner, 1989; Yaws, 2003), TEGMBE (Boatman & Knaak, 2001; Flick, 1998), DA (Ohe, 1976; Zhao, *et al.*, 2010), TDA (Haynes, 2014; Korosi & Kovats, 1981), DOS (Jasper, 1972; Small, *et al.*, 1948), OA (Daubert & Danner, 1989; Riddick, *et al.*, 1985), BEHA (Felder, *et al.*, 1986; Wypych, 2013), BEHP (Hinckley, *et al.*, 1990; Yaws & Richmond, 2009), SA (Daubert & Danner, 1989; Young & Grinstead, 1949).

Upon coating, the soot particles initially decreased in size (*Gfd* < 1) with increasing coating mass (*Gfm* > 1) for all coating materials (Figure 3.1) This was attributed to

restructuring, a process that transforms fractal soot aggregates into compact globules of a smaller mobility diameter (Cross, *et al.*, 2010; Ghazi & Olfert, 2013; Schnitzler, *et al.*, 2014). For larger sized aggregates, the decrease in Gfd was more significant due to larger void spaces for compaction (Zhang, *et al.*, 2008). As the soot particles acquired more coating mass, Gfd began to increase signifying condensational growth of the compact soot aggregate. The curves for coated and coated-denuded soot diverged sharply at the point where the aggregates restructured fully.

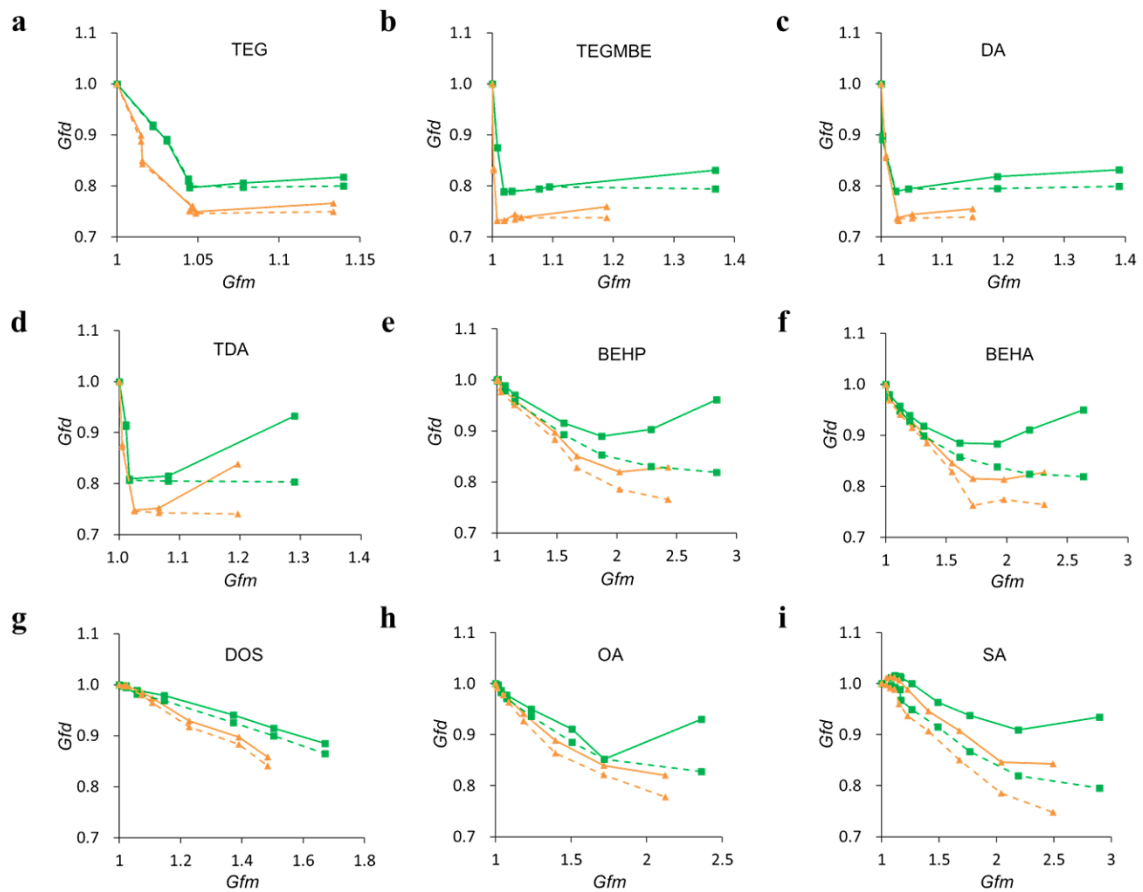


Figure 3.1 Mobility diameter change (Gfd) as a function of mass change (Gfm) for soot aggregates coated with (a) TEG, (b) TEGMBE, (c) DA, (d) TDA, (e) BEHP, (f) BEHA, (g) DOS, (h) OA and (i) SA. Squares (green) and triangles (orange) represent aggregates with initial mobility diameters of 240 nm and 350 nm respectively. Solid and dashed lines correspond to coated and coated-denuded soot respectively. See Table 3.1 for acronyms.

For easier comparison of restructuring caused by the different coating materials, experimental results were summarized and plotted as a function of the coating mass fraction (f_m) in Figure 3.2a for coated-denuded soot aggregates with 240 nm initial mobility diameter. This representation revealed that all the coating materials clustered into two distinct groups based on their restructuring ability. For materials shown in red, such as BEHA, BEHP, DOS, OA, and SA (see Table 3.1 for acronyms), the particle mobility diameter decreased gradually with an increase in coating mass. The particle mass had to be nearly doubled ($Gfm > 2$ or $f_m > 50\%$) before the aggregates could attain a nearly fully compact structure ($Gfd \sim 0.8$), requiring a saturator temperature of 50 °C and above. This behavior agreed with previous observations, such as for OA and DOS condensation on soot (Ghazi & Olfert, 2013). On the other hand, materials shown in blue, such as DA, TDA, TEGMBE, and TEG, induced a complete restructuring when present at a mass fraction as low as ~5%, corresponding to $Gfm = 1.05$. Notably, for these materials, some minor vapor condensation ($Gfm \leq 1.03$) and partial restructuring ($Gfd \sim 0.90$) occurred even with the saturator held at room temperature (subsaturated conditions). The mobility diameter of fully collapsed aggregates was comparable between the two groups of materials, corresponding to $Gfd \sim 0.8$.

Particle convexity, derived from the analysis of scanning electron microscopy (SEM) images of soot confirmed the results of mass-mobility measurements. For instance, a 350 nm mobility diameter fractal aggregate with initial convexity of 0.54 (Figure 3.2b) became compact after gaining a 10% mass fraction of DA (convexity 0.87, Figure 3.2c), but not after gaining 13% OA (convexity 0.60, Figure 3.2d). Instead, a 43% coating fraction was required to induce significant restructuring of fractal aggregates when OA was used

(convexity 0.78, Figure 3.2e). Overall, for a $13 \pm 2\%$ coating fraction, all materials clustered into two groups (Table 3.2), e.g., materials shown in blue in Figure 3.2a induced significant soot aggregate compaction, as reflected by convexities of 0.86 ± 0.01 , whereas materials shown in red had a minor structural impact, with convexities of 0.62 ± 0.02 .

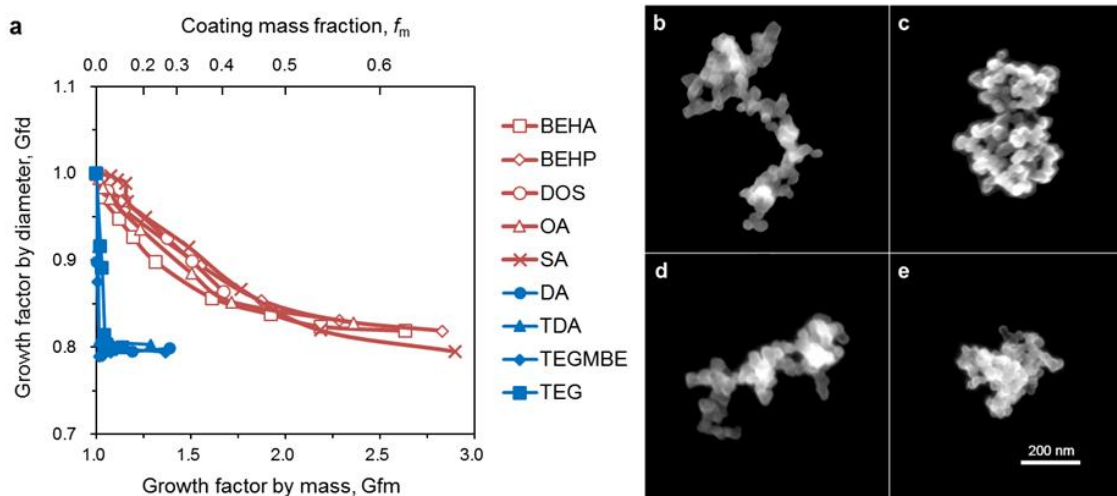
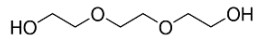
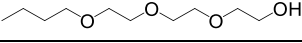
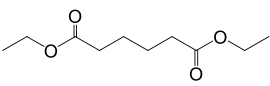
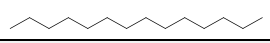
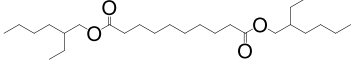
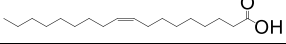
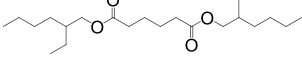
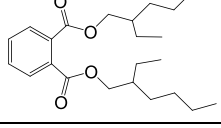


Figure 3.2 Morphological changes in soot aggregates that were exposed to condensable vapors of different chemicals and then denuded. (a) Mass-mobility relationship showing the dependence of mobility diameter change (G_{fd}) on mass change (G_{fm}) and coating mass fraction (f_m). (b-e), Scanning electron microscopy images of soot aggregates, where (b) is an uncoated aggregate, (c) is a coated aggregate with 10% mass fraction DA, (d) is a coated aggregate with 13% OA, and (e) is a coated aggregate with 43% OA. Initial mobility diameter is 240 nm in (a) and 350 nm in (b-e). See Table 3.1 for acronyms.

The loss of the coating material upon denuder-induced evaporation led to an additional small, but consistent compaction of the aggregates. For coated soot with $f_m \sim 10\%$, the convexity increased from 0.77 ± 0.03 to 0.86 ± 0.01 for the materials shown in blue and from 0.59 ± 0.02 to 0.62 ± 0.02 for the materials shown in red. This additional compaction only occurred to the airborne soot, but not to the aggregates deposited on SEM substrates because in the latter case restructuring was restricted by aggregate-substrate interactions (Chen, *et al.*, 2017).

Table 3.2 Morphological Changes in Thinly Coated Soot Aggregates ($13 \pm 2\%$ coating fraction) Based on Convexity Determined from Scanning Electron Microscopy Images

Coating material	Molecular structure	Convexity	
		Coated	Coated -Denuded
none		0.54	
Intermediate volatility liquids			
TEG		0.81	0.86
TEGMBE		0.77	0.85
DA		0.73	0.87
TDA		0.76	0.86
Low volatility liquids			
DOS		0.58	0.61
OA		0.60	0.63
BEHA		0.56	0.65
BEHP		0.59	0.60
SA	H ₂ SO ₄	0.61	0.62

3.1.2 Trends between Soot Morphology and Coating Material Properties

Unlike the reported trends of gradual aggregate restructuring with increased coating mass (Ghazi & Olfert, 2013), in our study, complete restructuring occurred for aggregates with very little condensate mass fraction ($\sim 5\%$). Also, no discernible correlation between coating surface tension and convexity, for the same condensate mass fraction could be seen (Figure 3.3a). Materials of vastly different surface tensions, such as SA (73 mN m^{-1}) and DOS (31.1 mN m^{-1}) produced small yet comparable restructuring, while some materials of comparable surface tensions, such as DOS and TEGMBE (31.4 mN m^{-1}) induced vastly

different restructuring. Most surprisingly, a nonpolar hydrocarbon TDA with $\gamma = 26.6 \text{ mN m}^{-1}$ was significantly more effective at restructuring than the polar SA.

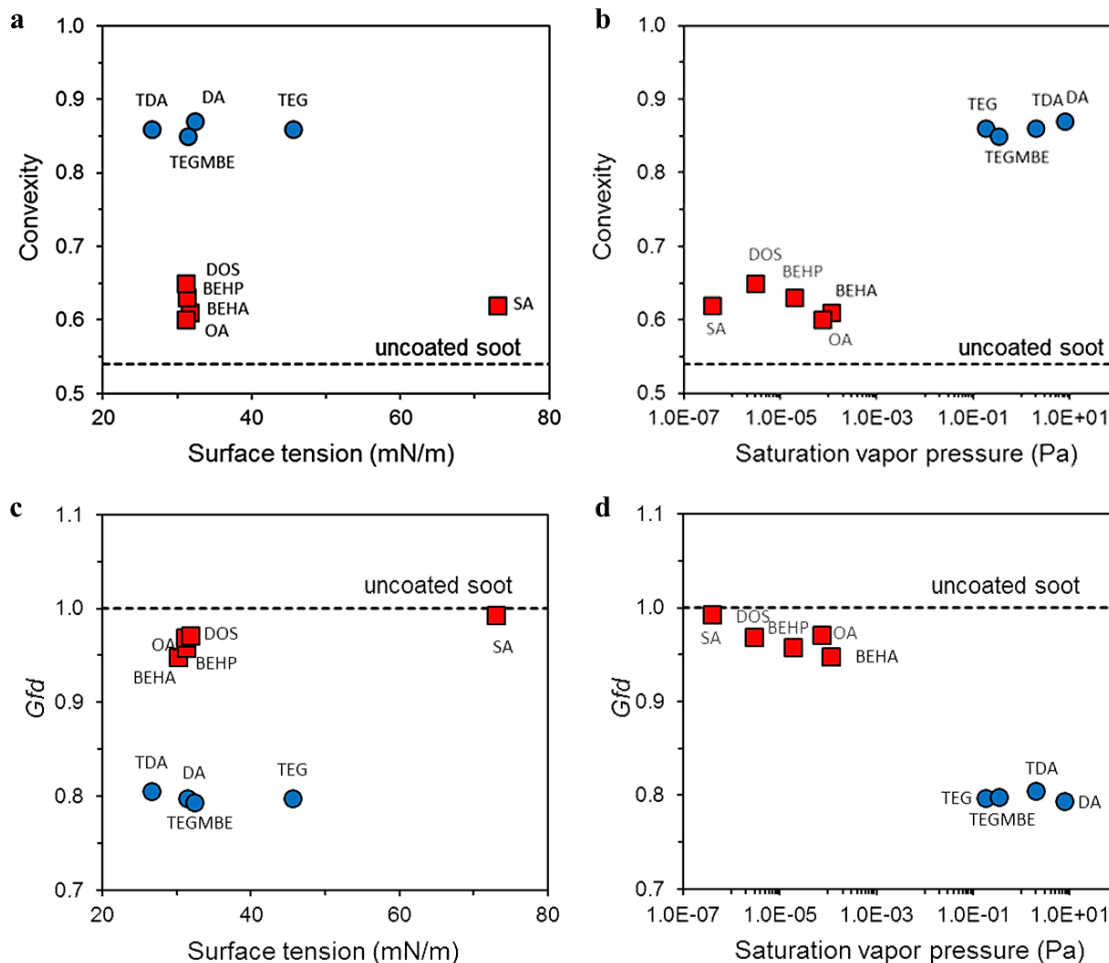


Figure 3.3 Dependence of convexity (top panel) and mobility diameter change, Gfd (bottom panel) on the surface tension (a, c), and saturation vapor pressure at 25 °C (b, d) of the coating material. The initial mobility diameter of soot aggregates is 350 nm and the coating mass fraction is $13 \pm 2\%$. The dashed line represents uncoated soot (convexity = 0.54, $Gfd = 1$). See Table 3.1 for acronyms.

No apparent correlation was also observed between the convexity of processed soot and the presence of specific chemical functions (Table 3.2). However, when aggregate restructuring was plotted against the saturation vapor pressure (p_{sat}), all coating liquids became clustered in two distinct groups. As shown in Figure 3.3b, liquids of intermediate-

volatility with p_{sat} in the range of 0.13 – 8 Pa induced significant restructuring, while the low-volatility liquids ($p_{sat} = 4 \times 10^{-7} - 1.2 \times 10^{-4}$ Pa) had a minor impact on the morphology of lightly coated soot ($f_m = 0.13 \pm 0.02$). Similar dependencies were observed when the surface tension and saturation vapor pressure were plotted against Gfd (Figure 3.3 c, d).

3.1.3 Two Distinct Morphological Mixing States

The restructuring behavior observed in our experiments posed two questions:

- How was aggregate restructuring driven by thin ($f_m \sim 5\%$) coatings?
- Why was there no dependence of aggregate restructuring on coating surface tension?

To explain the unexpected restructuring in the presence of a small coating mass and the drastic difference in the restructuring behavior between the two groups of coating materials (Figure 3.2), we suggest the formation of one of two different morphological mixing states, a uniform coating layer (Figure 3.4a) and a pendular ring (Figure 3.5b). Using Equation (3.1) below, we estimated that a condensate mass fraction of 5% corresponds to a single monolayer, if distributed uniformly over the monomers in the aggregate, with a thickness of $\Delta R_s = 0.3$ nm:

$$\Delta R_s = \left(\left[(Gfm - 1) \frac{\rho_{soot}}{\rho_{coating}} + 1 \right]^{\frac{1}{3}} - 1 \right) R_s \quad (3.1)$$

where $R_s = d_p/2$ is the monomer radius, $d_p = 28 \pm 6$ nm is the average monomer diameter determined from SEM. Pendular ring thickness, r_m , can be determined using the relationship (see Section 3.1.4) between the volume of condensate in the gap, V_{gap} , derived from experimental measurements via Equation (3.3) and the filling angle, θ :

$$r_m = R_s \sin \theta \quad (3.2)$$

$$V_{gap} = (Gfm - 1) \frac{\rho_{soot}}{\rho_{coating}} \times \frac{4}{3} \pi R_s^3 \quad (3.3)$$

If present in the junctions between the spheres, condensate with a 5% mass fraction forms pendular rings of significant thickness ($r_m = 8$ nm), exerting sufficiently strong capillary force to induce restructuring of soot aggregates, especially when located at weaker junctions. If distributed as a uniform 0.3 nm layer, condensate induces only a minor restructuring because a monolayer cannot provide sufficient mechanical load.

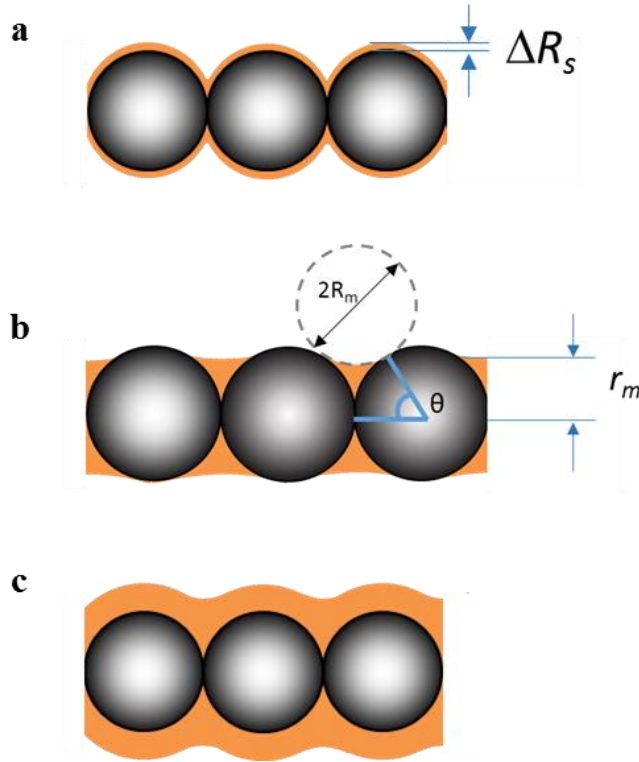


Figure 3.4 Two models representing the morphological mixing state of coated soot aggregates. (a) A coating layer with effective thickness ΔR_s is distributed uniformly over monomer spheres. (b) Pendular rings of radius r_m are formed by capillary condensation at the junctions between monomer spheres. R_m is the radius of curvature of the meniscus. The extent to which the gap is filled by condensate is described in terms of the angle θ . (c) A thickly coated aggregate with $r_m \sim \Delta R_s$.

For condensate located in the junctions, the extent of morphological change (Gfd) can be related to the pendular ring thickness (r_m); for uniform coatings, ΔR_s serves as a good approximation of r_m . The application of this concept is illustrated in Figure 3.5, where the Gfd of the coated and denuded soot is plotted against r_m and ΔR_s for the intermediate-volatility and low-volatility coatings, respectively. The two important features revealed by Figure 3.5 are that the behavior of all substances follows a similar trend, where the Gfd decreases gradually with r_m , independently of the surface tension, and that for all coating materials a nearly complete restructuring is achieved for $r_m = 6 - 8$ nm. The merging of all Gfd curves into a nearly single curve when plotted against r_m reconciled the significant apparent differences in behavior between the two groups of materials in Figure 3.2a. It can be deduced that the intermediate volatility materials condensed nearly exclusively in the junctions, leading to a rapid increase in r_m . The low volatility materials produced uniform coats, and hence a much larger Gfm was required to achieve the critical pendular ring thickness, as shown in Figure 3.4c. In either case, the aggregates undergo restructuring only when the junctions become sufficiently filled. This critical pendular ring thickness is estimated to be about half of the primary sphere radius.

We deduced that the two mixing states (uniform and pendular ring) were correlated to the condensing vapor supersaturation used to control coating mass during aging experiments. Our conceptual description was converted to an analytical model by Dr. Gennady Gor. Through this model, the parameter behind the formation of the two mixing states was identified.

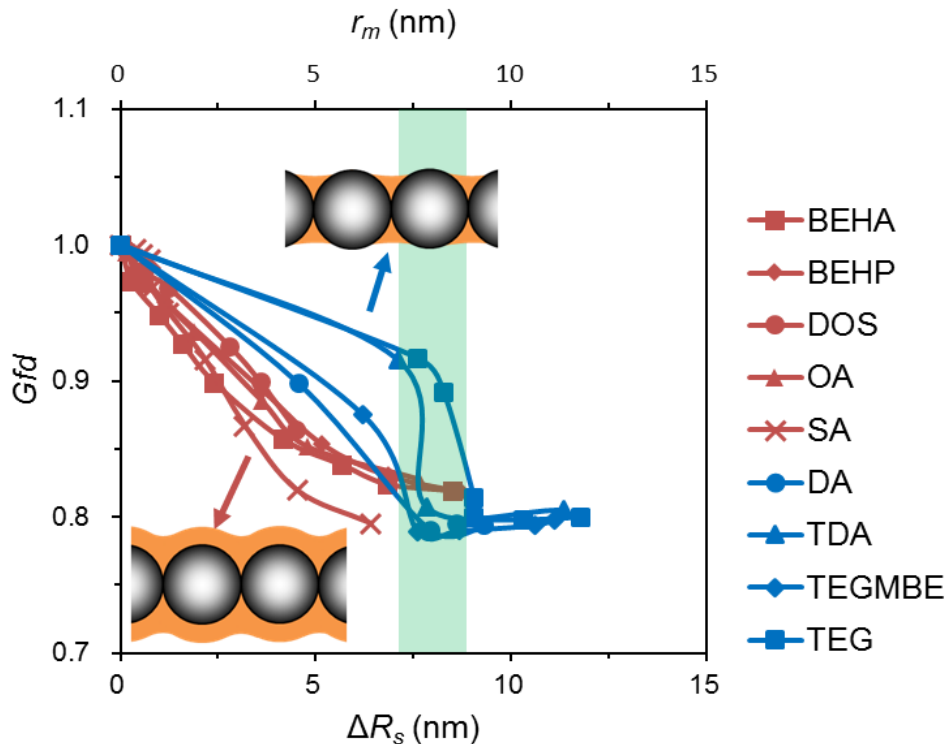


Figure 3.5 Mobility diameter change (Gfd) as a function of pendular ring thickness (r_m , blue, low supersaturation) and effective coating thickness (ΔR_s , red, high supersaturation) for soot aggregates that were coated and then denuded. The range of ΔR_s and r_m corresponding to nearly complete restructuring of soot is indicated by the vertical green band. See Table 3.1 for acronyms.

3.1.4 Model for Competitive Condensation on Soot Aggregates

As described above, the two limiting cases considered for condensate distribution on the aggregate surface are: a uniform shell on the surface of each monomer sphere (Figure 3.4a), or the localization of the condensate in the gap between adjoining spheres (Figure 3.4b). An analytical model is derived for the kinetics of condensation for each case.

It is assumed that condensational growth takes place in the kinetic regime since the monomer spheres are small relative to the mean free path of the vapor molecules. Under these conditions, condensate deposition is governed by flux of molecules to its surface (Seinfeld & Pandis, 2006):

$$J = \frac{\alpha A v_T N_A}{4R_g T} (p - p_{sat,R}) \quad (3.4)$$

where α is the molecular accommodation coefficient, A is the droplet surface area, v_T is the mean thermal velocity of the molecules, N_A is the Avogadro constant, R_g is the gas constant, T is the temperature of the liquid, p is the vapor pressure far from the droplet, $p_{sat,R}$ is the saturated vapor pressure near the droplet's surface of radius R .

The droplet growth rate due to vapor condensation is determined by the material balance and the rate of change of the number of molecules in the droplet N , equals the total flux to its surface:

$$\frac{dN}{dt} = J \quad (3.5)$$

Below Equations (3.4) and (3.5) are considered for the two cases: growth of a uniform film on a spherical surface and capillary condensation in the gap between two spherical particles.

Condensational droplet growth on a spherical surface: The saturated vapor pressure near the droplet's surface $p_{sat,R}$ depends on the droplet's radius R through the Kelvin equation:

$$p_{sat,R} = p_{sat} \exp\left\{\frac{l_K}{R}\right\} \quad (3.6)$$

where p_{sat} represents the saturated vapor pressure at the flat surface of the liquid and

$$l_K \equiv \frac{2\gamma V_m}{R_g T} \equiv \frac{2\gamma}{p_L} \quad (3.7)$$

is the characteristic Kelvin length, γ is the vapor-liquid surface tension, and p_L is the pressure of the liquid phase. For condensation on the monomer sphere's convex surface, $p_{sat,R} > p_{sat}$ and the driving force for condensation ($p - p_{sat,R}$) is smaller than that for a flat surface. When the radius of the droplet noticeably exceeds the Kelvin length, $R \gg l_K$, Equation (3.7) can be linearized:

$$p_{sat,R} \simeq p_{sat} \left\{ 1 + \frac{l_K}{R} \right\} \quad (3.8)$$

For substances studied, linearization produced an average error of 11% in the Kelvin factor but did not exceed 26%. Substituting the dependence of $p_{sat,R}$ on curvature via Equation (3.8) and the number of molecules in the spherical shell droplet N :

$$N = \frac{4}{3} \pi (R^3 - R_s^3) \frac{p_L N_A}{R_g T} \quad (3.9)$$

into Equations (3.4) and (3.5) gives the following equation for the droplet radius as a function of time:

$$\frac{dR}{dt} = \frac{1}{4} \alpha v_T a \left(1 - \frac{1}{\zeta} \frac{l_K}{R} \right) \quad (3.10)$$

where the following dimensionless parameters are introduced: vapor supersaturation

$$\zeta = \frac{p - p_{sat}}{p_{sat}} \quad (3.11)$$

and droplet growth rate parameter

$$a \equiv \frac{p - p_{sat}}{p_L} \quad (3.12)$$

The initial condition for this equation stems from the fact that the condensational growth takes place on a surface of the spherical soot monomer with radius R_s : $R(t)|_{t=0}$. Since the radius of the sphere R_s sets the main length scale in the problem, it is convenient to introduce the reduced droplet radius as $\tilde{R} \equiv R/R_s$. The characteristic time scale of the droplet growth in the kinetic regime can be defined as:

$$\tau \equiv \frac{4R_s}{\alpha v_T a} \quad (3.13)$$

and the reduced time $\tilde{t} \equiv t/\tau$. Integrating Equation (3.10) and writing the result in terms of dimensionless variables gives:

$$\tilde{t} = \tilde{R} - 1 + \chi \ln \left[\frac{\tilde{R} - \chi}{1 - \chi} \right] \quad (3.14)$$

where

$$\chi = \frac{l_K}{R_s} \frac{1}{\zeta} \quad (3.15)$$

Note that all the physical parameters of the problem are contained in the dimensionless parameter χ , which reflects the competition between the Kelvin effect (l_K/R_s) and vapor supersaturation (ζ).

Condensational droplet growth in the gap between two spherical particles: For condensation in the gap between adjoining spheres, the liquid interface can be concave $p_{sat,Rm} < p_{sat}$ and the driving force ($p - p_{sat,Rm}$) can exceed that of the flat surface. The extent to which the gap is filled is expressed in terms of the filling angle θ (see Figure 3.4b). For the case of perfect wetting of the solid spheres by the condensing liquid, the liquid-vapor

interface of the pendular rings is well approximated as arcs of circles (Rose, 1958). The analytical expressions for the area and volume of the pendular rings in the gap are rather cumbersome (Rose, 1958) for use in Equations (3.4) and (3.5). Therefore, for further analysis the area and volume of the cylindrical surface of the condensate that are given by simpler analytical expressions are used and written in terms of θ . The area is given then by:

$$A_{gap} = 4\pi R_s^2 \sin \theta (1 - \cos \theta) \quad (3.16)$$

The volume of the fluid accumulated in the gap is the difference between the volume of the cylinder and the volumes of two spherical caps:

$$V_{gap} = \frac{2\pi}{3} R_s^3 (\cos \theta - 1)^2 (2 \cos \theta + 1) \quad (3.17)$$

The perfect wetting condition assumed here gives the following equation for the radius of the meniscus R_m :

$$R_m = R_s \frac{1 - \cos \theta}{\cos \theta} \quad (3.18)$$

Using this relation, similarly to Equation (3.6), the saturated vapor pressure at the concave interface is given by the Kelvin equation in the following linearized form:

$$p_{sat,R_m} \simeq p_{sat} \left(1 - \frac{\ell_K}{2R_s} \frac{\cos \theta}{1 - \cos \theta} \right) \quad (3.19)$$

Substituting Equations (3.16), (3.17), and (3.19) into Equations (3.4) and (3.5), and using the definitions for τ , $\tilde{\ell}$ and χ gives:

$$\frac{\cos\theta d\theta}{1 + \frac{\chi}{2} \frac{\cos\theta}{1 - \cos\theta}} = d\tilde{t} \quad (3.20)$$

Integration of Equation (3.20) for an arbitrary value of χ in the interval (0, 1) gives

$$\tilde{t} = \frac{2}{2 - \chi} \left\{ \sin\theta + \frac{\chi}{2 - \chi} [\theta - I] \right\} \quad (3.21)$$

where

$$I = \frac{1}{\sqrt{(4 - \chi)\chi}} \arctan \left(\sqrt{\frac{4 - \chi}{\chi}} \tan \frac{\theta}{2} \right) \quad (3.22)$$

Competition between the two solutions given by Equation (3.14) and Equation (3.21) determines the localization of the condensing fluid. Note that both could be solved analytically only for \tilde{t} , and not for θ or \tilde{R} . In these equations, χ is the only parameter, which determines the condensation scenario and contains all the physical parameters of the problem: vapor supersaturation ζ , monomer size R_s , surface tension γ , and molar volume V_m of the condensate. To compare the two solutions, the dependence of the reduced amount of condensate, \tilde{N} in the gap or on a sphere is plotted where:

$$\tilde{N} \equiv \frac{N}{\left(\frac{2}{3} \pi R_s^3 \frac{p_L N_A}{R_g T} \right)} \quad (3.23)$$

as a function of the reduced time \tilde{t} . The complete filling of the gap corresponds to $\tilde{N} = 1$

Having prior knowledge of the coating material properties (Table .3.1) and monomer size from our SEM images, validation of the analytical model only requires the

vapor supersaturation of the coating materials based on the temperature conditions in our flow reactor. The accuracy of the simulation results will be dependent on estimates for ζ .

3.1.5 Study Objectives

The main objective of this study was to test the hypothesis that vapor supersaturation controls the χ parameter and is responsible for the formation of the two mixing states previously proposed and their restructuring behavior. To determine the actual vapor supersaturations generated in our previous experiments, we developed a model for condensation on spherical particles in our aerosol flow reactor. Gas and wall temperatures were measured experimentally to perform predictions of vapor supersaturation. The model was tested by conducting temperature-controlled condensation experiments (as described in Chapter 2) on nanosized particles of spherical geometry (PSL). Conditions that yielded a match between experimental and simulation measurements of particle growth proved that the predicted vapor supersaturation was accurate. The use of the χ parameter to reconcile discrepancies reported in previous soot aging studies is discussed as well as its potential to be incorporated into aerosol models to obtain predictions of soot aging.

3.2 Modeling of Vapor Supersaturation in Condenser

Time profiles of saturation ratio, $\zeta + 1$, and particle radius, R , in the saturator/condenser were obtained by solving Equations (3.24-3.26) for a given coating liquid and experimentally measured gas and wall temperatures, using a model implemented in Python. The first term on the right-hand side of Equation (3.24) accounts for condensational vapor loss to aerosol particles and the second term describes loss to the condenser walls. The vapor loss to particles was modeled using the continuum regime equation (with transition

correction) because the spherical particles utilized in condensation experiments to verify the calculations were larger than the gas mean free path.

$$\frac{dp}{dt} = - \left[4\pi R n_p D_v C_{BL} (p - p_{sat,R}) + k_{loss} \left(p - p_{sat} \frac{T}{T_w} \right) \right] \quad (3.24)$$

where n_p is the number concentration of aerosol particles, D_v is the diffusion coefficient of vapor in the air, C_{BL} is the transition correction, T and T_w are the gas and wall temperatures, and k_{loss} is the first-order rate constant for diffusion-limited vapor loss on the wall in a laminar flow (Hanson & Eisele, 2000),

$$k_{loss} = \frac{3.66 D_v}{r_{tube}^2} \quad (3.25)$$

where $\mu = 3.66$ is the Sherwood number for a cylindrical tube of radius r_{tube} . The change in the particle radius due to vapor condensation is described as

$$\frac{dR}{dt} = \frac{D_v C_{BL} V_m}{R_g T} \frac{1}{R} (p - p_{sat,R}) \quad (3.26)$$

The diffusion coefficient was estimated using the approach by Fuller, *et al.* (1966). The particles typically contributed little to vapor loss, with loss on the wall accounting for over 95% of the change in vapor concentration. The transition correction, C_{BL} is based on the method of Bademosi and Liu (Bademosi, 1971)

$$C_{BL} = \frac{J}{J_c} \quad (3.27)$$

where

$$\frac{J}{J_c} = \left[1 + \frac{J_c}{J_k} - \frac{1}{\left(1 - \frac{0.13J_c}{\beta Kn J_k}\right)^{-1} + \frac{6.08\beta J_k}{J_c}} \right]^{-1} \quad (3.28)$$

$$\frac{J_c}{J_k} = \frac{4\beta Kn}{E} \quad (3.29)$$

and

$$\beta = (1 + \delta) \frac{3\pi}{8\sqrt{8}} \left(\frac{M_L + M_{air}}{M_{air}} \right)^{0.5} \quad (3.30)$$

In Equations (3.27-3.30), J , J_c and J_k are the mass fluxes in the transition, continuum and kinetic regimes respectively, β is a constant, Kn is the Knudsen number, E is the evaporation coefficient taken as unity (Davis & Ray, 1978), the factor δ is taken as 0.132 (Davis & Ray, 1978), M_{air} and M_L are the molar mass of air and coating, respectively.

3.3 Results and Discussion

3.3.1 Vapor Supersaturation Profiles

The saturation ratio $\zeta + 1$ and particle diameter growth profiles modeled for the condensation of OA and DA vapors exiting the saturator are illustrated in Figures 3.6 and 3.7, respectively. Experimental measurements of the PSL aerosol growth were used to verify the calculated vapor pressure. Modeled particle growth was found to be higher than experimentally measured growth because of the unaccounted vapor loss to the wall due to turbulence experienced by the aerosol flow as it exited the saturator through a right-angle outlet (see Chapter 2, Figure 2.2). To account for vapor loss, an iteratively derived correction factor was applied to the initial vapor pressure at the exit point in each case. The plots shown in Figures 3.6-3.7 include the appropriate corrections. Overall, the maximum

saturation ratio of intermediate-volatility materials (1.3-1.4) was significantly lower than that of low-volatility materials (22-33).

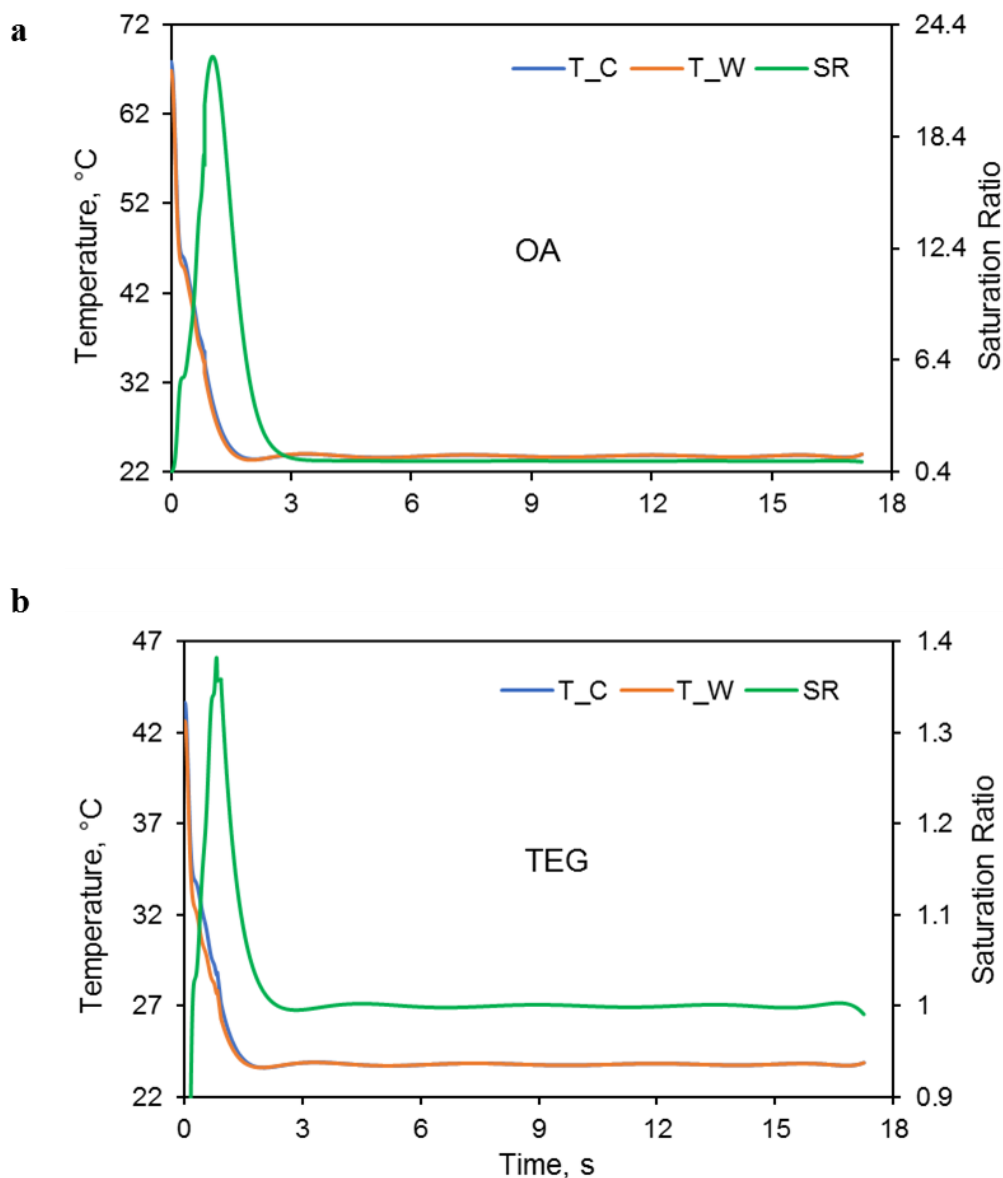


Figure 3.6 Saturation ratio ($\zeta+1$) calculated for OA (a), and TEG (b) vapor condensation on PSL aerosol in the coating reactor. T_C is the centerline temperature and T_W is the wall temperature, both experimentally measured. See Table 3.1 for acronyms.

For low volatility materials, applying a uniform correction factor resolved the overestimations of 30-40% in calculated vapor supersaturation. This was corroborated by

the close match in measured and predicted particle growth (Figure 3.7a). Conversely, predicted particle growth for intermediate volatility vapors was significantly larger, on the order of several hundred percent, than experimental measurements (Figure 3.7b).

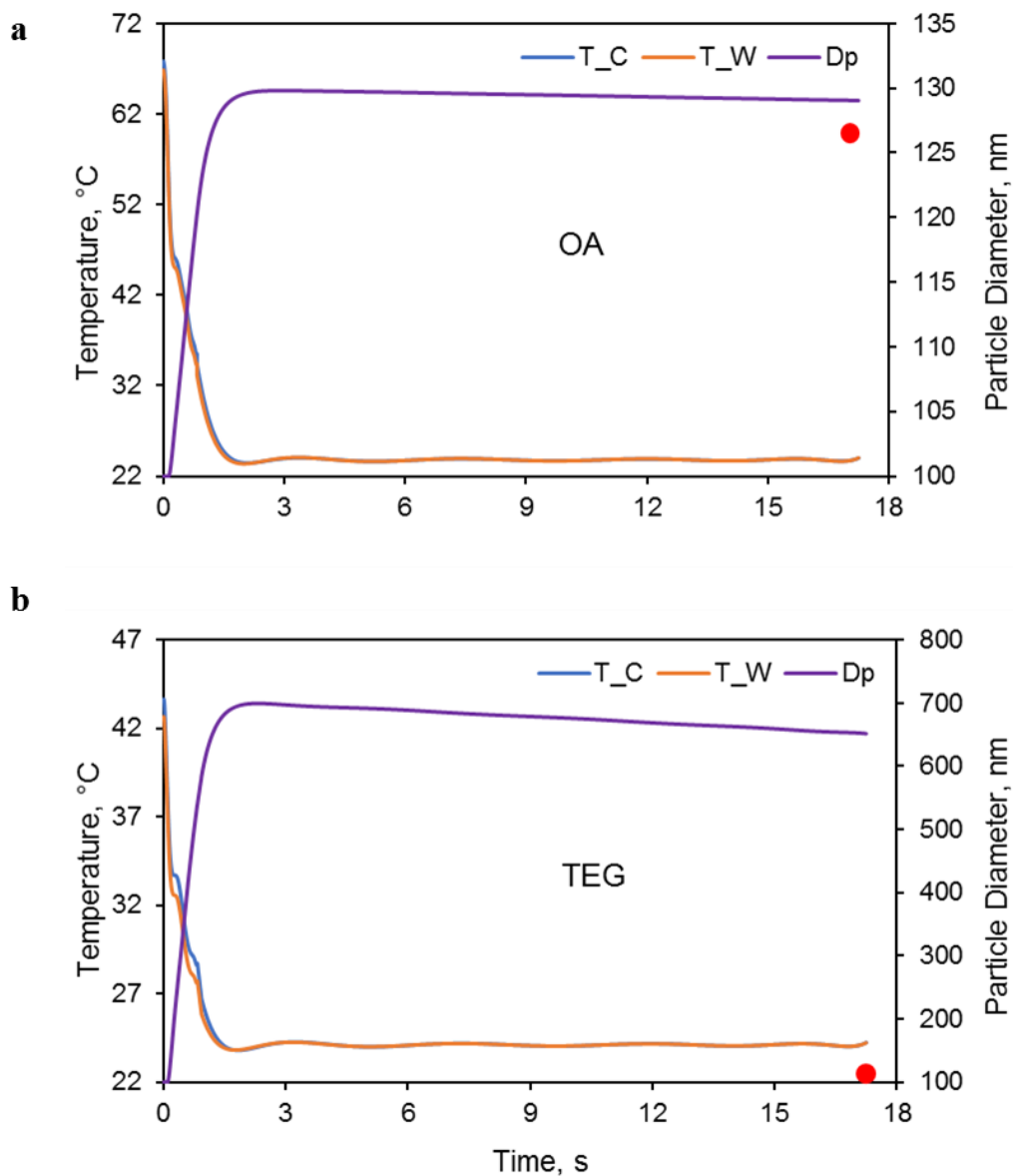


Figure 3.7 Particle diameter (D_p) calculated for OA (a), and TEG (b) vapor condensation on PSL aerosol in the coating reactor. T_C is the centerline temperature and T_W is the wall temperature, both experimentally measured. Experimentally measured values (red dots) were 126 and 108 nm, respectively. See Table 3.1 for acronyms.

We surmised that there was a possibility of coating loss occurring via evaporation for intermediate volatility materials prior to detection by the second DMA which would explain the discrepancy between measured and modeled particle growth. To confirm this, we designed and built a compact electrostatic particle classifier (EPC) for the immediate measurement of particle size upon exit from the saturator. The results are presented in Figure 3.8 for TEG, an intermediate volatility chemical.

At elevated saturator temperatures ($T > 30\text{ }^{\circ}\text{C}$), DMA-EPC measurements revealed an exponential growth in particle size. However, as seen in Figure 3.8, this considerable particle growth was not observed by tandem differential mobility analysis (DMA-DMA). It is very likely that coating evaporation from the particles during transit to the second DMA, which was located at 3.5 m from the saturator exit, resulted in a significant measurement bias by DMA-DMA. On the other hand, the true particle size behavior was reflected by the DMA-EPC given that the EPC was positioned within 0.04 m from the saturator exit to prevent coating loss. Since the DMA-EPC measurements in Figure 3.8 are comparable with the modeled particle growth in Figure 3.7, this proves that the calculated vapor supersaturations for intermediate volatility materials were not grossly overestimated. A more detailed explanation of the experiments conducted, design and operation of the EPC is provided in Chapter 4.

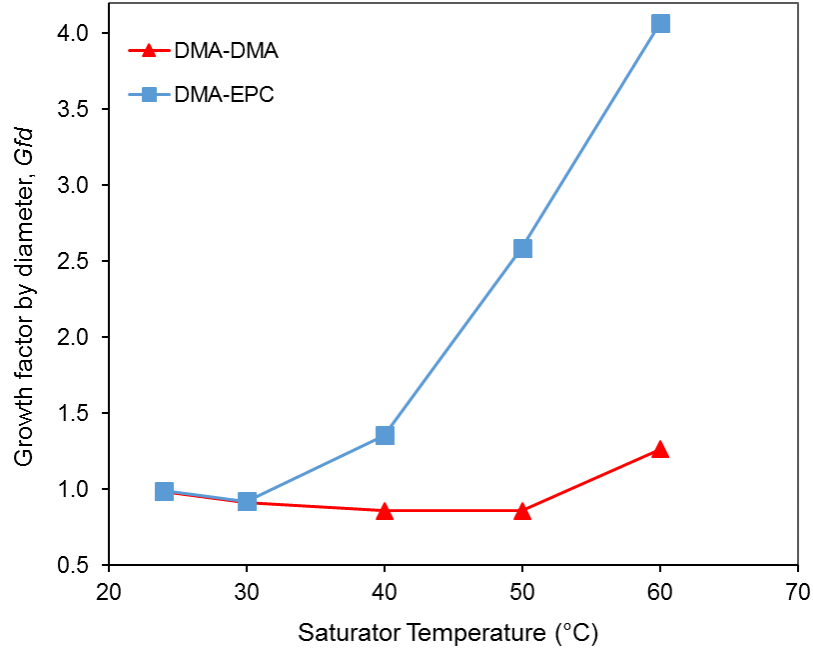


Figure 3.8 Mobility diameter change (Gfd) of soot aggregates with increasing saturator temperature, measured by tandem differential mobility analysis (DMA-DMA) and electrostatic particle classification (DMA-EPC) methods. Particle size measurements were conducted at a distance of 3.5 m and 0.04 m for DMA-DMA and DMA-EPC, respectively. The initial mobility diameter of soot is 240 nm and the coating material is triethylene glycol (TEG).

3.3.2 Mechanism Leading to Two Distinct Morphological Mixing States

One can envision two alternative mechanisms leading to the formation of a non-uniform coating: redistribution of the uniform coating layer and direct condensation into junctions. On the time scale of our experiments, coating redistribution can be ruled out because of slow surface transport (Gao & Bhushan, 1995). Thus, pendular rings can only form by direct vapor condensation into the junctions. Since all substances explored in our study wetted perfectly the aggregate surface, the condensation was not limited by the rate of heterogeneous nucleation, but occurred promptly at the rate that depended on the vapor flux J towards the surface (Donahue, *et al.*, 2011), as:

$$J \propto p_{sat} \times (\zeta + 1 - K) \quad (3.31)$$

where

$$K = \exp\left(\frac{l_K}{R_c}\right) \quad (3.32)$$

is the Kelvin factor, and the radius of curvature, R_c , equals either R_s or R_m . For a given supersaturation, preferential condensation into junctions (capillary condensation) may occur due to significantly lower vapor pressure above concave rings ($R_m < 0$, $K < 1$) relative to the convex spheres ($R_s > 0$, $K > 1$) (Crouzet & Marlow, 1995). In the case of low-volatility liquids such as oleic acid (OA), with a maximum ζ as large as 20 – 30, variation in K between convex ($K \sim 1.4$) and concave ($K \sim 0.6$) surfaces had a relatively minor effect on J in Equation (3.31), leading to condensation with little spatial preference. However, in the case of intermediate volatility chemicals, such as diethyl adipate (DA), ζ never exceeded 0.3–0.4, resulting in a significant preference for concave locations over convex locations and nearly exclusive capillary condensation.

This observed preference of the condensation location is fully supported by the χ -model, which describes analytically the competition between the rate of condensation on a sphere and in the junction between two spheres, using a single parameter, $0 < \chi < \infty$ (Equation 3.15). The lower limit of χ corresponds to infinite supersaturation where condensation on spheres prevails (Figure 3.9). As χ reaches 0.65, rates of condensation on spheres and in junctions become comparable. For larger χ , condensation in the junctions is the dominant process. In the integrated analytical solution, discontinuities appear at χ values of 1, 2 and 4. The first is imposed by the minimum supersaturation required for the condensation on a sphere in Equation (3.14); the other two are imposed by discontinuities in Equations (3.21) and (3.22).

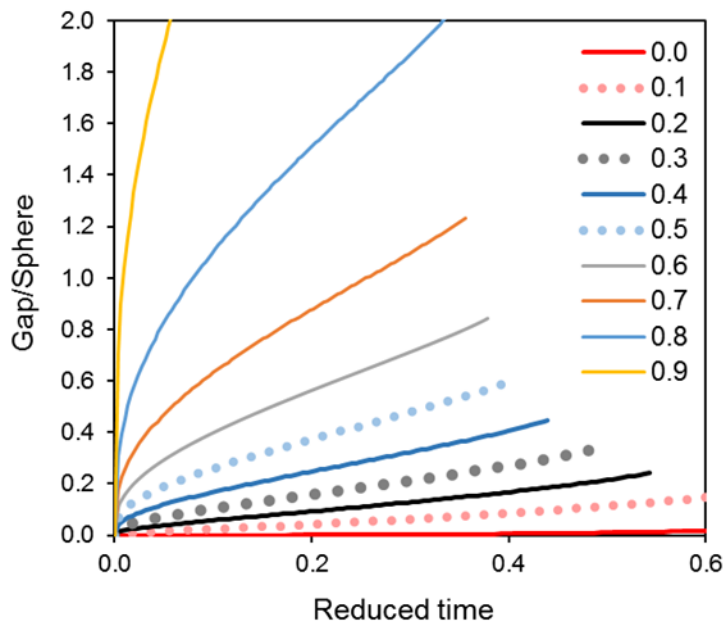


Figure 3.9 Time variation in the calculated ratio of the condensate amount in the gap and on the sphere for different χ . The monomer diameter is 28 nm. As χ increases, condensation in the gap becomes more competitive. The amount of condensate in the gap becomes equal to the amount of condensate on the sphere at $\chi \sim 0.65$.

Figure 3.10a shows that in the case of DA ($\zeta = 0.36$, $\chi = 1.042$), condensation on the convex spheres was suppressed and the vapor condensed exclusively in the gap between spheres. However, in the case of OA with its significantly higher supersaturation ($\zeta = 20.5$, $\chi = 0.029$), there was negligible thermodynamic preference between convex and concave locations, and condensation occurred on the spheres (Figure 3.10b) because of their significantly larger surface area. There was little change in the outcome for OA when its supersaturation in the model was decreased to an atmospherically relevant $\zeta = 4$ (Donahue, *et al.*, 2011) ($\chi = 0.147$, Figure 3.12b).

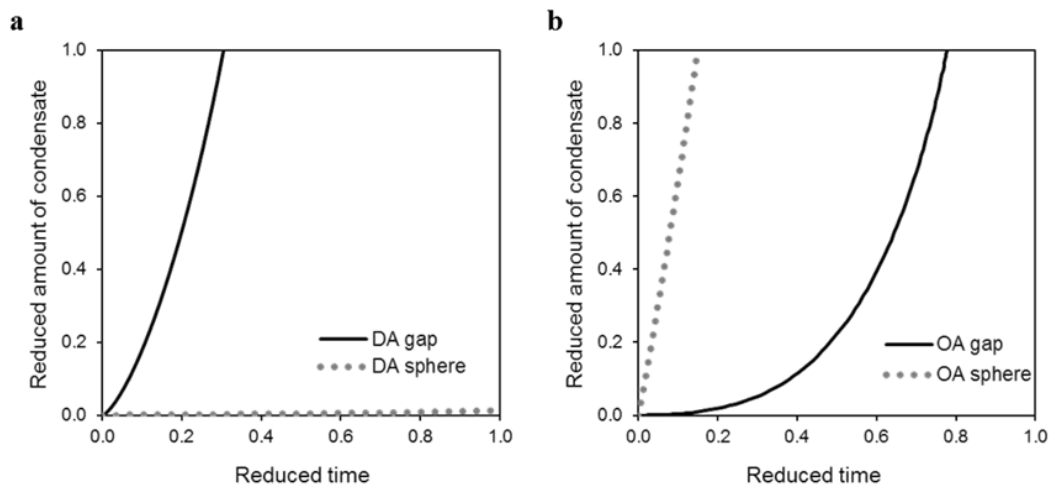


Figure 3.10 Calculated competition between the uniform vapor condensation over the entire aggregate (sphere) and capillary condensation in junctions (gap): (a) DA ($\zeta = 0.36$, $\chi = 1.042$) and (b), OA ($\zeta = 20.5$, $\chi = 0.029$). Reduced amount of condensate equaling 1.0 corresponds to half of the volume of the monomer sphere. The monomer sphere diameter is 28 nm. See Table 3.1 for acronyms.

Using our predicted values of vapor supersaturation, χ was calculated for all coating materials used in this study and plotted as a function of aggregate restructuring. The clustering of the coating materials to produce two different restructuring behaviors signified the different coating distributions. From Figure 3.11, it is clear that low volatility coatings are characterized by low χ values whereas intermediate volatility chemicals congregate around χ values close to 1. Most notably, the difference in χ between low and intermediate coatings span 2 orders of magnitude. Figure 3.11 illustrates the ability of χ to predict both coating distribution and extent of restructuring.

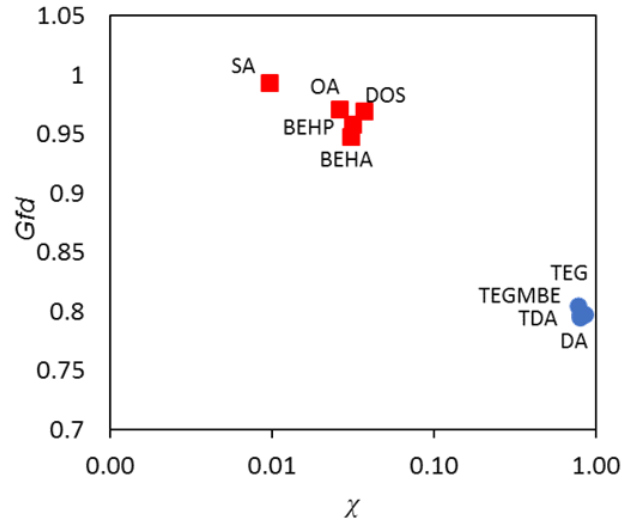


Figure 3.11 Extent of restructuring (Gfd) as a function of the dimensionless parameter χ . The monomer sphere diameter is 28 nm. See Table 3.1 for acronyms.

According to Equation (3.15), for a given substance, only the product of ζ and R_s is important in determining the value of χ . Thus, for a fixed ζ , the distribution of the condensate must be affected by the size of the monomer spheres R_s . Such dependence is indeed confirmed by our calculations for the condensation of OA at a fixed $\zeta = 4.0$ on monomers of different diameters. When the monomers are relatively large (28 and 45 nm), the condensation shows no spatial preference (Figure 3.12b, c), resulting in a uniform coating. However, for smaller, 7 nm monomers, capillary condensation in the junctions competes with condensation on spheres (Figure 3.12a). With this information in hand, we can explain the vastly different restructuring behavior reported by research groups who used different types of soot. For instance, the commonly recognized ease of restructuring of spark-discharge (Palas) aggregates (Lu, *et al.*, 2008; Saathoff, *et al.*, 2003; Weingartner, *et al.*, 1997) can be explained by the small, 7 – 11 nm diameter monomers (Weingartner, *et al.*, 1997), where condensation occurs mostly in the junctions, placing the condensate

where it has the largest impact on morphology. Such capillary condensation may explain the unexpected restructuring of spark-discharge aggregates exposed to products of propene ozonolysis, which have a high vapor pressure and typically do not exist in the aerosol phase (Lu, *et al.*, 2008). Similarly, the significant restructuring of the lightly coated soot (OA, $f_m \sim 0.05$) observed by Bambha, *et al.* (2013) could be due to the small, 11 nm diameter of the monomer spheres, while the minor restructuring of the heavily coated soot (OA and DOS with $f_m \sim 0.5$) observed by Ghazi and Olfert (2013) and Cross, *et al.* (2010) could be due to the large, ~ 40 nm monomers. The monomer diameter also defines the number of monomer spheres in aggregates of comparable size and hence the maximum extent of compaction (Leung, *et al.*, 2017a).

The dependence of χ on surface tension is not very significant because for most chemicals a higher surface tension is negatively correlated with molar volume so that the product of these two quantities results in little variation in l_k (Equations 3.7 and 3.15, Table 3.1). For this reason, SA ($\gamma = 73 \text{ mN m}^{-1}$) was only marginally more effective at restructuring than other materials ($\gamma = 27\text{-}46 \text{ mN m}^{-1}$), and only when coating thickness exceeded $\Delta R_s > 3 \text{ nm}$ (Figure 3.5). Similarly, Kütz and Schmidt-Ott (1992) have reported comparable restructuring for non-polar *n*-hexane and polar 2-propanol, when the supersaturation was sufficiently high for the condensate to engulf the soot aggregates. Also, Schnitzler, *et al.* (2017) have shown that glycerol (64 mN m^{-1}) and ethylene glycol (47 mN m^{-1}) produced marginally larger compaction than tridecane (26 mN m^{-1}), even when applied as a thick layer.

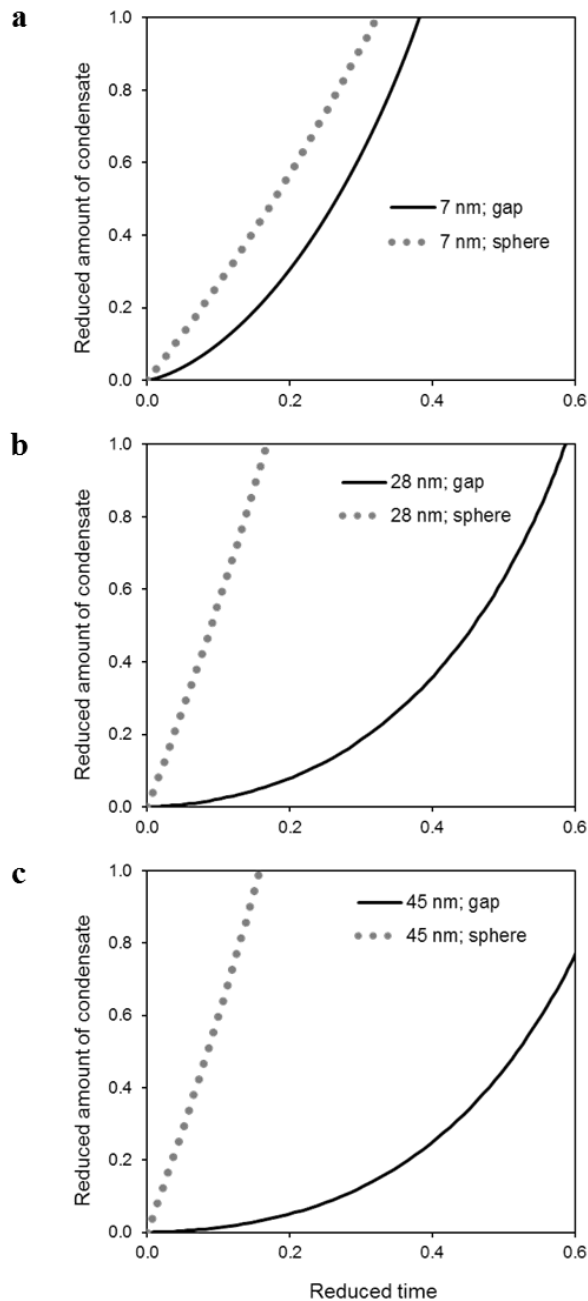


Figure 3.12 Calculated competition between the uniform vapor condensation over the entire aggregate surface (sphere) and capillary condensation in junctions (gap) for different monomer diameters: (a), 7 nm ($\chi = 0.590$), (b), 28 nm ($\chi = 0.147$), and (c), 45 nm ($\chi = 0.092$). Reduced amount of condensate equaling 1.0 corresponds to half of the volume of the monomer sphere. The condensing vapor is oleic acid, OA ($\zeta = 4.0$).

3.4 Conclusions

We propose the use of the dimensionless parameter, χ , to evaluate the distribution of coating material on atmospheric soot aggregates, and hence predict their morphological mixing state and extent of compaction. This parameter can be computed straightforwardly for a specified soot monomer diameter and coating material properties. The monomer diameter is readily available from imaging studies of soot particles collected during multiple field campaigns, varying in a relatively narrow range of 20–50 nm (Adachi, *et al.*, 2007; Chakrabarty, *et al.*, 2006a; Wentzel, *et al.*, 2003). Coating material properties, including surface tension, molar volume, and volatility, can be inferred from the particle analysis by high-resolution aerosol mass spectrometry (Jimenez, *et al.*, 2009) in conjunction with aerosol volatility measurements (Riipinen, *et al.*, 2010) and modified volatility basis set theory (Kroll, *et al.*, 2011). The parameterization can be applied even for diesel exhaust and biomass combustion particles that are already coated, as long as their morphological mixing state is known.

Sulfuric acid vapor is nearly always highly supersaturated, but supersaturation of organic vapors can vary broadly both spatially and seasonally because of vast differences in emission sources and photochemical oxidation rates. Accordingly, a range of mixing states and morphologies of aged soot can be produced, leading to significant variation in light absorption enhancement between different locations, as reported in recent field studies (Cappa, *et al.*, 2012; Liu, *et al.*, 2017; Liu, *et al.*, 2015). These differences, at least for lightly aged soot, can be reconciled using the χ methodology. Furthermore, the χ framework, in differential or integral form, can be incorporated into particle resolved models (Rierner, *et al.*, 2009) to improve predictions of the morphological mixing state and

morphology of soot. Such predictions have not yet been possible because of the commonly used spherical shape assumption for black carbon particles.

CHAPTER 4

IS IT CONDENSATION OR EVAPORATION THAT DRIVES AGGREGATE RESTRUCTURING?²

A large body of work has concluded that aggregate restructuring is caused by liquid shells when they form by vapor condensation. However, some recent studies argue that soot remains fractal even when engulfed by shells, collapsing when the shells evaporate. In this chapter, we reconcile this disagreement by investigating soot restructuring under conditions ranging from capillary condensation to full encapsulation, also including condensate evaporation. The contributions from condensation and evaporation to aggregate restructuring are discriminated, and the importance of coating wettability is discussed.

4.1 Introduction

Studies have shown that initially fractal aggregates restructure and become compact due to the presence of liquid coatings acquired via condensation (Bambha, *et al.*, 2013; Ghazi & Olfert, 2013; Pagels, *et al.*, 2009; Saathoff, *et al.*, 2003; Schnitzler, *et al.*, 2014; Zhang, *et al.*, 2008). Contrastingly, the results of the study by Ma, *et al.* (2013a) showed that restructuring occurred only during droplet evaporation for water-coated aggregates. A recent study by Bhandari, *et al.* (2019) on cloud-processed soot aerosol also implied the occurrence of aggregate restructuring only after water evaporation, not during condensation. This prompted (Heinson, *et al.*, 2017) to make a bold conclusion that the

² The findings presented for this chapter have been submitted to the peer-review journal, Environmental Science & Technology.

debate on whether vapor condensation or coating evaporation is primarily responsible for soot restructuring is ‘ultimately settled’.

Based on current literature (Mikhailov, *et al.*, 2006; Popovicheva, *et al.*, 2008; Zuberi, *et al.*, 2005) it is clear that for water, a non-wetting liquid, evaporation induces most of aggregate restructuring. However, for wetting liquids, which make up most of the other organic and inorganic condensates in the atmosphere, the relative roles of condensation and evaporation on aggregate restructuring are still not well established. So far, the conclusions made are piecewise due to the use of different types of soot, condensing vapors, saturation conditions, and processing methods. Since soot particles in the atmosphere can undergo both condensation and evaporation, it is important to understand how each of these two processes affects the evolution of soot structure for better quantification of its environmental impacts. In this study, we present experimental measurements of aggregate restructuring for a single type of soot exposed to organic vapors, which wet the soot surface, at both sub and supersaturated conditions. Aggregate collapse was determined via standard aerosol mobility instrumentation. Additionally, we measured sizes of encapsulated aggregates and tracked their evolution as the coating was lost by using a custom-built electrostatic particle classifier, which was placed at predetermined distances after the point of soot exposure to the condensable vapors.

4.2 Particle Growth Measurements and Modeling

Soot particles were generated, size-classified and exposed to condensable vapors of TEG, TEGMBE, DA and OA (see Table 3.1 for acronyms and properties) in the manner described previously in Chapter 2. The effect of coating on particle mobility diameter was

quantified via tandem differential mobility analysis (DMA-DMA) and electrostatic particle classification (DMA-EPC) techniques (see Figure 4.1). In DMA-DMA, the first analyzer was maintained at a constant voltage to select particles of a specified mobility diameter. The size-classified particles were processed and then sent through a second DMA. Voltage in the second DMA was scanned and particle concentration at the exit measured by the CPC.

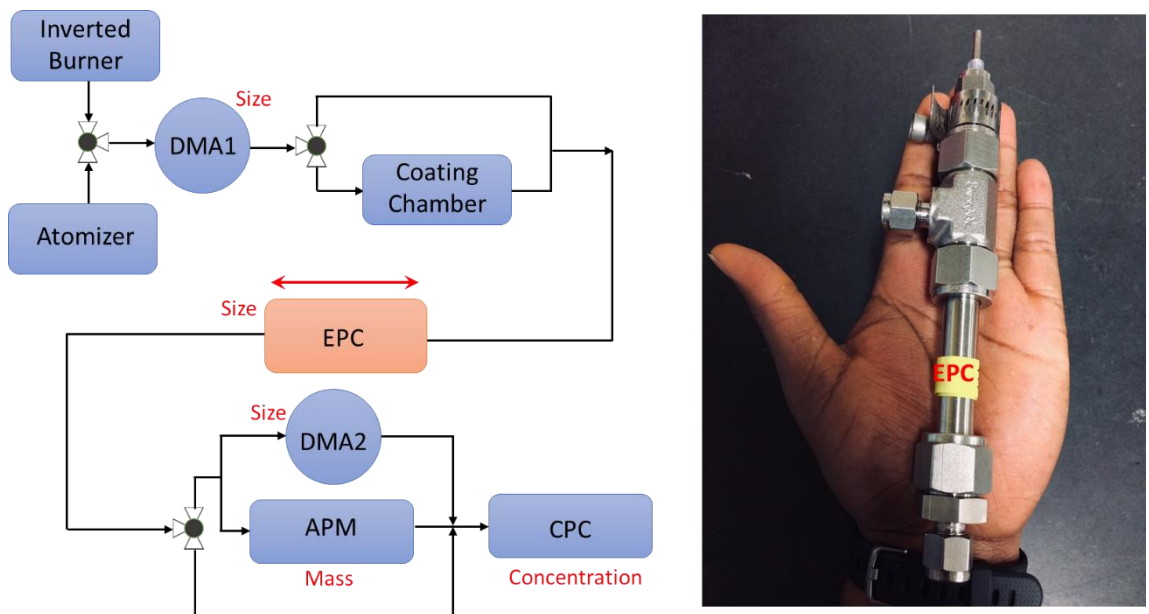


Figure 4.1 Schematic of the system for aerosol generation, processing and measurement. The electrostatic particle classifier (EPC), shown on the right, is sufficiently compact to be placed at any location after the saturator exit. DMA is the differential mobility analyzer, APM is the aerosol mass analyzer and CPC is the condensation particle counter.

In DMA-EPC, changes in particle size due to coating condensation or evaporation were measured by placing the EPC at the exit of the saturator. Also, the EPC was sufficiently compact to be placed at several locations after the exit of the coating chamber that allowed the tracking of particle size evolution (see Figure 4.1). Details of the principle of design and calibration of the EPC are provided the following subsection.

4.2.1 Electrostatic Particle Classifier

Principle of design: The design of the electrostatic particle classifier (EPC) is based on the use of electrical force to move particles out of a flowing gas stream and onto a collector electrode. (Hinds, 1999; Reist, 1993) The miniature EPC, designed and built in our lab, consisted of a stainless-steel outer tube with an inner diameter of 9.5 mm, and a coaxial stainless-steel collector rod with a diameter of 3.2 mm. The collector rod was connected to a positive DC high voltage supply (0-10 kV) while the outer tube was grounded. By maintaining a high voltage on the collector electrode, an electric field is generated that forces charged particles in the aerosol flow to the collector rod surface.

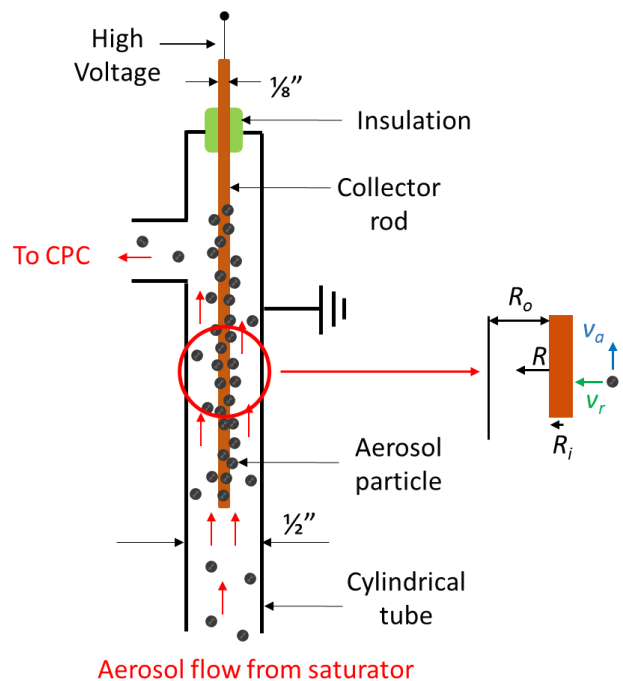


Figure 4.2. Schematic of the electrostatic particle classifier. The high voltage collector rod is coaxial with the stainless steel tube which is grounded. The red arrows indicate the aerosol flow path.

From Figure 4.2, it can be observed that the collection process is a competition between electrical and dispersive forces acting on the charged particles within the laminar region close to the collector rod. The efficiency, η of this process is described by

$$\eta = \frac{v_r}{v_a} \quad (4.1)$$

where v_r and v_a are the radial (migration) and axial velocities of the charged particle, respectively. For high collection efficiency, the particle migration velocity should be much higher than the axial velocity component which is a function of the collection rod area, A and the gas volumetric flow rate, Q :

$$v_a = \frac{Q}{A} \quad (4.2)$$

The migration velocity is the average velocity attained by the charged particles due to the influence of the electric field. It can be expressed as:

$$v_r = ZE_c \quad (4.3)$$

where E_c is the electric field strength and Z , the particle mobility, is a function of the viscous drag force of the gas and is related to the particle diameter, D_p by using Stoke's law as:

$$Z = \frac{neC_c}{3\pi\mu D_p} \quad (4.4)$$

where n is the number of elementary charges on the particle, e is the elementary unit of charge (1.61×10^{-19} C), C_c is the Cunningham slip correction factor, and μ is the gas

viscosity. The field strength inside a grounded cylindrical tube with a high voltage rod along its axis is given by:

$$E_c = \frac{\Delta V}{R \ln(R_o/R_i)} \quad (4.5)$$

where ΔV is the voltage difference between the tube and the rod, R is the radial position of the field, R_o and R_i are the radius of the tube and rod, respectively. Combining Equations (4.1 – 4.5), we obtain:

$$\eta = \frac{AZ\Delta V}{QR \ln(R_o/R_i)} \quad (4.6)$$

Equation (4.6) shows that the collection efficiency of the EPC is proportional to the voltage difference for a fixed particle mobility diameter. Thus, for particle size measurements, voltage in the EPC was stepped while the number concentration of transmitted particles was measured by CPC.

Calibration: The EPC was calibrated using spherical particles of ammonium sulfate generated by atomizing a 50 mM aqueous solution of the salt. Particles of known size (100 - 650 nm) produced by size classification with DMA1 were sent to the EPC, and the voltage dependence of the particle collection efficiency was obtained (Figure 4.3a). From this dependence, the voltage corresponding to 50% collection efficiency was recorded, and plotted as function of the particle diameter (Figure 4.3b). A linear fit to the data in Figure 4.3b was then used to estimate particle size from voltage scans obtained during our experiments.

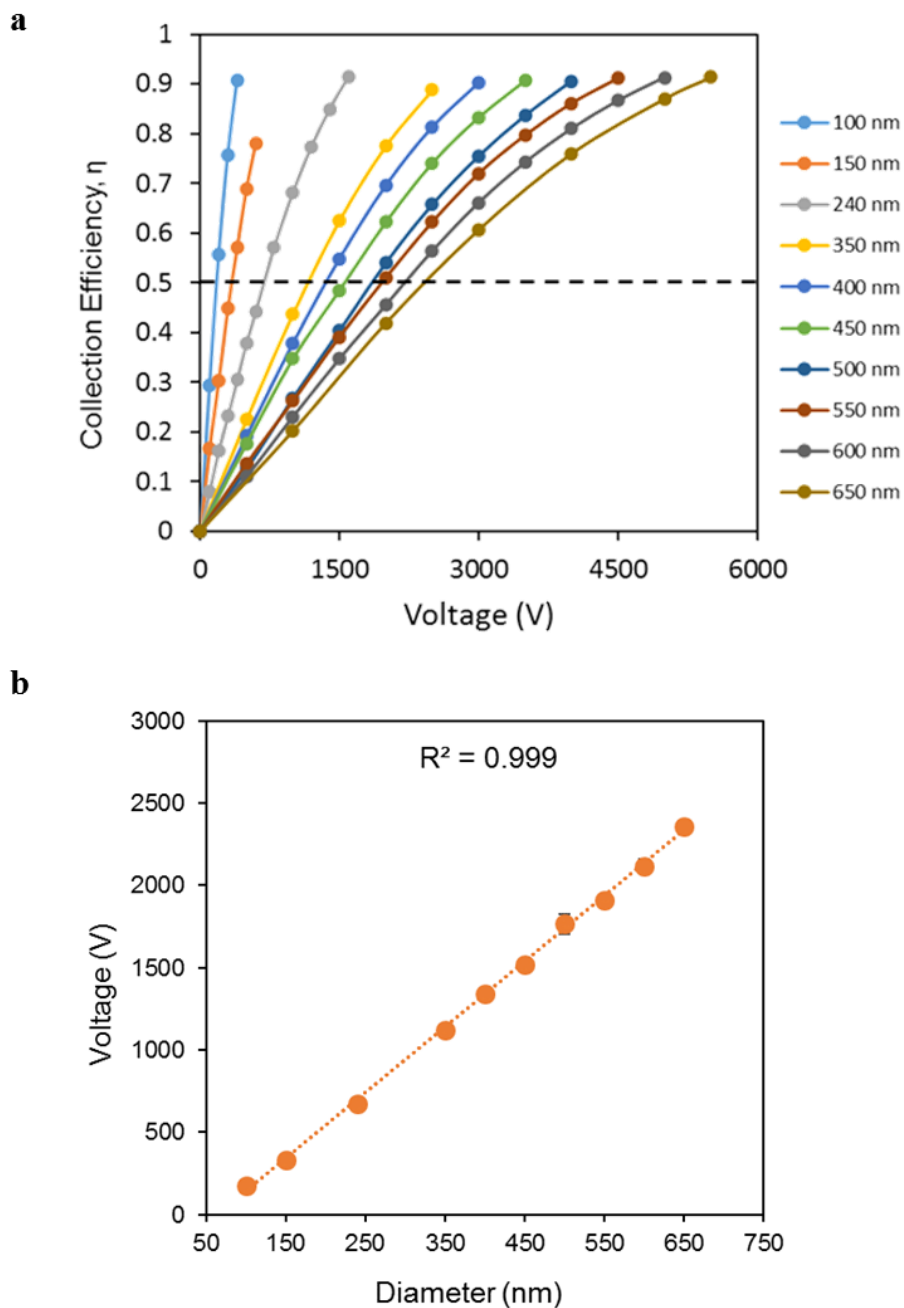


Figure 4.3 Calibration of the electrostatic particle classifier: (a) collection efficiency as a function of applied voltage for different particle diameters, (b) voltage-size dependence for a 50% collection efficiency. The error bars are smaller than the symbols used for the data points.

Changes in particle size were reported in terms of the diameter growth factor, Gfd
 $= D_{processed} / D_{initial}$. Here $D_{processed}$ is the coated particle mobility diameter determined by

the second DMA or the electrostatic classifier, and $D_{initial}$ is the fresh soot mobility diameter selected by the first DMA. The relative error in TDMA measurements was less than 1%. Relative error in EPC measurements was ~6%.

Using the model implemented in Python as previously described in Chapter 3 (Section 3.2), changes in size of spherical aerosol particles due to vapor condensation and coating evaporation were modeled. Modeled particle sizes were compared against electrostatic particle classifier measurements for the same initial particle diameters and distance from the exit of the coating chamber.

4.3 Results and Discussion

4.3.1 Three Distinct Regions in Vapor Supersaturation for Aggregate Restructuring

Experiments to determine the relative roles of the condensation and evaporation of wetting liquids on soot structural behavior were conducted by passing size-classified soot particles through a saturator partially filled with an organic liquid. The temperature of the saturator was varied from 24 to 60 °C and that controlled both p_{sat} and vapor supersaturation, ζ (Equation 3.11) of the coating.

Upon exiting the saturator, vapor condensation occurred on the soot particles and the change in particle size was measured. As is typical of most soot studies (Ghazi, *et al.*, 2013; Miljevic, *et al.*, 2012; Pagels, *et al.*, 2009), these particle size measurements were done using tandem differential mobility analysis (DMA-DMA). However, due to the volatile nature of most coatings used in our experiments (see Table 3.1 for properties), there was a possibility of coating loss via evaporation occurring prior to measurement by the second DMA, which was located at a distance of 3.5 m from the saturator exit. Thus,

we also employed an electrostatic particle classifier (EPC) which we placed at 0.04 m from the saturator exit to capture particle size behavior before they had a chance to lose the coating by evaporation. The EPC operates without a sheath flow, preventing bias in measurement due to coating evaporation that can be caused by sheath air. The results of our particle size measurements, expressed in terms of diameter growth factor (Gfd), are illustrated in Figure 4.4 for triethylene glycol (TEG) coating.

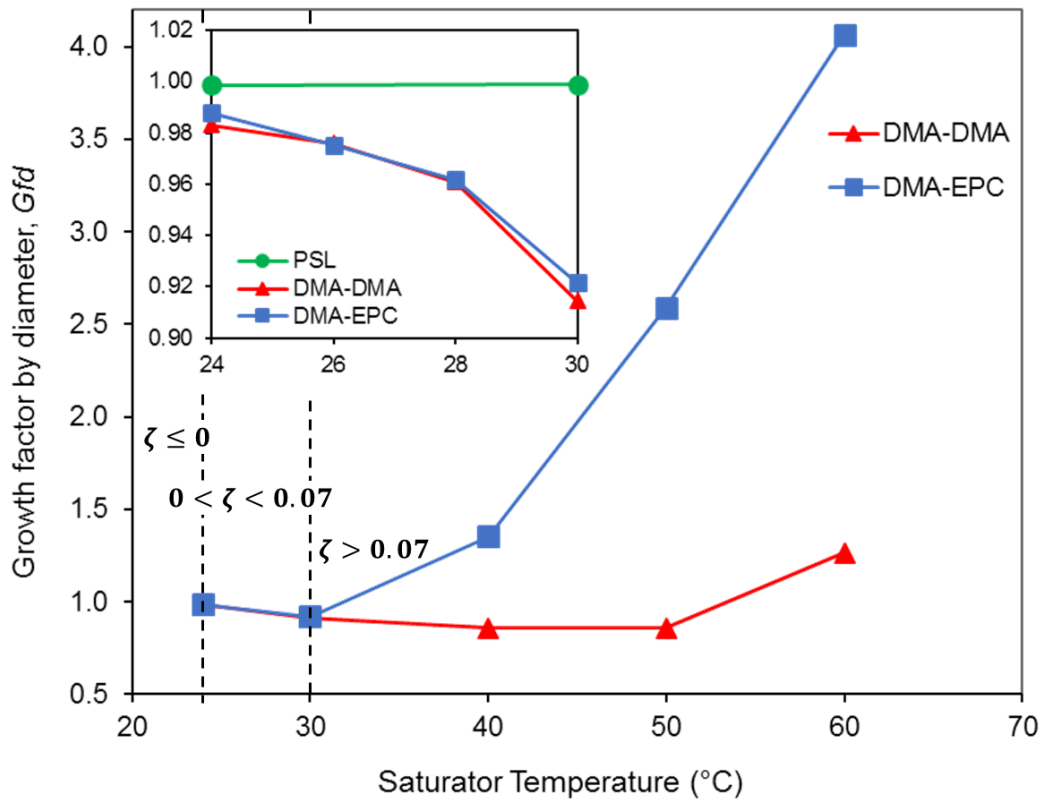


Figure 4.4 Evolution in particle growth factor (Gfd) of soot aggregates with increasing saturator temperature, measured by tandem differential mobility analysis (DMA-DMA) and electrostatic particle classification (DMA-EPC) methods. The initial mobility diameter of soot is 240 nm and the coating material is triethylene glycol (TEG). The dashed lines highlight the different regions of vapor supersaturation. Inset shows an expanded view of Gfd at low saturator temperatures. The green circle represents PSL with a 150 nm initial mobility diameter.

From Figure 4.4, it can be observed that both DMA-DMA and DMA-EPC yield similar Gfd curves for soot at low saturator temperatures ($T \leq 30$ °C), but diverge for temperatures above 30°C. With the DMA-DMA, Gfd starts at 0.98 at 24 °C (room temperature), passes through a minimum (0.86) at 40°C, after which it increases again, reaching to 1.26 at 60 °C. Since for an uncoated aggregate, particle mobility is unchanged and $Gfd = 1$, the changes in Gfd observed in Figure 4.4 reflect the superposition of a decrease in the particle mobility diameter ($Gfd < 1$) due to restructuring of the soot backbone and an increase ($Gfd > 1$) due to addition of condensed coating. This trend in particle mobility diameter has been observed previously in Chapter 3 and in other studies (Khalizov, *et al.*, 2013; Zhang, *et al.*, 2008).

In the DMA-EPC measurements, similar to the DMA-DMA results, Gfd starts at 0.99 and decreases to 0.92 as the saturator temperature is elevated to 30 °C. However, additional increase in temperature causes a rapid rise in Gfd till it attains a value of 4.1 at 60°C. The sharp rise in Gfd at temperatures above 30 °C indicates the presence of significant coating volume, which forms on the partially restructured soot aggregates. This significant growth was not observed in the DMA-DMA measurements due to coating evaporation during transit from the saturator exit to the second DMA. The rate of coating loss was further investigated by using the DMA-EPC to measure coated particle size as a function of distance from the saturator exit (Figure 4.5). The results show a decrease in coated particle diameter with increasing distance, indicating that the tubing walls act as a vapor sink for coating evaporated from the convex surfaces of soot aggregates. Our model predictions for spherical particles of equivalent initial volume diameter, also displayed in Figure 4.5, agree well with our experimental measurements (see Section B.2, Appendix B

for more details). It is clear that our DMA-DMA measurements underestimated the amount of condensate at elevated saturator temperatures, introducing bias in analysis of the aggregate restructuring behavior. The DMA-EPC method, on the other hand, captured the true particle growth behavior. Similar results were also obtained for the more volatile TEGMBE and DA (Appendix B.1, Figure B.1). Given the volatile nature of these coatings, such accurate size measurement is paramount for separating the effects of vapor condensation and coating evaporation on aggregate restructuring.

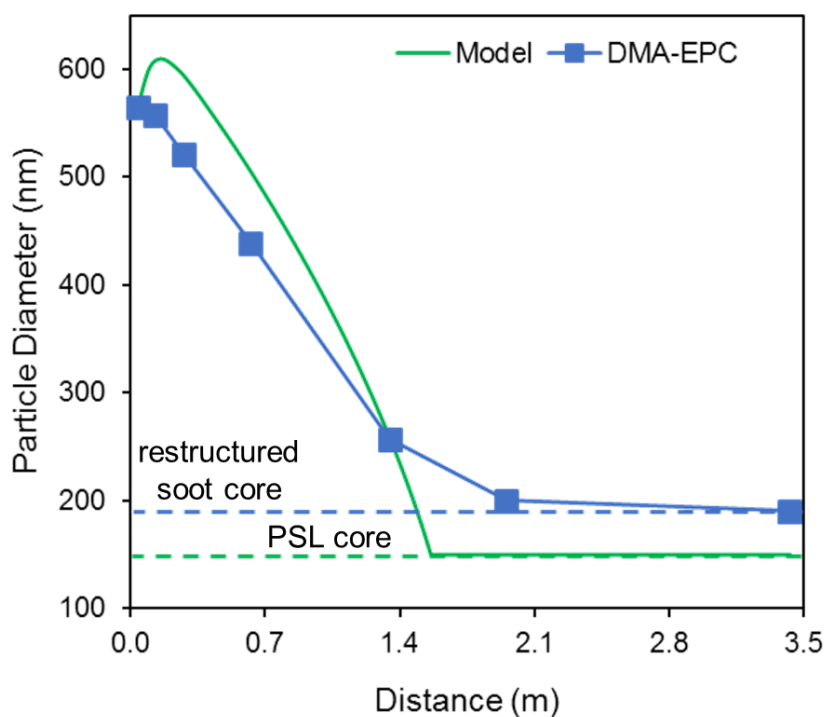


Figure 4.5 Modeled (line) and measured (squares) profiles of particle diameter as a function of distance from the exit of the saturator during soot aging with triethylene glycol (TEG). The blue solid line in the experimental data is provided to guide the eye. The dashed blue lines represent the final compact soot morphology while the dashed green lines represent uncoated PSL. The saturator temperature is 50°C and the initial (uncoated) particle mobility diameter is 240 nm.

Evidence that vapor condensation already leads to aggregate restructuring is illustrated in the inset of Figure 4.4. When the saturator is maintained at room temperature

(24 °C), growth factors measured by DMA-DMA and DMA-EPC were observed to be comparable and less than unity for fractal soot aggregates. For 150 nm spherical PSL particles, which is equivalent in volume to 240 nm soot, Gfd is unity and hence no condensation occurred on convex particle surfaces, confirming that the change in Gfd for soot was not due to measurement error or temperature fluctuations that could change saturation conditions. Since $\zeta = 0$ at room temperature, the observed aggregate restructuring is solely due to capillary condensation. This can be explained via Equations (3.31) and (3.32) which are shown again below:

$$J \propto p_{sat} \times (\zeta + 1 - K) \quad (3.31)$$

$$K = \exp\left(\frac{l_K}{R_c}\right) \quad (3.32)$$

From Equation (3.31), it can be seen that a positive vapor flux to the aggregate surface can occur even for $\zeta \leq 0$, if the Kelvin term, K is less than unity. This scenario arises when the radius of curvature, R_c in Equation (3.32) is negative as shown previously in Chapter 3. Thus, preferential condensation occurs in the concave junctions between monomers in the aggregate, leading to the formation of pendular rings of coating that induce partial aggregate restructuring. As the monomer junctions become gradually filled, K approaches unity and condensation stops. As the particles travel along the tubing, they retain their condensate because at $\zeta = 0$ there is no evaporation ($J = 0$ in Equation 3.31). The supersaturation remains zero because the tubing wall is coated with a thin layer of condensate, acting as a zero source or sink of vapor. We confirmed this wall-less behavior experimentally by flowing soot aerosol through an empty chamber, which was pre-exposed

to TEG vapor to build a coating film on chamber walls, producing capillary condensation and inducing minor, but notable restructuring ($Gfd = 0.96$) of the soot aggregates.

For saturator held at slightly above room temperatures (see Figure 4.4 inset), a gradual decrease in particle size was observed, with DMA-DMA measuring somewhat stronger restructuring than DMA-EPC at 30 °C ($Gfd = 0.91$). However, particle size remained unchanged for PSL ($Gfd = 1$), indicating lack of condensation on convex particles under these conditions. Using Equation (3.32), we estimated that at 30 °C, $K \sim 1.07$ for TEG on 150 nm PSL. Thus, in order to overcome the effect of positive PSL curvature, ζ must exceed 0.07 for condensation to occur (Equation 3.31). Similarly, for condensation to occur on the convex surfaces of the 28 nm monomers in the soot aggregates, ζ must be above 0.42. Since no growth was observed for PSL, it shows that $\zeta < 0.07$ for $T \leq 30$ °C. Thus, the decreased soot particle mobility shown in Figure 4.4 inset proves the occurrence of capillary condensation only, placing the condensate in the monomer junctions of aggregates. As the liquid volume in the junctions rises, the menisci transition from flat to slightly convex. Mean curvature for the aggregate, however, remains within that of 150 nm PSL, because ‘normal’ condensational growth does not occur ($Gfd < 1$). Given that at 30 °C the factor K is slightly above unity, there existed a possibility that some of the coating evaporated and this contributed to the measured aggregate restructuring. This concern, however, can be refuted using Figure 4.5, which shows that coating loss is minimal ($< 1\%$) within 0.2 m from the saturator exit for particle size measurements conducted at 50 °C. In fact, our model calculations, assuming laminar behavior throughout the entire saturator region, predict some additional condensational growth during the initial 0.2 m segment. Thus, no coating evaporation is expected during transition of the coated aerosol to the EPC

located within ~ 0.04 m from the saturator exit. This implies that at $T \leq 30$ °C, aggregate restructuring still stems from capillary condensation and not evaporation. Condensation-induced restructuring was further corroborated by measurements conducted with low volatility coatings, such as oleic acid (OA), which does not evaporate off the particles at room temperature, unlike TEG. Soot aggregates exposed to OA experienced a progressive restructuring with increasing condensate volume (see Appendix B.3, Figure B.2a). Similar to measurements with TEG, the particles started growing only after complete collapse at increased saturator temperatures corresponding to higher ζ and coating mass fraction ($\sim 42\%$). Particle growth occurred at a slower rate for OA than for TEG due to a lower condensational flux associated with a lower p_{sat} of OA (Appendix B.3, Figure B.2b).

At saturator temperatures above 30 °C, the saturation of TEG vapor becomes sufficiently large to overcome the Kelvin effect of the convex shell, resulting in ‘normal’ condensation. This condensational growth could only be detected by placing the EPC at the exit of the saturator. When measuring particle size at extended distances by either the EPC or second DMA, most of this ‘extra’ condensate becomes lost by evaporation during transit, as shown in Figure 4.5. However, some of the remaining condensate could be still observed even at a long distance for saturator temperatures above 50 °C, when the particles grow to such large sizes that some of the coating survives the transit. This condensate evaporation during transit may have contributed to an additional restructuring of soot aggregates.

While in the case of TEG, coating evaporation occurred already at room temperature, for OA it was necessary to pass the coated particles through a thermal denuder to remove the coating (Appendix B.3, Figure B.2a). In the latter case, the effect of thermal

denuding on compaction was noticeable only at saturator temperatures above 55 °C. For both chemicals, TEG and OA, an increase in compaction in the experiments with higher saturator temperatures could be caused by either the addition of extra condensate, evaporation of condensate, or both. Further studies are required to decouple the contributions from these two processes, for instance using the approach described by Ma, *et al.* (2013a). However, we can already tell that the effect of evaporation is not negligible. As shown previously in Chapter 3, the loss of coating material upon denuder-induced evaporation led to an additional small, but consistent compaction of coated aggregates, as reflected by the 12% and 5% increases in convexity for the intermediate and low volatility coating materials, respectively (see Table 3.2).

From Figure 4.4, three distinct regions in aggregate structural behavior can be observed, which are controlled by the coating vapor supersaturation. At $\zeta \leq 0$, capillary condensation occurs and leads to a slight decrease in particle mobility diameter due to a minor restructuring of the aggregate backbone. Under conditions of mild vapor supersaturation, the structural collapse of soot is enhanced by additional condensation in concave junctions. At higher vapor supersaturations, condensation on both concave and convex surfaces takes place and any further collapse in the soot backbone is eclipsed by the large amount of condensate formed on the aggregate. However, for volatile coatings this significant particle growth is noticeable only when measurements are conducted directly at the exit of the saturator chamber. At longer transit times, measurements show a significantly lower mobility diameter because most of the condensate is lost by evaporation, which can also promote some additional restructuring of the aggregates.

4.3.2 Vapor Supersaturation Required to Fully Encapsulate a Soot Aggregate

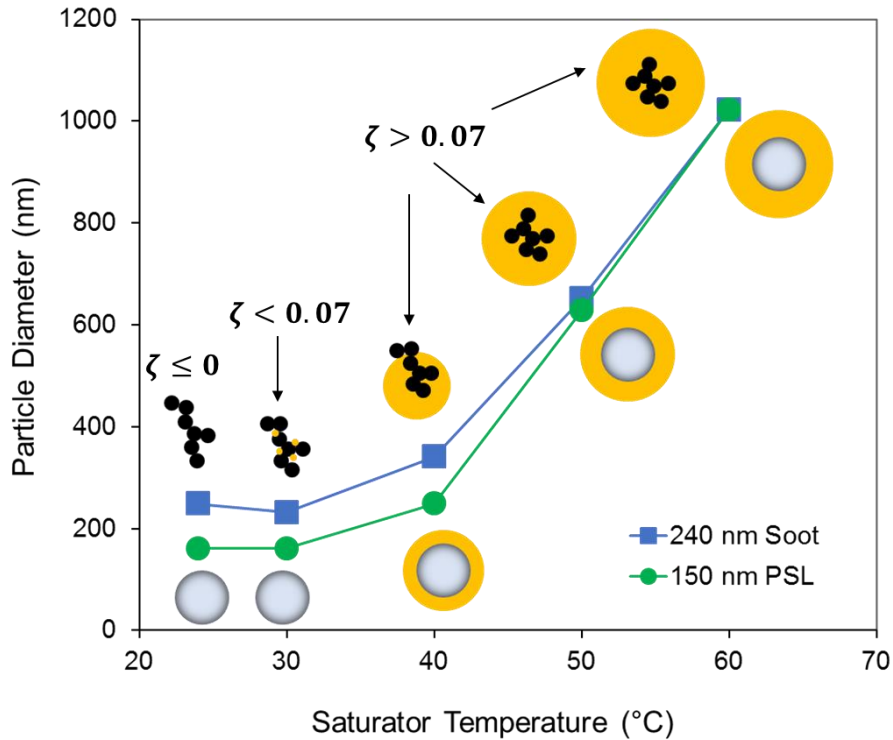


Figure 4.6 Measured diameter of soot and PSL particles exposed to TEG vapor produced at different saturator chamber temperatures. The electrostatic particle classifier (EPC) was placed at a distance of 0.04 m from the exit of the saturator chamber. The initial mobility diameters of PSL and soot particles are 150 and 240 nm, respectively.

In the previous section, it was shown that massive condensational growth takes place when soot particles are exposed to TEG vapor at $T \geq 40$ °C, but it is unclear if the aggregates ever become fully encapsulated to become core-and-shell, or assume some other configuration, e.g., an aggregate located at the periphery of the droplet with branches sticking out. To determine this, we compared growth profiles of soot against spherical PSL particles of a comparable volume equivalent diameter (150 nm), as shown in Figure 4.6. As noted before, at $T \leq 30$ °C, corresponding to $\zeta < 0.07$, no condensational growth was observed for PSL due to an elevated equilibrium vapor pressure above its convex sphere surface. However, at $T > 30$ °C, supersaturation was sufficiently high to overcome the

Kelvin term and the PSL spheres grew progressively larger with increasing temperature, reaching six times their original diameter at 60 °C. Notably, at 50 °C, soot and PSL growth profiles converge, signifying that the aggregates become fully encapsulated in spherical droplets when reaching a diameter of about 620 nm. As shown by electron microscopy (Chen, *et al.*, 2017), the average maximum length of fractal soot aggregates of a 240 nm mobility diameter is within 500-600 nm. Thus, full encapsulation occurs for aggregates that are already nearly fully restructured, and it depends primarily on the growth of the coating shell rather than on folding of aggregate branches. Further increase in temperature above 50 °C, yields nearly identical particle growth behavior for soot and PSL. Our model calculations also support the significant condensational growth at elevated p_{sat} and ζ observed in the experiments (Appendix B, Figure B.3).

4.3.3 Dependence of Aggregate Restructuring on Coating Volatility

In the atmosphere, photochemical degradation of volatile organic compounds (VOCs) can result in the formation of a broad range of oxidation products (Hallquist, *et al.*, 2009). The volatility of these oxidation products will influence their condensation and/or evaporation behavior during interaction with soot aggregates, potentially inducing varying levels of restructuring. We explored the effects of coating volatility on the restructuring of soot driven by capillary condensation by exposing the aggregates to different organic chemicals of intermediate volatility, for which reversible condensation is expected in the atmosphere. Since excessive condensational growth dominates aggregate restructuring at elevated temperatures, we kept the saturator temperature at $T \leq 30$ °C (corresponding to $\zeta < 0.07$) for the three organic coatings used in these experiments (TEG, TEGMBE and DA in Table 3.1). Particle size measurements via EPC were conducted at a short distance immediately

after the exit of the saturator. The entire system was purged with particle free air in between changes of the organic liquid.

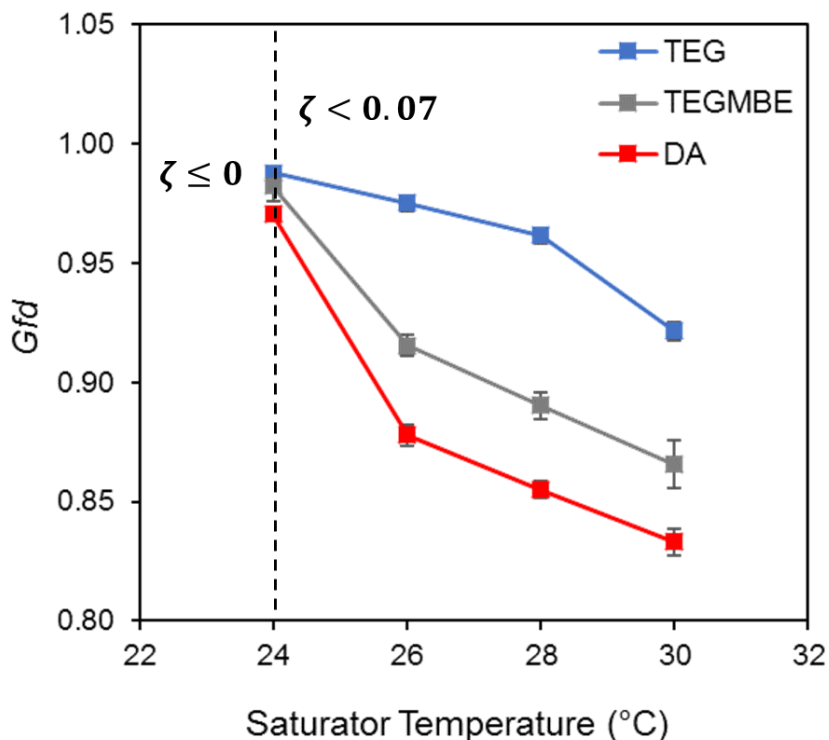


Figure 4.7 Dependence of soot aggregate restructuring on coating volatility at near saturated ($\zeta \leq 0$) and mildly supersaturated ($\zeta < 0.07$) conditions. The electrostatic particle classifier (EPC) was placed at 0.04 m from the exit of the saturator. Initial aggregate mobility diameter is 240 nm. See Table 3.1 for acronyms.

As shown in Figure 4.7, at room temperature (24 °C), Gfd drops below unity due to restructuring of the aggregate backbone with values of 0.99, 0.98, and 0.97 for TEG, TEGMBE and DA, respectively. Since for experiments conducted at room temperature there is no temperature gradient at the outlet of the coating chamber, ζ remains zero regardless of the coating liquid. Thus, condensational flux (Equation 3.31) to the aggregates is determined entirely by the Kelvin factor ($K < 1$), leading to capillary condensation in monomer junctions. The vapor flux to the junctions ceases once they are

filled, and the Kelvin factor becomes unity. The characteristic time for this condensation process for intermediate volatility organic compounds has been estimated to be ~ 1 ms (Donahue, *et al.*, 2011). By accounting for the curvature of the meniscus, we determined that the monomer junctions in the soot aggregate are filled within 1-10 ms for TEG, TEGMBE and DA. These times are short compared to the residence time of the aggregates in the saturator (~ 10 s), indicating that the coating meniscus forms rapidly and remains in dynamic equilibrium with its vapor. Thus, no appreciable difference is observed in restructuring between the three coating liquids at room temperature, when $\zeta = 0$.

Above room temperature ($T > 24$ °C), ζ remains zero within the chamber, soot particles are surrounded by saturated vapor, and the menisci formation proceeds as previously described. However, as the aerosol flow exits the saturator, the temperature decrease results in $\zeta > 0$, leading to a positive vapor flux and additional condensation. Given that K and ζ are similar for the three organic coatings, the difference in vapor flux in Equation (3.31) is mostly governed by the difference in p_{sat} (see Table 3.1). For instance, at 28 °C, p_{sat} is 0.23 Pa, 0.44 Pa, 9.3 Pa for TEG, TEGMBE and DA, respectively. Thus, condensate amount will be greatest for DA and lowest for TEG. Indeed, as seen from Figure 4.7, the aggregates attain their most compact configuration when exposed to DA due to a larger condensed coating volume. On the other hand, the difference in surface tension plays negligible role in this case. Amongst the three chemicals, TEG has the highest surface tension (46.5 mN m⁻¹), but causes least restructuring. TEGMBE and DA have lower and similar surface tensions (31.4 and 32.7 mN m⁻¹), but induce progressively larger restructuring.

4.4 Conclusions

We show in this study that liquids capable of wetting the surface of soot aggregates can induce a significant restructuring already upon condensation. The crucial role of soot wettability by the condensate in restructuring upon exposure to sub and supersaturated vapors has been shown previously. Kütz and Schmidt-Ott (1992) have reported significant restructuring for fractal aggregates exposed to subsaturated vapors of n-hexane and 2-propanol, but not with subsaturated vapor of water. Only at high supersaturations, a comparable significant restructuring was observed for all three condensates and the authors hypothesized that capillary condensation only occurred for n-hexane and 2-propanol because these liquids wet the graphitic surface nearly perfectly (low contact angle), unlike water, which wets graphite poorly. The theoretical calculations of Crouzet and Marlow (1995) confirmed that only for low contact angles, a stable pendular ring of condensate could exist between contacting spheres exposed to subsaturated water vapor. If the aggregate surface is hydrophobic, no capillary condensation and restructuring can occur under subsaturated water vapor conditions (Khalizov, *et al.*, 2009b; Mikhailov, *et al.*, 2006; Popovicheva, *et al.*, 2008) because of the large contact angle. If the aggregate surface is made hydrophilic, either by priming with a monolayer of hydrophilic adsorbate (Dusek, *et al.*, 2006b; Khalizov, *et al.*, 2009b; Weingartner, *et al.*, 1995) or by oxidation (Decesari, *et al.*, 2002; Weingartner, *et al.*, 1995), capillary condensation of water occurs due to the reduced contact angle (Xie & Marlow, 1997), and it is often followed by partial restructuring.

Since soot aggregate restructuring is most commonly associated with condensation (Ghazi & Olfert, 2013; Schnitzler, *et al.*, 2017; Slowik, *et al.*, 2007; Tritscher, *et al.*, 2011;

Xue, *et al.*, 2009a), the study by Ma, *et al.* (2013a) stands out for its opposing conclusion about prevalence of evaporation-induced restructuring. In this study, a very high supersaturation of water vapor (in excess of 0.20 – 0.26%) was used to force condensation on uncoated hydrophobic soot and the aggregates quickly became encapsulated within droplets. Aggregate morphology was then measured via light scattering while still inside the droplet and was found to be fractal. The soot aggregates restructured only after the droplets were allowed to evaporate. For a non-wetting liquid with high surface tension such as water, it is possible that at such high supersaturations, condensation on hydrophobic soot occurs as heterogeneous nucleation on a favorable location, such as a surface defect (Kousaka, *et al.*, 1995). Preferential condensation on the defect causes the water nucleus to grow rapidly outward from that point till the aggregate is engulfed. Since monomer junctions remain unfilled because of the high contact angle (Crouzet & Marlow, 1995), it is likely that aggregate restructuring would not occur during condensation, as shown by Ma, *et al.* (2013a) because the aggregates become encapsulated rapidly and within such an encapsulated aggregate capillary forces are absent. However, during droplet evaporation, surface tension forces from the shrinking droplet interface with air are directed inward, resulting in structural collapse of the aggregates.

While evaporation rather than condensation has been shown to drive the structural collapse of soot in the presence of water (Ma, *et al.*, 2013a), the suggestion that coating evaporation is the only path to aggregate restructuring, as indicated by Ma, *et al.* (2013a) and Heinson, *et al.* (2017) is too categorical. The conclusion made in those studies is certainly valid for non-wetting liquids, of which the most abundant species in the natural environment is water. However, water vapor supersaturations required to activate

hydrophobic soot particles into fog or cloud droplets are not commonly achievable in the atmosphere. One scenario where such conditions may arise would be in the tailpipe exhaust of vehicles running on low sulfur fuel during cold weather. Rapid cooling of hot exhaust gases may create water supersaturations that are sufficiently high to activate hydrophobic soot particles, and further dilution of the exhaust plume would result in water droplet evaporation and associated evaporation-induced restructuring. In all other cases, most chemicals that condense on soot particles wet the soot surface nearly perfectly. Hence filling of the junctions and significant restructuring would occur already during vapor condensation, unless the condensate is a solid or a viscous liquid at ambient conditions. Thus, future studies should focus on elucidating conditions that lead to the formation of solid (or viscous) versus liquid coatings.

CHAPTER 5

VALIDATION OF CHI MODEL WITH MULTICOMPONENT SYSTEM³

In Chapter 3, a theoretical framework for predicting the morphological mixing state and extent of compaction of soot aggregates was presented. This framework was designed for and used to rationalize the condensation behavior of single component coatings. However, atmospheric processes usually generate a wide range of gaseous oxidation products that may condense simultaneously on soot aggregates to form multicomponent coatings. In this chapter, we use our knowledge of coating distribution to explain the restructuring behavior of soot aggregates exposed to a more realistic multicomponent system of condensable vapors.

5.1 Introduction

Given their atmospheric abundance, gaseous products derived from the photochemical oxidation of volatile organic compounds (VOCs) account for a significant fraction of condensable species on soot (Adachi & Buseck, 2008). Laboratory studies on soot aging due to the condensation of organic coatings from biogenic precursors (isoprene (Khalizov, *et al.*, 2013; Li, *et al.*, 2017), α -pinene (Ma, *et al.*, 2013b; Saathoff, *et al.*, 2003), and limonene (Pei, *et al.*, 2018)) and anthropogenic precursors (aromatic hydrocarbons (Guo, *et al.*, 2016; Qiu, *et al.*, 2012; Schnitzler, *et al.*, 2014) and diesel exhaust mixtures (Nakao,

³ The findings presented for this chapter have been published in the peer-review journal, Atmospheric Research under the reference listing:
Chen, C.; Enekwizu, O. Y.; Ma, X.; Jiang, Y.; Khalizov, A. F.; Zheng, J.; Ma, Y., Effect of Organic Coatings Derived from the OH-Initiated Oxidation of Amines on Soot Morphology and Cloud Activation. *Atmospheric Research* **2020**, 239, 104905.

et al., 2011; Tritscher, *et al.*, 2011)) have shown varying degrees of aggregate restructuring. For instance, it was observed that soot aggregates exposed to small amounts of photochemically oxidized isoprene decreased in size due to restructuring (Khalizov, *et al.*, 2013) whereas an increase in size with no structural change was reported for a comparable mass of coating derived from aromatic precursors (Ma, *et al.*, 2013b; Schnitzler, *et al.*, 2014).

Amines are atmospherically ubiquitous species and can be co-emitted with soot from a variety of natural and anthropogenic sources (Ge, *et al.*, 2011). For example, monoethanolamine (MEA) is used to remove acidic chemicals (and in some cases CO₂) from flue gases produced by power generation plants. Amines can also be co-emitted with soot in polymer combustion, rocket and automobile exhaust. Although gasoline engines do not produce much soot, they are on the same road as diesel powered engines, which are a significant soot source. Biomass burning events can also result in the co-emission of amines with soot. Once emitted, these chemicals can contribute to atmospheric particulate matter loading through gas phase oxidation by ozone, hydroxyl radical, and nitrate radical followed by gas-particle partitioning (Murphy, *et al.*, 2007; Price, *et al.*, 2016). The basic nature of amines also leads to the formation and growth of new particles via heterogeneous reactions with acidic clusters and aerosols (Wang, *et al.*, 2010c; Wang, *et al.*, 2010d), and the reactive substitution of ammonia with aminium salts (Bzdek, *et al.*, 2010; Chan & Chan, 2012). It has been suggested that amines may contribute significantly to the organic content of ambient particles (Qiu & Zhang, 2013), thus altering their physicochemical properties (Ge, *et al.*, 2016). While some progress has been made in understanding the

heterogeneous chemistry of amines (Qiu, *et al.*, 2011; Wang, *et al.*, 2010b), relatively little is known about the interactions between their photooxidation products and soot aerosol.

In this study, the modification of soot by products of OH-initiated oxidation of monoethanolamine (MEA), triethylamine (TEA), and aniline was investigated. Experiments were conducted in an environmental chamber and changes in particle size, mass and cloud condensation nuclei (CCN) activity were measured simultaneously. From trends in mass growth factor, diameter growth factor, effective density, and dynamic shape factor conclusions are made about the restructuring and CCN activation of soot aged in the presence of amines, and their atmospheric implications are discussed.

5.2 Chamber Experiments

All experimental measurements were conducted by Dr. Chao Chen and Dr. Yan Ma at the Nanjing University of Information Science and Technology (NUIST) in China. For clarity, a brief summary of their experiments is provided. A more detailed description can be found in Chen, *et al.* (2020).

To create a multicomponent system of multiple condensing vapors, soot aging experiments were conducted in an environmental chamber which was operated in batch mode. Unlike the flow reactor method which was used in all other soot aging studies for this dissertation, chamber experiments are more representative of atmospheric conditions and are designed to share nonlinearities and other complicating factors experienced by aerosols during transport in the real atmosphere.

Soot particles were generated and size-classified in the manner described previously in Chapter 2. Size selected soot particles were then injected into the

environmental chamber and initial measurements of particle size, mass and CCN activity were obtained simultaneously. Hydrogen peroxide (H_2O_2) and the amine precursor were then flushed into the chamber, in a flow of air from their respective solutions. The air in the chamber was mixed by a fan for about 10 s and then ultraviolet lamps were turned on to initiate OH-induced oxidation of the amine precursor via H_2O_2 photolysis. Gas phase concentrations of H_2O_2 and the amine precursor estimated based on the injected amount were 5 parts per million (ppm) and 15 or 100 parts per billion (ppb), respectively. In selected experiments, to investigate the restructuring of the soot particle core, aerosol flow was passed through a thermodenuder to remove organic coatings, and then the size distribution was determined. Temperature and humidity in the chamber in all experiments were maintained at 25 ± 3 °C and 15%, respectively. Between measurements, the chamber was flushed and filled with purified air to ensure that the background number concentration was less than $10 \text{ particles cm}^{-3}$.

5.3 Results and Discussion

5.3.1 Fresh Soot Measurements

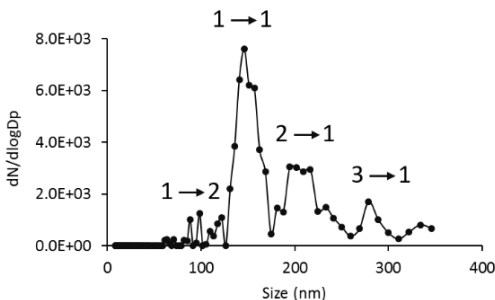


Figure 5.1 Multimodal distribution of mobility-classified fresh soot aerosol showing the existence of multiply charged particles. Recharging processes are indicated above the corresponding size modes.

Initial measurements of soot particle size revealed the presence of several distinct modes, although only particles of 150 nm mobility diameter were injected into the empty chamber by DMA1. The additional particle modes were identified when aerosol flow from the chamber was passed through another diffusion charger before entering DMA2. The main mode at about 150 nm represents singly charged soot particles. The modes at 210 nm and 280 nm indicate particles that had two and three charges on exiting DMA1, and entering the chamber, but became singly charged after passing through another diffusion charger. During analysis, the mean particle diameter of $170 \text{ nm} \pm 11 \text{ nm}$ was used to track changes in particle size during aging.

5.3.2 Soot Aging with Low Initial Amine Concentration

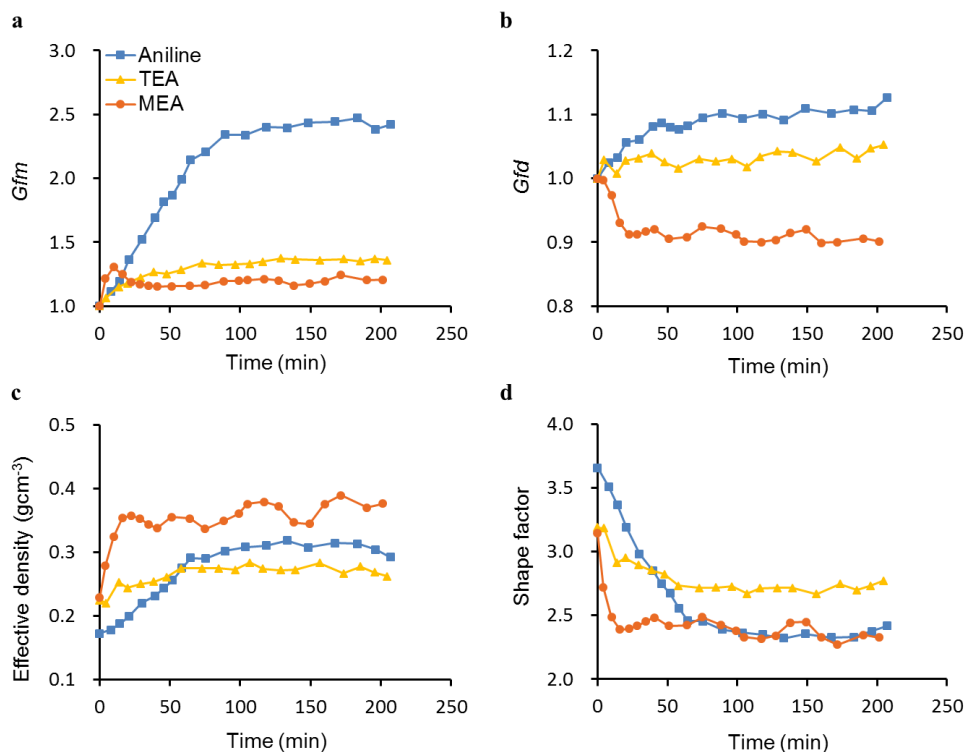


Figure 5.2 Evolution in (a) mass growth factor (G_{fm}), (b) diameter growth factor (G_{fd}), (c) effective density (ρ_{eff}), and (d) shape factor (χ_{shape}) of soot particles upon photochemical aging in the presence of 15 ppb amines with 150 nm initial diameter.

Morphological changes in soot particles during aging with 15 ppb amine precursor are illustrated in Figure 5.2. For aniline (Figure 5.2a), the mass growth factor, G_{fm} increased gradually to 2.42 ($f_{org} = 59\%$) in the first 118 min and remained steady. The increase in G_{fm} represents the formation and subsequent condensation of low volatility oxidation products on the soot aggregates, while the plateau suggests equilibrium between the gas and particulate phases with no additional condensation. A similar to aniline growth profile was observed when TEA was used as precursor, but G_{fm} was lower and stabilized at about 1.36 ($f_{org} = 26\%$). This implies that the oxidation products of TEA are more volatile and a smaller fraction partitions into the particulate phase. A different behavior was observed with MEA as precursor. The G_{fm} rapidly increased to 1.31 in the first 10 min and decreased in the next 30 min to 1.16. Minor oscillations seen in Figure 5.2a may be the effect of temperature variations in the chamber during photooxidation because of heating by lamps and cooling by AC. The unusual presence of a maximum can be caused by rapid oxidation of MEA to produce relatively high volatility products, which condense on the soot particles. As MEA reacts away and the steady-state concentration of its gas-phase oxidation products decreases, some of those products present in the particle coating may begin to evaporate, resulting in a decrease in particle mass. The upward trend in G_{fm} after 60 min can be attributed to the condensation of higher generation oxidation products either from MEA or from background VOCs that persist even after purging the chamber and may react when all of the MEA is consumed. As shown in Figure 5.3a, G_{fm} was about 1.15 ($f_{org} = 13\%$) during blank experiments performed in the absence of amine precursors. Condensation of oxidation products of those VOCs resulted in negligible changes in size, while changes in density and shape factor were within 10% (Figure 5.3 b-d).

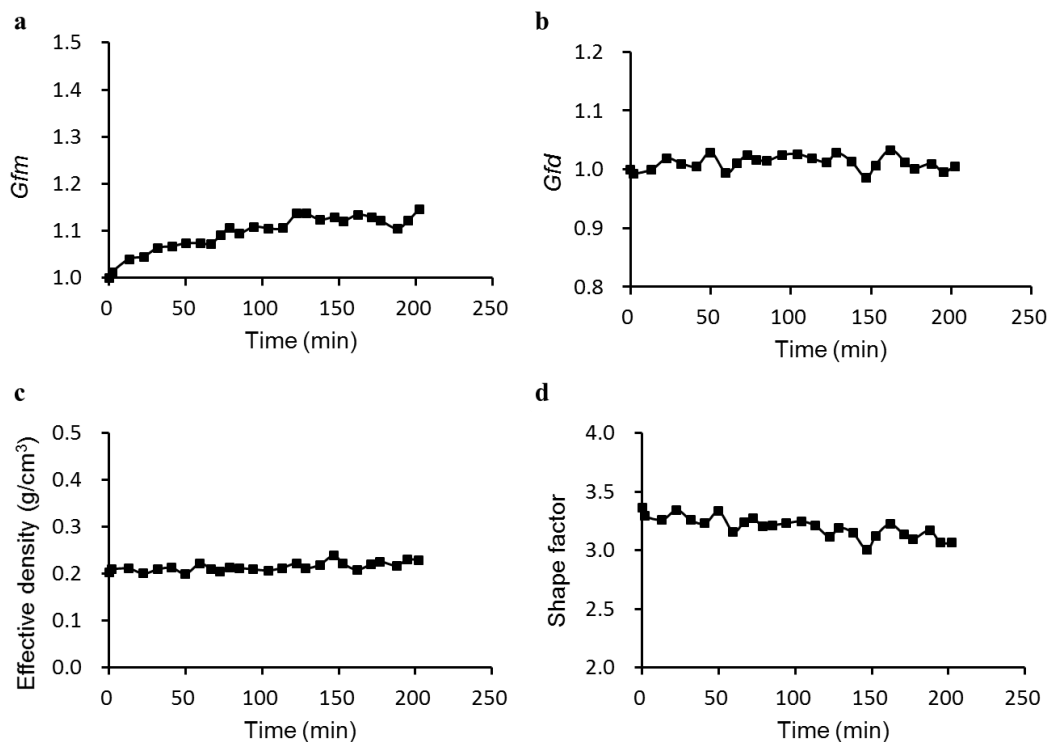


Figure 5.3 Evolution in (a) mass growth factor (G_{fm}), (b) diameter growth factor (G_{fd}), (c) effective density (ρ_{eff}), and (d) shape factor (χ_{shape}) of soot particles upon photochemical aging in the presence of H_2O_2 with 150 nm initial diameter.

Aging of soot from photochemical aging of VOC has been reported in previous studies (Guo, *et al.*, 2016; Khalizov, *et al.*, 2013; Li, *et al.*, 2017; Ma, *et al.*, 2013b; Qiu, *et al.*, 2012; Schnitzler, *et al.*, 2014), and several examples are listed in Table 5.1. For similar particle diameters and aging times, oxidation of aromatic compounds, like toluene and m-xylene, led to a higher G_{fm} compared with isoprene, even at lower initial concentrations. α -Pinene exhibited the highest G_{fm} increase. The difference suggests that α -pinene and aromatic compounds generate a higher yield of condensable vapors compared with isoprene. Similarly, photochemical oxidation of the three amines used in this study displayed different condensate yields, with aniline and MEA producing the largest ($f_{org} = 59\%$) and smallest ($f_{org} \sim 17\%$) amounts, respectively.

Table 5.1 Comparison of the Effects of Organic Coatings from the Photooxidation of Different Precursors on the Mass Growth Factor (G_{fm}) and Size Growth Factor (G_{fd}) of Soot Particles

Precursor	Concentration (ppb)	Reaction time (min)	Soot diameter (nm)	G_{fm}	G_{fd}	References
Isoprene	340	200	150	1.4	0.93	Khalizov, <i>et al.</i> (2013)
Toluene	250	200	150	2.5	1.07	Qiu, <i>et al.</i> (2012)
α -Pinene	37	120	126	11	1.42	Ma, <i>et al.</i> (2013b)
m-Xylene	200	200	100	6.5	1.3	Guo, <i>et al.</i> (2016)

Figure 5.2b shows that the three amine precursors produce vastly different diameter growth factor, G_{fd} profiles during soot aging. For aniline, G_{fd} increased with time reaching 1.13, whereas it remained unchanged for TEA (1.00 ± 0.01). For MEA, G_{fd} decreased rapidly to 0.91 and then remained constant. It is known that changes in particle mobility size during aging is the combined action of a decrease from soot backbone restructuring and an increase from condensed coating (Khalizov, *et al.*, 2013; Zhang, *et al.*, 2008). From Figure 5.2b, it is evident that restructuring occurred in the case of MEA because of the decreased mobility size. For TEA, even though f_{org} increased to 26%, the size remained unchanged during aging. There are two possible reasons for this phenomenon: the increase in size caused by the coating might be offset by restructuring or the coating might fill the void spaces without soot aggregates restructuring, resulting in an apparent constant size. In the case of aniline, restructuring might have partially compensated the size increase.

Heating the soot aerosol to remove the organic coatings revealed a constant core diameter (Figure 5.4) for aniline and TEA that suggests the absence of restructuring during photochemical aging with 15 ppb initial concentration of these amines. No denuding was performed in the case of MEA because the restructuring was already obvious with coated particles. Also, the mass of coating on soot was relatively small during aging ($f_{org} = 17\%$),

and therefore the difference between Gfd of coated and coated-denuded particles would be negligible. By comparing the respective changes in Gfm and Gfd in the presence of different precursors where a small f_{org} in the case of MEA corresponds to a more significant restructuring, one may conclude that the oxidation products of MEA have stronger restructuring abilities compared with organic coatings from TEA and aniline photooxidation.

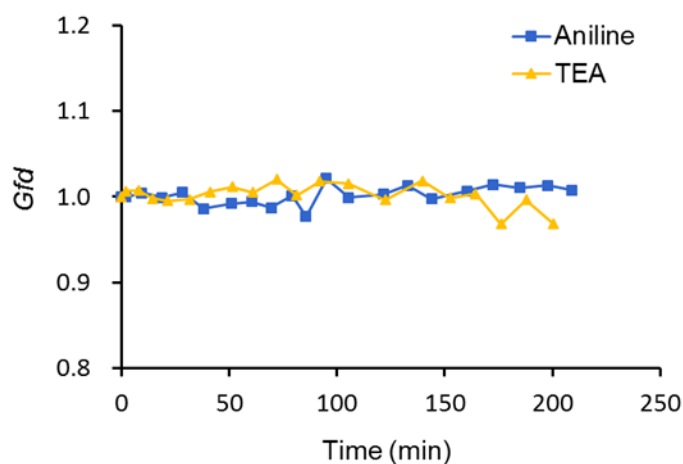


Figure 5.4 Evolution in Gfd of soot particles upon photochemical aging and coating removal process in the presence of 15 ppb amines.

The change in effective density of soot particles during aging is shown in Figure 5.2c. The initial effective densities of soot for the aniline, TEA and MEA runs were 0.17, 0.22 and 0.23 gcm^{-3} , respectively. Since no restructuring occurred in the soot core, the 70% and 17% increase in density observed for coated particles with aniline and TEA was caused solely by the increasing mass of condensate filling the voids. For MEA, the 65% increase in density was mainly caused by the restructuring of the soot core. The filling of voids in fractal soot and restructuring of the soot core both contribute to the reduced drag on particles and is reflected by a decrease in the dynamic shape factor (Figure 5.2d). The trend

in shape factor of coated soot was similar for all three amine precursors with final values of 2.42, 2.77, and 2.33 for aniline, TEA, and MEA, respectively.

5.3.3 Soot Aging with High Initial Amine Concentration

Morphological changes in soot during photochemical aging with 100 ppb amines are illustrated in Figure 5.5. Consistent with the experiments at low amine concentration, the largest condensate mass ($G_{fm} = 5.74$, $f_{org} = 83\%$) was observed when aniline was used as the precursor (Figure 5.5a). The aged soot particles grew continuously during 200 min of photooxidation, indicating that only a small fraction of aniline was consumed. For TEA, the trend in G_{fm} was similar to Figure 5.5a, however, the high amine concentration resulted in a significant increase in coating mass ($G_{fm} = 2.33$, $f_{org} = 55\%$) relative to the 15 ppb experiment. In the case of MEA, increasing the amine concentration to 100 ppb did not lead to an appreciable increase in particle mass growth ($G_{fm} \sim 1.30$, $f_{org} \sim 23\%$) compared to the run at 15 ppb ($f_{org} \sim 17\%$). This may be due to the preferential reaction of OH radical with the excess MEA to generate relatively volatile organic compounds rather than its reaction with MEA oxidation products to produce condensable vapors. Alternatively, the insensitivity to increase in MEA concentration may indicate the occurrence of capillary condensation of subsaturated vapor due to the inverse Kelvin effect (see Chapters 3 and 4). Little to no additional condensation could be because the concave junctions between adjoining monomers in the soot aggregates are already fully filled with 15 ppb MEA and condensation on the convex surface of the monomers is unlikely due to the significant direct Kelvin effect.

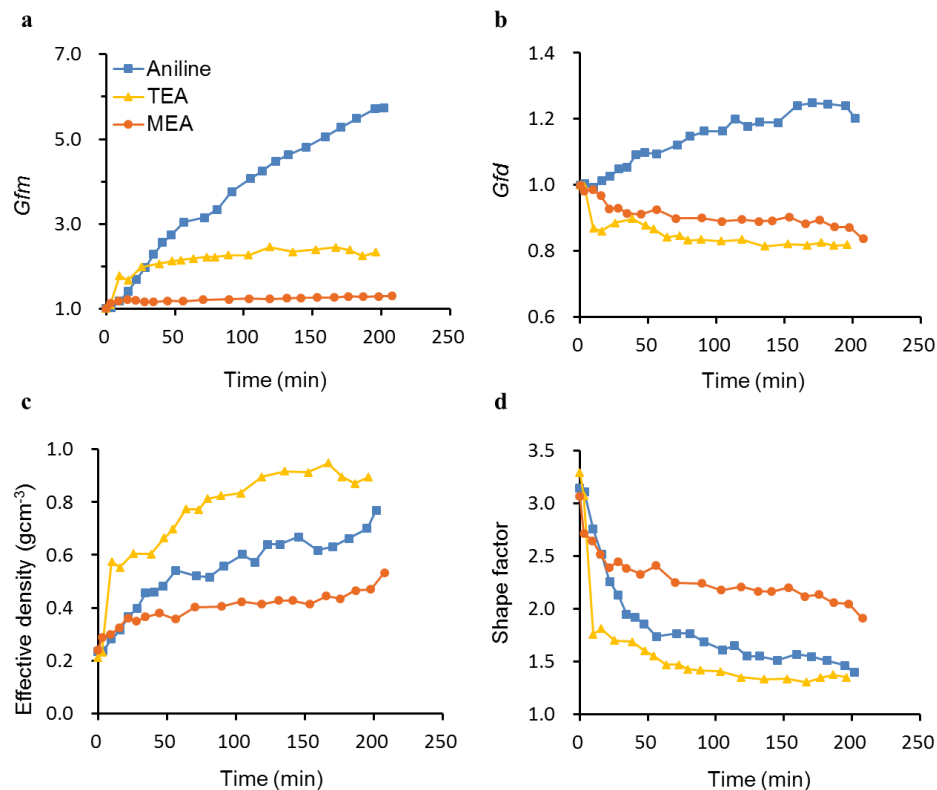


Figure 5.5 Evolution in (a) mass growth factor (G_{fm}), (b) diameter growth factor (G_{fd}), (c) effective density (ρ_{eff}), and (d) shape factor (χ) of soot particles upon photochemical aging in the presence of 100 ppb amines with 150 nm initial diameter.

The major products from photochemical oxidation of MEA by OH radical are formamide (b.p. 210 °C) and formaldehyde (b.p. -20 °C) (Nielsen, *et al.*, 2011). Second and third generation oxidation products include isocyanic acid (b.p. -40 °C), oxazolidine (b.p. 109 °C), oxazolidinone (b.p. 346 °C), and several imines (Barnes, *et al.*, 2010; Borduas, *et al.*, 2013). Most of these oxidation products are too volatile to condense on soot at room temperature. However, capillary condensation of formamide and later generation products might correspond to the rise and fall in G_{fm} when partial pressure of these chemicals increases and then decreases. The major product of TEA photo oxidation is diethylacetamide (b.p. 182-186 °C) (Nielsen, *et al.*, 2012). Further oxidation of diethylacetamide would produce relatively high boiling point acetamide products (Barnes,

et al., 2010). The oxidation products of aniline generally have lower volatilities compared with TEA and MEA (Huang, *et al.*, 2013) and are more likely to condense uniformly and remain on the soot surface. Thus, the wide range in volatility of the oxidation products from the different amine precursors may explain the different *Gfm* trends that occur during aging.

Figure 5.5b illustrates trends in *Gfd* associated with aging in the presence of 100 ppb of amines. For aniline, a more significant increase in *Gfd* was observed compared with the run at low initial concentration. Because of more vapor condensation, *Gfd* reached around 1.23 at the end of aging. However, a decrease in mobility size was observed both for TEA and MEA that indicates the occurrence of restructuring. In the case of MEA, *Gfd* dropped rapidly to 0.91 in the first 35 min and then further decreased to 0.84 at the end of the run. For TEA, there were three regions observed in *Gfd*: a rapid decrease to 0.86 in the first 16 min followed by an increase to 0.90 in the next 20 min, and then a gradual decline to 0.83 after which it remained constant. The decrease and subsequent increase in *Gfd* has been observed in previous studies (Chen, *et al.*, 2016; Ghazi & Olfert, 2013), where the first decrease in size is controlled by the restructuring of soot and the growth in size is controlled by the increase in volume of coating. Because there was no corresponding decrease in *Gfm*, the decline in particle size in the third region may be due to coating evaporation as a result of the DMA sheath flow.

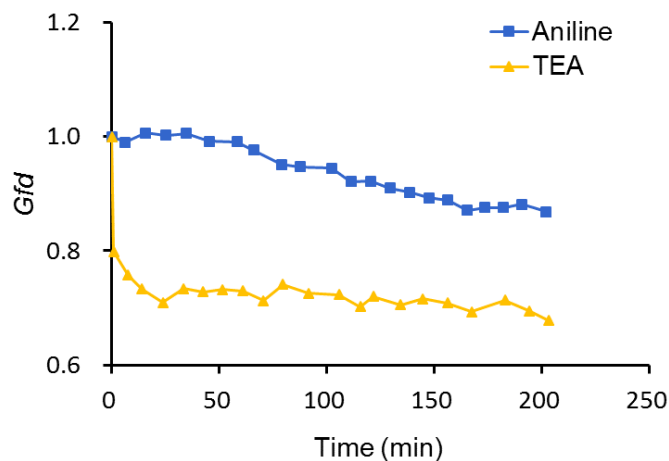


Figure 5.6 Evolution in G_{fd} of soot particles upon photochemical aging and coating removal process in the presence of 100 ppb amines.

The change in core size after coating removal is shown in Figure 5.6. For aniline, G_{fd} of coated-denuded soot remained unchanged in the first 58 min, and gradually decreased to 0.87 at the end of the run. This behavior is similar to a previous study (Schnitzler, *et al.*, 2014), in which a series of aromatic compounds were used as precursor. The similarity may be due to similar chemical structure between aniline and other aromatic compounds, leading to comparable oxidation products. For TEA, G_{fd} of coated-denuded soot decreased sharply to 0.71 during the first 24 min due to restructuring and remained approximately constant. A constant G_{fd} implied that the soot core reached the maximum compaction (Chen, *et al.*, 2018; Schnitzler, *et al.*, 2014). The sharp decrease in G_{fd} of coated-denuded soot for TEA is consistent with the previously described G_{fd} change for coated soot, where the size of soot particles first decreased because of restructuring and then increased because of the continuous condensation of organic coating. Although thermodenuders have been widely used to investigate the restructuring of the soot core by coating removal (Liu, *et al.*, 2017; Schnitzler, *et al.*, 2014; Zhang, *et al.*, 2008), it should be noted that additional restructuring can be introduced by coating melting and evaporation

(Bhandari, *et al.*, 2017; Ma, *et al.*, 2013a). It is possible that the higher generation oxidation products of aniline and TEA that condensed on the soot aggregates do not induce notable restructuring prior to denuding because of their high viscosity or existence in a solid state (Leung, *et al.*, 2017a; Schnitzler, *et al.*, 2017). Given the relatively high volatility of oxidation products and low coating mass ($f_{org} \sim 23\%$) from the MEA precursor, the observed aggregate restructuring could be a combined effect of capillary condensation (due to the inverse Kelvin effect) and condensate evaporation as previously discussed in Chapters 3 and 4.

The change in effective density with higher initial amine concentration is more significant in all cases due to the larger increase in G_{fm} and/or soot restructuring (Figure 5.5c). For aniline, TEA, and MEA, the density of coated soot increased from 0.23, 0.21 and 0.24 gcm^{-3} to 0.77, 0.89 and 0.63 gcm^{-3} , respectively. A larger reduction in shape factor was observed compared to 15 ppb concentration, with final values approaching 1.39, 1.35 and 1.91 for aniline, TEA, and MEA, respectively. Since particles with $\chi_{shape} = 1$ are spherical in shape, the aggregates assumed a nearly spherical morphology after aging.

5.3.4 CCN Activity of Aged Soot

The presence of hydrophilic organic coatings can convert hydrophobic soot into cloud condensation nuclei (CCN) active particles. Experiments to determine CCN activity of the aged soot particles were conducted at three water vapor supersaturation levels: $\zeta = 0.23\%$, 0.42% , and 0.81% . The activation ratio (AR) of the aged soot particles was obtained from the total number concentration measured by the CPC and the CCN number concentration as (N_{CCN}/N_{CN}). As shown in Figure 5.7, fresh soot particles ($t = 0$ min) do not activate into cloud droplets, but become more CCN active as the mass of water-soluble oxidation

products on the particle surface increases. At the highest precursor concentration and water supersaturation (Figure 5.7f), all coated particles were activated. However, at lower concentration and supersaturation levels (Figures 5.7a-e), the trend in CCN activity differed with the different amine precursors.

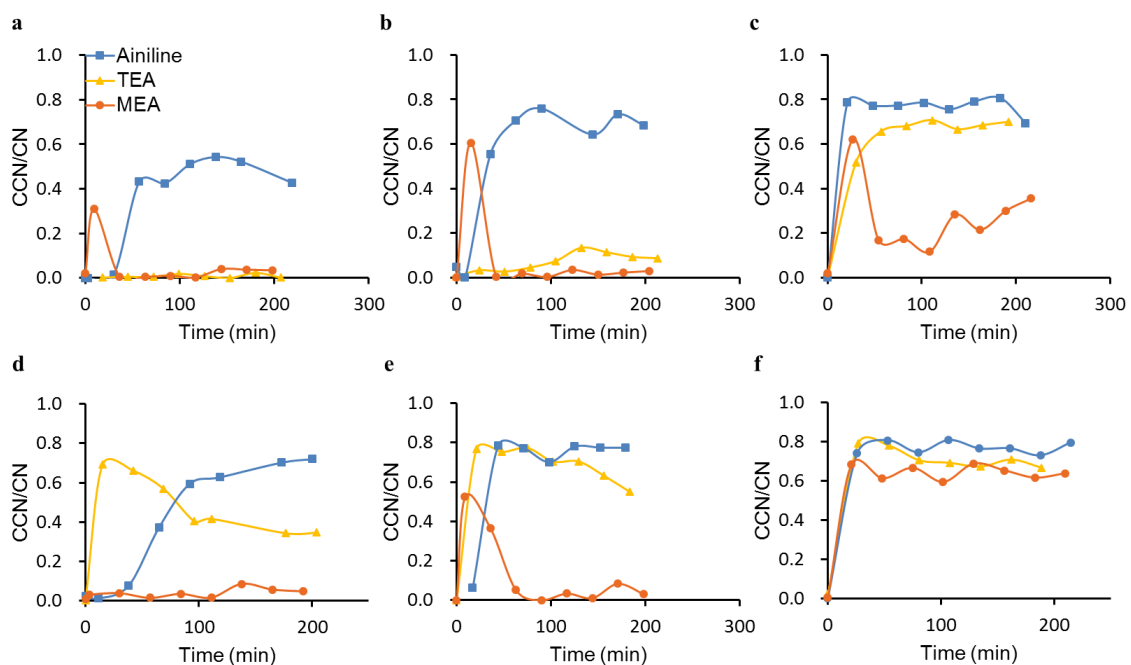


Figure 5.7 CCN/CN (activation ratio) evolution during the aging process, (a-c) are for 15 ppb initial amine concentration, (d-f) are for 100 ppb initial amine concentration; (a, d) represent $\zeta = 0.23\%$, (b, e) represent $\zeta = 0.42\%$, (c, f) represent $\zeta = 0.81\%$.

In the case of aniline, an abundance of non-volatile oxidation products resulted in thickly coated aggregates ($f_{org} = 59 - 83\%$) whose activation ratio (AR) increased with time before leveling off. For MEA, the activated fraction rose sharply with aging time, then dropped off rapidly. This behavior tracks the change in volatile fraction of the coating material discussed in Section 5.3.2. The rise and fall in AR is not prominent in Figure 5.7d because of the larger interval between adjacent points of CCN measurements, missing the moment when particles had larger coating mass. The oscillations in CCN activity seen at

15 ppb MEA concentration and $\zeta = 0.81\%$ (Figure 5.7c) may be attributed to temperature variations, which affect the equilibrium partitioning between the vapor and condensed phases. Despite having a larger condensate mass fraction than MEA, little to no particles activated at $\zeta = 0.23\%$ and $\zeta = 0.42\%$ when 15 ppb initial concentration of TEA was used (Figures 5.7a-b). A possible explanation for this behavior may be that the oxidation products of MEA are more water soluble. At a higher TEA concentration (Figures 5.7d-e), the activated fraction of soot particles became significant, but decreased with aging time. This may reflect the concentration of the gaseous products generated during photooxidation. During the initial oxidation stage when TEA is abundant, these products are also present in a higher concentration and their presence may result in co-condensation with water inside the CCN instrument. Co-condensation of volatile organic oxidation products either adds to the soluble mass of the droplets or reduces the droplet surface tension (Ovadnevaite, *et al.*, 2017), facilitating the uptake of additional water leading to an increase in the number of cloud droplets that can activate (Topping, *et al.*, 2013). As the amine precursor is depleted and fewer gas-phase organic oxidation products are generated, co-condensation decreases resulting in a decline in CCN activity. At higher supersaturation levels (Figure 5.7c, f), the oxidation of background VOCs may contribute to a slight increase in CCN activity (see Figure 5.8).

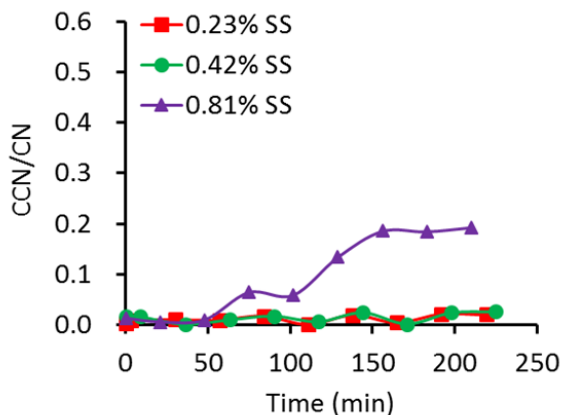


Figure 5.8 CCN/CN (activation ratio) evolution of 150 nm soot particles at three water vapor supersaturations (SS) during photochemical aging in the presence of H₂O₂.

From CCN measurements, critical supersaturations (S_c) of 0.23, 0.81, and 0.23 were estimated for aniline, MEA and TEA respectively, which were used to calculate hygroscopicity parameters for the organic coatings (κ_{coating}) based on the equations in (Petters & Kreidenweis, 2007). These values are 0.14, 0.08 and 0.13 for aniline, MEA and TEA respectively. The κ_{coating} estimate for MEA may be slightly inaccurate due to the high volatility of its condensation products and small condensate fraction. Since the κ_{coating} values for the three amine precursors are comparable, we can surmise that a more significant enhancement in CCN activity for aniline is due to a quicker depression of the Kelvin effect than the solute effect in the Köhler equation (see Equation 1.3), as a result of the generation of significant amounts of condensable oxidation products. The κ_{coating} values obtained in this study are also comparable to values obtained for isoprene SOA (Engelhart, *et al.*, 2011; Khalizov, *et al.*, 2013).

In previous studies with various precursors, the CCN activity of soot particles during photochemical aging usually increases before leveling off (Guo, *et al.*, 2016; Khalizov, *et al.*, 2013; Ma, *et al.*, 2013b). On the contrary, in our study a more complex

behavior was observed with some amines as precursors. The trend in CCN activity is largely consistent with the pattern observed in the mass growth of aged soot particles and reflects the range in volatility of the generated oxidation products.

5.4 Conclusions

In this study, we have shown that the morphology and cloud activation behavior of soot aerosol with organic coatings generated from OH-initiated photochemical oxidation of amines varies between different amine precursors, mostly due to differences in volatility of oxidation products. The photooxidation of aniline yielded low-volatility products that condensed uniformly and irreversibly on the soot aggregates. The amount of condensate increased with time and initial amine concentration, resulting in an f_{org} as high as 83%. No aggregate restructuring was observed for aniline, except at a high initial concentration and after thermodenuding, indicating that the condensate was highly viscous or existed in a solid state. The aged soot particles were CCN active at all supersaturations, reflecting the presence of thick hydrophilic coatings.

The oxidation products derived from MEA and TEA precursors were of intermediate volatility as evidenced by reversible condensation on the particles. For a high initial TEA concentration, oxidation products induced aggregate restructuring at $f_{org} = 55\%$ whereas preferential capillary condensation of relatively volatile oxidation products of MEA was sufficient to cause a partial aggregate collapse even at low initial concentrations and $f_{org} = 17\%$. Given the volatile nature of the oxidation products from MEA and TEA, CCN activation is aided by the co-condensation of gas-phase oxidation products with water inside the CCN counter.

In general, aromatic amines (such aniline) and tertiary amines (such TEA) can form significant amounts of condensable oxidation products whereas primary amines like MEA cannot.

CHAPTER 6

AN ALGORITHM FOR SOOT AGGREGATE RESTRUCTURING

Restructuring has been shown to be a largely irreversible process (Bambha, *et al.*, 2013) brought about by the presence of a layer of adsorbate which facilitates the rolling and sliding of monomer spheres in a soot aggregate. In the absence of accurate structural information, most atmospheric models treat soot particles as solid spheres (Croft, *et al.*, 2005; Koch, 2001), overlooking aggregate restructuring. Such simplified treatment cannot account for the effects associated with structural changes during atmospheric aging, severely limiting the accuracy of evaluations made by atmospheric models regarding the fate and impacts of soot. The following chapter addresses this issue with the development of an algorithm to simulate the condensation-induced restructuring of soot aggregates.

6.1 Introduction

The fractal-like structure of soot aggregates undergoes significant restructuring due to the forces exerted by liquid coatings acquired through the condensation of atmospheric trace gas species. As previously discussed in Chapter 3, the extent of restructuring is dependent on the coating vapor supersaturation which governs the distribution of the condensate and thus, restructuring forces on the aggregate surface. These restructuring forces, which act in addition to the existing attractive forces between contacting monomers in the aggregate, are a function of the properties of the coating such as its wettability, viscosity and surface tension.

The wettability of a condensable material is dependent on its liquid-solid interactions (surface energy). If the coating material wets the surface, the molecules will creep along the surface and replace the contact between the solid surfaces by a contact of liquid to liquid (Kütz & Schmidt-Ott, 1992) facilitating the rolling and sliding of the monomers. This liquid migration may take a significant amount of time depending on the viscosity of the material (Gao & Bhushan, 1995). Additional restructuring occurs due to the surface tension of the liquid when the menisci overlap to form bridges across monomer spheres.

For accurate predictions of morphologically dependent soot properties, understanding the dynamics of aggregate restructuring is important. However, in-situ examination of evolving aggregate structure is difficult to accomplish experimentally. The high vacuum conditions in a scanning or transmission electron microscope (SEM, TEM) are such that the coating material is lost by evaporation (Bambha, *et al.*, 2013; Chakrabarty, *et al.*, 2006b) and only initial or final morphologies can be visualized. Exposure of the aggregate to the electron beam also leads to thermal evaporation and surface charging, reducing the image resolution and contrast. One way to preserve the coating and minimize damage to the soot aggregate is by using environmental electron microscopy methods (i.e., ESEM, ETEM) where the aggregate sample is held at several millibar or even atmospheric pressure. With the ESEM/ETEM, in-situ analysis of the evolving aggregate structure can be achieved. However, in a previous study, we showed that interactions between the aggregate and the collection substrate can hinder aggregate restructuring and bias measurements (Chen, *et al.*, 2017). An alternative solution would be to model the aggregate

restructuring process and compare the final morphologies obtained against those derived from experimental measurements for accuracy.

An attempt to model aggregate restructuring was done by Schnitzler, *et al.* (2017) and is, to the best of our knowledge, the only one. This qualitative model, hereafter referred to as the Schnitzler model, accounts for the adhesion forces between the soot monomers, viscous dissipation forces, capillary forces due to coating trapped in junctions between monomers, and forces exerted by liquid bridges between non-contacting monomers.

6.1.1 The Schnitzler Model

In the Schnitzler model, soot restructuring is simulated numerically by solving Newton's equations of motion of each monomer in an aggregate:

$$m \frac{d^2 \mathbf{r}}{dt^2} = \sum_i \mathbf{F}_i \quad (6.1)$$

where \mathbf{r} is the position of the center of mass of the monomer, and $\sum_i \mathbf{F}_i$ is the sum of the all forces acting on each monomer. These forces are briefly described below.

Adhesive force, F_{adh} : This attractive force arises from inter-particle interactions between contacting monomers in the bare soot aggregate. Such short-range interactions are usually described by the JKR model (Johnson, *et al.*, 1971) where the effects of adhesion is considered only inside the area of contact. In the Schnitzler model, the adhesive force between monomers is replaced with a simple harmonic oscillator and is described by:

$$F_{adh} = k_{adh} \mathbf{x} \quad (6.2)$$

where k_{adh} is the adhesion force constant and \mathbf{x} is the distance between surfaces of interacting monomers. This simplification of the JKR model has been justified by previous works on solid-solid interactions in particles (Grzybowski, 2005; Reeks, *et al.*, 1988; Ziskind, *et al.*, 2000), but is only valid for small values of \mathbf{x} .

Viscous dissipation force, F_{visc} : Monomers in the bare soot aggregate are also assumed to be acted upon by viscous drag forces, which oppose particle motion. This damping force is attributed to the surrounding gas medium and is represented by Stoke's law:

$$F_{visc} = \beta \mathbf{v} = 6\pi\mu R_s \mathbf{v} \quad (6.3)$$

where β is the damping coefficient, v is the velocity and μ is the viscosity of the medium.

Liquid forces, F_{liq} : The force arising from the presence of the liquid coating presents itself in two ways: as a capillary force for contacting monomers (Figure 6.1a), and as a bridging force for monomers that are separated by large interparticle distances (Figure 6.1b). The liquid bridging force is well predicted by an expression derived by Maugis (1987) of the form:

$$F_{lb} = 4\pi R_s \gamma G_f \cos \vartheta \quad (6.4)$$

where ϑ is the contact angle and G_f is a coefficient that depends on the volume of the liquid bridge and the distance between monomers. In the Schnitzler model, the capillary and bridging forces are summed up and approximated by another harmonic oscillator model:

$$F_{liq} = \lambda k_{liq} \mathbf{x} \quad (6.5)$$

where the constant k_{liq} is proportional to the coating surface tension. The coefficient λ accounts for the dependence of F_{liq} on the mean volume of liquid, V_L deposited on each monomer in the aggregate. Since the model is strictly qualitative, the exact form of λ was not deemed to be critical. The coefficient is zero when no coating is present, goes through a maximum as V_L increases, and approaches zero as becomes V_L exceedingly large.

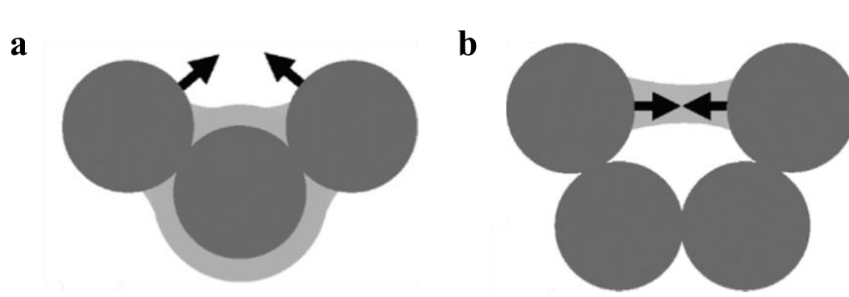


Figure 6.1 Illustration of the (a) capillary, and (b) bridging forces used in the Schnitzler model (Schnitzler, *et al.*, 2017).

The forces described in Equations (6.2), (6.3) and (6.5) are substituted into Equation (6.1) which is then integrated at small time steps to determine the new positions and velocities of each monomer at the end of each time step. In the Schnitzler model, integration of Equation (6.1) is done via a modified Verlet algorithm (Gac, *et al.*, 2008) and the resulting expression for the displacement of the i th monomer during each time step Δt is:

$$r_i(t + \Delta t) = \frac{1}{1 + \frac{\beta}{2m_i} \Delta t} \left[\begin{aligned} & 2r_i(t) - \left(1 - \frac{\beta_i}{2m_i} \Delta t\right) r_i(t - \Delta t) \\ & + \frac{1}{2m_i} \left(\sum_j F_{adh,i,j}(t) + \sum_j F_{liq,i,j}(t) \right) (\Delta t)^2 \end{aligned} \right] \quad (6.6)$$

where $\sum_j F_{adh,i,j}$ and $\sum_j F_{liq,i,j}$ are the adhesive and liquid forces, respectively, between the i th and j th monomers.

6.1.2 Study Objectives

The approximation of the adhesive and liquid forces as a simple harmonic oscillator in the Schnitzler model is valid only at short distances between monomers in the coated aggregate. For liquid bridges that occur over longer separation distances, the approximation breaks down. Also unaccounted for in the model is the enhanced frictional force between the monomers due to the higher viscosity of the liquid in the contact region compared to the surrounding gas. Furthermore, the model is completely qualitative with no indication of the magnitude of the forces acting on the monomers in the aggregate. Despite its shortcomings, the Schnitzler model provides a starting point for simulating aggregate restructuring. In this study, the Schnitzler model was modified for the purely utilitarian purpose of generating restructured aggregates for morphological comparison with the aggregate generation algorithms used in our optical calculations (see Chapter 8). The resulting restructuring algorithm was tested on an ensemble of initially fractal aggregates and the morphological evolution of the aggregate backbone was tracked.

6.2 Modeling Aggregate Restructuring with the Morse Potential

To make the computation of forces in our restructuring algorithm more rigorous, the harmonic approximation used in the Schnitzler model was replaced by the Morse potential (Morse, 1929) which is described by:

$$E_{Morse} = D_e(1 - e^{-a(x-x_0)})^2 \quad (6.7)$$

where D_e is the dissociation energy, $a = \sqrt{k_e/2D_e}$, k_e is the force constant at the minimum of the well, and x and x_e are the actual and equilibrium distances between the monomers.

The first derivative of Equation (6.7) gives the force acting on the monomers:

$$F_{Morse} = 2aD_e(e^{-a(x-x_0)} - e^{-2a(x-x_0)}) \quad (6.8)$$

As illustrated in Figure 6.2, the Morse force is strongest when the monomers overlap but decays to zero at infinite separation distance. The harmonic potential on the other hand is always proportional to the monomer displacement. The combination of a short-range repulsive term and a long-range attractive term makes the Morse approximation a better model than the harmonic potential for describing the forces on the monomers.

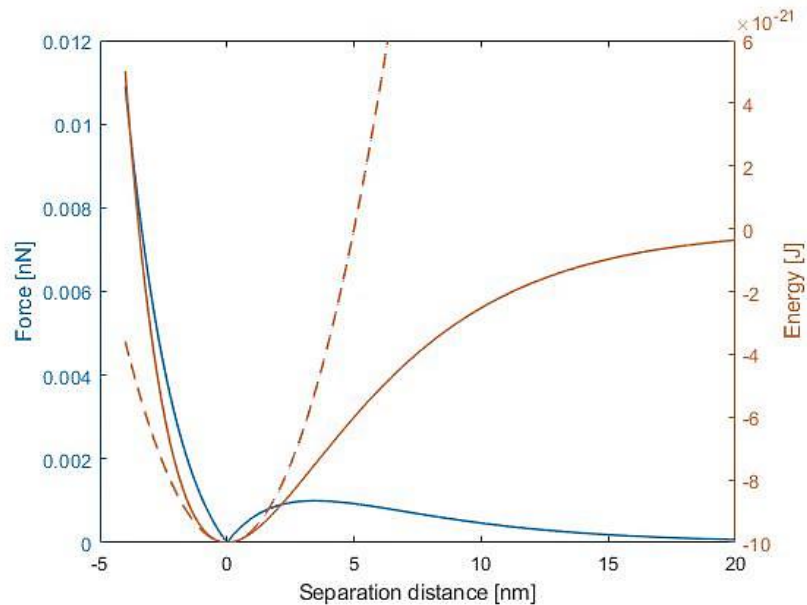


Figure 6.2 The Morse potential (red line), force (blue line) and harmonic potential (red dashes).

In the restructuring algorithm, monomer-monomer adhesion was represented by the Morse force which was truncated at separation distances exceeding 5% of the monomer diameter:

$$F_{adh} = F_{Morse} \quad x < 0.05d_p \quad (6.9a)$$

$$F_{adh} = 0 \quad x > 0.05d_p \quad (6.9b)$$

As a first approximation, the liquid capillary force was described as:

$$F_{cap} = cF_{adh} \quad (6.10)$$

where c is a coefficient that determines the magnitude of the capillary force relative to the adhesion force. The coating was treated implicitly as an “effective thickness” centered around each monomer in the soot aggregate. Thus, the capillary force only acted at short-range separations between coated monomers characterized by a $1/e$ decrease in the Morse potential. Liquid bridging forces were not modeled as they were considered outside the scope of this study. As was done in the Schnitzler model, Equation (6.3) was used to calculate the viscous dissipation forces. Though not a fully physical representation, the restructuring algorithm still serves as an improvement over the Schnitzler model for simulating aggregate restructuring. Explicit calculations of all the forces in a coated soot aggregate are beyond the scope of this study and will be done in a separate project via the discrete element method (DEM) (Cundall & Strack, 1979).

6.3 Results and Discussion

The Verlet algorithm was once again adopted to predict the positions and velocities of the monomers in the aggregate at each time step. The entire simulation was implemented in

MATLAB. Parameters used to run the restructuring algorithm are presented in Table 6.1 below.

Table 6.1 Simulation Parameters for Restructuring Algorithm

Parameter	Symbol	Set Value
Timestep	Δt	10^{-8} s
Dissociation Energy	D_e	10^{-20} J
Force Constant	k_e	8×10^{-4} N.m ⁻¹
Viscosity	μ	1.81×10^{-4} Pa.s
Capillary force coefficient	c	0.5
Root mean square displacement	$RMSD$	10^{-20} m
Root mean square force	$RMSF$	10^{-20} N
Maximum displacement	$Max d$	10^{-20} m
Maximum force	$Max F$	10^{-20} N
Maximum iteration steps		10^7

The choice of the Morse parameters, D_e and k_e , were based on order of magnitude estimates of the viscous dissipation force ($\sim 10^{-14}$ N) which provided the only source of resistance to the sliding and rolling motions of the monomers in the aggregate. The parameter c was chosen such that the capillary force was $\sim 50\%$ of the adhesive force. Convergence criteria for aggregate restructuring was determined by calculating the root mean square (rms) displacement, rms force, maximum displacement, and maximum force of each monomer (Figure 6.3). The threshold values chosen for each of these parameters (Table 6.1) correspond to the point of zero fluctuations in the calculated fractal dimension D_f , and energy of the aggregate relative to its initial state (Figure 6.4). During each restructuring run, monomer coordinates were extracted and saved at predefined values of D_f and prefactor k_o .

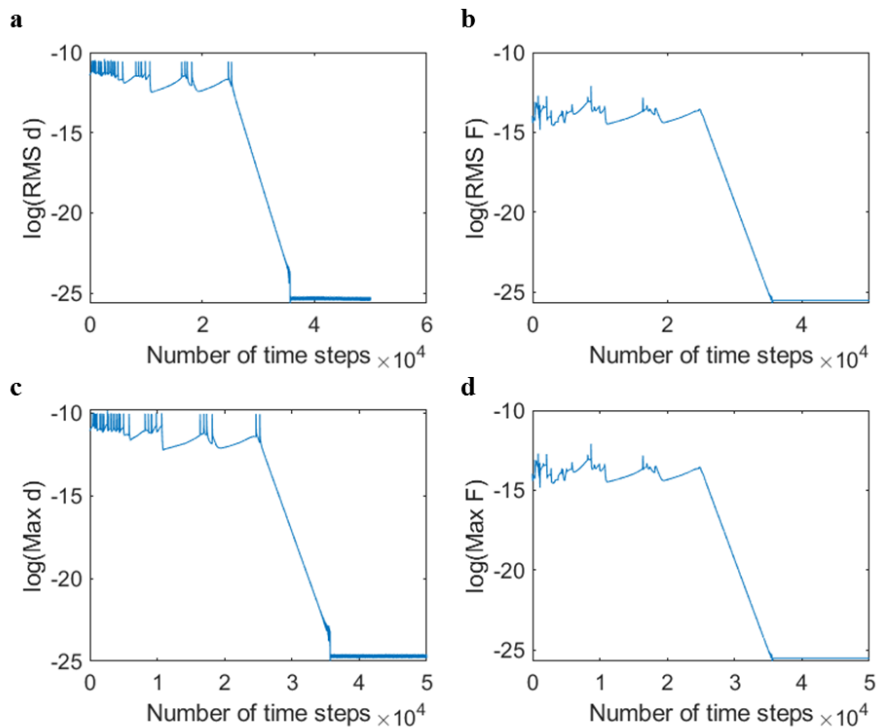


Figure 6.3 Sample illustration of convergence criteria for aggregate restructuring: (a) root mean square displacement (RMSD), (b) root mean square force (RMSF), (c) maximum displacement, and (d) maximum force.

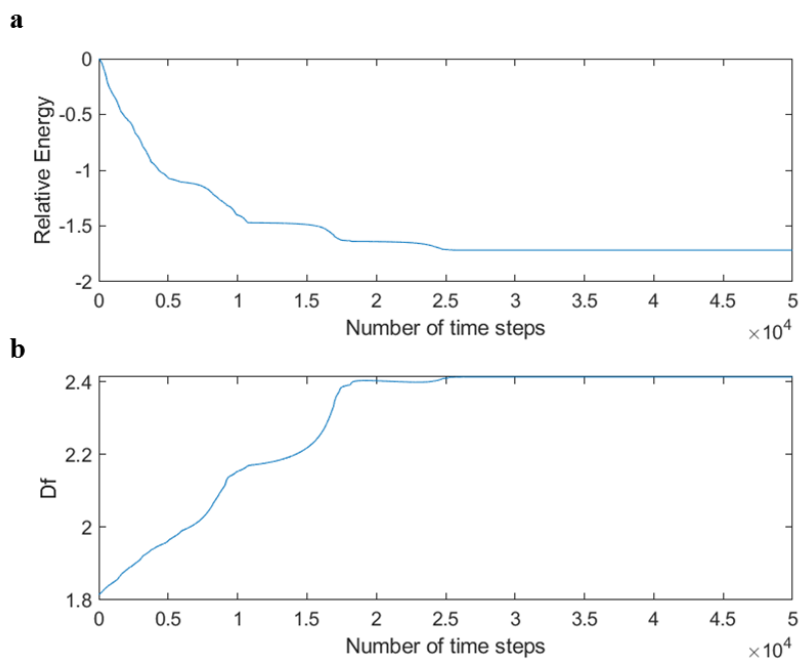


Figure 6.4 Evolution in the Morse energy (a) and fractal dimension (b) of an aggregate of 20 monomers during a restructuring run.

The evolution in structure of representative soot aggregate models comprising 20 and 120 monomers of 28 nm diameter is shown in Figure 6.5. The monomers in the soot aggregate are colored for better visualization. The smaller aggregate (Figure 6.5a) experienced a greater structural collapse and reached a final D_f of 2.69. As indicated by the partial collapse ($D_f = 2.02$) of the larger aggregate (Figure 6.5b), short-range capillary forces were not sufficient to completely restructure the aggregate. This structural behavior has been observed in our experimental studies for thinly coated soot shown via SEM images in Figure 6.6. Thus, the choice of the Morse potential for describing the forces in the aggregate gives a more realistic prediction of structural evolution.

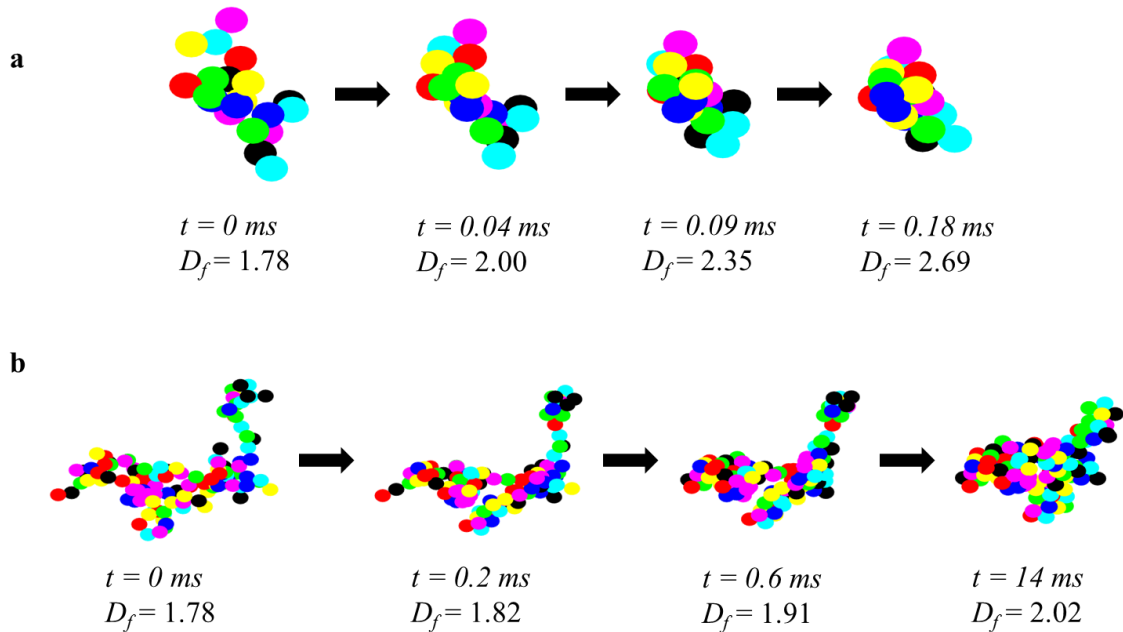


Figure 6.5 Evolution of particle morphology (D_f) with time of an initially fractal aggregate comprising (a) 20 monomers, and (b) 120 monomers. The monomers in the aggregate are colored for better visualization.

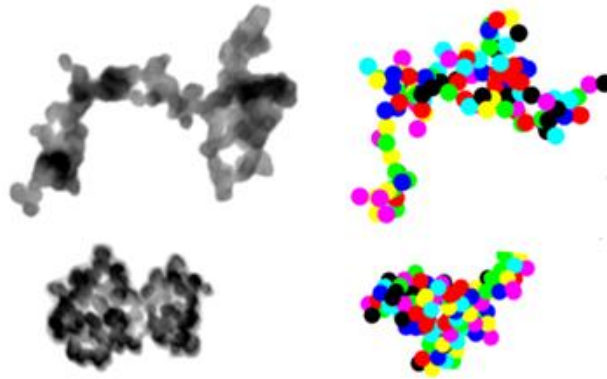


Figure 6.6 Experimental (left) and modeled (right) restructuring of soot aggregates. Particle structure before aging is shown at the top and the final partially compacted structure after aging is given at the bottom.

The algorithm was also applied to an ensemble of fractal aggregates with the same initial D_f and k_o . Since the number of timesteps required to converge to a solution increased significantly with size, the number of monomers in each aggregate was restricted to 20.

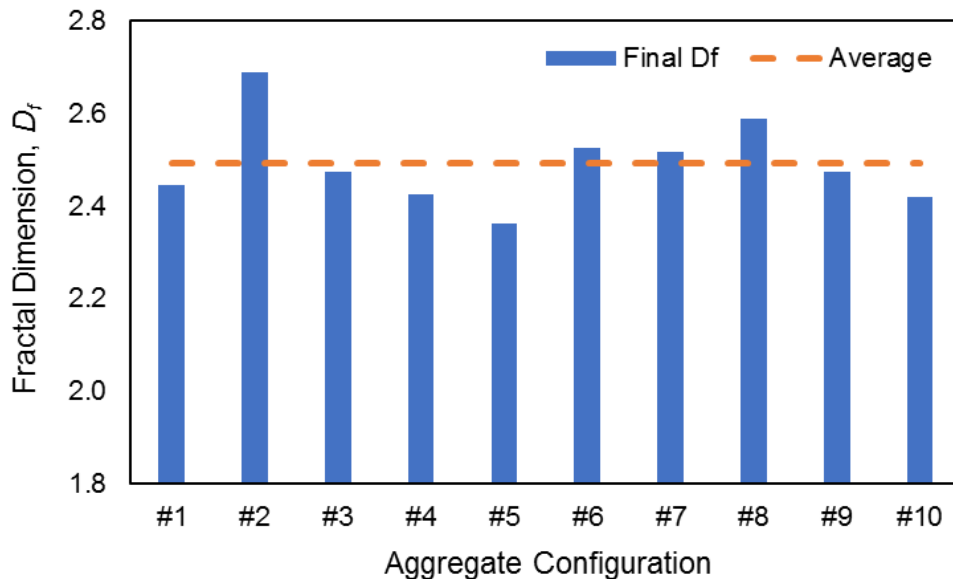


Figure 6.7 Levels of structural collapse for an ensemble of 10 different aggregates. Each aggregate configuration is comprised of $N_s = 20$ monomers with initial fractal parameters of 1.78 and 1.3 for D_f and k_o , respectively. Monomer radius, $R_s = 14$ nm.

As shown in Figure 6.7, different levels of structural collapse were observed in the aggregate ensemble. The average fractal dimension was found to be 2.49 and 60% of the aggregates were recorded with below average D_f . The different levels of aggregate compactness point to the variability of initial aggregate geometries for the same set of fractal parameters (Figure 6.8). For the purpose of our study, it is important to know whether these aggregate realizations are optically equivalent (i.e., particles belonging to the same fractal class $|N_s, R_s, D_f, k_o|$ have nearly identical optical properties) or not to prevent any bias in the predictions of light absorption and scattering by soot. The effects of particle morphology on soot optical properties are explored in Chapter 8.

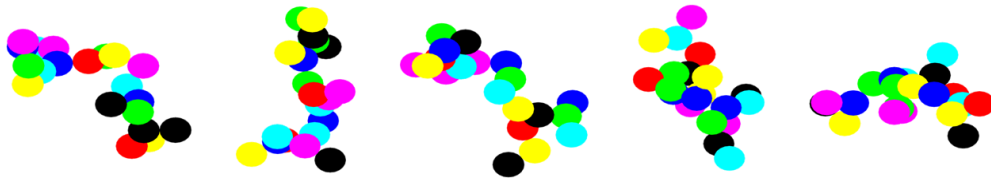


Figure 6.8 Different realizations of aggregates with the same initial fractal parameters ($N_s = 20$, $D_f = 1.78$, $k_o = 1.3$, $R_s = 14$ nm).

6.4 Conclusions

A restructuring algorithm for the prediction of the structural evolution of coated soot aggregates was developed based on the work of Schnitzler, *et al.* (2017). The description of the monomer-monomer adhesion and liquid capillary forces in the algorithm as Morse potentials resulted in more realistic predictions of aggregate restructuring for initially fractal soot. This was corroborated by SEM images which showed partial aggregate collapse for thinly coated soot where only capillary forces were dominant. Additionally, the algorithm predicted varying levels of structural collapse for an ensemble of individual

aggregates with the same initial fractal parameters. This finding could potentially impact estimates of the optical properties of soot with evolving morphology.

CHAPTER 7

EXPERIMENTAL MEASUREMENTS OF LIGHT ABSORPTION AND SCATTERING BY SOOT

It is well established that soot aerosols absorb solar radiation and have a strong warming effect on climate. However, the amount of absorption (and scattering) of light by soot has been difficult to quantify, due, in part, to the challenges in measuring soot optical properties, which depend on the size, shape, chemical composition, and changes in morphology of the soot aggregate. In this chapter, methods for obtaining accurate optical properties of soot with well-defined morphologies are discussed. Additionally, the size (and mass) dependency of the mass absorption cross-section (MAC) is examined.

7.1 Introduction

The absorption and scattering of light by aerosol particles contributes the largest uncertainties in quantifying the radiative balance of the Earth (Myhre, *et al.*, 2013). Thus, there is a growing need to understand and measure atmospheric aerosol optical properties in order to better constrain their direct and semi-direct climatic effects. Of particular importance is soot which is considered to be the greatest anthropogenic aerosol contributor to global warming (Bond, *et al.*, 2013). The radiative impacts of soot are very sensitive to its interaction with other pollutants present in the atmosphere. Furthermore, structural transformations that may arise from mixing further influences the optical properties of soot. If the relationship between morphology and optical properties is known, then the latter can be evaluated for soot particles from a specific source or after undergoing atmospheric

processing. To establish the relationship, the optical properties can be either calculated or measured for soot with well-characterized morphology.

The main parameters of interest from soot optical studies which serve as inputs for atmospheric models are the mass absorption cross-section (MAC) and the single scattering albedo (SSA). Both MAC and SSA (see Equations 2.10 and 2.11 in Chapter 2) are derived from measurements of light absorption, scattering, or extinction. However, the accuracy of these measurements have always posed a significant problem for the aerosol community (Bond & Bergstrom, 2006). This is because optical measurements for soot are typically conducted on size selected particles obtained via differential mobility analysis (DMA), the primary method for aerosol characterization in the 1-1000 nm particle size regime. A single DMA system, in addition to selected particles, transmits larger multiply charged particles. These larger particles with double or triple charges (Figure 7.1) scatter and absorb light more efficiently than singly charged particles of the same electrical mobility. Since light absorption and scattering vary nonlinearly with the particle size, even a small fraction of these larger particles in the soot aerosol can lead to significant overestimation of the measured optical parameters. The elimination of this bias is crucial to obtaining accurate measurements of light absorption and scattering. Acquiring a truly monodisperse soot aerosol flow for optical measurements is, however, quite challenging.

In this study, two procedures for reducing measurement uncertainty in the optical properties of soot were investigated: experimental re-charging and mathematical data re-processing. Both methods were adopted for the accurate determination of the MAC and SSA of uncoated soot aggregates. Also, the size dependency of the optical parameters was evaluated.

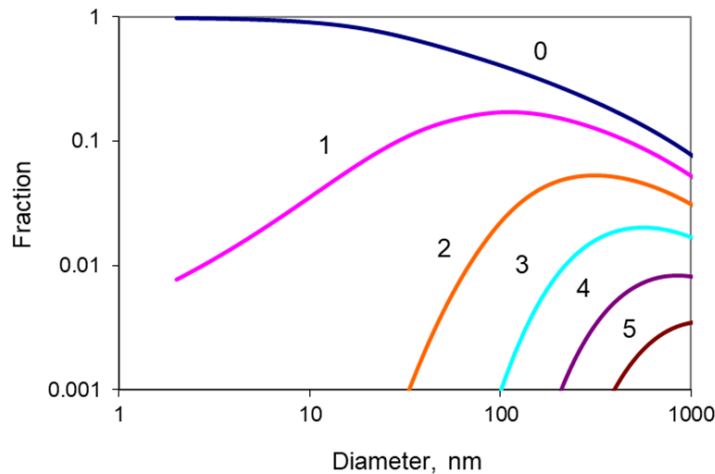


Figure 7.1 Size dependence of the aerosol charging probability. The values above curves indicate the number of particle charges. Adapted from Wiedensohler (1988).

7.2 Eliminating the Effects of Multiple Charging

Optical measurements of uncoated soot aggregates were conducted in the manner previously described in Chapter 2 using a cavity attenuated phase shift single scattering albedo (CAPS PM_{SSA}) monitor. In summary, generated particles were charged in a bipolar charger, to attain a well-known charge distribution (Figure 7.1) and scanned or size classified by DMA1 to either characterize the aerosol size distribution or select particles of a specific size (Figure 7.2a). As mentioned in the previous section, size-classified particles still contain a fraction of particles with larger sizes (Figure 7.2b). To account for those, in the first method, multiply charged particles that bias the measurements were removed, and in the second method, their contribution was accounted for mathematically from measured mass and size distributions. A more detailed description of each method is provided below.

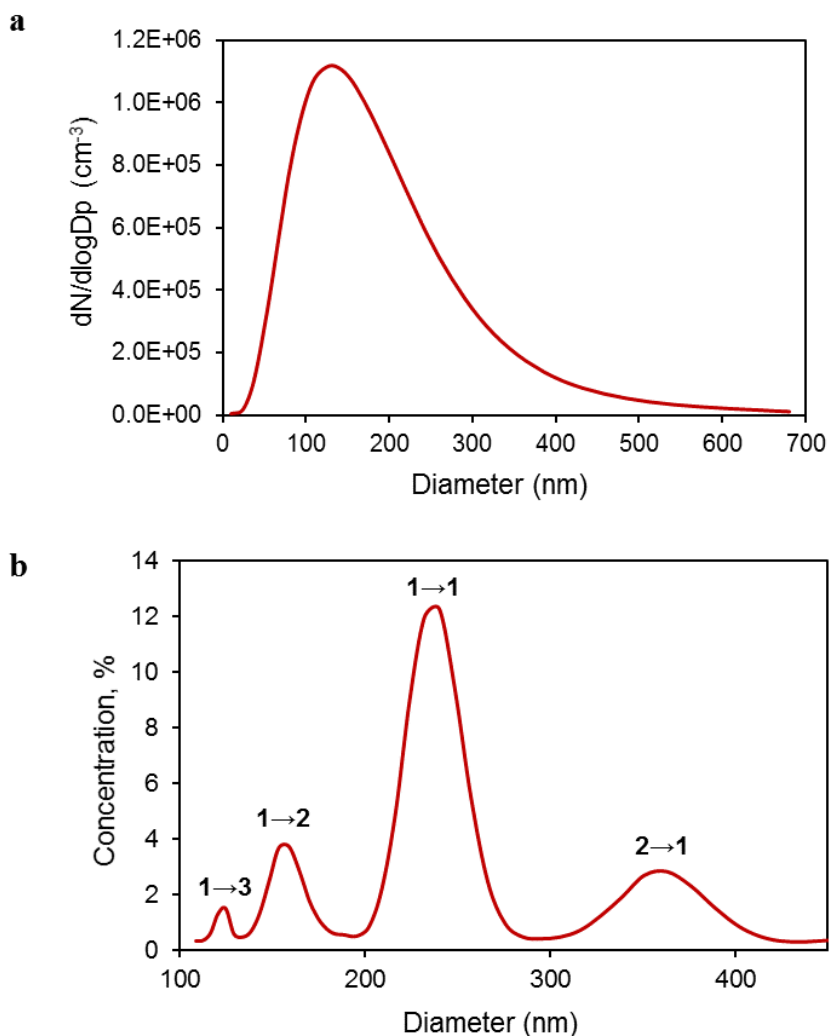


Figure 7.2 (a) Aerosol size distribution, (b) Multi-modal distribution of a recharged soot aerosol showing the existence of multiply charged particles. Recharging processes are indicated above the corresponding size modes.

7.2.1 Experimental Re-Classification

Size-selected soot particles exiting DMA1 were directed through a second bipolar charger and scanned by DMA2 so that multiply charged particles could be identified (see Chapter 2, Figure 2.3). The particle size mode with the least contribution of multiple charges was then sent to the CAPS PM_{SSA} monitor to measure the optical coefficients, and the condensation particle counter (CPC) to measure the number concentration of that particle

mode. For instance, four distinct modes were distinguished during recharging for an initially selected size of 240 nm (Figure 7.2b). The most intense size mode (1→1) occurred for particles which remained singly charged after recharging. However, multiple charge contamination was still high for this mode. The mode at 2→1, for particles with double charges that became singly charged, contained the least fraction of multiply charged particles (Khalizov, *et al.*, 2009a). Thus, this size mode was used for optical measurements to obtain the absorption coefficient, σ_{abs} (Mm^{-1}) from CAPS PM_{SSA} . Combining σ_{abs} and particle concentration, N (cm^{-3}), the absorption cross-section, C_{abs} (m^2) was obtained (Equation 2.9). MAC was determined from C_{abs} and particle mass m (g), measured via the aerosol particle mass analyzer (APM). Eliminating multiply charged particles significantly reduced the number concentration of particles available for optical measurements, as most particles became neutrally charged (Figure 7.1) and could not be size-classified by DMA2. This limitation of recharging became more severe with increasing particle diameter because of the decreasing particle concentration (Figure 7.2a). Thus, this method was only used to determine MAC and SSA for particles of smaller sizes, approximately up to 250 nm, initial concentration of which was high.

7.2.2 Mathematical Adjustment

Due to multiple charging, the measured absorption cross-section C_{abs} of a given particle size is considered to be made up of the absorptions of several different sizes. If the contributions of these particle sizes are known, then C_{abs} can be deconvoluted. This was done via Equation (7.1) using the measured size distribution and mass of the recharged particles:

$$C_{abs} = \sum_i MAC \times f_i \times m_i \quad (7.1)$$

where f_i is fractional contribution of each particle mode (obtained by integrating the recharged size distribution curve, Figure 7.2b), and m_i is the mass of the mode. The masses of certain modes were determined from APM scans, and the rest were calculated using the mass-mobility relationship:

$$m = k_s D_m^{D_{fm}} \quad (7.2)$$

where k_s is a scaling coefficient, and D_{fm} is a mass-mobility exponent (Park, *et al.*, 2003). Currently, a uniform value of MAC is often assumed to be 7.5 ± 1.2 m²/g at 550 nm wavelength (Bond & Bergstrom, 2006). However, there is conflicting information on whether MAC is size-dependent (Radney, *et al.*, 2014). Thus, MAC was also defined as a function of diameter (Equation 7.3) and the widely adopted constant value used as a reference:

$$C_{abs} = \sum_j MAC(D_{m,j}) \times f_j \times m_j \quad (7.3)$$

where $D_{m,j}$ is the mobility equivalent diameter and the subscript j denotes individual particles in the distribution. Unlike the experimental re-classification method, this approach was not limited by aerosol number concentration and was used for all particle sizes.

7.3 Results and Discussion

In the sections below, optical results (MAC and SSA) from both methods of re-classification and mathematical data reprocessing are compared) and the deviations between both solutions analyzed. Measured optical data and mass-mobility results are provided in Appendix C.

7.3.1 Calibration Measurements

Before conducting studies on soot, the CAPS PM_{SSA} monitor was calibrated for accurate measurements since absorption values are derived from the difference of measured extinction and scattering:

$$\sigma_{abs} = \sigma_{ext} - \sigma_{sca} \quad (7.4)$$

Optical calibrations were performed on size-classified, monodisperse aerosol flow of polystyrene latex (PSL) spheres (Thermo Scientific™ Nanosphere™ 3000). PSL spheres are non-absorbing particles, therefore light extinction and scattering are equal and the measured values should match. Also, the refractive index of PSL is well known and measured values can be compared against calculations via Mie theory (Bohren & Huffman, 1983).

The measured and calculated scattering and extinction coefficients of PSL for a particle size of 240 nm are illustrated in Figure 7.4 for number concentrations up to 1000 cm⁻³. Similar profiles were also obtained for other particle sizes of 150 and 350 nm. The maximum deviation from a 1:1 correlation for PSL measurements was 3%. Experimentally measured scattering cross-sections for PSL spheres were 5%, 9% and 11% higher than the values calculated with Mie theory for 350 nm, 240 nm and 150 nm diameters, respectively.

The error for the smallest particle size was larger due to the very low scattering signal intensity ($\sim 3 \text{ Mm}^{-1}$).

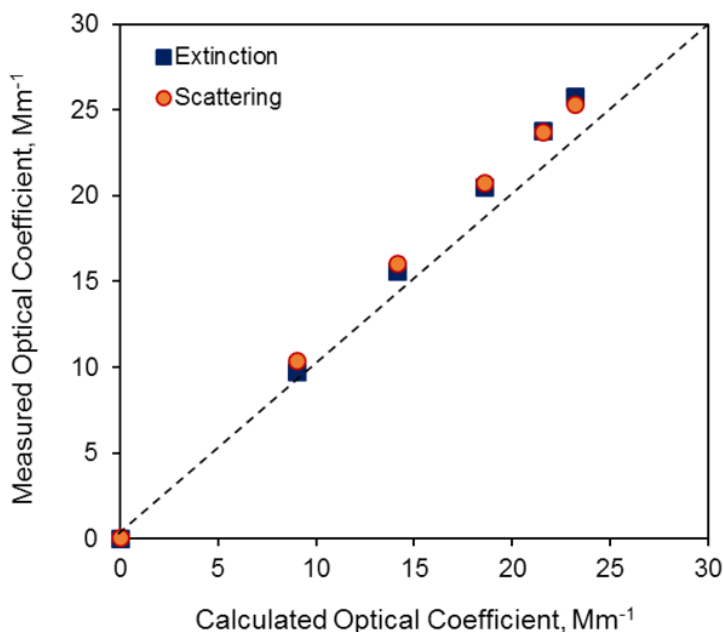


Figure 7.3 Extinction and scattering coefficients as a function of number concentration for 240 nm PSL spheres used the calibration of CAPS-SSA monitor. The dashed line represents a 1:1 correlation.

7.3.2 MAC Determination via Re-Classification

Obtaining a strong signal intensity for both scattering and extinction via experimental re-classification was difficult due to the low number concentrations of the soot aerosol. Smaller particles, though present in higher number concentrations, usually give off weak scattering signals. Larger particles, which interact with light more strongly, are limited in their number density. Adjusting the fuel-air ratios to increase the initial number density of soot resulted in significant variability in day to day measurements. Thus, our results obtained via this method are not supported by sufficient statistics and are presented for only one set of measurements taken over the course of a single day.

Without particle reclassification, MAC values decreased with increasing particle size (and mass) as shown in Figure 7.5a. The results obtained were well above the commonly adopted value of $7.5 \pm 1.2 \text{ m}^2/\text{g}$ (Bond & Bergstrom, 2006). Removing the contribution of multiply charged particles resulted in lower MAC values and a weaker dependence on particle size. For comparison to MAC values of other fractal soot measurements, Cross, *et al.* (2010), Zhang, *et al.* (2008), and Forestieri, *et al.* (2018), obtained $8.11 \pm 1.7 \text{ m}^2/\text{g}$, $8.7 \text{ m}^2/\text{g}$, and $9.1 \pm 1.1 \text{ m}^2/\text{g}$, respectively at 532 nm. MAC values of soot produced in this study ($9\text{-}11.3 \text{ m}^2/\text{g}$) via particle reclassification were higher than all the above listed values. The observed differences may be due in part to the type of soot used, particle classification methods and optical instrumentation

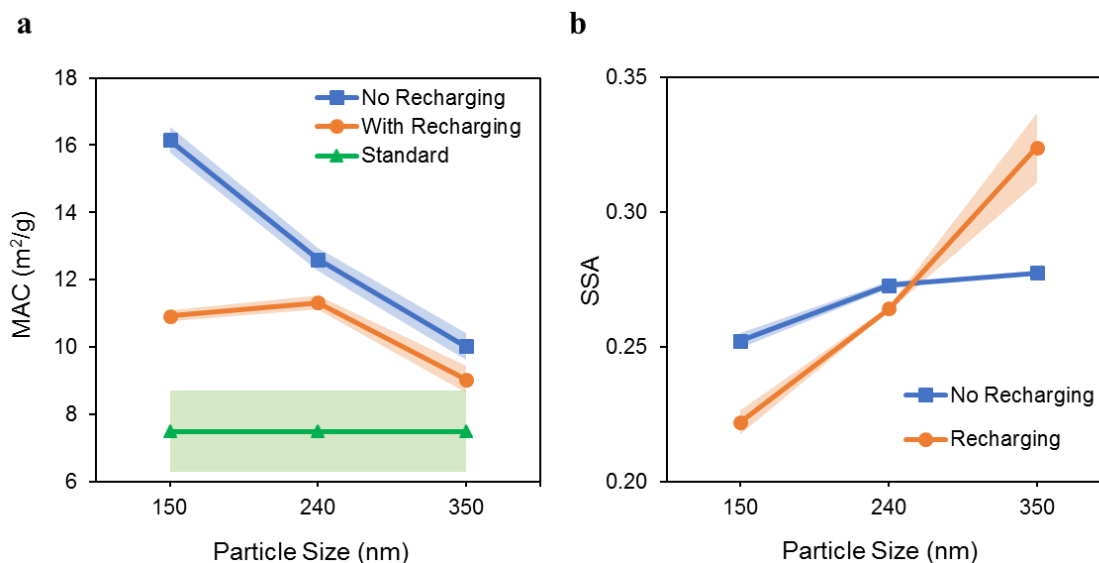


Figure 7.4 (a) Mass absorption cross-section (MAC), and (b) single scattering albedo (SSA) of uncoated soot as a function of particle size. Values for MAC and SSA were obtained with and without experimental reclassification of the soot aerosol. The standard MAC value of $7.5 \text{ m}^2/\text{g}$ is also shown. Error bands are indicated for each measurement.

SSA values obtained without reclassification showed minimal variation with size and fell within the range reported in previous studies (Forestieri, *et al.*, 2018; Kahnert,

2010c; Schnaiter, *et al.*, 2003). After reclassification, SSA values decreased for 150 and 240 nm sizes, but increased significantly for 350 nm. Increased SSA values would typically indicate the presence of coating (Kahnert, *et al.*, 2013) or a more compact morphology (Liu & Mishchenko, 2005). However, since uncoated fractal aggregates were used in this study, this deviation may stem from measurement inaccuracy due to low number concentration (<100 p/cc).

7.3.3 MAC Determination via Data Reprocessing

To calculate MAC via Equation (7.1), fractional contributions of each mode f_i in a particle size distribution were determined by Gaussian fits of experimental data (Figure 7.2b). For the three main particle sizes of interest used in our study (150, 240, and 350 nm), f_i values are listed in Table 7.1. As observed from the calculated standard deviations, there was very little variation in f_i values obtained over the entire duration of the study that signified a very stable output from our soot burner. From the mass-mobility relationship described by Equation (7.2), the D_{fm} and k_s factors were 2.28 and 8.39×10^{-21} g, respectively. These values were used to obtain the masses of particles that were not directly measured by the APM.

Table 7.1 Fractional Contributions of Modes in a Size Distribution

Initial size	150 nm			240 nm		350 nm	
Mode	150 nm	227 nm	298 nm	240 nm	388 nm	350 nm	586 nm
Fraction	0.767	0.210	0.023	0.898	0.102	0.951	0.048
Std Dev.	1.8%	1.5%	1.5%	0.6%	0.6%	0.6%	0.6%

As illustrated in Figure 7.5, mathematically accounting for the contributions of larger sized particles resulted in MAC values comparable to those reported in studies previously mentioned (Cross, *et al.*, 2010; Forestieri, *et al.*, 2018; Zhang, *et al.*, 2008). Our calculated values were well within the range of the standard MAC with a maximum

deviation of 8-20%. Additionally, very little variation in MAC was observed for the three sizes considered (8.08-8.94 m²/g) which implied that it was independent of particle size (Zangmeister, *et al.*, 2018). With or without correction, SSA values remained relatively constant and insensitive to variations in size. The largest difference (~7%) observed after applying corrections was for 150 nm particles. The constancy in SSA for this size range and wavelength (530 nm) has also been confirmed in a previous study (Forestieri, *et al.*, 2018).

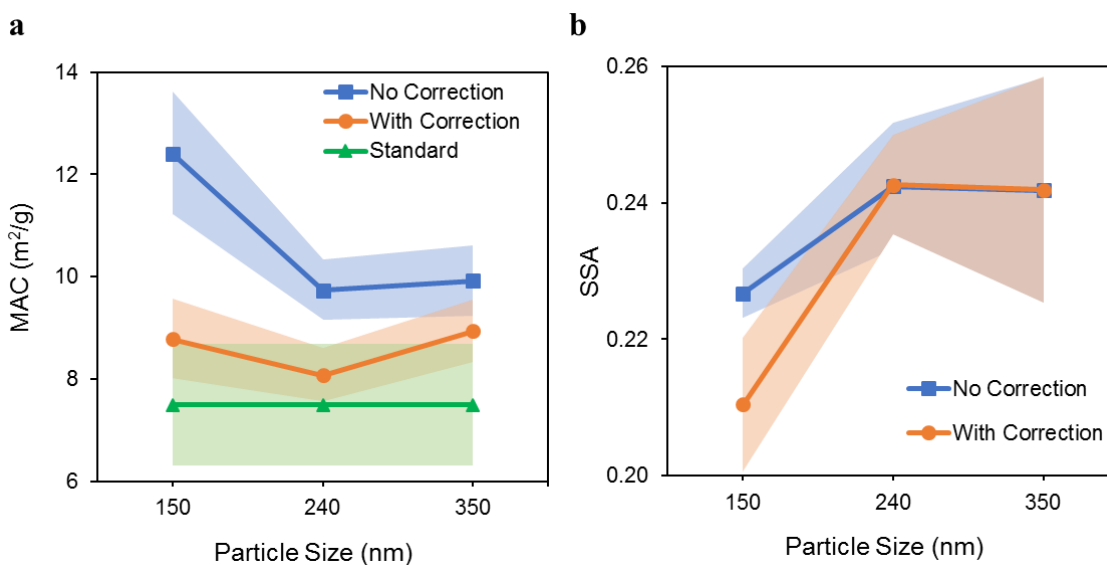


Figure 7.5 (a) Mass absorption cross-section (MAC), and (b) single scattering albedo (SSA) of uncoated soot as a function of particle size. Values for MAC and SSA were obtained with and without mathematical correction for the contribution of multiply charged particles. The standard MAC value of 7.5 m²/g is also shown. Error bands are indicated for each measurement.

In the results presented in Figure 7.5a, only the particle mode contributions are accounted for in the determination of MAC. In reality, each individual particle in the distribution contributes to the measured C_{abs} . Thus, we calculated a size dependent MAC using Equation (7.3) where MAC ($D_{m,i}$) was either expressed as a linear or quadratic function. The coefficients of each function was adjusted till a minimum deviation was

obtained between calculated and measured C_{abs} . The resulting expressions for MAC are given below:

$$MAC_{lin} = 4.75 + 0.01D_m \quad (7.5)$$

$$MAC_{quad} = 0.0001D_m^2 - 0.05D_m + 11.41 \quad (7.6)$$

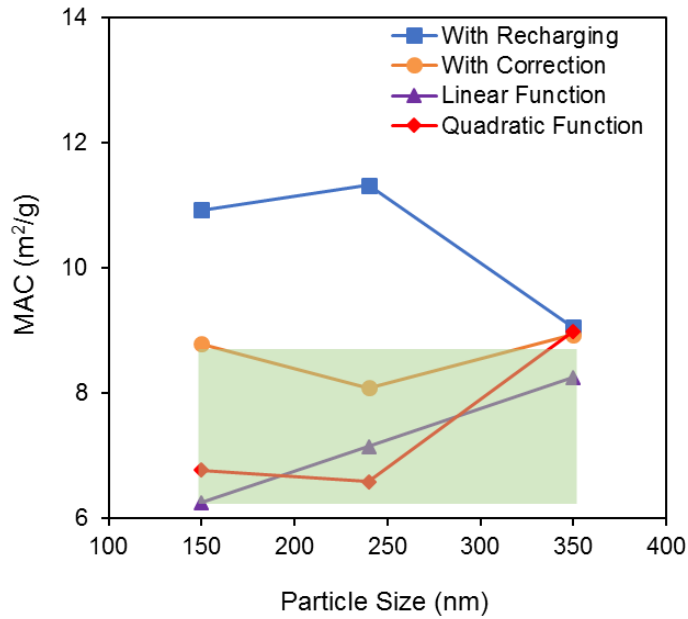


Figure 7.6 Mass absorption cross-section (MAC) of uncoated soot obtained via experimental recharging (blue squares), mathematical correction of peak mode contributions (orange circles), linear (purple triangles), and quadratic (red diamonds) on particle size. The green band represents the range for the standard MAC value of $7.5 \text{ m}^2/\text{g}$.

A comparison of MAC values determined from experimental recharging and calculated via Equations (7.1), (7.4), (7.5) and (7.6) is presented in Figure 7.6. With the exception of the linear fit, the MAC passes through a minimum or maximum at 240 nm and converges to $9 \text{ m}^2/\text{g}$ at 350 nm. A similar value of $8.7 \text{ m}^2/\text{g}$ was reported by Zhang, *et al.* (2008) and Khalizov, *et al.* (2009a) for 320 nm soot at 532 nm wavelength. A larger variation in MAC between the methods employed in this study was observed for 150 and

240 nm sizes. However, MAC determined from data reprocessing methods all fall within the range of the standard MAC (shown as a green band in Figure 7.6), and literature reported values (Khalizov, *et al.*, 2009a; Radney, *et al.*, 2014; Zangmeister, *et al.*, 2018).

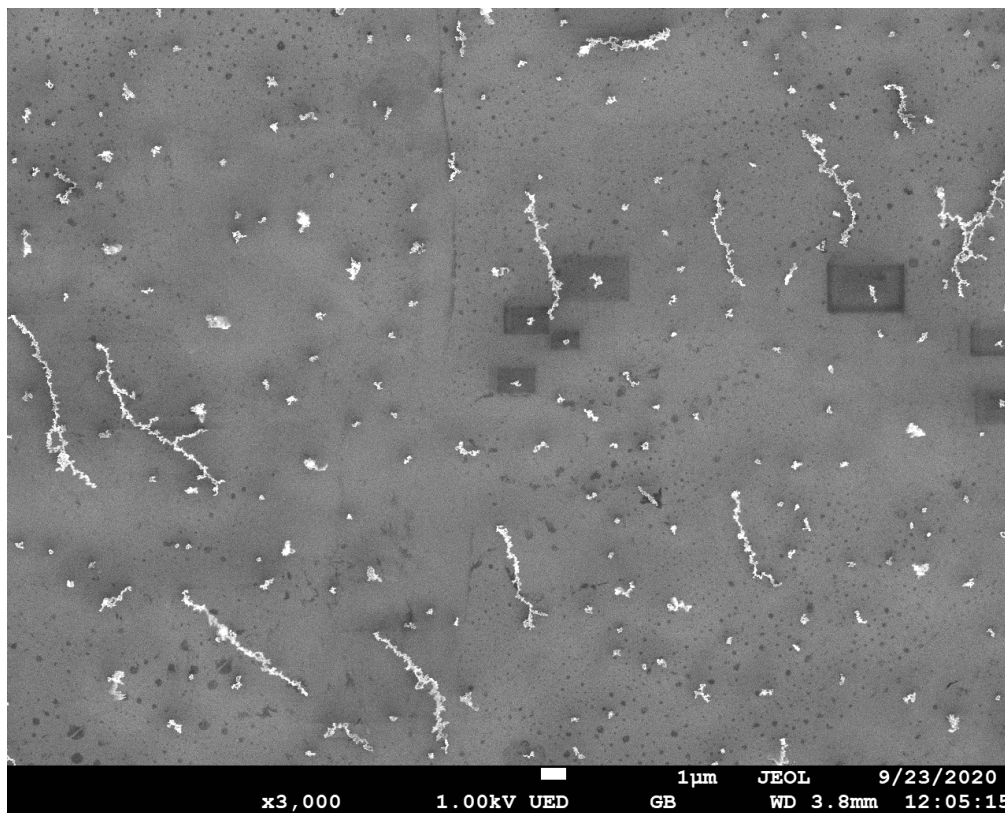


Figure 7.7 An SEM micrograph of mobility classified fresh soot showing the existence of long, linear chain aggregates that are likely to bias optical measurements. Initial mobility diameter of soot is 240 nm.

As stated earlier, the poor performance of the experimental re-classification method in estimating MAC (Figure 7.6) is due in part to number concentration limitations (~90% of the particles became neutral upon recharging and could not be detected by DMA2). It is also likely that some multiply charged particles were not removed and thus contributed to the measured absorption cross-section. Our recent SEM images for fresh soot have revealed the existence of long, linear chain particles (Figure 7.7) that are likely to carry more than

one charge. Given that these linear chain particles were very large (on the order of several microns), the presence of a single particle would be sufficient to skew measured optical coefficients to higher values.

7.4 Conclusions

In this study, we investigated the application of two methods for resolving bias due to multiple charging in laboratory measurements of the mass absorption cross-section (MAC) and single scattering albedo (SSA) of uncoated soot. MAC values obtained via experimental reclassification of soot aerosol were significantly higher (21-51%) than the standard value of $7.5 \text{ m}^2/\text{g}$ reported in literature and exhibited some dependency on particle size. Observed MAC values determined by mathematically accounting for larger sizes from measured mass and size distributions were in good agreement with other studies and only showed deviations of 8-19% from the standard MAC. Additionally, MAC values showed negligible dependence on particle size. Results obtained by expressing the mass absorption cross-section as linear and quadratic functions of particle size were 5-17% lower than the standard MAC value of $7.5 \text{ m}^2/\text{g}$ for particle sizes less than 240 nm. SSA values obtained via experimental recharging showed a strong dependence on particle size. In contrast, SSA calculated by mathematical adjustment was constant for particle sizes greater 240 nm and showed no deviation from the uncorrected data. Given the challenge of generating sufficient number concentration for experimental recharging, accounting for measurement bias in optical properties of soot due to the presence of multiply charged particles is best achieved by data reprocessing.

CHAPTER 8

OPTICAL SIMULATIONS OF LIGHT ABSORPTION AND SCATTERING BY SOOT⁴

Understanding the interaction of light absorbing aerosols, such as soot, with radiation is essential for modeling the direct radiative forcing effect of aerosols. However, developing physical parameterizations that would aid atmospheric models in more accurate estimates for radiative forcing requires an enormous amount of data that cannot be obtained solely from field studies and lab measurements, hence the need for optical calculations. Such calculations can be used to generate rigorous optical predictions of soot during aging for a wide range of aggregate morphologies, mixing states and solar wavelengths. In this chapter, the optical properties of fresh and coated numerically generated aggregates with morphologies ranging from fractal to compact are presented. Calculated optical parameters for fresh soot are compared against direct optical measurements detailed in Chapter 7 to provide closure. Additionally, the effects of the two coating distributions described in Chapter 3 on soot optical properties are explored.

8.1 Introduction

Light scattering and absorption are described by electromagnetic (EM) theory, which predicts the changes in the EM field within the particle and its surrounding medium due to the interaction between the particle and the EM wave from the incoming light. This

⁴ The findings presented for this chapter have been published in the peer-review journal, *Journal of Aerosol Science* under the reference listing:
Enekwizu, O.; Singh, D.; Khalizov, A., Absorption and Scattering of Light by Soot Aggregates with Uniform and Pendular Ring Coatings. *Journal of Aerosol Science* **2020**, *147*, 105583.

interaction is governed by Maxwell's equations, which relate the incident and scattered EM waves. Computer-aided analytical solutions to these equations exist for spherical particles. However, non-spherical particles of arbitrary shape, like soot, require complex algorithms to obtain a solution.

Computations for soot optical properties can be done using more advanced numerical methods described in Chapter 2, such as the Multiple Sphere T-Matrix (Mackowski & Mishchenko, 2011) and Discrete Dipole Approximation (Draine & Flatau, 1994) or via approximations such as Rayleigh-Debye-Gans (Bohren & Huffman, 1983; Sorensen, 2001) and core-shell Mie theory (Ackerman & Toon, 1981). However, incorrect or oversimplified assumptions about the morphological properties of soot can introduce considerable errors in radiative forcing computations. Studies have shown that light absorption and scattering differ significantly between fractal, compact, and spherical particles of the same volume (Kahnert & Devasthale, 2011; Li, *et al.*, 2010; Liu, *et al.*, 2008). For instance, a fractal aggregate model of soot results in radiative forcing estimates (Kahnert, 2010a, 2010b) that are higher by a factor of 2 than corresponding estimates from a volume equivalent spherical model.

Recent optical studies have adopted more realistic model geometries for soot by using algorithms, such as those described in Chapter 2, that build up clusters of spheres that satisfy the fractal scaling law (Equation 1.1). However, majority of these simulation studies of morphologically realistic soot still underestimate observed mass absorption cross section (MAC) and single scattering albedo (SSA) of soot aggregates. Sensitivity studies (Kahnert, 2010c; Liu & Mishchenko, 2005) have suggested that the monomer size has a significant impact in the calculation of these parameters, especially SSA. The extensive

study of Olfert and Rogak (2019) showed that for flame generated soot, larger aggregates are comprised of larger monomers while smaller sized aggregates have smaller monomers. They developed an empirical relationship between monomer size and measured mobility diameter of lab generated soot. Thus, the approximation of a constant monomer diameter for different aggregate sizes in optical simulations is likely to cause some discrepancy. A more severe approximation is the assumption of point touch contacts (Figure 8.1a) between the monomers comprising the soot aggregates. Transmission electron microscopy images have revealed this notion of point contact to be an idealization (Dobbins & Megaridis, 1987; Megaridis & Dobbins, 1990; Yon, *et al.*, 2015). Realistic aggregates are often made of overlapping monomers (Figure 8.1b) with necking (a smooth transition in contact area) between neighboring spheres (Figure 8.1c). The composition of the necking material has been thought to be either organic carbon or brown carbon, and in some cases the same as the parent soot monomer. The study by Yon, *et al.* (2015) reported a strong influence of necking on the SSA of bare soot aggregates in the ultraviolet region. Thus, neglecting these subtle morphological features may have significant impacts in optics simulations.

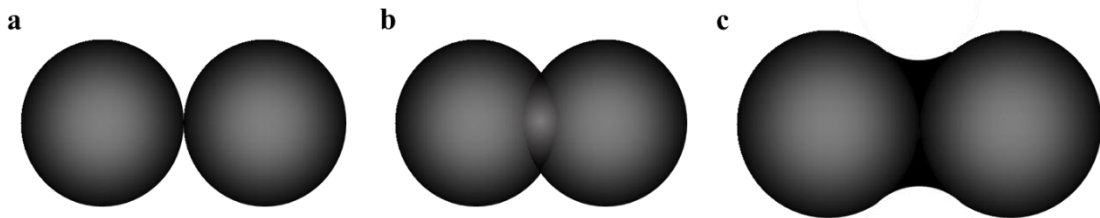


Figure 8.1 Monomer-monomer contacts observed in soot aggregates: (a) point-touch, (b) overlap, and (c) necking.

Similar to particle morphology, accurate representation of the soot mixing state is just as important for the evaluation of radiative forcing. Coatings acquired by soot

aggregates during aging often result in an internally mixed aerosol (Adachi & Buseck, 2008; Moffet & Prather, 2009). To compute the optical properties of mixed soot, different simplifying assumptions are adopted in atmospheric models. The two simplest border cases are to assume that soot and other chemicals are either present as separate particles or mixed homogeneously within the same particles. These approaches underestimate and overestimate the resulting light absorption (Jacobson, 2000, 2001b), respectively. More realistic models employ the core-shell representation where a spherical soot core is embedded in a shell of condensable material (Bueno, *et al.*, 2011; Kahnert, *et al.*, 2012; Shiraiwa, *et al.*, 2008). Though studies have shown that the acquisition of thick coatings result in full aggregate collapse, even compact soot particles are not solid spheres. Moreover, the coating material may not be evenly distributed nor the soot core fully encapsulated. As such, adopting a core-shell geometry can introduce significant inaccuracies in estimating soot optical properties (Adachi, *et al.*, 2010; Liu & Mishchenko, 2018; Luo, *et al.*, 2018; Zeng, *et al.*, 2019). Internally mixed soot also has the added complexity of backbone restructuring that is often unaccounted for. In Chapter 3, we identified two distinct coating distributions that differed significantly in their restructuring ability, i.e., aggregates restructured promptly in the presence of small coating volumes in junctions, but required a larger coating volume in the case of a uniform coating distribution. Thus, an important question is how these coating distributions and associated structural changes affect the determination of soot optical properties.

8.1.1 Study Objectives

The main goal of this study was to perform a systematic investigation of the sensitivity of soot optical properties to atmospheric aging. The common theme in much of this work is

an endeavor to understand the significance of specific morphological and compositional features on the optical properties of soot aggregates. By identifying those features that dominate soot optical properties, parameterizations can be constructed for utilization in large-scale applications, such as atmospheric models.

Thus, our studies began with the reconciliation of measured and modeled optical properties (MAC and SSA) of fresh soot aggregates by accounting for subtle features such as necking, and the variation in monomer size based on measured aggregate mobility diameter (Section 8.4). Next, the impact of two distinct coating distributions, spherical shells around monomers and pendular rings in junctions between monomers, on the optical properties of fractal soot (Section 8.5) were explored. The aggregates were initially kept fractal to decouple the effects from changes in backbone structure and coating distribution. Finally, the combined impacts of structural collapse and coating distribution on the optical properties of soot were determined (Section 8.6). Optical calculations were performed using MSTM and DDA methods. Additionally, simulation results of coated soot aggregates were compared against the commonly used simple core-shell and RDG models, which are treated as benchmarks.

8.2 Numerical Simulation of Bare and Coated Soot Aggregates

To determine the optical properties of soot, the cluster forming algorithms (PCA and CCA) described in Chapter 2 were used to generate aggregates made of graphitic spherical monomers. The coating material was then applied to obtain uniform and pendular ring coating distributions, corresponding to the two different scenarios of vapor condensation. The optical properties of coated soot aggregates were determined exclusively by DDA.

Coating distribution on the soot aggregates was generated via a dipole discretization algorithm, implemented in MATLAB.

Aggregate discretization using dipoles: Using the x , y , z coordinates of the monomer centers, the discretization algorithm first generates a high-resolution cuboidal lattice of dipoles that is sufficiently large to accommodate both the aggregate and its coating. Next, for a specified coating volume fraction (CVF), the algorithm determines which dipoles in the lattice belong to the graphitic monomers or monomers plus their coating, and finally distinguishes between the coating and monomers. Dipoles which satisfy the condition, $l_i \leq R_s$ where l_i is the distance of each dipole in the lattice from the i^{th} monomer center and R_s is the radius of a single monomer, are assigned to the graphitic monomers. Dipoles belonging to the coating material are distinguished using two different approaches, depending on the prescribed coating distribution. Dipoles that meet the requirements of $l_i \leq R_s + t$ describe a uniformly coated aggregate, where t is the thickness of a uniform coating layer. To describe necked and pendular ring coated aggregates, we adapted the equation for necking as defined by Yon, *et al.* (2015). In brief, necking or coating material is added around the contact point between monomers according to a Levelset function described by Equation (8.1). The contribution of the i^{th} monomer to the function ψ for any location on the dipole lattice tends towards 1 if the point is close to the monomer center and towards zero if it is outside. Given the exponential dependence of ψ on distance, only the closest monomers to the point in consideration contribute to the ψ value. Dipoles which satisfy the condition of $\psi \geq 0.5$ as determined by Equation (8.1) for a specified necking parameter α , are assigned to the ring coated or necked aggregate.

$$\psi = \sum_{i=1}^{N_s} \left[\frac{1}{2} \left(1 + \operatorname{erf} \left(-\frac{1}{\alpha} \left(\frac{l_i}{R_{s,i}} - 1 \right) \right) \right) \right] \quad (8.1)$$

The summation is performed over all the N_s monomers in the aggregate. The coating volume fraction is defined as:

$$CVF = \frac{V_{coating}}{V_{soot} + V_{coating}} \quad (8.2)$$

$$V_{soot} = \frac{4}{3} N_s \pi R_s^3 \quad (8.3)$$

where V_{soot} and $V_{coating}$ are the volumes of the bare aggregate and coating, respectively.

Since monomers in the aggregate are in contact, dipoles representing the coating form shells that overlap. The degree of overlapping increases with increasing CVF and structural collapse of the aggregate. Thus, these extra dipoles in the overlap volume were removed via an iterative approach to prevent inaccuracies in the representation of coated aggregates. Details on the relationships of $V_{coating}$ with t and α , along with the procedure for removing overlapping coating volumes are provided in the Appendix D. A visualization of bare, uniformly coated, and pendular ring-coated aggregates generated by the algorithm is depicted in Figure 8.2. All fractal aggregates were generated with a fractal dimension, D_f and scaling prefactor k_o of 1.78 and 1.30, respectively. D_f for aggregates with evolving morphology was varied from 1.78 to 2.7. CVF was varied between 0 and 0.9 for all simulations performed in this study.

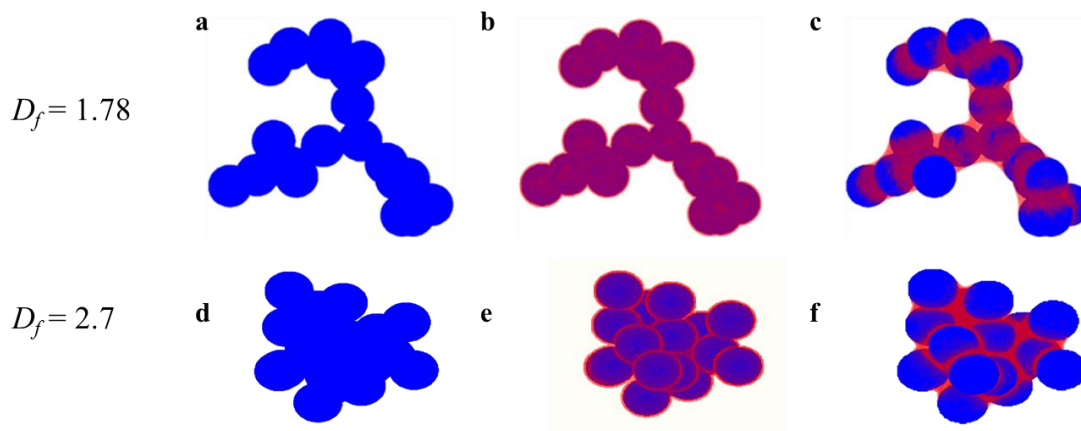


Figure 8.2 Dipole representation of a bare (a, d), uniformly coated (b, e), and pendarular ring coated (c, f) soot aggregates of 20 monomers. The blue colored dipoles are the graphitic monomers and the red colored dipoles are the coating material. *CVF* for the coated aggregates in this case is 0.27.

8.3 Optical Models

Soot optical properties were determined by MSTM and DDA methods described previously in Chapter 2. Given the restriction related to point contact surfaces between monomers, the MSTM method was used only for optical predictions of uncoated (fresh) soot aggregates. The DDA approach, with no restrictions on particle geometry, was used for both uncoated and coated soot. However, optical calculations by DDA were restricted to aggregates with $N_s \leq 120$ monomers because of the computationally intensive operations. For MSTM, there were no limitations on aggregate size due to its high computational efficiency.

For each soot aggregate, orientation-averaged extinction, scattering, and absorption cross-sections ($C_{ext}, C_{sca}, C_{abs}$) were investigated using a wavelength-dependent refractive index of soot in the spectral range of 300 to 850 nm. Other useful radiative properties determined were SSA, MAC, and the asymmetry parameter, $\langle g \rangle$ (Equations 2.10, 2.11

and 2.12, respectively). Since in several cases coating distributions of a monolayer thickness (see Chapter 3) had to be considered, the interdipole separation, d was varied from 2 nm down to 0.4 nm, resulting in approximately 1400 to 179,000 dipoles per single monomer volume. The maximum dipole size of 2 nm was only used for thickly coated aggregates (i.e., $CVF \geq 0.5$). Small dipole sizes ensured that both the coating and morphological features were accurately represented i.e., there were no shape approximation errors. Under these circumstances $|m|kd$, (see Chapter 2) was less than 0.1 even for the shortest wavelength of 300 nm and satisfied the restriction set by Kahnert, *et al.* (2012) for obtaining accurate optical predictions for soot aggregates.

The refractive indices used for soot in this study were based on the expressions reported by Chang and Charalampopoulos (1990):

$$n = 1.811 + 0.1263 \ln \lambda + 0.027(\ln \lambda)^2 + 0.0417(\ln \lambda)^3 \quad (8.4)$$

$$k = 0.5821 + 0.1213 \ln \lambda + 0.2309(\ln \lambda)^2 - 0.01(\ln \lambda)^3 \quad (8.5)$$

where n and k represent the real and imaginary parts of the refractive index. For a wavelength of 530 nm, the refractive index was $1.73 + 0.6i$, falling within the range recommended in the review by Bond and Bergstrom (2006) for visible light. Refractive indices at other wavelengths considered in this work are given in Table 6.1. The refractive index of the organic coating was assumed to be $1.43 + 0i$ and is representative of many organic materials, including tetradecane and oleic acid, which were used in our previous experiments (Chapter 3). The refractive indices of brown carbon, used as the necking material in simulations for fresh soot aggregates, were $1.65+0.003i$ and $1.65+0.03i$ and are representative of moderately absorbing brown carbon and strongly absorbing brown carbon, respectively (Feng, *et al.*, 2013).

Table 8.1 Soot Refractive Indices

Wavelength (nm)	n	k
300	1.63	0.79
450	1.71	0.64
530	1.73	0.60
630	1.75	0.58
850	1.79	0.57

The accuracy of cross-sections for uncoated soot aggregates was tested by comparing results from DDA against MSTM. Depending on the size of the aggregate, the two methods agreed within 2% and 0.3% for absorption and scattering, respectively (see Table E.1, Appendix E). These low relative errors in calculated optical properties fall within the range recommended by Liu, *et al.* (2018), further corroborating our choices for dipole size.

In Chapter 6, we showed that aggregates generated with the same initial set of fractal parameters (N_s , R_s , D_f , k_o) can have variable geometries (Figure 6.8). Thus, to prevent any bias in calculated optical properties, we tested the optical equivalence of an ensemble of aggregates belonging to the same class of fractal parameters. The relative standard deviations (RSD) obtained were less than 1% for 5 individual fractal aggregate realizations (see Table E.2, Appendix E). This signified that the same radiative properties obtained for one realization of a soot aggregate can represent those of the entire ensemble of clusters having the same fractal parameters (Kahnert, 2010b; Liu & Mishchenko, 2007). Thus, for all other aggregate sizes considered in this work, a single realization was used for optical calculations

Additionally, for coated aggregates, the results from DDA predictions were compared against the core-shell and RDG methods. The core-shell predictions are based

on volume equivalent diameter approximations for the soot core and coating material shell (Figure 8.3a).

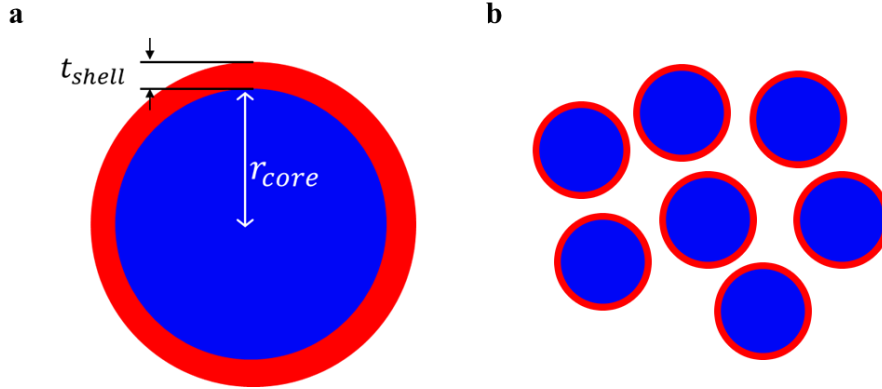


Figure 8.3 Approximate models for mixing state representation: (a) volume equivalent core-shell model, (b) RDG-Mie model. Blue represents soot and red is represents the coating.

The volume equivalent core diameter is given by:

$$d_{core} = \left(\frac{6V_{soot}}{\pi} \right)^{\frac{1}{3}} \quad (8.6)$$

Core-shell calculations were conducted using the Mie code implemented in MATLAB by Mätzler (2002). In the RDG-Mie model (Figure 8.3b), scattering and absorption cross-sections of coated aggregates ($C_{abs}^{agg}, C_{sca}^{agg}$) are represented as functions of scattering and absorption of individual core-shell monomers ($C_{abs}^{csm}, C_{sca}^{csm}$). Mie theory is used to calculate the optical cross-section of a coated monomer and then RDG scaling laws of N_s and N_s^2 are applied for absorption and scattering, respectively:

$$C_{abs}^{agg} = N_s C_{abs}^{csm} \quad (8.7)$$

$$C_{sca}^{agg} = N_s^2 C_{sca}^{csm} G \quad (8.8)$$

$$G = \left(1 + \frac{4}{3D_f} k^2 R_g^2\right)^{-D_f/2} \quad (8.9)$$

G in Equation (8.9) represents the total scattering factor adopted from Sorensen (2001) and Yon, *et al.* (2008).

8.4 Reconciling the Measured and Modeled Optical Properties of Fresh Soot

Despite the significant advances in numerical computations for predicting soot properties, there still exists a mismatch between measured and modeled optical parameters. As stated previously, an agreement between experimental observations and theoretical calculations is important for identifying representative morphological features that can be adopted in larger-scale models. We hypothesize that this agreement can be achieved by varying the monomer sizes in the aggregate and including necking material between monomers. The effects of these two features in the determination of MAC and SSA were assessed.

The variation in monomer size was implemented based on the empirical relationship developed by Olfert and Rogak (2019):

$$d_p = 17.8 \text{ nm} \times (D_m/100 \text{ nm})^{0.35} \quad (8.10)$$

where d_p is the monomer diameter ($2R_s$) and D_m is the mobility diameter. Additionally, the relationship between the mobility radius R_m ($D_m/2$) and aggregate gyration radius, R_g (Sorensen, 2011) was used to uphold the fractal scaling law (Equation 1.1) in the generation of aggregates with different monomer sizes (Table 8.2). The monomer radii chosen are within the range observed in lab and field measurements of soot (i.e., 5-25 nm) (Adachi, *et*

al., 2007; Wentzel, *et al.*, 2003). MAC was determined via Equation (2.11) from the computed C_{abs} and aggregate mass, m ($m = V_{soot} \times \rho_{soot}$).

Table 8.2 Dependence of Particle Mobility Diameter, Gyration Radius and Aggregate Size on Monomer Size Variation

Monomer Radius, R_s (nm)	Mobility Diameter, D_m (nm)	Gyration Radius, R_g (nm)	Number of spheres, N_s
9	103	69	49
10	140	93	69
12	235	157	126
14	365	243	209
15	444	296	263
16	534	356	326
18	748	499	481
20	1011	674	681
22	1327	885	933

Our simulation results showed that variation in monomer radius with aggregate mobility diameter has a negligible effect on MAC, which ranged between 5.3-5.6 m²/g (Figure 8.4a). These values were much lower than our experimentally measured MAC (8.08-8.94 m²/g, see Chapter 7) and the standard MAC (7.5 ± 1.2 m²/g, Bond and Bergstrom (2006)). Also, there was very little deviation in MAC for the assumption of a constant monomer radius of 14 nm (as observed in our experimental SEM images). The insensitivity of MAC to monomer size variation can be interpreted as a saturation effect, i.e., the monomers are still small enough that the electromagnetic field interacts with the entire monomer mass. This behavior was also observed in studies where the monomer radius was fixed as the aggregate size was varied (Kahnert, 2010c). On the other hand, SSA (Figure 8.4b) showed a stronger dependence on aggregate size variation with variable monomers and our experimentally measured values were attained for $R_s \geq 18$ nm.

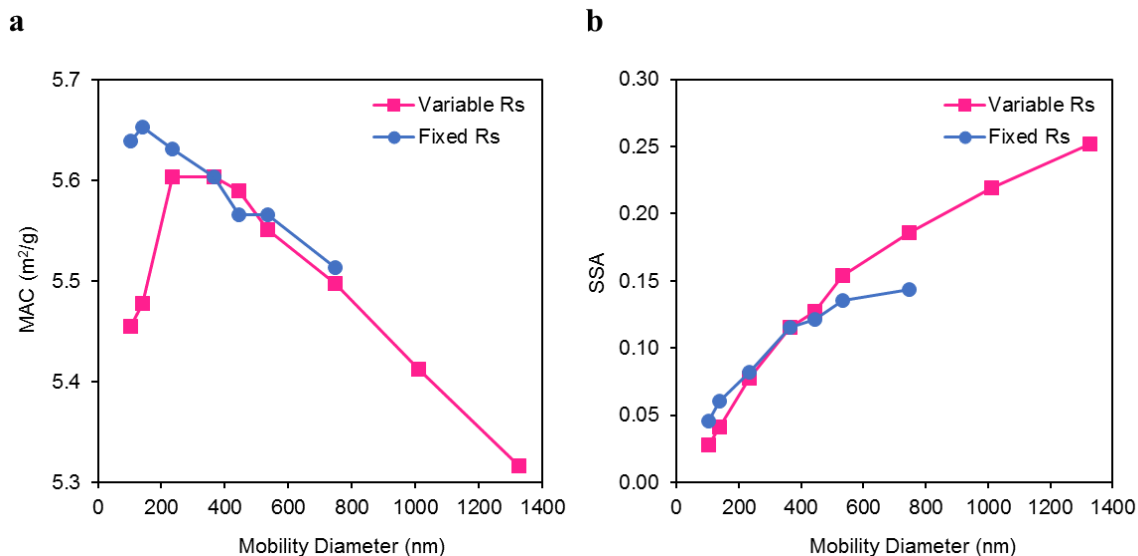


Figure 8.4 Calculated (a) mass absorption cross-section (MAC) and (b) single scattering albedo (SSA) as a function of aggregate mobility diameter for fixed and variable monomer radius. The fractal dimension, D_f is 1.78, structure factor k_o is 1.3, and the incident wavelength λ is 530 nm.

Next, we investigated the effect of necking between neighboring monomers in an aggregate in the determination of MAC and SSA. The results illustrated in Figure 8.5 are for an aggregate comprising 40 monomers with $R_s = 14$ nm (equivalent to a D_m of ~ 150 nm). The fraction of the necking material was varied from 0 (point touch) to 0.27 (full neck). The calculated MAC (Figure 8.5a) showed a very strong dependence on the type of necking material used. For necking material with the same composition as the monomer ($RI = 1.73 + 0.6i$), MAC was $6.6 \text{ m}^2/\text{g}$ for 0.27 necking fraction. This value was 20% lower than our measurements for fresh soot and well within range of the standard MAC. Necks composed of the less absorbing brown carbon ($RI = 1.65 + 0.003i$ and $1.65 + 0.03i$) increased MAC when the necking fraction was minimal (0.08), but decreased MAC as the necking fraction increased. The inclusion of necks increases both mass and absorption. However, our results suggest that absorption enhancement exceeds mass increase when the necking material is strongly absorbing (graphitic), but becomes less significant when the

necking material is less absorbing (organic). As shown in Figure 8.5b, the presence of necks did not yield a significant increase in calculated SSA, which grossly underestimates our experimental measurements of 0.18-0.26. Aggregates with brown carbon necks fared slightly better in SSA predictions than those with black carbon (soot) necks.

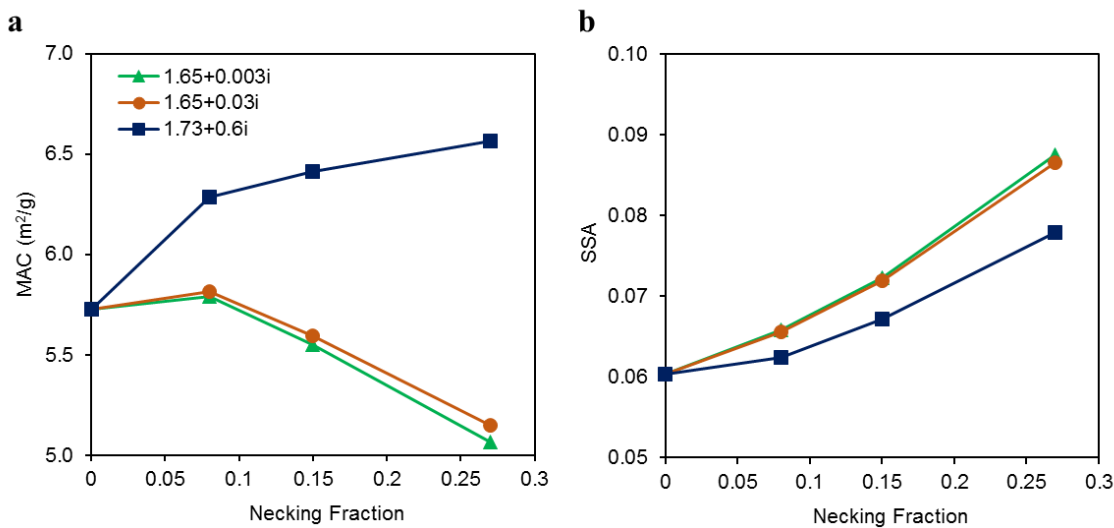


Figure 8.5 Calculated (a) mass absorption cross-section (MAC) and (b) single scattering albedo (SSA) as a function of necking fraction for fresh soot. Necks are comprised of lightly absorbing brown carbon ($1.65+0.003i$), strongly absorbing brown carbon ($1.65+0.03i$) and graphitic carbon ($1.73+0.6i$). D_f is 1.78, k_o is 1.3, monomer radius R_s is 14 nm, and the incident wavelength λ is 530 nm.

Our simulation results are quite promising since they indicate that the key to reconciling measured and modeled optical properties of fresh soot lies in the combination of using variable monomer size (for SSA) and graphitic necks (for MAC). To test this hypothesis, we conducted a single optical simulation for an aggregate of 40 monomers, with a monomer radius of 18 nm, and a necking fraction of 0.27. Calculated MAC and SSA values were $6.5 \text{ m}^2/\text{g}$ and 0.18, both of which are within the range of experimental and literature values. More extensive calculations to cover a broader range of monomer sizes and necking fractions will be done in a future project.

8.5 Optical Predictions for Coated Fractal Aggregates

8.5.1 Dependence of Soot Optical Properties on the Coating Distribution

Studies have shown that the optical properties of coated soot aggregates depend on the underlying aggregate backbone and the coating. Though the presence of coatings on soot typically leads to aggregate restructuring, coated aggregates may retain their fractal morphology if the coating material is solid or highly viscous (Leung, *et al.*, 2017b). Depending on how the coating material is distributed, aggregates with the same backbone morphology may differ significantly in their optical properties. In this section, we compare the effects of two different coating distributions, pendular ring and uniform shells, on soot optical properties.

Absorption and scattering cross-sections for fractal soot aggregates with varying coating amount (indicated by CVF) are illustrated in Figure 8.6 for the two coating distributions (DDA uniform and DDA ring). Additionally, the results obtained using core-shell Mie and RDG-Mie approximations are also shown.

Absorption: Similar to other studies (Bond, *et al.*, 2006; He, *et al.*, 2015; Knox, *et al.*, 2009), all four optical models predicted an increase in absorption of about 25-75% relative to uncoated soot, which is significantly smaller than the increase in scattering (>100%). The calculated absorption enhancements for a thickly coated ($CVF = 0.9$) aggregate of 40 monomers relative to same bare aggregate ($CVF = 0$) are 1.54 (DDA uniform and ring), 1.25 (RDG-Mie), and 1.73 (core-shell), and fall within the range of previously reported values (Luo, *et al.*, 2018; Zhang, *et al.*, 2017).

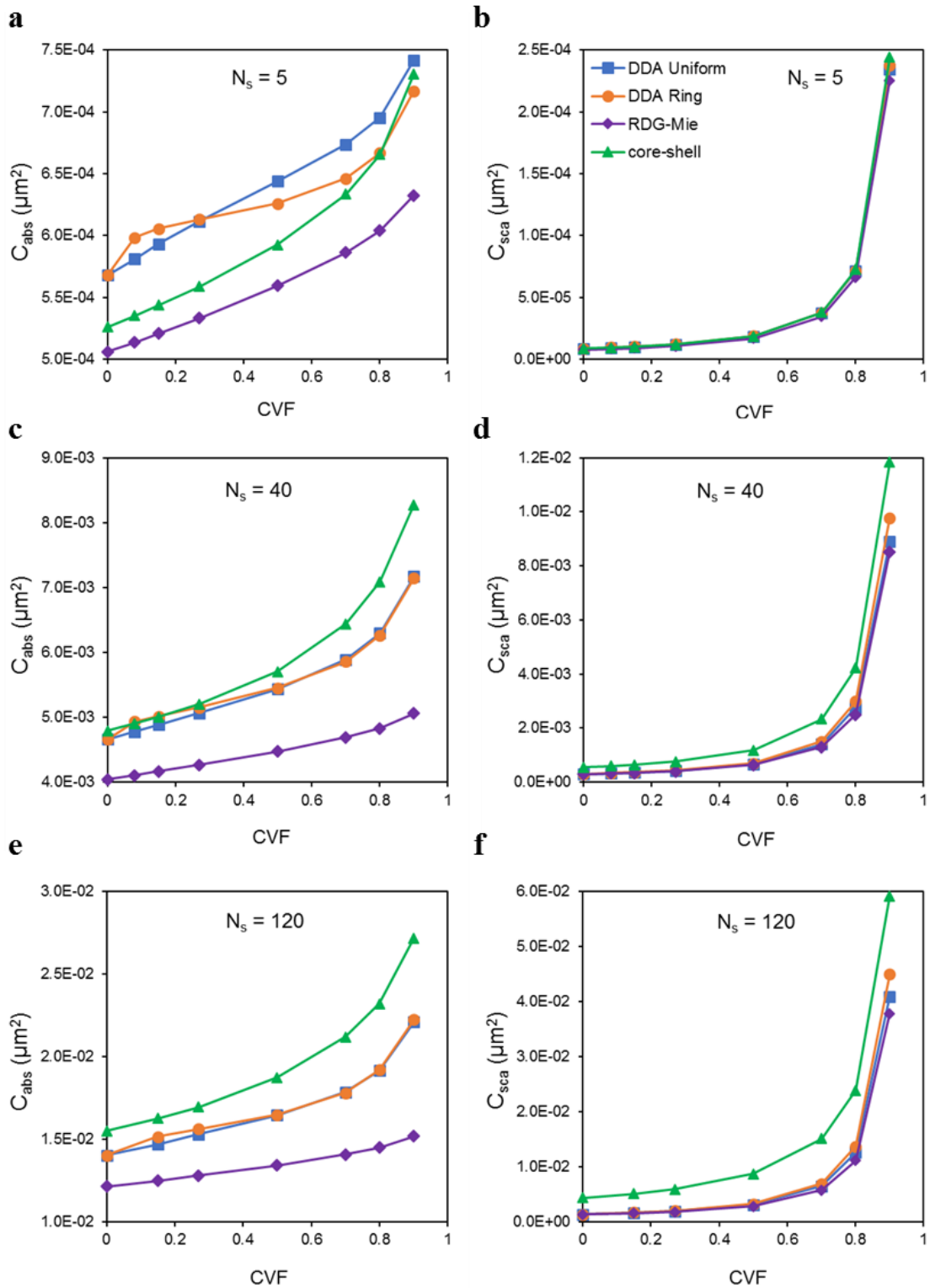


Figure 8.6 Cross-sections for light absorption and scattering by coated fractal aggregates comprising 5 monomers (a, b), 40 monomers (c, d) and 120 monomers (e, f) at various coating volume fractions, CVF ($D_f = 1.78$, $k_o = 1.3$, $R_s = 14$ nm, $\lambda = 530$ nm).

For small aggregates comprising 5 monomers (Figure 8.6a), DDA calculations for aggregates with pendar rings (Figure 8.2c) produced a higher absorption than with uniform shells (Figure 8.2b) when coatings were thin, but at $CVF = 0.23$ the two curves crossed and the pendar rings case became less absorbing. At higher coating fractions, absorptions produced by the two models appear to converge. For aggregates comprising 40 monomers (Figure 8.6c), the small difference in absorption between the two cases was still present for thin coatings, with pendar rings being 3% more absorbing, but the two cases converged for large condensate fractions ($CVF \geq 0.5$). A similar behavior was displayed by aggregates of larger sizes, up to $N_s = 120$, as illustrated in Figure 8.6e.

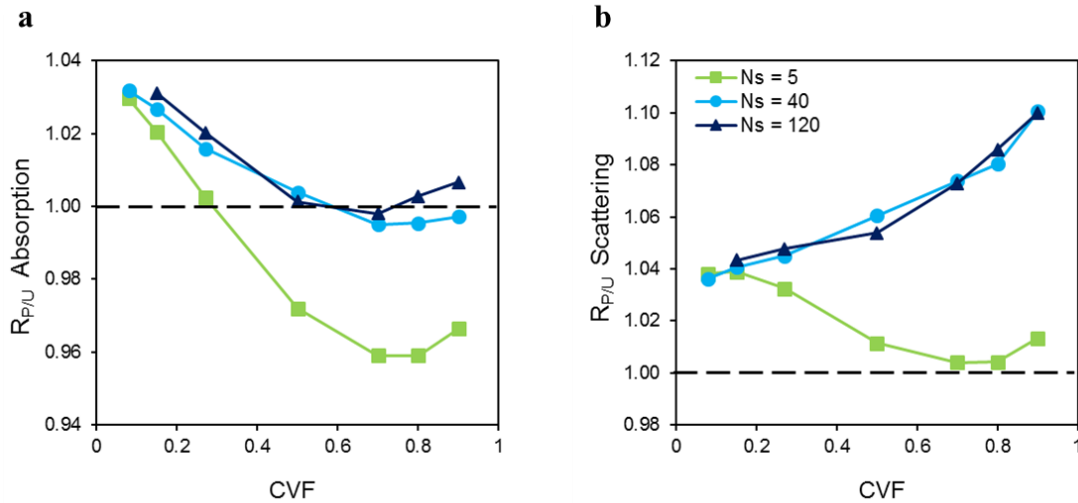


Figure 8.7 Absorption (a) and scattering (b) cross-section ratio, $R_{P/U}$ of pendar ring coated aggregates to uniformly coated aggregates for different coating volume fractions ($N_s = 5, 40$ and 120 , $D_f = 1.78$, $k_o = 1.3$, $R_s = 14$ nm, $\lambda = 530$ nm). The dashed line shows when the optical properties for the two coating distributions are the same (i.e., $R_{P/U} = 1$).

To visualize the difference between the two mixing states more clearly, the ratios of pendar ring over uniform case absorption cross-sections $R_{P/U}$ are plotted in Figure 8.7a, where a departure above unity implies that absorption by pendar ring coated aggregates is stronger. For the largest aggregates, $R_{P/U}$ was 1.03 for the smallest coating volume (CVF

= 0.08), decreasing gradually to unity as the volume fraction of coating approached that of soot ($CVF = 0.5$), and then increasing again as the aggregates became fully embedded ($CVF > 0.7$). For the smallest aggregates, $R_{P/U}$ decreased sharply with increasing coating volume, falling below unity for $CVF > 0.27$. A possible explanation for the difference in absorption cross-section between the two mixing states could be that the electromagnetic coupling between interacting monomers is enhanced when coating is present in junctions, which occurs for pendular ring coated aggregates even at small coating fractions. For instance, a CVF of 0.27 corresponds to fully filled monomer junctions in the aggregate (Figure 8.2c). As the aggregate acquires more coating, the difference between pendular ring and uniform cases disappears because at $CVF \geq 0.5$ the junctions of the uniformly coated aggregates also become filled. Furthermore, dipole renderings of pendular ring coated soot aggregates with $CVF \geq 0.5$ indicate that the condensate tends to ‘spill over’ from the junctions, making them very similar in appearance to the uniformly coated soot (Figure 8.8).

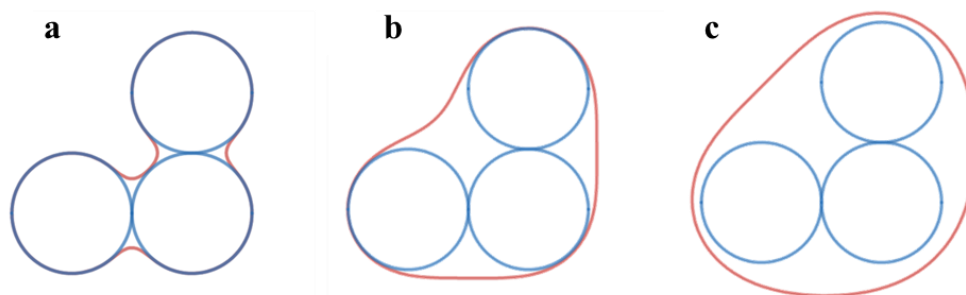


Figure 8.8 2D representation of a pendular ring coated aggregate showing coating spill from monomer junctions to aggregate surface as the coating volume fraction increases; the CVF is 0.27 for (a), 0.5 for (b) and 0.8 for (c).

Scattering and SSA: In contrast to absorption, pendular ring and uniform coating distributions produced a more significant difference for scattering (Figure 8.7b). For $N_s = 5$, scattering $R_{P/U}$ was 1.04 for thinly coated aggregates, declined rapidly with increasing

coating volume, and then increased again. For aggregates comprising 40 or more monomers, the scattering $R_{P/U}$ was 1.04 for thin coatings, but increased rapidly with CVF till it reached 1.1 for thick coatings. It follows that multiple scattering effects are more amplified for fractal soot aggregates with a pendarular ring coating distribution (Yon, *et al.*, 2015). Calculated scattering enhancements for a thickly coated ($CVF = 0.9$) aggregate of 40 monomers relative to same bare aggregate ($CVF = 0$) were large reaching 30 and 33 for the uniform and pendarular ring, cases, respectively.

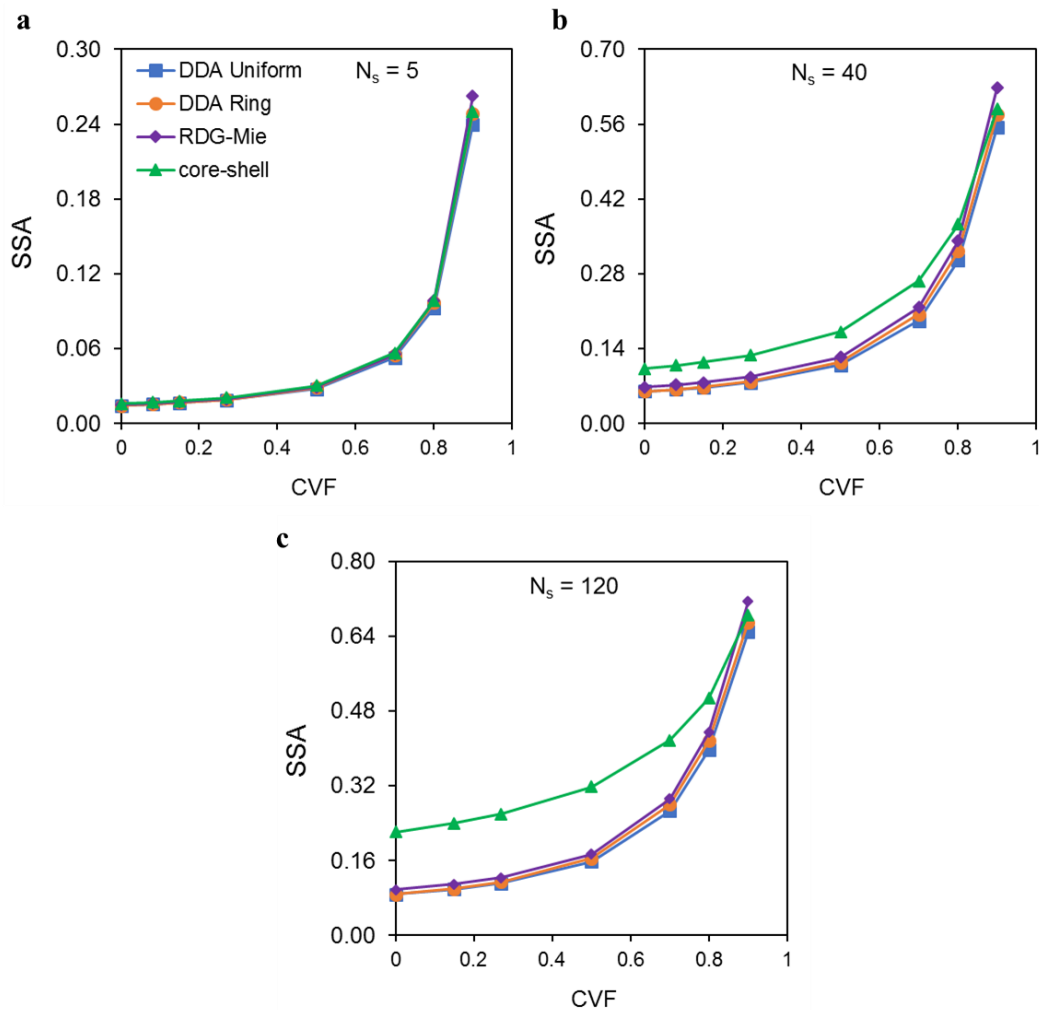


Figure 8.9 Dependence of single scattering albedo (SSA) for coated fractal aggregates comprising (a) 5 monomers, (b) 40 monomers, and (c) 120 monomers on the coating volume fraction ($D_f = 1.78$, $k_o = 1.3$, $R_s = 14$ nm, $\lambda = 530$ nm).

Compared to scattering, for the SSA the difference between the two mixing states was less significant. Calculated SSA for pendular rings was ~2% larger when $CVF < 0.5$ and ~5% larger when $CVF \geq 0.5$ for the aggregates of all sizes (Figure 8.9). This behavior in SSA confirms that placing non-absorbing coating material in junctions enhances scattering somewhat more than absorption.

Asymmetry parameter: The most significant difference between the two mixing states was observed in the behavior of the asymmetry parameter $\langle g \rangle$ (Figure 8.10), which is used in the evaluation of aerosol contribution to radiative forcing (Chýlek, *et al.*, 1995). Depending on the mixing state, the application of a moderately heavy coating ($CVF < 0.6-0.8$) to bare soot aggregates may either increase or decrease the asymmetry parameter (Dong, *et al.*, 2015), thus changing how the scattered radiation is distributed. We found that our calculated $\langle g \rangle$ was always higher in the uniform case than in ring case for all coating fractions. Specifically, for the uniform case, the asymmetry parameter was unaffected by the presence of coating for $CVF \leq 0.27$, retaining the same value as the uncoated aggregate. As the coating became thicker, $\langle g \rangle$ increased nearly exponentially, which indicated that light was scattered progressively more in the forward direction. This behavior was similar between aggregates of all sizes. In contrast, the presence of coating material in monomer junctions initially decreased the asymmetry parameter which made scattering more isotropic (Yon, *et al.*, 2015). The value of $\langle g \rangle$ increased rapidly only when the aggregates were fully embedded and the amount of coating for which this transition occurred was dependent on the aggregate size (Figure 8.10).

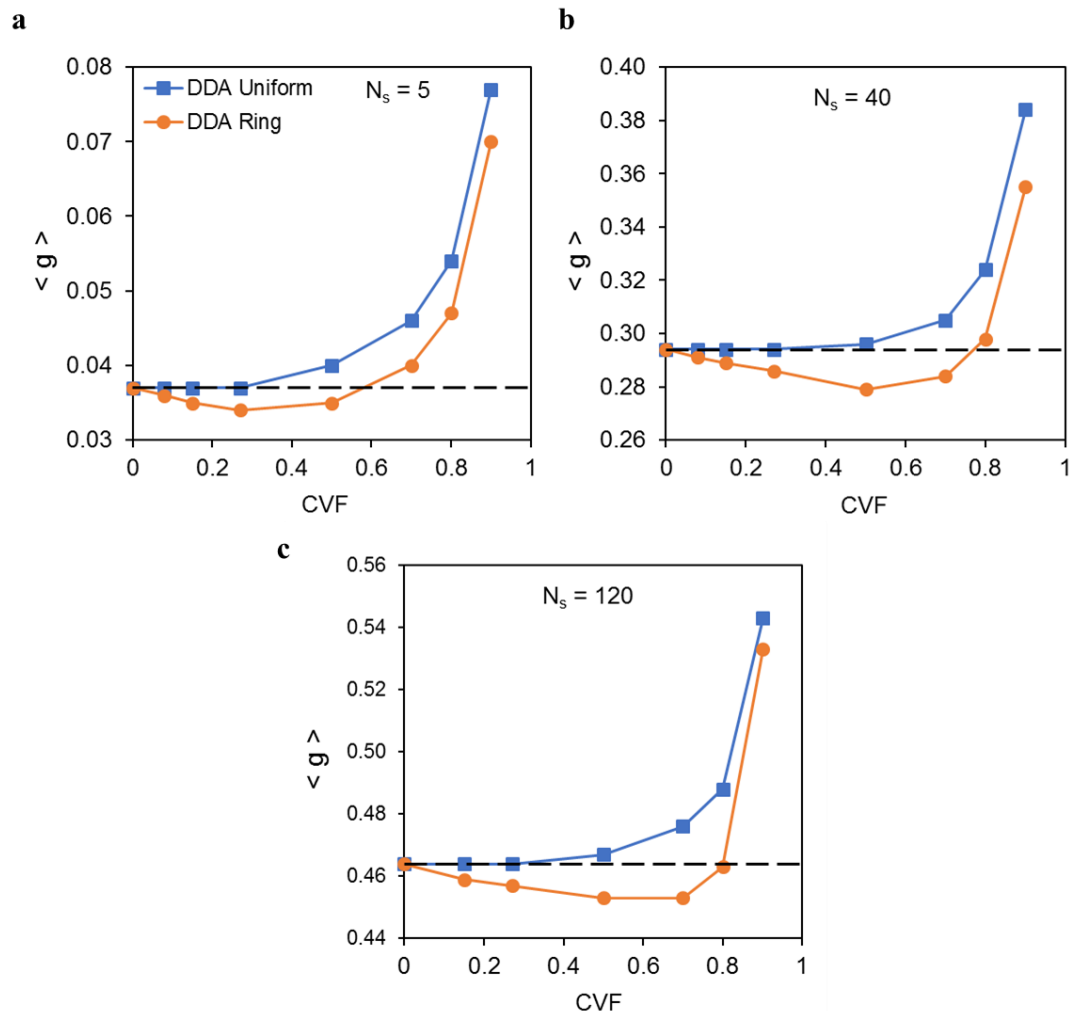


Figure 8.10 Dependence of asymmetry parameter, $\langle g \rangle$ for coated fractal aggregates comprising (a) 5 monomers, (b) 40 monomers, and (c) 120 monomers on the coating volume fractions ($D_f = 1.78$, $k_o = 1.3$, $R_s = 14$ nm, $\lambda = 530$ nm). The dashed line represents the asymmetry parameter for uncoated soot.

A plausible explanation for the different behaviors in $\langle g \rangle$ between the two coating distributions can be deduced from the study by Videen, *et al.* (1998). The authors showed that the asymmetry parameter for aggregates is comprised of two terms, interference and interaction. The first term accounts for the effects of the electromagnetic fields radiating from individual monomers while the second is due to the scattered field from all other monomers striking the monomer of interest. The interference term is always positive, leading to an increased $\langle g \rangle$ while the interaction term is negative, decreasing $\langle g \rangle$. At low

coating fractions ($CVF \leq 0.27$), a uniform distribution may result in comparable interference and interaction effects. This would explain the unity ratio for uniformly coated soot to bare soot asymmetry parameters. A similar trend was observed by Dong, *et al.* (2015) for partially coated aggregates. On the other hand, increased electromagnetic coupling between monomers due to pendular ring coatings causes interaction effects to dominate, decreasing $\langle g \rangle$. For thicker coatings, interference effects were stronger for both coating distributions, as evidenced by the rise in $\langle g \rangle$. The difference in asymmetry parameter between the two coating distributions increased with CVF but became less significant with increasing aggregate size, with maximum deviations of 13%, 8% and 5% for aggregates comprising 5, 40 and 120 monomers, respectively. Our calculated difference is significant because a study by Andrews, *et al.* (2006) estimated that a 10% decrease in $\langle g \rangle$ could result in as much as a 19% reduction in top of the atmosphere (TOA) radiative forcing at 550 nm wavelength. Thus, the choice of a coating distribution may significantly affect estimates for TOA radiative forcing by soot.

Comparison with RDG-Mie and core-shell Mie: We also compared the results of our DDA predictions against simpler methods, RDG-Mie and core-shell. For the core-shell model, the volume equivalent diameter of the core was 56 nm, 96 nm and 138 nm, respectively for aggregates comprising 5, 40 and 120 monomers. In RDG-Mie, the monomer radius was the same as in DDA, but the shell thickness was made smaller to maintain the same coating volume fraction because in the RDG-Mie model, there are no monomer-coating and coating-coating overlaps (Figure 8.3). As shown in Figures 8.6a, c, e, the RDG-Mie approach consistently underestimated absorption, regardless of aggregate size and coating volume fraction. This underestimation can be attributed to the assumption that each

individual monomer interacts with incident light independently of all the other monomers in the aggregate in the RDG limit (Bohren & Huffman, 1983; Sorensen, 2001). Relative deviations from the DDA uniform case for absorption were about -12 to -31%, depending on the monomer shell thickness, in agreement with the values reported earlier for bare soot aggregates (Chakrabarty, *et al.*, 2007; Sorensen, *et al.*, 2018). The core-shell model underpredicted absorption for smaller aggregates for nearly all coating fractions, but exceeded DDA predictions as the size of the aggregate increased to $N_s = 120$. For thin coatings, core-shell absorption was 3-11% greater than the DDA uniform prediction for larger aggregates. This discrepancy became more significant (~23%) as the coating volume fraction increased (Figure 8.6e).

The scattering cross-sections estimated by RDG-Mie were consistent with DDA for all coating volume fractions and aggregate sizes, with DDA uniform being ~4% greater (Figures 8.6b, d, f). The scattering cross-sections obtained by the core-shell model were in excellent agreement with DDA for small aggregates (Figure 8.6b), but diverged for larger aggregates and higher *CVF* (Figures 8.6d, f). The core-shell model consistently overestimated scattering within the range of aggregate sizes considered in our study. The discrepancy between the core-shell model and DDA was largest for uncoated or thinly coated fractal soot, but decreased as the coating fraction increased. As an example, for $N_s = 120$, the discrepancy was ~217% for *CVF* = 0.15, and 45% for *CVF* = 0.9 (Figure 8.6f). This trend agreed with the observation reported by Wu, *et al.* (2016), but contrasted the results of Soewono and Rogak (2013) where the DDSCAT/Mie ratio increased for thicker coatings. A reason for this could be that the mixing state representation used in Soewono and Rogak (2013) underestimated the number of the coating dipoles when correcting for

overlapping volumes. The SSA also reflected the significant overestimation of light scattering by the core-shell model at higher aggregate sizes and soot volume fractions (Figure 8.9). SSA obtained using the RDG-Mie approximation agreed well with DDA uniform, but deviated slightly for thickly coated aggregates due to an underestimation of the absorption cross-section. We surmise that the core-shell model introduces significant errors for scattering by thinly coated fractal soot and should generally be avoided in such cases. A recent review by Kahnert and Kanngießer (2020) has also suggested the retirement of the core-shell model.

8.5.2 Sensitivity to Monomer Radius and Wavelength

The sensitivity of the radiative properties of coated fractal soot aggregates to variations in monomer radius and light wavelength were also investigated. These calculations were performed for a fixed aggregate of 40 monomers, which is small enough to save on computational time yet large enough to represent typical atmospheric soot. Additionally, the convergence of many optical properties at $N_s \geq 40$ was observed.

The dependence of $R_{P/U}$ on the monomer radius for light absorption and scattering by thinly ($CVF = 0.08$) and thickly ($CVF = 0.7$) coated aggregates at a fixed incident wavelength of 530 nm is illustrated in Figure 8.11. For $CVF = 0.08$, the absorption $R_{P/U}$ was 1.028 for the smallest monomer, increased to 1.033 at $R_s = 7$ nm and then remained constant for larger monomers (Figure 8.11a). For thickly coated aggregates ($CVF = 0.7$), the absorption $R_{P/U}$ was 0.984 for $R_s = 3.5$ nm, but gradually approached unity as the monomer radius increased to 28 nm. Similar to absorption, the scattering $R_{P/U}$ for thinly coated aggregates increased from 1.028 at $R_s = 3.5$ nm to 1.034 at $R_s = 7$ nm, and stabilized at 1.04 for $R_s \geq 21$ nm (Figure 8.11b). For thick coatings, $R_{(P/U)}$ for scattering was 1.01 at

$R_s = 3.5$ nm, climbed rapidly to 1.07 (at $R_s = 14$ nm) and leveled off at 1.09 when the monomer size increased to 28 nm. From our observations, we can infer that for thinly coated aggregates, monomer size variation will not significantly alter the effect of the coating distribution on light absorption and scattering, as shown by the nearly constant $R_{P/U}$ for all R_s . However, for thicker coatings, the influence of the mixing state on scattering becomes more prominent with increasing monomer size and should be explicitly considered.

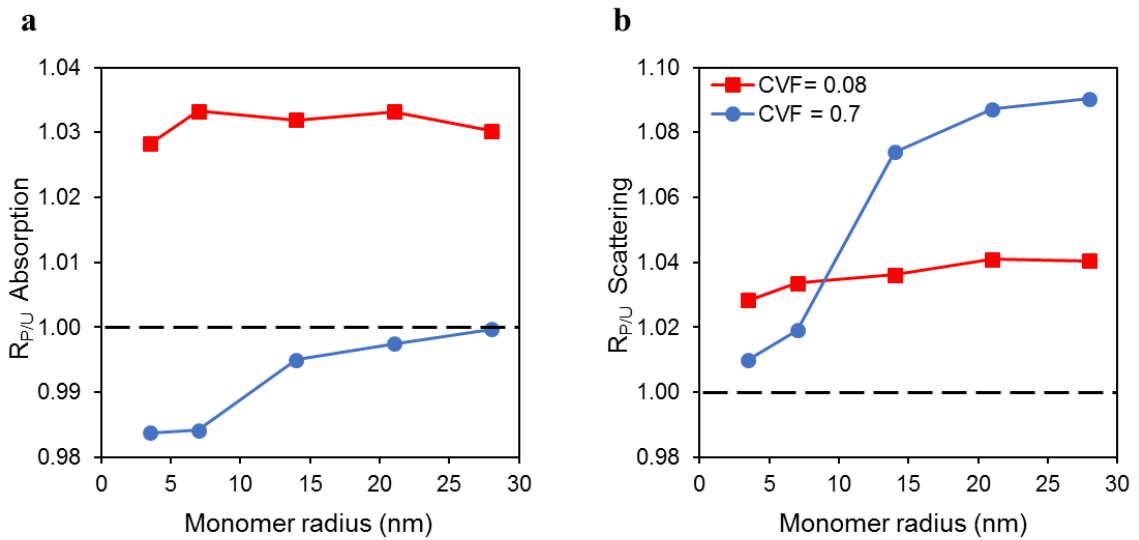


Figure 8.11 Dependence of calculated (a) absorption and (b) scattering cross-section ratio $R_{P/U}$ (pendular ring coated aggregates to uniformly coated aggregates) on the monomer radius, using $CVF = 0.08, 0.7, N_s = 40, D_f = 1.78, k_o = 1.3,$ and $\lambda = 530$ nm. The dashed line corresponds to $R_{P/U} = 1$.

Figure 8.12 shows the effect of incident wavelength on $R_{P/U}$ for coated fractal aggregates with a fixed monomer radius of 14 nm, calculated using wavelength-dependent refractive indices given in Table 6.1. Thinly coated aggregates exhibited a nearly constant absorption $R_{P/U} \sim 1.03$ across the entire UV-Vis-IR wavelength spectrum (Figure 8.12a). In contrast, for thickly coated aggregates, a gradual decline from unity in absorption $R_{P/U}$ with

increasing wavelength was observed. The scattering $R_{P/U}$ for thinly coated aggregates was essentially constant across all wavelengths considered (Figure 8.12b), same as for absorption. For thicker coatings, a stronger wavelength dependency was observed in the scattering $R_{P/U}$, which decreased from 1.1 at 300 nm to 1.035 at 850 nm (Figure 8.12b). This 6% difference may be attributed to multiple scattering effects which are more significant at shorter wavelengths (Yon, *et al.*, 2015).

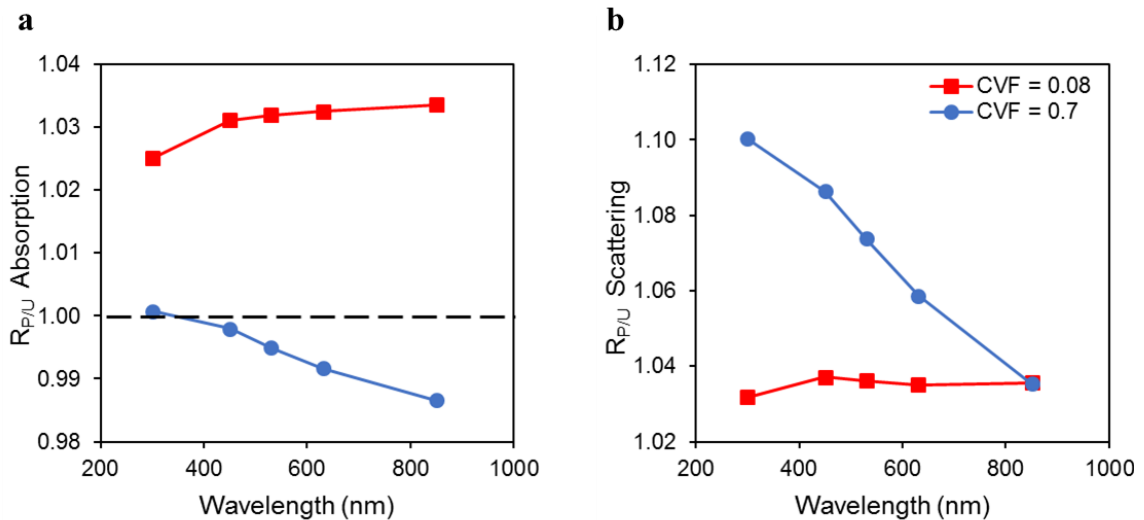


Figure 8.12 Dependence of calculated (a) absorption and (b) scattering cross-section ratio $R_{P/U}$ (pendular ring coated aggregates to uniformly coated aggregates) on the incident wavelengths, using $CVF = 0.08, 0.7$, $N_s = 40$, $D_f = 1.78$, $k_o = 1.3$, and $R_s = 14$ nm. The dashed line corresponds to $R_{P/U} = 1$.

8.6 Optical Predictions for Coated Compact Aggregates

Our previous experiments have shown that condensation in monomer junctions results in aggregate restructuring at $CVF \sim 0.05$, whereas a uniform condensation does not (Chapter 3). In the previous section, only the effects of the coating distribution were examined. However, restructuring may have a significant effect on the radiative properties of coated

aggregates (China, *et al.*, 2015; Dong, *et al.*, 2015; Radney, *et al.*, 2014; Scarnato, *et al.*, 2013; Xue, *et al.*, 2009b). Thus, we also conducted computations of the radiative properties of coated compact aggregates (Figure 8.2d-f) to determine the effects of both coating distribution and evolving aggregate morphology. For all the results presented below, an aggregate size of 40 monomers was used for reasons previously stated in Section 8.5.2.

The effects of the structural evolution of the aggregate backbone on soot optical properties are displayed in Figure 8.13. Similar to other studies (Liu & Mishchenko, 2005), the transition from fractal ($D_f = 1.8$) to compact ($D_f = 2.7$) morphology of the aggregate in the absence of coating had a small impact on the absorption cross-section, but significantly affected the scattering related quantities, i.e., scattering cross-section, single scattering albedo, and the asymmetry parameter. Absorption increased slightly with increasing fractal dimension due to more interactions between monomers. The minor change in the absorption cross-section (~2%) may be due to the aggregate size employed. In the study by Liu, *et al.* (2008), a stronger sensitivity to increasing fractal dimension was reported for aggregates comprising 200 – 800 monomers. The scattering cross-section increased significantly as the aggregates became more compact that signaled the intensification of scattering interaction between monomers. The same pattern was observed in the SSA. The asymmetry parameter was strongly sensitive to the fractal dimension and decreased by a factor of ~3 as D_f increased from 1.8 to 2.7. Compared to fractal aggregates, light scattering was more isotropic for compact soot.

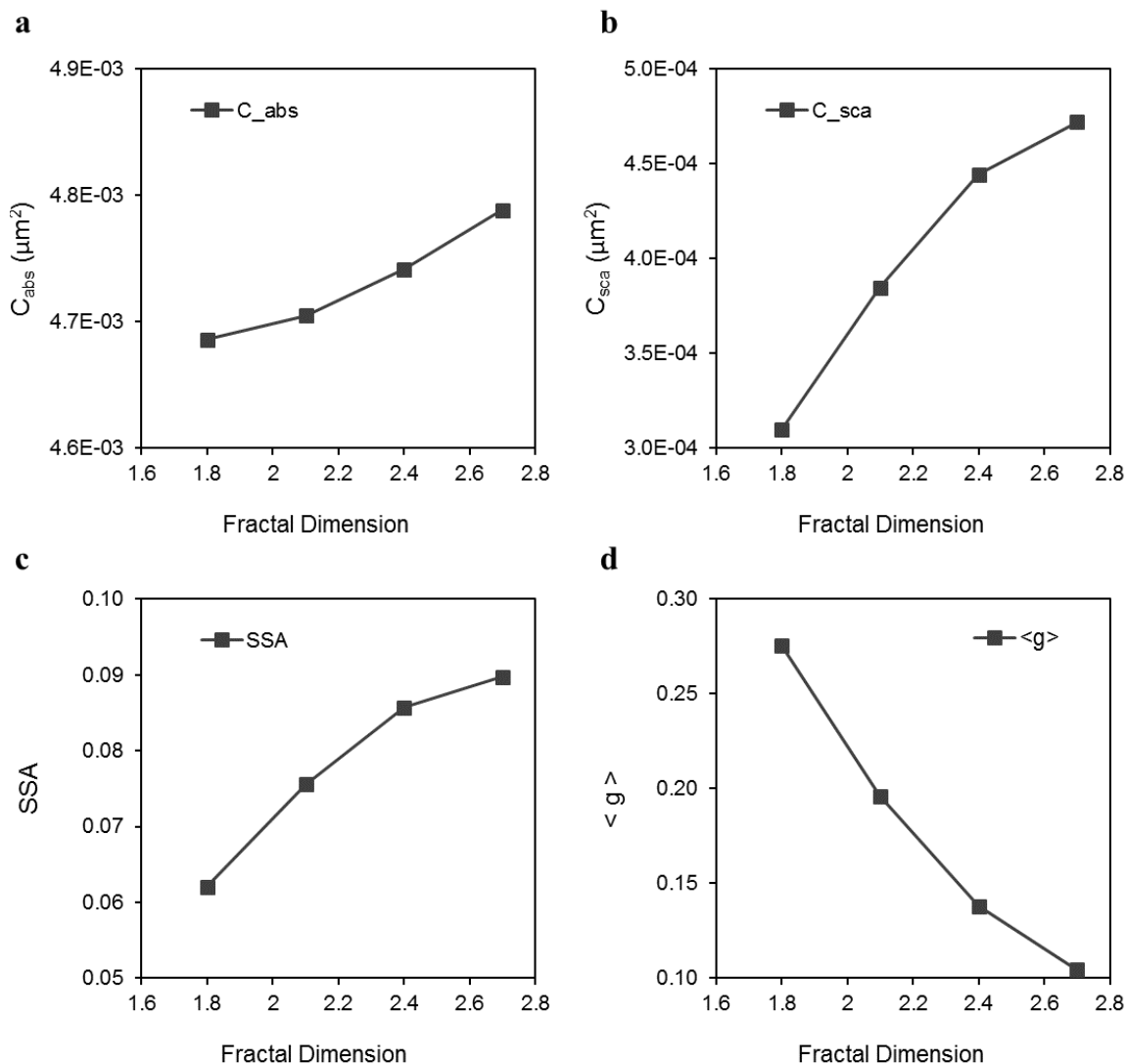


Figure 8.13. Dependence of calculated (a) absorption cross-section (b) scattering cross-section (c) single scattering albedo (SSA) and (d) asymmetry parameter $\langle g \rangle$ on aggregate fractal dimension for $N_s = 40$ monomers ($k_o = 1.3$, $R_s = 14$ nm, $\lambda = 530$ nm).

The effects of coating distribution on the optical properties of fractal soot are contrasted against those of compact soot in Figure 8.14. Results for the intermediate cases ($D_f = 2.1$ and 2.4) are provided in the Appendix E. Both absorption and scattering cross-sections were higher for coated compact soot at all coating fractions, but there was little observable difference between the uniform and pendular ring coating distributions.

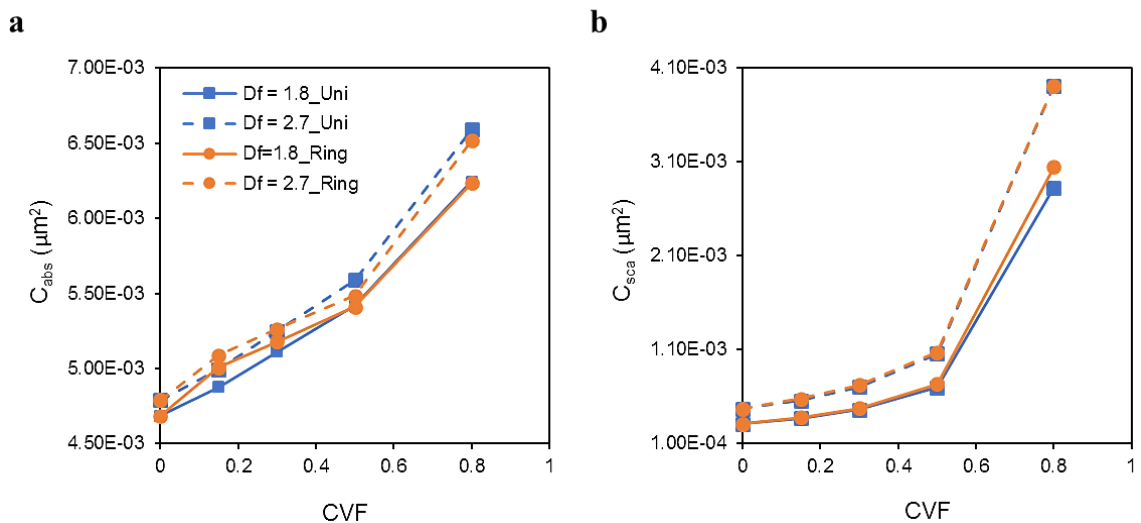


Figure 8.14 Cross-sections for light absorption (a) and scattering (b) by coated fractal (solid lines) and compact (dashed lines) aggregates comprising 40 monomers at various coating volume fractions, CVF . ($k_o = 1.3$, $R_s = 14$ nm, $\lambda = 530$ nm).

Plotting our results in terms of $R_{P/U}$ provided a clearer indication of the combined effects of coating distribution and aggregate restructuring (Figure 8.15). At low coating fraction ($CVF = 0.15$), the effect of coating distribution was minimal on the absorption $R_{P/U}$ which ranged from 1.02-1.03 for all fractal dimensions as seen in Figure 8.15a. As the coating fraction increased ($CVF \geq 0.3$), there was a clear deviation between fractal ($D_f = 1.8, 2.1$), partially compact ($D_f = 2.4$), and compact ($D_f = 2.7$) aggregates. A uniform coating distribution resulted in slightly higher ($\sim 2\%$) absorption cross-sections for the more compact aggregates. For fractal aggregates, this only occurred when the aggregates were embedded ($CVF = 0.8$). As before, the difference between the coating distributions was much more evident for scattering as shown in Figure 8.15b. The scattering $R_{P/U}$ increased with coating fraction for fractal aggregates and a maximum difference of 8% was observed at $CVF = 0.8$. For partially compact soot, $R_{P/U}$ rose slightly for $CVF \leq 0.5$ but decreased gradually to unity when the aggregates were embedded. In the case of compact soot, $R_{P/U}$

was constant at 1.03 for light coatings ($CVF \leq 0.3$) and declined rapidly to unity as the coating thickness increased. Our results indicate that the effect of coating distribution on absorption and scattering is significant for fractal aggregates, but is diminished by restructuring.

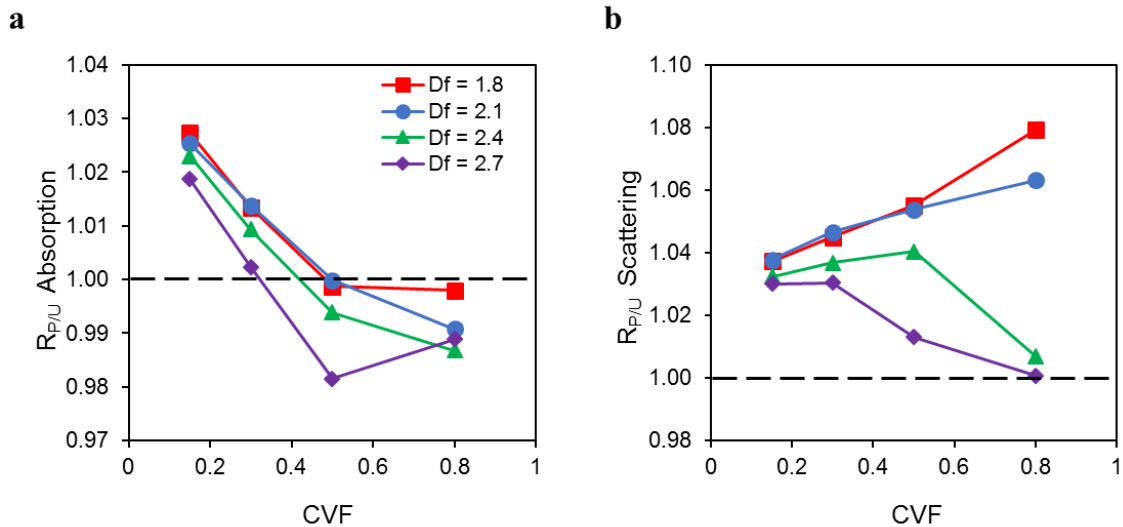


Figure 8.15 Absorption (a) and scattering (b) cross-section ratio, $R_{P/U}$ of pendular ring coated aggregates to uniformly coated aggregates as a function of coating volume fraction for different fractal dimensions, D_f ($N_s = 40$, $k_o = 1.3$, $R_s = 14$ nm, $\lambda = 530$ nm). The dashed line shows when the optical properties for the two coating distributions are the same (i.e., $R_{P/U} = 1$).

The most significant impact of coating distribution and evolving structure was seen in the asymmetry parameter illustrated in Figure 8.16. As discussed previously in Section 8.5.1, a uniform coating distribution resulted in an equal or higher $\langle g \rangle$ relative to uncoated soot and was always higher than the pendular ring case for all fractal dimensions. Interaction effects were dominant for $CVF \leq 0.8$ for the pendular ring case as evidenced by the decrease in $\langle g \rangle$ for both fractal and partially compact soot (Figures 8.16a, b and c). However, for compact soot, little ($\sim 3\%$) to no difference in $\langle g \rangle$ was observed between both uniform and pendular distributions for all coating fractions. Thus, similar to scattering,

aggregate restructuring diminishes the impact of coating distribution on the asymmetry parameter.

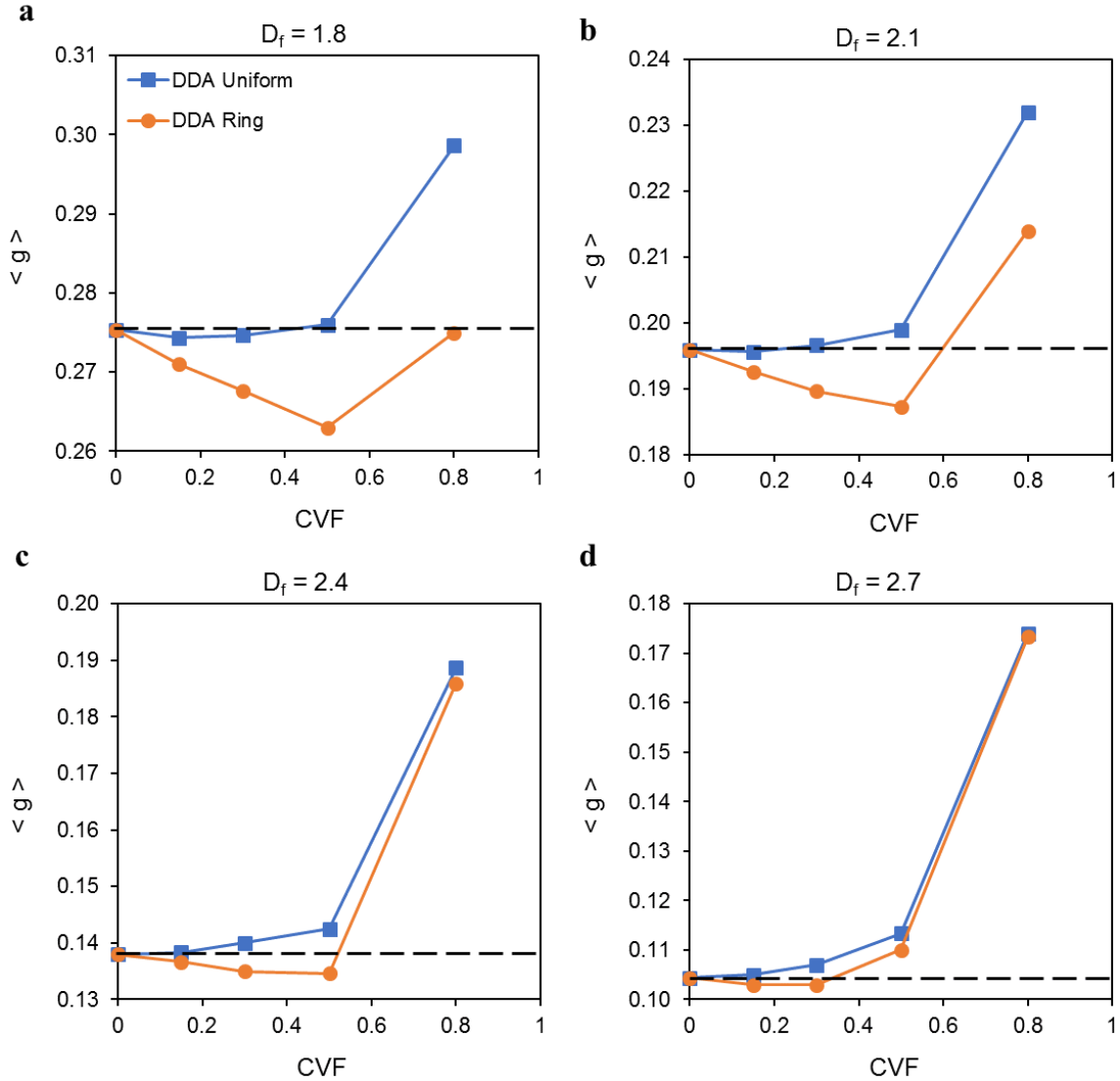


Figure 8.16 Dependence of asymmetry parameter, $\langle g \rangle$ for coated fractal (a, b) and compact (c, d) aggregates comprising 40 monomers on the coating volume fraction ($k_o = 1.3$, $R_s = 14$ nm, $\lambda = 530$ nm). The dashed line represents the asymmetry parameter for uncoated soot corresponding to the aggregate fractal dimension, D_f .

DDA predictions for absorption and scattering were in better agreement with the core-shell Mie model for compact aggregates (see Appendix E, Figure E.1) at all coating fractions. For instance, at $CVF = 0.15$, the discrepancy in scattering between DDA uniform

and core-shell Mie decreased from 77% to 17%. The RDG-Mie model on the other hand, still underpredicted absorption and scattering by about the same amount (-26% and -5%, respectively), similar to fractal aggregates (Appendix E, Figure E.1).

8.7 Conclusions

Modeling the optical properties of morphologically complex light absorbing soot aerosols is a highly challenging and computationally demanding task. The present study aims at identifying features, both morphological and compositional, that are key to reconciling measured and modeled optical properties, and can be parameterized for use in atmospheric models. Model simulations were conducted, using MSTM and DDA, on numerically generated aggregates with well-defined morphology and coating distribution representative of both fresh and aged soot particles in the atmosphere.

For optical simulations of fresh soot aggregates, we found that variable monomer sizes, yielded more realistic SSA values while the inclusion of graphitic necks between neighboring monomers in the aggregate resolved MAC discrepancies. We propose that the key to resolving the differences in measured and modeled optical properties of fresh soot is a combination of large monomers and necking. This idea was tested on a model aggregate and the predicted values of MAC and SSA were a good match with experimental observations.

In the case of coated aggregates, the differences between two distinct coating distributions, a uniform layer and coating in junctions, were relatively minor in the radiative properties of fractal soot aggregates. Only in the case of the asymmetry parameter was the difference substantial. For thinly coated aggregates, the two coating distributions

were within 3% for absorption and 4% for scattering and were insensitive to variations in monomer size and incident wavelength. For thickly coated soot, the difference between the two coating distributions increased to 10% for scattering but decreased to 0.2% for absorption. The asymmetry parameter was always larger for uniformly coated aggregates, with the highest difference of 8-13% in the case of thick coatings. The presence of even small amounts of coating in the monomer junctions lowered the asymmetry parameter, making aggregate scattering more isotropic.

Structural evolution of the aggregate backbone from fractal to compact morphology had a stronger impact on scattering related quantities than on absorption. However, aggregate restructuring diminished the difference between the two coating distributions in the determination of soot radiative properties. Most notably, the optical properties of compact soot aggregates were largely insensitive to the coating distribution. For thickly coated soot, the 10% discrepancy in scattering observed for fractal aggregates dropped to 0% for compact aggregates. The 8-13% difference previously observed in the asymmetry parameter was only 3% for thin coatings and 0% for thick coatings. RDG-Mie predictions for coated aggregates (fractal and compact) agreed with DDA predictions for scattering, but not for absorption. The use of the core-shell approximation for coated fractal aggregates resulted in the highest deviations from DDA, especially when modeling thinly coated soot aggregates.

Our findings highlight the importance of using correct morphological features and coating distributions (mixing states) for accurate predictions of the radiative properties of fractal soot. For compact soot aggregates, these aspects may not play a significant role. However, explicit consideration of the complex morphology and coating distribution of

internally mixed soot in large-scale aerosol and climate models is beyond current computational capabilities necessitating the need for parameterizations. The core-grey-shell (CGS) model proposed by Kahnert and Kanngießer (2020) shows great potential as a tool for further modeling studies. By adjusting the fraction of the soot core f_{core} , the CGS model potentially can be parameterized to describe the optical properties of coated fractal aggregates with uniform and pendular ring coating distributions.

CHAPTER 9

NOVEL PARAMETERIZATIONS FOR PARTICLE RESOLVED AEROSOL MODELS

PartMC-MOSAIC is a unique model that provides a platform to simulate aerosol composition on a per particle basis and develop coarse-scale parameterizations for better climate predictions. However, particle morphologies are fixed and do not evolve during aging which can lead to substantial uncertainties in model estimates of soot impacts on air quality and climate. Thus, there is a need to implement an explicit treatment of soot mixing state and morphology. With the recent introduction of fractal soot representation in PartMC, and development of the dimensionless χ parameter described in Chapter 3, such implementation has become possible. In this chapter, the development and incorporation of a χ -based restructuring module into PartMC-MOSAIC is presented.

9.1 Introduction

To predict associated environmental impacts, most atmospheric models treat soot and other atmospheric aerosol particles as spheres. Furthermore, the models represent their size distributions using either modal (Figure 9.1a) or bin (Figure 9.1b) methods, with the simplifying assumption that all particles (within a mode or size bin) have the same composition. These simplified representations severely affect the ability to predict the fate and impacts of soot. Recently, Riemer, *et al.* (2009) developed a particle-resolved aerosol model (Figure 9.1c), PartMC-MOSAIC, to simulate the evolution of diverse particle populations under a range of atmospheric compositions. PartMC-MOSAIC is a coupling of the Particle Monte Carlo (PartMC) model, which explicitly stores the composition of

many individual particles in a well-mixed volume and, the Model for Simulating Aerosol Interactions and Chemistry (MOSAIC) (Zaveri, *et al.*, 2008), which simulates gas and particle phase chemistries (Zaveri & Peters, 1999), particle phase thermodynamics (Zaveri, *et al.*, 2005) secondary organic aerosol (SOA) formation (Schell, *et al.*, 2001) and gas-particle mass transfer (Zaveri, *et al.*, 2008). MOSAIC allows for the inclusion of important atmospheric species such as sulfate, nitrate, ammonium, chloride, carbonate, methanesulfonic acid, sodium, calcium, primary organic matter, secondary organic aerosols and soot.

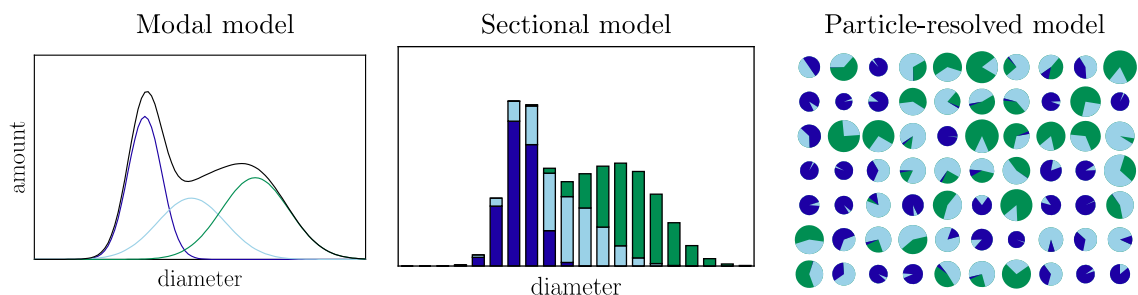


Figure 9.1 (a) Modal aerosol models represent aerosol size distribution as a sum of nodes. (b) Sectional models store the number or mass of aerosol per bin. Both models cannot accurately represent aerosol mixing state. A particle-resolved model (c) such as PartMC can easily store complex mixing states that represent diversity in particle composition.

The coupled model simulation of aerosol state occurs via a two-step approach – first, particle composition can change as chemical species condense from and evaporate to the gas phase, second, the particle population changes via addition and removal through coagulation between particles, emissions from and dilution of the computational volume with background air. Condensation/evaporation events are determined from the input parameter values and initial conditions of the atmospheric species via MOSAIC. On the other hand, coagulation, emission and dilution processes are treated stochastically by PartMC as memoryless events that are approximated by a Poisson distribution. Thus,

PartMC-MOSAIC has the predictive capabilities for number, mass and composition distributions and has been successfully applied to studies of soot mixing state (Hughes, *et al.*, 2018), aging timescales (Riemer, *et al.*, 2010), CCN activity (Ching, *et al.*, 2017) and optical properties (Willis, *et al.*, 2016). However, despite the advantages of particle scale resolution, PartMC-MOSAIC still approximates soot particles as spheres, while real soot particles have complex structures which evolve over time during aging. This limitation of the aerosol model hinders accurate predictions of the morphology dependent impacts of soot.

The dimensionless parameter χ developed in Chapter 3 can be used to describe the distribution of coating material on atmospheric soot aggregates, and hence make predictions about their restructuring, i.e., prompt if $\chi \sim 1$ or delayed if $\chi \ll 1$. However, relying solely on the value of χ could be misleading since it is an intensity and not a capacity parameter. For instance, a chemical with $\chi \sim 1$ will not cause prompt structural collapse if its concentration is low relative to other more abundant chemical species. A more quantitative approach for predicting restructuring would be to track the amount of condensate formed in the monomer junctions and initiate aggregate collapse when the amount exceeds a certain threshold.

The developer of PartMC, Dr. Nicole Riemer (University of Illinois Urbana Champaign) has initiated a new project to introduce fractal soot representation to improve predictions of its fate and impacts, but she needs help from experimentalists to account for the morphological transformations of soot aggregates during aging. Thus, in collaboration with the group of Dr. Riemer, I designed and implemented a coarse scale restructuring module based on the χ parameter into PartMC-MOSAIC. Additionally, I conducted a test

run of the modified aerosol model using a small aerosol population of soot containing particles and tracked the morphologies of the aggregates. The module design, implementation and test results are presented in the sections below.

9.2 A Restructuring Module for PartMC-MOSAIC

The general premise of the restructuring module is simple: mass increments due to condensation events in the PartMC-MOSAIC computational volume are repartitioned to the junctions or spheres of fractal soot containing particles based on conditions imposed by χ . In Chapter 3, we showed that for single component coatings, χ can be computed easily via Equation (3.15). However, as discussed in Chapter 5, soot aggregates are often exposed to a multicomponent system of condensable vapors in the atmosphere. Thus, I adopted this scenario in my design of the restructuring module since the PartMC-MOSAIC aerosol model is capable of simulating compositional diversity within a single particle and across the entire particle population.

Module design: For fractal soot containing particles, the restructuring module calculates an array of χ values, with individual elements $\chi[i]$ dependent on the monomer radius, supersaturation of each condensable vapor, the average surface tension and average molar volume of the condensate on the particle. This array of χ values is calculated at each timestep (condensation event) in PartMC-MOSAIC. As shown previously in Chapter 3, preferential condensation in monomer junctions is defined by high χ values while uniform condensation on monomer spheres is defined by low χ values. Accordingly, I designed the restructuring module to allocate condensate to junctions for $\chi[i] > 0.65$ and to the sphere for $\chi[i] < 0.65$. The reference value of 0.65 describes the scenario where the amount of

condensate in the gap and on the sphere are equal (Figure 3.9). This binary approach is used as a first approximation for describing coating distribution in the framework. Structural collapse is triggered once there is sufficient coating present in monomer junctions (Figure 3.5) as determined by the filling angle, θ or the pendular ring radius r_m . The filling angle is calculated from Equations (3.3) and (3.17) and the resulting expression is:

$$(2 \cos \theta + 1)(\cos \theta - 1)^2 = F \times (Gfm - 1) \frac{2\rho_{soot}}{\rho_{coating}} \quad (9.1)$$

where Gfm represents the mass increment in the particle due to condensation, ρ_{soot} and $\rho_{coating}$ are the soot and condensate densities, and F is used as a bifurcation coefficient to specify how condensation occurs. The coefficient F is set to 1 for $\chi[i] > 0.65$ to mimic prompt restructuring and to 0.1 for $\chi[i] < 0.65$ for delayed restructuring. The real valued positive root of Equation (9.1) is chosen as the solution for θ . From previous calculations, the threshold value for the filling angle is 45° for a monomer radius of 28 nm. Once the soot aggregate is collapsed, the evolution of χ after each condensation event for that particle is no longer tracked. Particles designated as compact are assigned a fractal dimension, D_f of 2.8. The code structure for the module is written in Python and provided Appendix F.1.

Module integration: To incorporate the restructuring module in the particle resolved aerosol model, I collaborated with the designer for PartMC, Dr Nicole Riemer and her research group. We configured the restructuring module (pmc_collapse) to function from within PartMC and interface with MOSAIC, which determines the mass increments at each time step during a condensation event (Figure 9.2). Data from MOSAIC is mapped onto

existing PartMC modules that contain the properties and concentrations of both aerosol (pmc_aerosol_state, pmc_aerosol_data) and gas (pmc_gas_state, pmc_gas_data) species. These modules serve as the inputs for the restructuring module which implements structural change for only soot containing particles. The output is returned to the aerosol and gas modules and then mapped from PartMC to MOSAIC. This process is repeated till the simulation ends. The overall approach is illustrated in Figure 9.2. The Fortran codes created for the restructuring subroutine are provided in Appendix F.2.

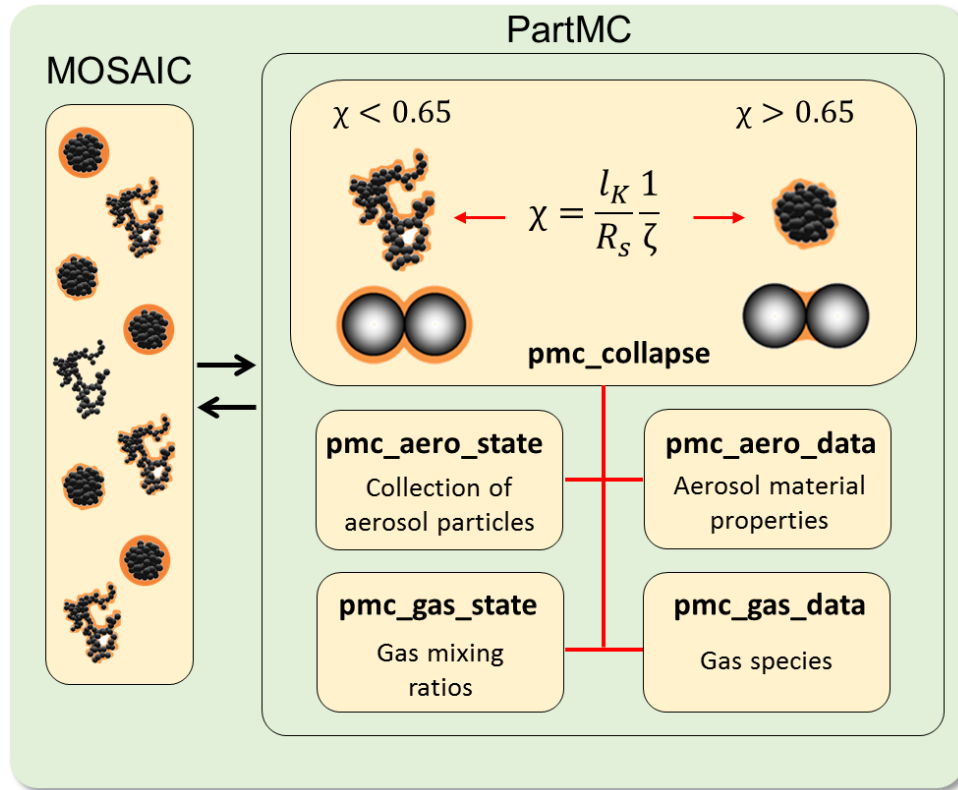


Figure 9.2 Schematic illustrating the overall approach for integrating the restructuring module (pmc_collapse) in PartMC-MOSAIC.

9.3 Results and Discussion

The modified PartMC-MOSAIC model was tested on an idealized computational volume: an urban plume scenario which was not representative of a particular physical location or climate event. Idealized conditions were chosen to test the feasibility of triggering structural collapse within PartMC based on inputs from MOSAIC for gas-particle interactions. These conditions are described in detail in Riemer, *et al.* (2009).

For this study, the evolution of gas phase species and aerosol particles were tracked in a Lagrangian air parcel over a period of 24 hours. A total of 20 aerosol species (including soot) and 77 gas species were used for the simulation. Carbonaceous aerosol emissions from gasoline vehicles, diesel engines, and meat cooking were considered. Diesel and gasoline exhaust particles were assumed to consist only of primary organic matter and soot. The fractal dimension of soot was initialized to 1.8, the monomer radius set at 14 nm, and a total of 500 particles was used in the simulation.

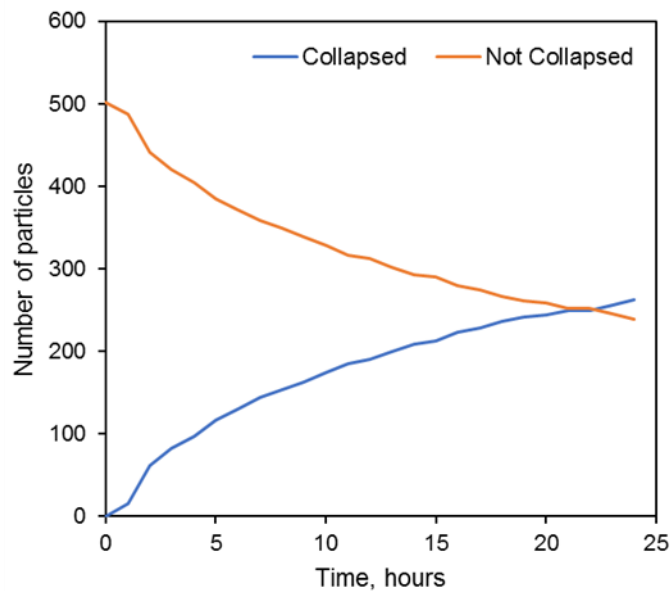


Figure 9.3 Particle structure evolution for soot containing particles in an idealized urban plume scenario.

The results from the simulation are illustrated in Figure 9.3. The number of particles with collapsed soot morphology increased with time over the 24-hour period of tracking. The particle population evolved from having 0% fractal particles ($D_f = 1.8$) to 52% compact particles ($D_f = 2.8$). Our results illustrate the applicability of the restructuring framework even in its most rudimentary form. The binary approach used for χ can be extended to include intermediate cases where the condensate is distributed to both the junctions and the spheres in some proportion as opposed to either one or the other. To make the framework even more rigorous, particle collapse can be modeled as a continuous function of the condensate total volume and its distribution on the soot aggregate. These steps will be undertaken in future research.

9.4 Conclusions

In this study, a coarse framework for simulating the structural evolution of aged soot particles was developed and successfully implemented in the particle resolved aerosol model, PartMC-MOSAIC. The framework was based on the calculated values of the morphology and mixing state parameter, χ , of condensing vapors within a particle. A sample run of the modified aerosol model for an idealized urban plume scenario resulted in aggregate collapse for 52% of the modeled particle population. The success of this rudimentary framework is a first step toward improving the representation of soot aerosols in aerosol models for better prediction of their environmental impacts.

CHAPTER 10

CONCLUSIONS AND FUTURE WORK

10.1 Conclusions

Accurate estimation of the impacts of atmospheric soot has proven to be a challenge owing to its variable composition and evolving morphology during aging. In this dissertation, a combination of laboratory experiments and modeling studies were performed to understand the underlying mechanisms controlling the atmospheric impacts of soot. From the results obtained, quantifiable relationships between the structure, composition and optical properties of soot were established for incorporation into aerosol models.

One of the main results of this dissertation is the development of a dimensionless parameter, χ , to evaluate the distribution of coating material on atmospheric soot aggregates, and hence predict their morphological mixing state and extent of restructuring. Since most atmospheric models adopt a spherical assumption for soot particles, the parameterization of mixing state and morphology in the form of χ is crucial to improving the accuracy of model predictions. The χ parameter can be computed straightforwardly for a specified soot monomer diameter and coating material properties, including vapor supersaturation, wettability, surface tension and volatility. For a fixed monomer size, vapor supersaturation was found to be the controlling factor in the determination of χ . Low χ values were characteristic of high vapor supersaturations which resulted in a uniform coating distribution of shells around monomers. On the other hand, high χ values were representative of low vapor supersaturations which led to a localized coating distribution in the concave junctions between monomers. Prompt aggregate restructuring occurred when condensation in the junctions dominated over condensation on monomer spheres.

Another major outcome of this study is the reconciliation of the dispute between the roles of condensation and evaporation in aggregate restructuring. Liquids capable of wetting the surface of soot aggregates were shown to induce significant restructuring already upon condensation, refuting the claim that coating evaporation was the sole path to aggregate restructuring. For these wetting liquids, which constitute majority of the chemicals in the atmosphere, the effect of evaporation-induced restructuring was evident only after full encapsulation of the soot particle. Additionally, differences in coating volatility were found to induce different levels of aggregate restructuring. This finding was supported by soot aging studies conducted with a more realistic multi-component system of condensable vapors derived from amine photooxidation. Aniline oxidation products were vapors of low volatility chemicals which condensed uniformly and required a large mass to cause restructuring while MEA and TEA oxidation products were vapors of intermediate volatility chemicals that caused prompt restructuring due to capillary condensation. These results further validated the use of the theoretical χ framework in describing condensate distribution and aggregate restructuring behavior.

To connect morphology with optics, experiments and simulations were conducted to determine the optical properties of soot particles as their composition and structure evolve during aging. The mass absorption cross-section (MAC) and single scattering albedo (SSA) values obtained from fresh soot measurements were in good agreement with literature values after measurement bias due to multiply charged particles was accounted for. Differences between measured and modeled values of MAC and SSA, a major issue in soot optical studies, were resolved by simultaneously varying the monomer radius and necking between monomers in numerically generated aggregates. This constituted another

major finding of this dissertation. In the optical simulations of coated soot aggregates, the magnitude of the difference between the effects of uniform and pendular ring coating distributions on soot radiative properties was shown to depend on the compactness of the aggregate. The light scattering related properties of fractal aggregates were more strongly influenced by the choice of coating distribution than those of compact aggregates. Simulated predictions of the asymmetry parameter in particular, were substantially different between the two coating distributions in fractal aggregates. The results obtained from our optical studies highlight the importance of using correct morphological features and coating distributions for accurate predictions of the radiative properties of soot.

Finally, the feasibility of incorporating the structural evolution of soot aggregates during atmospheric aging in atmospheric models was investigated by implementing the χ framework (in its analytical form) in the particle resolved aerosol model, PartMC-MOSAIC. When applied to an idealized urban plume scenario of carbonaceous aerosols, the χ framework successfully triggered particle collapse within a specified aging period for the fraction of the aerosol population that met the conditions for restructuring i.e., the presence of sufficient condensate in monomer junctions. The coupling of vapor condensation and aggregate restructuring was further explored in the development of a restructuring algorithm based on the simple model of Schnitzler et al., 2017. Partial aggregate restructuring observed in experimental studies of thinly coated soot was replicated with the algorithm by adopting Morse potentials to describe the adhesive and restructuring forces in the aggregate. Though semi-quantitative, the success of the χ framework and restructuring algorithm in describing the structural transformation of soot

during aging has demonstrated the suitability of this approach in facilitating accurate predictions of the optical and other morphology-dependent soot properties.

10.2 Directions for Future Study

This work has produced a parameterization for describing the morphological mixing state and morphology of soot in atmospheric models. In its current form, the χ framework can only provide qualitative predictions of the coating distributions for boundary cases i.e., $\chi \ll 1$ or $\chi \sim 1$, but lacks quantitative predictive capability for intermediate χ values. For more quantitative predictions, the χ model needs to be integrated numerically by solving the differential equations governing vapor condensation and meniscus growth. In this way, particle collapse can be described as a continuous function of the condensate total volume and its distribution on the soot aggregate. Furthermore, the χ framework should be expanded to include multi-component coatings and multiple condensing vapors, to better reflect atmospheric soot aging.

In the current dissertation, a modified restructuring algorithm was used to predict the structural evolution of coated soot aggregates. However, the algorithm is limited in its representation of monomer-monomer and monomer-coating interactions which are approximated as simple potentials. To properly simulate the mechanics of condensation induced restructuring, all the forces in a coated soot aggregate must be explicitly calculated. This may be accomplished with discrete element modeling (DEM), where tangential forces and angular motion of the monomers are considered in addition to adhesion, repulsion and dissipative forces. By capturing all the monomer-monomer rolling, sliding and separation events due to the stresses induced by the coating, aggregate restructuring can be

quantitatively predicted. Furthermore, the DEM model can be parameterized against in-situ images of aggregate restructuring captured via environmental transmission electron microscopy (ETEM).

Explicit consideration of the complex morphology and coating distribution of internally mixed soot in atmospheric models is beyond current computational capabilities, hence the common use of the core-shell (CS) model for determining soot radiative properties. However, the core-grey-shell (CGS) model developed by (Kahnert, *et al.*, 2013) offers a more accurate reference geometry for representing coated soot aggregates and has been suggested as a replacement for the conventional CS model. Thus, a final direction of this study is the parameterization of the CGS model with rigorous discrete dipole approximation (DDA) calculations that explicitly account for the effects of coating distribution and soot morphology. The CGS model can easily be tuned via a single adjustable parameter, f_c (soot core fraction) which only depends on the wavelength of light and is applied in the determination of all optical properties of interest.

APPENDIX A
AEROSOL INSTRUMENTATION

The working principles of the main instruments used in this study and in the field of atmospheric research are described in the sections below.

A.1 Differential Mobility Analyzer (DMA)

The differential mobility analyzer classifies charged airborne particles according to their mobility in an electric field. The DMA essentially consists of two concentric metal electrodes with the inner electrode maintained at a controlled positive/negative voltage, while the outer electrode is electrically grounded (Figure A.1). This creates an electric field between the two electrodes. The polydisperse charged aerosol (Q_a) and particle-free sheath air (Q_s) are introduced at the top of the DMA and flow down the annular space between the electrodes. The aerosol surrounds the inner core of sheath air, and both flows pass down the annulus with no mixing of the two laminar streams. The electric field causes charged particles to be attracted through the sheath air to the positive/negative charged collector rod. Particles are collected along the length of the collector rod. Particles with a high electrical mobility are collected along the upper portion of the rod. Particles with a low electrical mobility are collected on the lower portion of the rod. Particles with a narrow range of electrical mobility exit with the monodisperse air flow through a small slit located at the bottom of the collector rod. These particles are transferred to a particle counter to determine the particle number concentration. The remaining particles are exhausted out as excess air flow. The size distribution is obtained by varying the applied voltage.

The axial location of the collected particles depends on the particle electrical mobility (Z_p), the gas flow rate, and the DMA geometry. The electrical mobility of the collected particles is a function of the dimensions of the DMA, the applied voltage, and the fluid flow rate, and it is given by:

$$Z_p = \frac{(Q_s + Q_a) \ln(R_2/R_1)}{2\pi LV} \quad (\text{A.1})$$

where R_1 and R_2 are the radii of the outer and inner electrodes, L is the effective electrode length, and V is the applied voltage. The electrical mobility is related to particle diameter, D_p , by using Stokes' law as:

$$D_p = \frac{neC_c}{3\pi\mu Z_p} \quad (\text{A.2})$$

where n is the number of elementary charges on the particle, e is the elementary unit of charge (1.61×10^{-19} C), C_c is the Cunningham slip correction factor, and μ is the gas viscosity. C_c is a function of the particle Knudsen number, Kn ($=2\lambda/D_p$, where λ is the mean free path of a gas molecule). For soot aggregates, the DMA provides an effective size measure where the mobility diameter, D_m is the diameter of a spherical particle of the same electrical mobility as a soot aggregate.

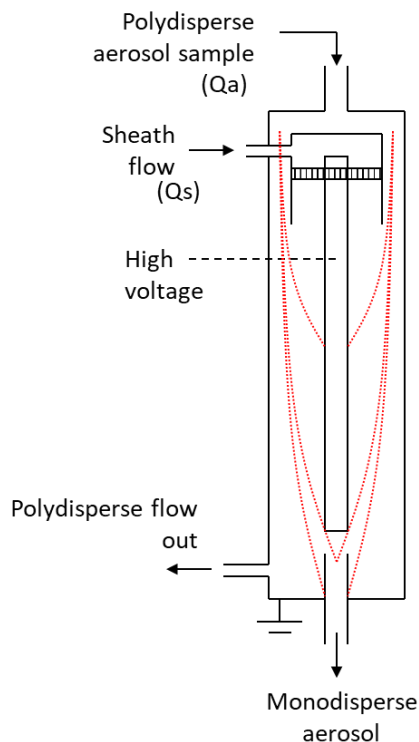


Figure A.1 Schematic of a differential mobility analyzer (DMA).

A.2 Aerosol Particle Mass Analyzer (APM)

While the DMA classifies particles by electrical mobility, the APM classifies particles by mass based on the balance between centrifugal force and electrostatic force. The APM consists of two cylindrical electrodes that rotate coaxially at the same speed (Figure A.2). Charged particles are introduced axially through the small annular gap between the two cylindrical electrodes and rotate at the same angular speed as the electrodes. A voltage is applied to the inner APM electrode with the outer cylindrical electrode grounded. Thus, particles experience centrifugal and electrostatic forces, which act in opposite directions. When these forces are balanced, particles penetrate through the APM with the gas flow and

reach the downstream particle detector. Particles of a certain mass can penetrate the APM for a fixed rotational speed and voltage. The equation that describes the force balance is

$$mr\omega^2 = \frac{\pi D_p^3}{6} \rho r \omega^2 = neE_{APM} \quad (A.3)$$

where m is the particle mass, r is the radial distance to the annular gap from the axis of rotation, ω is the APM rotational speed, ρ is the particle density, and E_{APM} is the electric field of the APM.

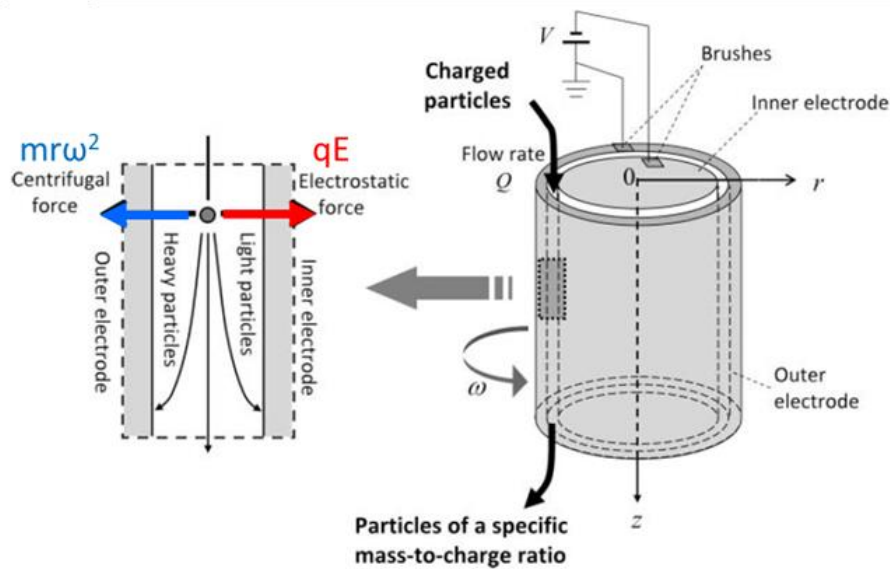


Figure A.2 Schematic of an aerosol particle mass analyzer (APM).

A.3 Condensation Particle Counter (CPC)

Condensation Particle Counters (CPCs) are used to measure total number concentration of an aerosol (Figure A.3). An aerosol sample is drawn continuously through a heated saturator in which a working fluid (usually butanol) is vaporized and diffuses into the

sample stream. Together, the aerosol sample and butanol vapor pass into a cooled condenser where the butanol vapor becomes supersaturated and ready to condense. Particles present in the sample stream serve as condensation nuclei. Once condensation begins, particles that are larger than a threshold diameter quickly grow into larger droplets and pass through an optical detector where they are counted easily.

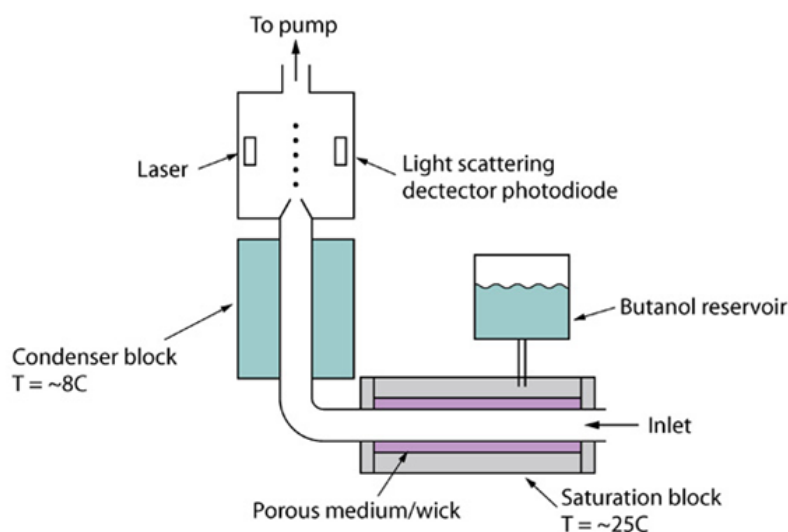


Figure A.3 Schematic of a condensation particle counter (CPC).

A.4 Cavity Attenuated Phase Shift Single Scattering Albedo (CAPS PM_{SSA}) Monitor

The CAPS PM_{SSA} monitor measures both light extinction and scattering by aerosols. The extinction measurement channel utilizes a visible light emitting diode (LED) as a light source, a sample cell incorporating two high reflectivity mirrors and a vacuum photodiode detector. The configuration of the monitor is quite simple and is shown below in Figure A.4. The extinction channel relies on measuring the average time spent by the light within the sample cell. The presence of particles causes this average time to decrease as the

particle concentration increases because of the tendency of particles to scatter or absorb light. Given the high velocity of light (0.3 m per nanosecond) and the very low concentrations of particles typically found in the ambient environment, a very long path length within the sample cell is required in order to accurately measure this change in time. This is achieved with high reflectivity mirrors directly attached to the ends of the sample cell, which provide an optical path length on the order of 1-2 km. The light emanating from the cell is directed into a vacuum photodiode and the resultant signal is processed.

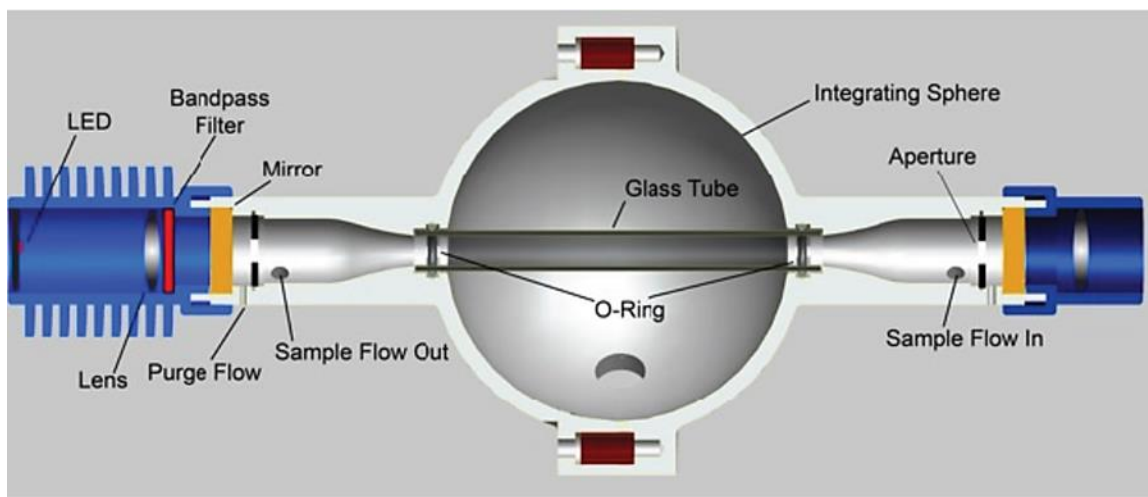


Figure A.4 Schematic of the cavity attenuated phase shift single scattering albedo (CAPS PM_{SSA}) monitor.

In order to perform the scattering measurement, an integrating sphere is incorporated into the extinction measurement cell. The particle path within the sphere is constrained by a glass tube which preserves the flow path so as to preserve the time response and keep the sphere surfaces from becoming contaminated. The integrating volume serves two purposes. The first is to maximize the collection of scattered light at the photomultiplier tube which views scattered light from the optical cell at right angles to the

optical beam. The second is to minimize the light collection bias with respect to scattering angle. The scattered light is detected by the PMT using single photon counting techniques with a suitable amplifier and discriminator, the output of which is sent to a separate digital counter. The output of the PMT is ratioed to the DC LED signal level measured by the vacuum photodiode used to detect extinction.

APPENDIX B

MEASUREMENTS OF COATED PARTICLE MOBILITY DIAMETER DURING VAPOR CONDENSATION AND COATING EVAPORATION EXPERIMENTS

Particle mobility diameter measurements using the methods described in Chapter 4 in the main text are presented here for soot aggregates exposed to vapors of DA and TEGMBE (the other coatings used for the study described in Chapter 4). Measured and modeled particle diameter profiles of soot due to coating evaporation of TEG (Figure 4.5 in the main text) are also discussed in further detail. Additionally, the effect of vapor condensation and coating evaporation of OA, a low volatility coating, on soot is contrasted against that of TEG.

B.1 Coated Particle Mobility Diameter Curves for DA and TEGMBE

Coated particle mobility diameter profiles (expressed in terms of Gfd) are illustrated in Figure B.1 for soot aggregates exposed to DA and TEGMBE coatings. The Gfd curves are similar to those for TEG (Figure 4.4 in the main text) and also show the underestimation of coating mass by tandem differential mobility analysis (DMA-DMA). Given its higher p_{sat} , DA shows higher condensate amount as indicated by DMA-EPC measurements, compared to the other two organic coatings. For instance, at 60 °C, Gfd is 4.07, 4.26, 4.48 for TEG, TEGMBE and DA, respectively.

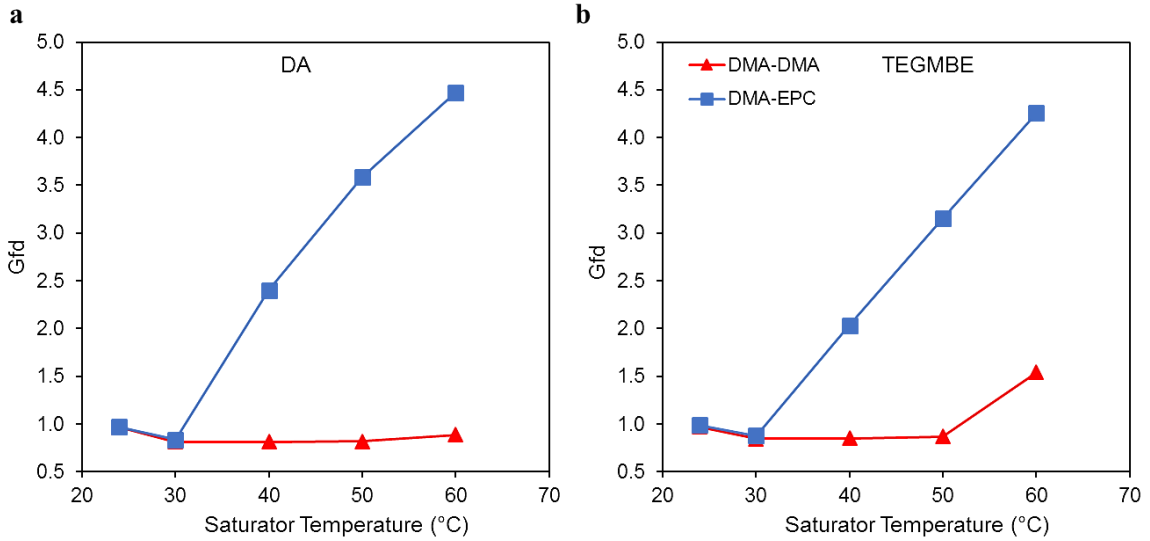


Figure B.1 Change in mobility diameter, Gfd of soot aggregates as a function of saturator temperature for (a) DA, and (b) TEGMBE determined via tandem mobility (DMA-DMA) and electrostatic classification (DMA-EPC) methods. DMA-DMA and DMA-EPC measurements were conducted at a distance of 3.5 m and 0.04 m, respectively from the exit of the saturator. Initial mobility diameter of soot is 240 nm.

B.2 TEG Evaporation During Transit

For TEG, coating loss with increased distance from the saturator exit is apparent in Figure 4.5 in the main text. At longer distances from the saturator exit, the tubing wall is not covered in condensate, resulting in $p \rightarrow 0$ and reducing Equation (3.31) to $J \propto -p_{sat}K$. This leads to substantial droplet evaporation rate, since p_{sat} is high for TEG. The particles shrink continuously, falling below their initial uncoated diameter of 240 nm (due to restructuring) at a distance of ~ 2 m. Further decrease ($\sim 5\%$) in particle diameter after 2 m may be due to the evaporation of interstitial condensate trapped within the crevices of the compact aggregate. At this juncture, coating loss is influenced by surfaces of both positive ($K > 1$) and negative ($K < 1$) curvature in the aggregate. Model predictions show that for spherical particles, vapor loss is accelerated until all coating evaporates and the uncoated particle

size is attained (at ~1.5 m) because K is always greater than unity. The distance of 3.5 m from the saturator exit in Figure 4.5 coincides with the measurement point for the second DMA, confirming the Gfd result at 50 °C shown in Figure 4.4 in the main text. Some condensational growth was still observed via DMA-DMA for saturator temperatures above 50 °C. This may happen because an enormous amount of condensate is formed so that the particles grow very large and some of the coating survives the transit.

B.3 Comparing the Gfd curves of TEG and OA

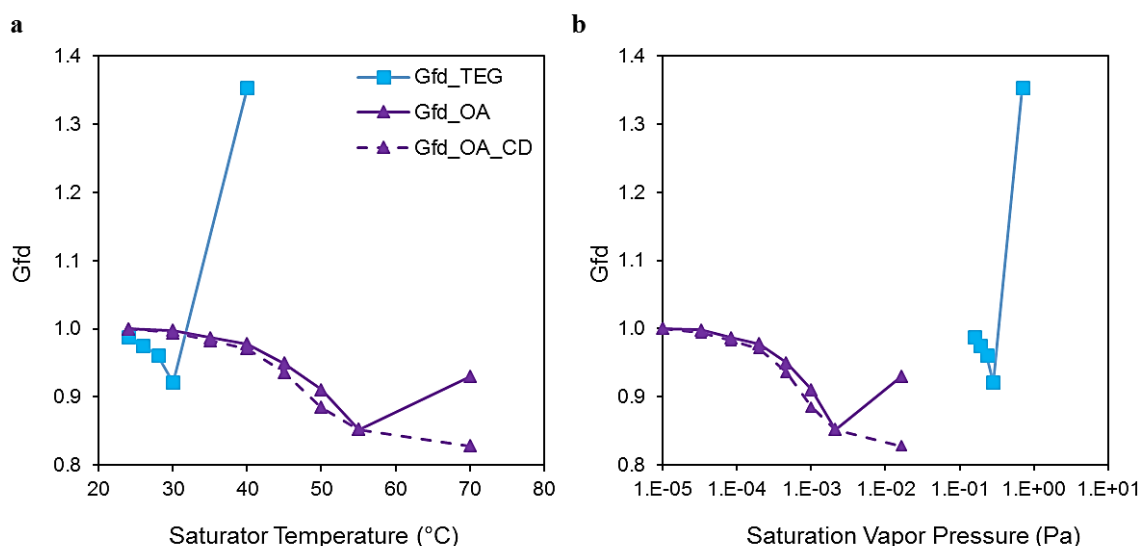


Figure B.2 Dependence of aggregate restructuring and growth on (a) the saturator temperature and (b) saturation vapor pressure of the coating at the experiment temperature. The coatings used are oleic acid (OA) and triethylene glycol (TEG). The initial mobility diameter of the soot aggregates is 240 nm. The solid lines are for coated soot and the dashed lines are for coated-denuded soot measurements.

Figure B.2 shows that aggregate restructuring occurs already during vapor condensation. Due to its low volatility, OA condensation on soot is essentially irreversible. There is little deviation in Gfd between coated and coated-denuded soot at saturator temperatures below 55°C because the amount of coating material is small and ‘hides’ within the aggregate. At

higher temperatures, the Gfd starts to climb rapidly due to condensational growth. However, the increase in Gfd for OA is not as rapid as observed for TEG. This can be explained via Equation (3.31) in the main text. Since the Kelvin term is comparable for both OA and TEG, vapor flux to the aggregate surface $J \propto p_{sat} \zeta$. At similar saturator temperatures, the vapor supersaturation of OA is higher than that of TEG. However, the saturation vapor pressure of TEG is several orders of magnitude greater (Figure B.2b). Thus, the product of p_{sat} and ζ for TEG is higher resulting in a larger condensational flux.

APPENDIX C

MEASURED MASS-MOBILITY AND OPTICAL DATA

Mass absorption cross-section (MAC) and single scattering albedo (SSA) provided in Chapter 7 were derived using both methods of experimental re-classification and mathematical adjustment to eliminate measurement bias. A summary of the optical and mass-mobility data of soot obtained from our experiments is provided in the sections below.

C.1 Optical Data for Re-Classification Method

Soot recharging experiments were conducted as described in Chapter 7. For each particle size considered, after a stable number concentration was achieved, optical measurements were obtained with a 5 second averaging time over a period of 10 mins. The raw data was then processed using an additional boxcar averaging function. The averaged extinction, absorption and scattering cross-sections (C_{ext} , C_{abs} , C_{sca}) before and after re-classification are provided in Table C.1.

Table C.1 Measured Optical Cross-Sections for Re-Classification

D_p (nm)	No Recharging			After Recharging		
	$C_{ext} \times 10^2$ (μm^2)	$C_{sca} \times 10^2$ (μm^2)	$C_{abs} \times 10^2$ (μm^2)	$C_{ext} \times 10^2$ (μm^2)	$C_{sca} \times 10^2$ (μm^2)	$C_{abs} \times 10^2$ (μm^2)
150	1.81	0.46	1.35	1.17	0.26	0.91
240	4.00	1.09	2.91	3.55	0.94	2.61
350	7.99	2.21	5.77	7.70	2.49	5.21

C.2 Optical and Mass-Mobility Data for Mathematical Adjustment Method

Averaged optical cross-sections for soot are provided in Table C.2. Measured mass-mobility data used to derive the fitting coefficients for Equation (7.2) are provided in Table C.3. Aggregate mass was calculated from APM voltage measurements via Equation A.3 in Appendix A.

Table C.2 Measured Optical Cross-Sections for Data Processing

Run #	150 nm			240 nm			350 nm		
	$C_{\text{ext}} \times 10^2$ (μm^2)	$C_{\text{sca}} \times 10^2$ (μm^2)	$C_{\text{abs}} \times 10^2$ (μm^2)	$C_{\text{ext}} \times 10^2$ (μm^2)	$C_{\text{sca}} \times 10^2$ (μm^2)	$C_{\text{abs}} \times 10^2$ (μm^2)	$C_{\text{ext}} \times 10^2$ (μm^2)	$C_{\text{sca}} \times 10^2$ (μm^2)	$C_{\text{abs}} \times 10^2$ (μm^2)
1	1.55	0.35	1.20	3.55	0.86	2.69	7.90	1.92	5.98
2	1.37	0.32	1.05	3.16	0.77	2.39	7.86	1.87	6.00
3	1.40	0.30	1.09	3.27	0.77	2.50	7.40	1.82	5.58
4	1.38	0.31	1.07	3.02	0.69	2.33	7.62	1.68	5.94
5	1.21	0.28	0.93	3.19	0.81	2.38	7.61	2.03	5.58
6	1.42	0.35	1.07	3.43	0.97	2.47	8.72	2.51	6.21
Avg	1.39	0.32	1.07	3.27	0.81	2.46	7.85	1.97	5.88
SD	0.11	0.03	0.09	0.19	0.09	0.13	0.46	0.29	0.25

Table C.3 Mass-Mobility Measurements

Dp (nm)	Set 1		Set 2		Set 3		Set 4	
	APM Voltage (V)	mass $\times 10^{15}$ (g)	APM Voltage (V)	mass $\times 10^{15}$ (g)	APM Voltage (V)	mass $\times 10^{15}$ (g)	APM Voltage (V)	mass $\times 10^{15}$ (g)
150	104.4	0.86	100.2	0.83	103.9	0.86	107.4	0.89
240	178.6	2.52	171.9	2.43	180.7	2.55	181.4	2.56
350	353.8	5.86	333.2	5.52	371.6	6.15	375.3	6.22
D_{fm}	2.26		2.24		2.33		2.30	
k_s	8.55×10^{-21}		8.77×10^{-21}		7.42×10^{-21}		8.82×10^{-21}	

APPENDIX D

COATING VOLUME CONVERSIONS FOR COATED SOOT AGGREGATES

Here, a detailed description is provided for the conversion of the coating volume and coating volume fraction ($V_{coating}$ and CVF , Equation 8.2 copied below from the main text) to coating thickness t and necking parameter α for uniform and pendular ring coating distributions, respectively. Also shown are the calculations of equivalent coating thicknesses for the core-shell and RDG-Mie models with the same CVF .

$$CVF = \frac{V_{coating}}{V_{soot} + V_{coating}} \quad (8.2)$$

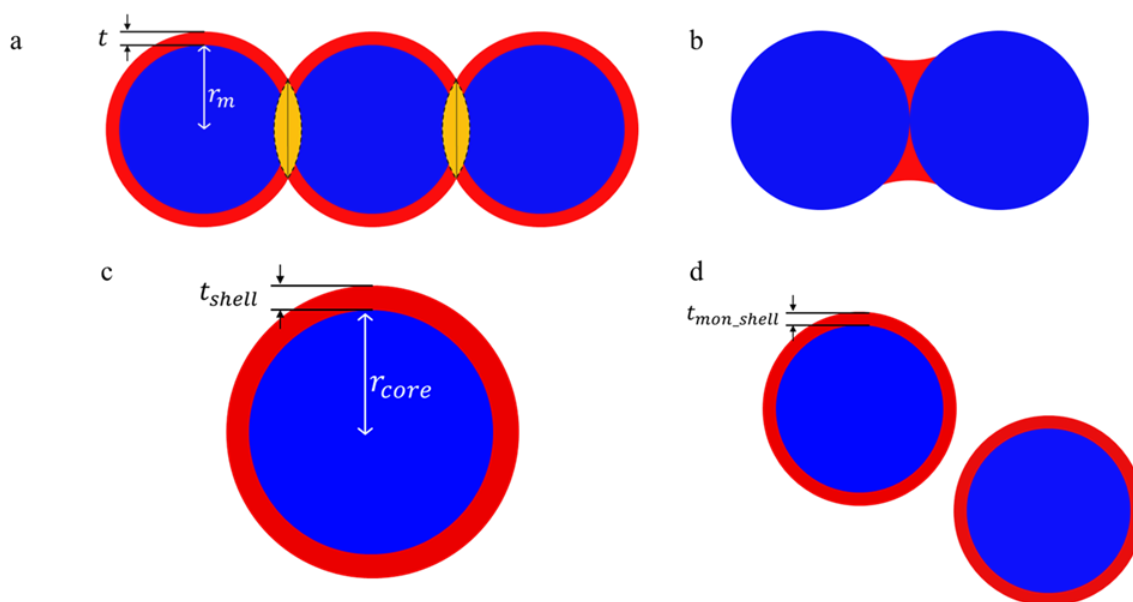


Figure D.1 Models for mixing state representation: (a) uniform distribution of coating material over soot monomers with effective coating thickness t (DDA Uniform), (b) pendular ring distribution at junctions between monomer spheres (DDA ring), (c) volume equivalent core-shell model with coating thickness t_{shell} (d) RDG-Mie model with coating thickness t_{mon_shell} .

D.1 Conversion of Coating Volume to Monomer Coating Thickness

Based on Figure D.1a, $V_{coating}$ is expressed as a function of monomer radius R_s , coating thickness t , and the number of monomers in the aggregate N_s . For each monomer, the shell volume (red) is estimated by subtracting the monomer volume (blue) from the volume of the coated monomer (red + blue) and then eliminating overlapping volumes (gold spherical caps) that arise due to point contact of the soot monomers:

$$V_{coating} = \left(\frac{2\pi}{3}\right) [3N_s R_s t (2R_s + t) + t^2 (3R_s + 2t)] \quad (D.1)$$

The derivation of Equation (D.1) is based on a linear chain configuration for the branched soot aggregate. This assumption leads to inaccuracies in the determination of t , especially for high CVF , due to overlapping coating volumes that appear in branched aggregates for monomers which are not in direct point contact. The linear chain approximation for soot aggregates has been replaced by a more rigorous approach described in Section D.3. For the initial generation of coated fractal aggregates, Equation (D.1) is used as a first-order approximation for estimating t from $V_{coating}$. A coated aggregate is generated with this initial guess t_0 and the volume of each region of the aggregate V_i (monomer or coating) is explicitly calculated by counting the number of dipoles belonging to each region, n_i and summing their volumes:

$$V_i = n_i d^3 \quad (D.2)$$

where i represents either coating or soot, and d is the size of the dipole. The exact solution for t is then obtained by calculating the CVF via Equations (8.2) and (D.2) for $t_{0+\hat{\delta}}$ and t_{0-}

δ where δ is a small number. A curve fit of the t versus CVF dependence (Figure D.2) is used to determine an exact monomer coating thickness for the required CVF .

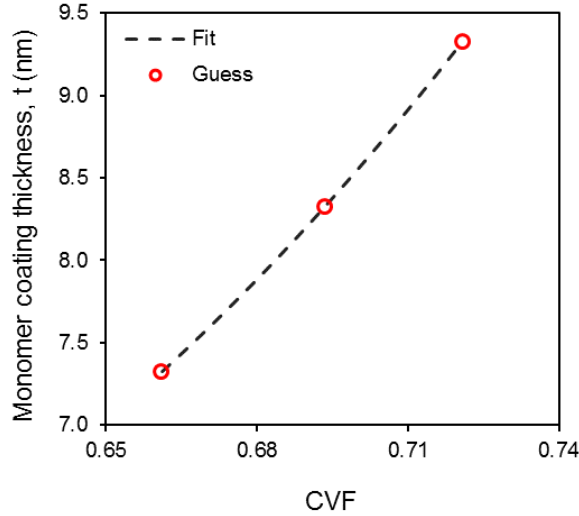


Figure D.2 Monomer coating thickness as a function of coating volume fraction (CVF). The red circles represent estimates of t for $CVF = 0.7$ ($N_s = 40$, $D_f = 1.78$, $k_o = 1.3$, $R_s = 14$ nm).

D.2 Conversion of Coating Volume to Necking Parameter

A similar two-step process is used to determine the necking parameter α for a desired CVF . Based on the method developed by Yon, *et al.* (2015), α determines how much coating is placed in the monomer junctions of the soot aggregate (Figure D.1b). The volume of coating in an average junction, V_j , is determined by sharing the total coating volume $V_{coating}$ between $N_s - 1$ junctions:

$$V_j = \frac{V_{coating}}{N_s - 1} \quad (D.3)$$

The relationship between V_j and α is determined from a coated dimer configuration. The volume of coating dipoles is then calculated via Equation (D.3) for α ranging from 0 (empty junction) to 0.8 (full junction). A curve fit of the data (Figure D.3) produces Equation (D.4) which also accounts for the monomer radius, R_s . This dimer assumption for determining the necking parameter was also discarded for the more rigorous approach described in Section D.3.

$$V_j = (3.88\alpha^2 - 0.634\alpha + 0.0403)R_s^3 \quad (D.4)$$

The above equation is employed as a first order approximation for obtaining α from $V_{coating}$ for any aggregate size. Exact solutions of α for any CVF are determined using the same steps as previously described for obtaining coating thickness in the uniform distribution case.

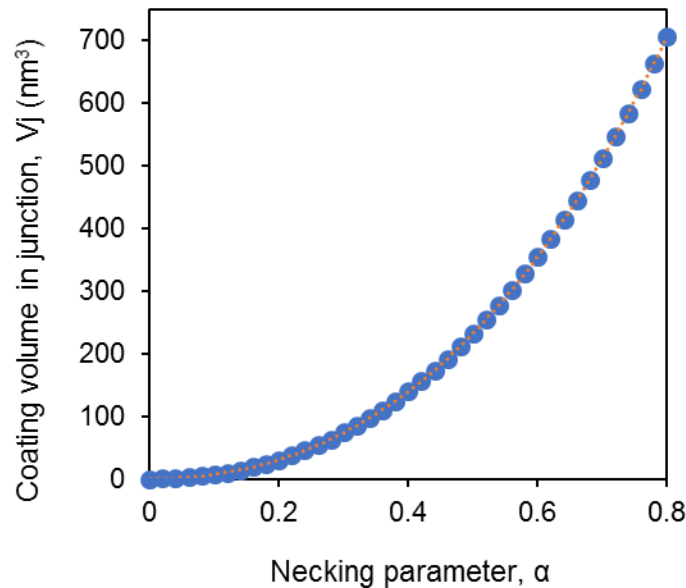


Figure D.3 Relationship between necking parameter and coating volume in monomer junction for a coated dimer.

D.3 Modified Approach for Conversion of Coating Volume to t and α

The methods described in Sections D.1 and D.2 for obtaining coating thickness and necking parameter worked well for fractal aggregates, but not for compact aggregates because of the significant increase in overlapping coating volumes. Thus, an explicit approach is employed for generating coated compact aggregates.

For each simulated compact aggregate, depending on the coating distribution, a predefined range of t or α values are used to calculate CVF by explicitly counting the dipoles in each region of the coated aggregate via Equation (D.2). A spline fit of the data is used to generate a relationship between t (or α) and CVF (Figure D.4). The resulting equation from the fit is used as a first order approximation for obtaining t (or α) from CVF for that specific aggregate. Exact solutions are obtained as previously described in Section D.1.

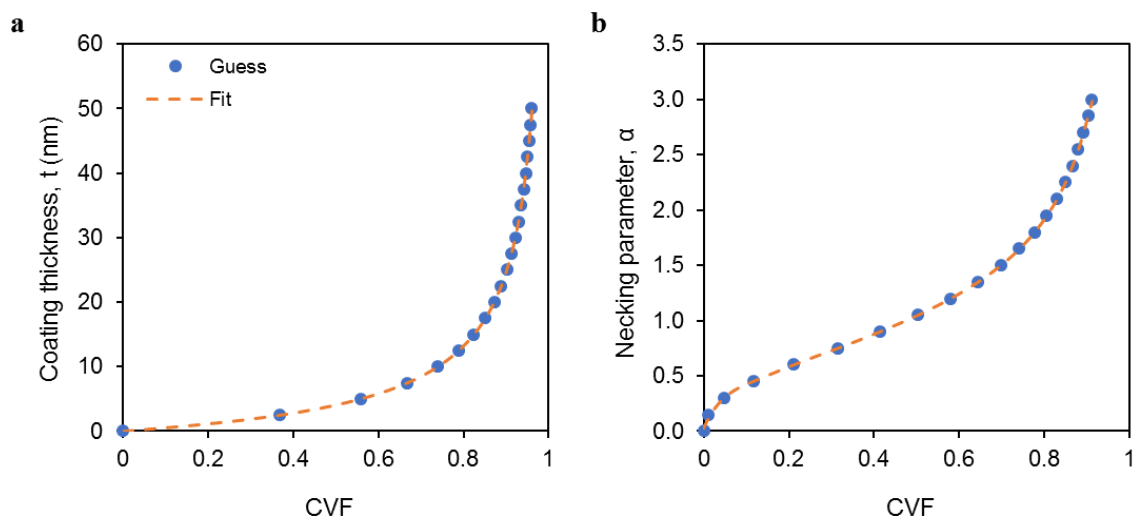


Figure D.4 Monomer coating thickness (a) and necking parameter (b) as a function of coating volume thickness. The blue dots represent calculated estimates of CVF based on predefined t and α values ($N_s = 40$, $D_f = 1.78$, $k_o = 1.3$, $R_s = 14$ nm).

D.4 Conversion of Coating Volume to Shell Thickness for Core-Shell Model

For the core-shell model, the volume equivalent core diameter is given by Equation (8.6) which is copied below from the main text. The shell thickness t_{shell} for any specified CVF can be derived from Equations (D.5) and (D.6):

$$d_{core} = \left(\frac{6V_{soot}}{\pi} \right)^{\frac{1}{3}} \quad (8.6)$$

$$d_{coated\ core} = \left(\frac{6(V_{soot} + V_{coating})}{\pi} \right)^{\frac{1}{3}} \quad (D.5)$$

$$t_{shell} = \frac{1}{2} (d_{coated\ core} - d_{core}) \quad (D.6)$$

D.5 Conversion of Coating Volume to Monomer Coating Thickness for RDG-Mie Model

For the RDG-Mie model, the core diameter is the same as the diameter of the individual monomers in the aggregate (i.e., $d_p = d_{core}$). For any desired CVF , coating volume for a single monomer is the total volume over the number of monomers:

$$V_{mon_shell} = \frac{V_{coating}}{N_s} \quad (D.7)$$

Similar to the core-shell model, coating thickness for each monomer is determined from the equations below:

$$d_{coated\ monomer} = \left(\frac{6(V_{monomer} + V_{mon_shell})}{\pi} \right)^{\frac{1}{3}} \quad (D.8)$$

$$t_{mon_shell} = \frac{1}{2}(d_{coated\ monomer} - d_p) \quad (D.9)$$

where

$$V_{monomer} = \pi d_p^3/6 \quad (D.10)$$

APPENDIX E

SIMULATED OPTICAL PROPERTIES FOR BARE AND COATED SOOT

In this section, calculated optical properties for numerically simulated bare and coated soot aggregates are provided. The results shown here are referenced in Chapter 8 of the main text, but were not included there for brevity.

E.1 Optical Model Comparisons for Bare Soot

The optical properties of uncoated soot aggregates were calculated via the Multiple Sphere T-Matrix (MSTM) method and the results are compared against predictions from other optical models used in this study (see Table E.1). The Discrete Dipole Approximation (DDA) solutions agreed with MSTM, with maximum differences of +2% and +0.3% for absorption and scattering, respectively. The RDG deviated from MSTM by about -11% for absorption and -4% for scattering. For the core-shell approximation, the differences with MSTM were size dependent, with maximum values of +13% and +225% recorded for absorption and scattering, respectively.

Table E.1 Radiative Properties of Uncoated Soot Aggregates Calculated Using Different Optical Models. Fractal dimension D_f is Fixed at 1.78, Scaling Prefactor k_o is Equal to 1.3, Monomer Radius R_s is Equal to 14 nm, and the Incident Wavelength λ is Fixed at 530 nm.

Optical Model	$N_s = 5$ ($d_{core} = 56$ nm)			$N_s = 40$ ($d_{core} = 96$ nm)			$N_s = 120$ ($d_{core} = 138$ nm)		
	$C_{abs} \times 10^4$ (μm^2)	$C_{sca} \times 10^6$ (μm^2)	SSA	$C_{abs} \times 10^3$ (μm^2)	$C_{sca} \times 10^4$ (μm^2)	SSA	$C_{abs} \times 10^2$ (μm^2)	$C_{sca} \times 10^3$ (μm^2)	SSA
MSTM	5.59	8.41	0.015	4.58	2.98	0.061	1.37	1.36	0.090
DDA	5.68	8.43	0.015	4.66	2.99	0.060	1.40	1.36	0.088
RDG	5.06	7.85	0.015	4.04	2.97	0.068	1.21	1.32	0.098
Core-shell	5.26	8.59	0.016	4.79	5.50	0.103	1.55	4.40	0.221

E.2 Configuration Averaging of Bare and Coated Soot

Using aggregate generation algorithms described in Chapter 2, five different realizations were obtained for a given aggregate size, fractal dimension D_f and prefactor k_o . We wanted to know the effect of different realizations of a soot aggregate with identical fractal parameters (D_f , k_o , R_s , N_s) on its orientation-averaged radiative properties determined by DDA. As shown in Table E.2 below, the properties of practical interest for this work (C_{abs} , C_{sca}) exhibited relatively small variation with aggregate realization.

Table E.2 Ensemble Averaged Cross-sections and Relative Standard Deviations (RSD) from Mean for 5 Realizations of Uniformly and Capillary Coated Fractal Aggregates ($N_s = 20$, $D_f = 1.78$, $k_o = 1.3$, $R_s = 14$ nm, $\lambda = 530$ nm).

<i>CVF</i>	Uniform				Capillary			
	$\overline{C_{abs}} \times 10^3$ (μm^2)	% RSD	$\overline{C_{sca}} \times 10^4$ (μm^2)	% RSD	$\overline{C_{abs}} \times 10^3$ (μm^2)	% RSD	$\overline{C_{sca}} \times 10^4$ (μm^2)	% RSD
0	2.33	0.33	1.04	0.39	2.33	0.33	1.04	0.39
0.08	2.39	0.38	1.13	0.41	2.47	0.52	1.17	0.49
0.15	2.44	0.41	1.23	0.43	2.51	0.56	1.28	0.59
0.27	2.53	0.42	1.46	0.45	2.57	0.42	1.52	0.48
0.5	2.69	0.46	2.30	0.25	2.68	0.61	2.40	1.03
0.7	2.87	0.46	4.69	0.46	2.84	0.61	4.97	0.70
0.8	3.04	0.47	9.30	0.86	3.00	0.45	9.98	1.16
0.9	3.40	0.26	30.8	0.69	3.35	0.23	32.2	1.38

E.3 Sensitivity of Optical Properties of Coated Fractal Soot to Variations in Monomer Radius and Incident Wavelength

Absorption and scattering cross-sections from which the $R_{P/U}$ ratios for Figures 8.11 and 8.12 were obtained are provided in Tables E.3 and E.4.

Table E.3 Optical Cross-sections of Uniformly Coated Fractal Aggregates Made of Monomers with Different Radii ($N_s = 40$, $D_f = 1.78$, $k_o = 1.3$, $\lambda = 530$ nm).

Monomer radius (nm)	$CVF = 0.08$		$CVF = 0.7$	
	C_{abs} (μm^2)	C_{sca} (μm^2)	C_{abs} (μm^2)	C_{sca} (μm^2)
3.5	7.07E-05	1.44E-07	7.95E-05	5.89E-07
7	5.83E-04	8.04E-06	6.71E-04	3.34E-05
14	4.78E-03	3.27E-04	5.89E-03	1.40E-03
21	1.65E-02	2.42E-03	2.09E-02	1.02E-02
28	3.90E-02	1.01E-02	5.12E-02	4.02E-02

Table E.4 Optical Cross-sections for Uniformly Coated Fractal Aggregates at Various Wavelengths ($N_s = 40$, $D_f = 1.78$, $k_o = 1.3$, $R_s = 14$ nm).

Wavelength (nm)	$CVF = 0.08$		$CVF = 0.7$	
	C_{abs} (μm^2)	C_{sca} (μm^2)	C_{abs} (μm^2)	C_{sca} (μm^2)
300	1.11E-02	1.92E-03	1.42E-02	6.82E-03
450	6.08E-03	5.47E-04	7.62E-03	2.30E-03
530	4.78E-03	3.27E-04	5.89E-03	1.40E-03
630	3.83E-03	1.91E-04	4.63E-03	8.22E-04
850	2.70E-03	7.29E-05	3.20E-03	3.08E-04

E.4 Optical Data for Coated Fractal and Compact Soot

Optical simulations for coated aggregates with evolving morphology are described in Section 8.6 of the main text. The calculated absorption and scattering cross-sections for the intermediate cases of $D_f = 2.1$ and 2.4 are illustrated in Figure E.1. As the aggregates become more compact, DDA predictions approach the calculated core-shell values.

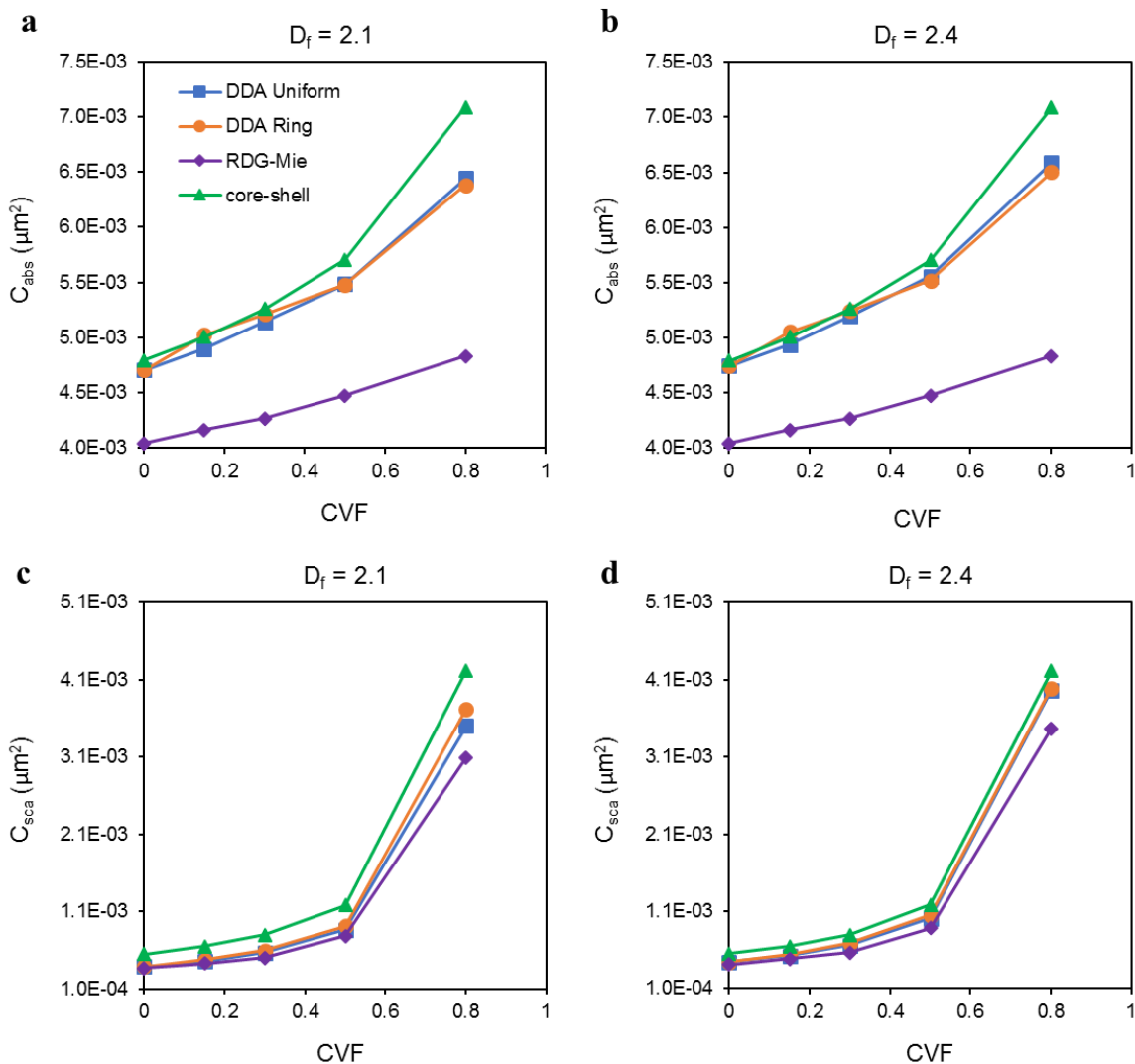


Figure E.1 Cross-sections for light absorption and scattering by coated fractal (a, c) and partially compact (b, d) aggregates comprising 40 monomers at various coating volume fractions, CVF . ($k_o = 1.3$, $R_s = 14$ nm, $\lambda = 530$ nm).

Single scattering albedo for coated fractal and compact aggregates are presented in Figure E.2. The trend is observed is very similar to scattering behavior described in Section 8.6 in the main text. Compaction of the aggregate backbone diminishes the difference in the calculated optical properties between the two coating distributions.

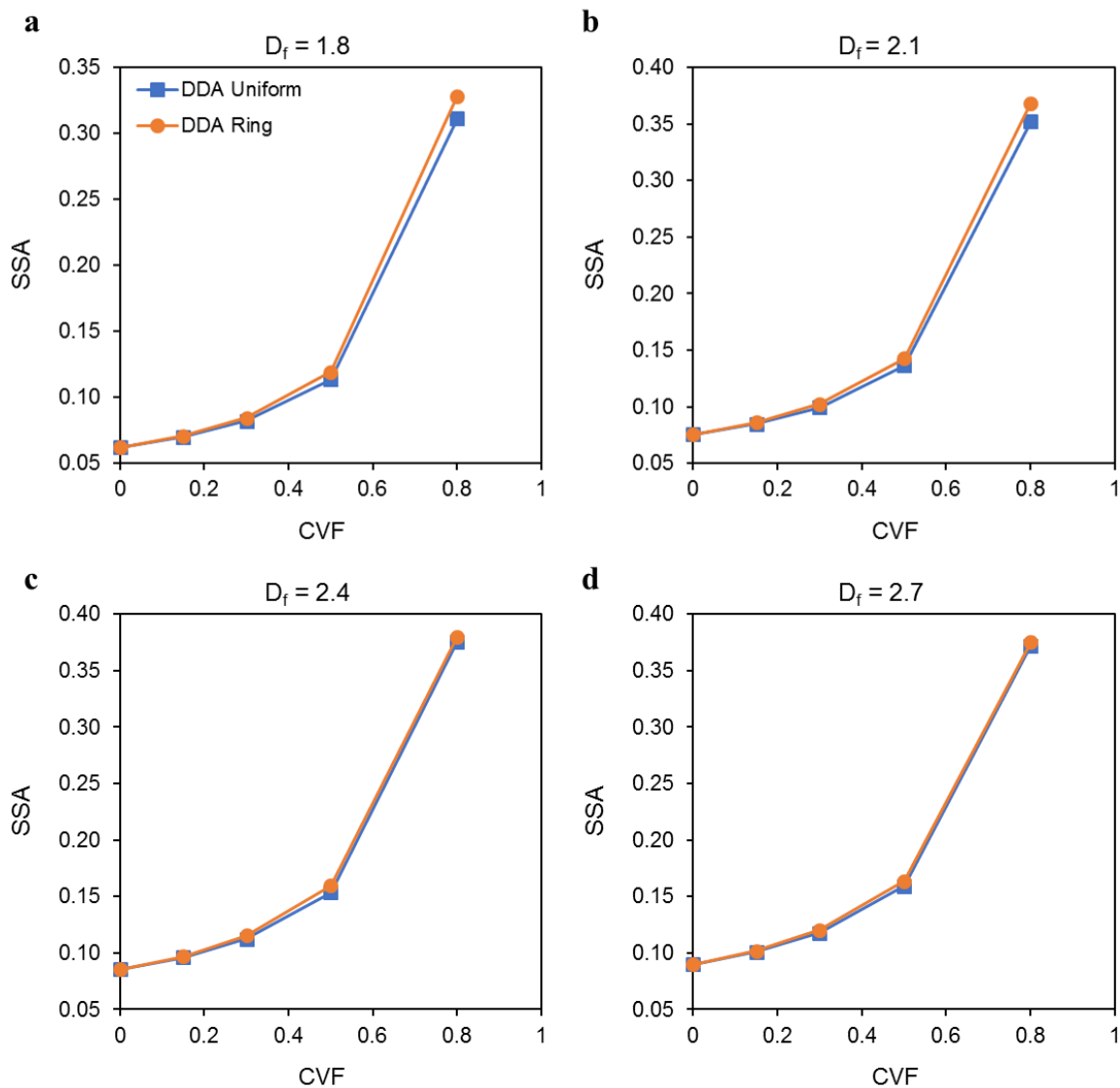


Figure E.2 Dependence of single scattering albedo (SSA) for coated fractal (a, b) and compact (c, d) aggregates comprising 40 monomers on the coating volume fraction ($D_f = 1.78$, $k_o = 1.3$, $R_s = 14$ nm, $\lambda = 530$ nm).

APPENDIX F

PYTHON AND FORTRAN CODES FOR IMPLEMENTING AGGREGATE RESTRUCTURING

The codes used to implement aggregate restructuring in the particle resolved model, PartMC-MOSAIC are provided in this section. The code structure is written in Python. The collapse (pmc_collapse) module implemented in PartMC is written in Fortran.

F.1 Python Code for Aggregate Restructuring

```
# -*- coding: utf-8 -*-

#Code structure for restructuring module in PartMC-MOSAIC
#Based on Chen, C.; Enekwizu, O. Y.; Fan, X.; Dobrzanski, C. D.;
#Ivanova, E. V.; Ma, Y., et al.,
#Single Parameter for Predicting the Morphology of Atmospheric
Black Carbon.
#Environmental Science & Technology 2018, 52, (24), 14169-14179.
#https://doi.org/10.1021/acs.est.8b04201

# Code is designed to trigger instantaneous particle collapse for
# fractal soot containing particles based on calculated
# chi values for condensing species provided by MOSAIC

import numpy as np
import pandas as pd
from sympy import Eq, Symbol, solve, cos

#####

# Required Constants
Rg = 8.3144598 # m3 Pa K-1 mol-1, gas constant
T = 300 # K, temperature
p = 101.325 # Pa, pressure
R_s= 14e-9 #m, monomer radius
rho_EC = 1770 # kg/m3, soot material density
N = 120 # primaries per soot aggregate

#####
```

```

# Functions
def kelvlen(gamma, rho_L, MW): # Kelvin length, Eqn 6
    Vm = MW/rho_L
    return 2.*gamma*Vm/(Rg*T)

def supsat (p, p_sat_0, x_f): # Vapor supersaturation, Eqn 9
    SR = p/(p_sat_0*x_f)
    return SR-1.

def chi (L_K, zeta): # Chi parameter, Eqn 12
    return L_K/(R_s*zeta)

def fillangle (F, Q): # Filling angle, Eqn 14, 24
    x = Symbol ('x', real = True, positive = True)
    eqn = Eq(((2.*cos(x)+1)*(cos(x)-1)**2), F*Q)
    sol = solve (eqn)
    return min(sol)*180/np.pi

#####

# Species Properties
# To be provided by MOSAIC. Use random numbers for test purposes
rho_L = 1000*np.random.uniform(0.1, 1.0, 10)
# kg/m3, densities of species
MW = np.random.random(10)
# kg/mol, molar masses of species
gamma = 0.1*np.random.random(10)
# N/m, surface tensions of species
p_sat_0 = 1000* np.random.random(10)
# Pa, pure sat vap pressures of species
x_f = np.random.random(10)
# mol fraction of species in each particle

#####

# Input array of particle masses containing masses of
# different species. Array contains both aerosol
# and gaseous species. Soot (BC) and condensable species
# need to be identified (SOAs).

Np = 5 # number of particles
A = 10 # number of species
df = pd.DataFrame(np.random.random((Np,A)),

```

```

                columns=['SO4', 'NO3', 'Cl',
'NH4','Na','AR01', 'LIM1', 'OC', 'BC', 'H2O'])
# Check if there is BC contained in each particle
if any (df.loc[df['BC']>0.3]):
    df = df.loc[df['BC']>0.3]
# select particles which contain soot (BC)
    L_K = np.zeros(df.shape)
# initialize array to store kelvin lengths
    zeta = np.zeros(df.shape)
# initialize array to store vap. supersats.
    chi_a = np.zeros(df.shape)
# initialize array to store chis
    for i in range (len(df)):
# loop over each particle
        for j in range(len(df.iloc[i])):
# loop over each species
            L_K = kelvlen(gamma, rho_L, MW)
# calculate kelvin length
            zeta = supsat(p, p_sat_0, x_f)
# calculate vap. supersats.
            chi_a = chi(L_K, zeta)
# calculate chis
            if j in [0,5,6]:
# condensing species (sulphate and SOAs)
                if chi_a[j]<0.65: # if uniform condensation
                    F = 0.1 #bifurcation coefficient
                    Q = df.iloc[i,j]/df.iloc[i,8] *
(2*rho_EC/(N*rho_L))
                    theta = fillangle(F,Q[j])
                    print (i, j, theta)
                if chi_a[j]>0.65: # if capillary condensation
                    F = 1.0 #bifurcation coefficient
                    Q = df.iloc[i,j]/df.iloc[i,8] *
(2*rho_EC/(N*rho_L))
                    theta = fillangle (F, Q[j])
                    print (i, j, theta)
                if theta >= 45.0: # threshold for collapse
                    print (i, j, 'Collapse')
                else:
                    print (i, j, 'Still fractal')

#####

```

F.2 Fortran Code for Particle Collapse Module (pmc_collapse)

```

!> \file
!> The pmc_collapse module.

!> Aerosol particle restructuring.

```

```

!!
module pmc_collapse

    use pmc_constants
    use pmc_env_state
    use pmc_aero_data
    use pmc_aero_state
    use pmc_gas_data
    use pmc_gas_state
    use pmc_mpi
#ifdef PMC_USE_MPI
    use mpi
#endif

contains

!!!!!!!!!!!!!!!!!!!!!!!!!!!!!!!!!!!!!!!!!!!!!!!!!!!!!!!!!!!!!!!!!!!!!!!!!!!!

!> Checks for collapse of fractal black carbon particles based
on coating.
    subroutine collapse(env_state, aero_data, aero_state, gas_data,
gas_state)

    !> Environmental state.
    type(env_state_t), intent(in) :: env_state
    !> Aerosol data.
    type(aero_data_t), intent(in) :: aero_data
    !> Aerosol state.
    type(aero_state_t), intent(inout) :: aero_state
    !> Gas data.
    type(gas_data_t), intent(in) :: gas_data
    !> Gas state.
    type(gas_state_t), intent(in) :: gas_state

    integer :: i_part
    integer :: i_cond_spec
    real(kind=dp), allocatable :: kelvin_length_species(:)
    integer, allocatable :: condensable_gas_index(:)
    integer, allocatable :: condensable_aero_index(:)
    real(kind=dp), allocatable :: surface_tension(:)
    real(kind=dp), allocatable :: vapor_pressure(:)
    integer :: bc_index, i_aero, i_gas
    real(kind=dp) :: F, zeta, chi, x_f, Q

    ! FIXME: Most of these parameters will be specified in input
files
    n_condensable = 2 ! Number of condensing species
    allocate(condensable_gas_index(n_condensable))
    allocate(condensable_aero_index(n_condensable))
    condensable_gas_index(1) = gas_data_spec_by_name(gas_data,
"H2SO4")

```

```

condensable_aero_index(1) = aero_data_spec_by_name(aero_data,
"SO4")
condensable_gas_index(2) = gas_data_spec_by_name(gas_data,
"AR01")
condensable_aero_index(2) = aero_data_spec_by_name(aero_data,
"AR01")
allocate(surface_tension(n_condensable))
surface_tension(1) = 72.0d0 / 1000d0 ! N/m
surface_tension(2) = 72.0d0 / 1000d0 ! N/m

! Compute kelvin length of each species
allocate(vapor_pressure(n_condensable))
allocate(kelvin_length_species(n_condensable))
do i_cond_spec = 1, n_condensable
i_gas = condensable_gas_index(i_cond_spec)
i_aero = condensable_aero_index(i_cond_spec)
kelvin_length_species(i_cond_spec) =
kelvin_length(surface_tension( &
i_cond_spec), aero_data%density(i_aero), &
aero_data%molec_weight(i_aero), env_state%temp)
vapor_pressure(i_cond_spec) = env_state%pressure &
* gas_state%mix_rat(i_gas) / 1d9
end do

bc_index = aero_data_spec_by_name(aero_data, "BC")
do i_part = 1, aero_state_n_part(aero_state)
bc_mass =
aero_particle_species_mass(aero_state%apa%particle( &
i_part), bc_index, aero_data)
if (bc_mass > 0d0) then
do i_cond_spec = 1, n_condensable
i_aero = condensable_aero_index(i_cond_spec)
i_gas = condensable_gas_index(i_cond_spec)
x_f = (aero_state%apa%particle(i_part)%vol(i_aero) *
&
aero_data%density(i_aero) &
/ aero_data%molec_weight(i_aero)) &
/
aero_particle_moles(aero_state%apa%particle(i_part), &
aero_data)
zeta = super_sat(vapor_pressure(i_cond_spec), &
gas_state%sat_vapor_pressure(i_gas), &
x_f)

chi =
coating_distribution(kelvin_length_species(i_cond_spec), &
zeta,
aero_state%apa%particle(i_part)%fractal%prime_radius)
if (chi < 0.6) then ! uniform condensation
F = 0.1d0
else
F = 1.0d0

```

```

        end if
        ! Possible to have particles that are too small
        N = max(fractal_vol_to_num_of_monomers( &
                aero_state%apa%particle(i_part)%fractal, &
aero_state%apa%particle(i_part)%vol(bc_index)),1d0)
        Q =
(aero_particle_species_mass(aero_state%apa%particle( &
                i_part), i_aero, aero_data) / bc_mass) &
        * ((2d0 * aero_data%density(bc_index)) &
        / (N * aero_data%density(i_aero)))
        if (F*Q > 1.0d0) then
            Q = (.99d0 / F)
        end if
        theta = fill_angle(F, Q)
        ! Test for collapse based on filling angle
        if (theta > 45.0d0) then
            aero_state%apa%particle(i_part)%fractal%frac_dim
= 2.8d0
        end if
    end do
end if
end do

end subroutine collapse

```

!!

```

!> Determine characteristic Kelvin length.
!!
!! Based on Equation 6 in Chen et al [2018].
real(kind=dp) function kelvin_length(surface_tension, density,
&
    molec_weight, temperature)

!> Surface tension of species.
real(kind=dp), intent(in) :: surface_tension
!> Density of aerosol species.
real(kind=dp), intent(in) :: density
!> Molecular weight of aerosol species.
real(kind=dp), intent(in) :: molec_weight
!> Temperature (K).
real(kind=dp), intent(in) :: temperature

kelvin_length = (2.0d0 * surface_tension * (molec_weight /
density)) / &
    (const%univ_gas_const * temperature)

end function kelvin_length

```

!!

```

!> Determines the supersaturation of a condensable species.
real(kind=dp) function super_sat(vapor_pressure,
sat_vapor_pressure, &
    mole_fraction)

!> Vapor pressure of species.
real(kind=dp), intent(in) :: vapor_pressure
!> Saturation vapor pressure of species.
real(kind=dp), intent(in) :: sat_vapor_pressure
!> Mole fraction of species.
real(kind=dp), intent(in) :: mole_fraction

    super_sat = (vapor_pressure / (sat_vapor_pressure *
mole_fraction)) - 1d0

end function super_sat

!!!!!!!!!!!!!!!!!!!!!!!!!!!!!!!!!!!!!!!!!!!!!!!!!!!!!!!!!!!!!!!!!!!!!!!!!!!!

!>
!!
!! Based on Equation 12 of Chen et al [2018].
real(kind=dp) function coating_distribution(kelvin_length,
super_sat, &
    prime_radius)

!> Characteristic Kelvin length.
real(kind=dp), intent(in) :: kelvin_length
!> Vapor supersaturation.
real(kind=dp), intent(in) :: super_sat
!> Radius of primary particle.
real(kind=dp), intent(in) :: prime_radius

    coating_distribution = kelvin_length / (prime_radius *
super_sat)

end function coating_distribution

!!!!!!!!!!!!!!!!!!!!!!!!!!!!!!!!!!!!!!!!!!!!!!!!!!!!!!!!!!!!!!!!!!!!!!!!!!!!

!> Solves for fill angle.
!!
!! Based on Equations 14 and 24 of Chen et al [2018].
real(kind=dp) function fill_angle(F_val,Q_val)

!>
real(kind=dp), intent(in) :: F_val
!>
real(kind=dp), intent(in) :: Q_val

real(kind=dp) :: f, df, x
real(kind=dp), parameter :: NEWTON_REL_TOL = 1d-4

```



```

integer, parameter :: NEWTON_MAX_STEPS = 20

! Set initial guess
x = 1.0d0
do newton_step = 1,NEWTON_MAX_STEPS
  f = (2.*cos(x)**3 - 3.0*cos(x)**2 + 1 - F_val *Q_val)
  df = -6.0*cos(x)**2*sin(x) + 3*sin(2*x)
  x = x - f / df
  if (abs(f / df) / (abs(x + f / df) + abs(x)) &
      < NEWTON_REL_TOL) exit
  if (x < .01) exit
  !print*, 'f =', f, 'theta =', x * 180d0 / const%pi
end do

call assert_msg(589404526, newton_step < NEWTON_MAX_STEPS, &
  "collapse Newton loop failed to converge")

fill_angle = x * 180d0 / const%pi

end function fill_angle

!!!!!!!!!!!!!!!!!!!!!!!!!!!!!!!!!!!!!!!!!!!!!!!!!!!!!!!!!!!!!!!!!!!!!!!!!!!!

end module pmc_collapse

```

REFERENCES

1. Ackerman, T. P.; Toon, O. B., Absorption of Visible Radiation in Atmosphere Containing Mixtures of Absorbing and Nonabsorbing Particles. *Applied Optics* **1981**, *20*, (20), 3661-3668. <https://doi.org/10.1364/AO.20.003661>.
2. Adachi, K.; Buseck, P. R., Internally Mixed Soot, Sulfates, and Organic Matter in Aerosol Particles from Mexico City. *Atmospheric Chemistry & Physics* **2008**, *8*, (21), 6469-6481. <https://doi.org/10.5194/acp-8-6469-2008>.
3. Adachi, K.; Chung, S. H.; Buseck, P. R., Shapes of Soot Aerosol Particles and Implications for Their Effects on Climate. *Journal of Geophysical Research: Atmospheres* **2010**, *115*, (D15). <https://doi.org/10.1029/2009JD012868>.
4. Adachi, K.; Chung, S. H.; Friedrich, H.; Buseck, P. R., Fractal Parameters of Individual Soot Particles Determined Using Electron Tomography: Implications for Optical Properties. *Journal of Geophysical Research: Atmospheres* **2007**, *112*, (D14). <https://doi.org/10.1029/2006JD008296>.
5. Andrews, E.; Sheridan, P. J.; Fiebig, M.; McComiskey, A.; Ogren, J. A.; Arnott, P., et al., Comparison of Methods for Deriving Aerosol Asymmetry Parameter. *Journal of Geophysical Research: Atmospheres* **2006**, *111*, (D5). <https://doi.org/10.1029/2004JD005734>.
6. Bademosi, F., Liu, B.Y.H. Diffusion Charging of Knudsen Aerosol - II. Theoretical. University of Minnesota, Minneapolis, MN, 1971.
7. Bambha, R. P.; Dansson, M. A.; Schrader, P. E.; Michelsen, H. A., Effects of Volatile Coatings and Coating Removal Mechanisms on the Morphology of Graphitic Soot. *Carbon* **2013**, *61*, 80-96. <https://doi.org/10.1016/j.carbon.2013.04.070>.
8. Barnes, I.; Solignac, G.; Mellouki, A.; Becker, K. H., Aspects of the Atmospheric Chemistry of Amides. *ChemPhysChem* **2010**, *11*, (18), 3844-3857. <https://doi.org/10.1002/cphc.201000374>.
9. Bhandari, J.; China, S.; Chandrakar, K. K.; Kinney, G.; Cantrell, W.; Shaw, R. A., et al., Extensive Soot Compaction by Cloud Processing from Laboratory and Field Observations. *Scientific Reports* **2019**, *9*, (1), 11824. <https://doi.org/10.1038/s41598-019-48143-y>.
10. Bhandari, J.; China, S.; Onasch, T.; Wolff, L.; Lambe, A.; Davidovits, P., et al., Effect of Thermodenuding on the Structure of Nascent Flame Soot Aggregates. *Atmosphere* **2017**, *8*, (9), 166. <https://doi.org/10.3390/atmos8090166>.

11. Bigg, E. K., Discrepancy between Observation and Prediction of Concentrations of Cloud Condensation Nuclei. *Atmospheric Research* **1986**, *20*, (1), 81-86. [https://doi.org/10.1016/0169-8095\(86\)90010-4](https://doi.org/10.1016/0169-8095(86)90010-4).
12. Boatman, R. J.; Knaak, J. B. (2001). Ethers of Ethylene Glycol and Derivatives. In *Patty's Toxicology* (5th ed.). NY: John Wiley & Sons.
13. Bohren, C. F.; Huffman, D. R. (1983). *Absorption and Scattering of Light by Small Particles*. NY: Wiley-VCH.
14. Bond, T. C.; Bergstrom, R. W., Light Absorption by Carbonaceous Particles: An Investigative Review. *Aerosol Science and Technology* **2006**, *40*, (1), 27-67. <https://doi.org/10.1080/02786820500421521>.
15. Bond, T. C.; Doherty, S. J.; Fahey, D. W.; Forster, P. M.; Berntsen, T.; DeAngelo, B. J., et al., Bounding the Role of Black Carbon in the Climate System: A Scientific Assessment. *Journal of Geophysical Research: Atmospheres* **2013**, *118*, (11), 5380-5552. <https://doi.org/10.1002/jgrd.50171>.
16. Bond, T. C.; Habib, G.; Bergstrom, R. W., Limitations in the Enhancement of Visible Light Absorption Due to Mixing state. *Journal of Geophysical Research: Atmospheres* **2006**, *111*, (D20). <https://doi.org/10.1029/2006JD007315>.
17. Borduas, N.; Abbatt, J. P. D.; Murphy, J. G., Gas Phase Oxidation of Monoethanolamine (MEA) with OH Radical and Ozone: Kinetics, Products, and Particles. *Environmental Science & Technology* **2013**, *47*, (12), 6377-6383. <https://doi.org/10.1021/es401282j>.
18. Browne, E. C.; Franklin, J. P.; Canagaratna, M. R.; Massoli, P.; Kirchstetter, T. W.; Worsnop, D. R., et al., Changes to the Chemical Composition of Soot from Heterogeneous Oxidation Reactions. *The Journal of Physical Chemistry A* **2015**, *119*, (7), 1154-1163. <https://doi.org/10.1021/jp511507d>.
19. Bueno, P. A.; Havey, D. K.; Mulholland, G. W.; Hodges, J. T.; Gillis, K. A.; Dickerson, R. R.; Zachariah, M. R., Photoacoustic Measurements of Amplification of the Absorption Cross Section for Coated Soot Aerosols. *Aerosol Science and Technology* **2011**, *45*, (10), 1217-1230. <https://doi.org/10.1080/02786826.2011.587477>.
20. Bzdek, B. R.; Ridge, D. P.; Johnston, M. V., Amine Exchange into Ammonium Bisulfate and Ammonium Nitrate Nuclei. *Atmospheric Chemistry and Physics* **2010**, *10*, (8), 3495-3503. <https://doi.org/10.5194/acp-10-3495-2010>.

21. Cappa, C. D.; Onasch, T. B.; Massoli, P.; Worsnop, D. R.; Bates, T. S.; Cross, E. S., et al., Radiative Absorption Enhancements Due to the Mixing State of Atmospheric Black Carbon. *Science* **2012**, *337*, (6098), 1078-1081. <https://doi.org/10.1126/science.1223447>.
22. Chakrabarty, R. K.; Garro, M. A.; Chancellor, S.; Herald, C.; Moosmüller, H., FracMAP: A User-Interactive Package for Performing Simulation and Orientation-Specific Morphology Analysis of Fractal-Like Solid Nanoagglomerates. *Computer Physics Communications* **2009**, *180*, (8), 1376-1381. <https://doi.org/10.1016/j.cpc.2009.01.026>.
23. Chakrabarty, R. K.; Moosmüller, H.; Arnott, W. P.; Garro, M. A.; Slowik, J. G.; Cross, E. S., et al., Light Scattering and Absorption by Fractal-Like Carbonaceous Chain Aggregates: Comparison of Theories and Experiment. *Applied Optics* **2007**, *46*, (28), 6990-7006. <https://doi.org/10.1364/AO.46.006990>.
24. Chakrabarty, R. K.; Moosmüller, H.; Arnott, W. P.; Garro, M. A.; Walker, J., Structural and Fractal Properties of Particles Emitted from Spark Ignition Engines. *Environmental Science & Technology* **2006a**, *40*, (21), 6647-6654. <https://doi.org/10.1021/es060537y>.
25. Chakrabarty, R. K.; Moosmüller, H.; Garro, M. A.; Arnott, W. P.; Walker, J.; Susott, R. A., et al., Emissions from the Laboratory Combustion of Wildland Fuels: Particle Morphology and Size. *Journal of Geophysical Research: Atmospheres* **2006b**, *111*, (D7). <https://doi.org/10.1029/2005JD006659>.
26. Chan, L. P.; Chan, C. K., Displacement of Ammonium from Aerosol Particles by Uptake of Triethylamine. *Aerosol Science and Technology* **2012**, *46*, (2), 236-247. <https://doi.org/10.1080/02786826.2011.618815>.
27. Chang, H.-c.; Charalampopoulos, T. T., Determination of the Wavelength Dependence of Refractive Indices of Flame Soot. *Proceedings of the Royal Society of London. Series A: Mathematical and Physical Sciences* **1990**, *430*, (1880), 577-591. <https://doi.org/10.1098/rspa.1990.0107>.
28. Chen, C.; Enekwizu, O. Y.; Fan, X.; Dobrzanski, C. D.; Ivanova, E. V.; Ma, Y., et al., Single Parameter for Predicting the Morphology of Atmospheric Black Carbon. *Environmental Science & Technology* **2018**, *52*, (24), 14169-14179. <https://doi.org/10.1021/acs.est.8b04201>.
29. Chen, C.; Enekwizu, O. Y.; Ma, X.; Jiang, Y.; Khalizov, A. F.; Zheng, J.; Ma, Y., Effect of Organic Coatings Derived from the OH-Initiated Oxidation of Amines on Soot Morphology and Cloud Activation. *Atmospheric Research* **2020**, *239*, 104905. <https://doi.org/10.1016/j.atmosres.2020.104905>.

30. Chen, C.; Enekwizu, O. Y.; Ma, Y.; Zakharov, D.; Khalizov, A. F., The Impact of Sampling Medium and Environment on Particle Morphology. *Atmosphere* **2017**, *8*, (9). <https://doi.org/10.3390/atmos8090162>.
31. Chen, C.; Fan, X.; Shaltout, T.; Qiu, C.; Ma, Y.; Goldman, A.; Khalizov, A. F., An Unexpected Restructuring of Combustion Soot Aggregates by Subnanometer Coatings of Polycyclic Aromatic Hydrocarbons. *Geophysical Research Letters* **2016**, *43*, (20), 11,080-011,088. <https://doi.org/10.1002/2016GL070877>.
32. China, S.; Mazzoleni, C.; Gorkowski, K.; Aiken, A. C.; Dubey, M. K., Morphology and Mixing State of Individual Freshly Emitted Wildfire Carbonaceous Particles. *Nature Communications* **2013**, *4*, (1), 2122. <https://doi.org/10.1038/ncomms3122>.
33. China, S.; Scarnato, B.; Owen, R. C.; Zhang, B.; Ampadu, M. T.; Kumar, S., et al., Morphology and Mixing State of Aged Soot Particles at a Remote Marine Free Troposphere Site: Implications for Optical Properties. *Geophysical Research Letters* **2015**, *42*, (4), 1243-1250. <https://doi.org/10.1002/2014GL062404>.
34. Ching, J.; Fast, J.; West, M.; Riemer, N., Metrics to Quantify the Importance of Mixing State for CCN Activity. *Atmospheric Chemistry & Physics* **2017**, *17*, (12), 7445-7458. <https://doi.org/10.5194/acp-17-7445-2017>.
35. Chýlek, P.; Videen, G.; Ngo, D.; Pinnick, R. G.; Klett, J. D., Effect of Black Carbon on the Optical Properties and Climate Forcing of Sulfate Aerosols. *Journal of Geophysical Research: Atmospheres* **1995**, *100*, (D8), 16325-16332. <https://doi.org/10.1029/95JD01465>.
36. Chylek, P.; Wong, J., Effect of Absorbing Aerosols on Global Radiation Budget. *Geophysical Research Letters* **1995**, *22*, (8), 929-931. <https://doi.org/10.1029/95GL00800>.
37. Coakley, J. A.; Cess, R. D.; Yurevich, F. B., The Effect of Tropospheric Aerosols on the Earth's Radiation Budget: A Parameterization for Climate Models. *Journal of the Atmospheric Sciences* **1983**, *40*, (1), 116-138. [https://doi.org/10.1175/1520-0469\(1983\)040%3C0116:TEOTAO%3E2.0.CO;2](https://doi.org/10.1175/1520-0469(1983)040%3C0116:TEOTAO%3E2.0.CO;2).
38. Coderre, A. R.; Thomson, K. A.; Snelling, D. R.; Johnson, M. R., Spectrally Resolved Light Absorption Properties of Cooled Soot from a Methane Flame. *Applied Physics B* **2011**, *104*, (1), 175-188. <https://doi.org/10.1007/s00340-011-4448-9>.
39. Colbeck, I.; Atkinson, B.; Johar, Y., The Morphology and Optical Properties of Soot Produced by Different Fuels. *Journal of Aerosol Science* **1997**, *28*, (5), 715-723. [https://doi.org/10.1016/S0021-8502\(96\)00466-1](https://doi.org/10.1016/S0021-8502(96)00466-1).

40. Croft, B.; Lohmann, U.; von Salzen, K., Black Carbon Ageing in the Canadian Centre for Climate Modelling and Analysis Atmospheric General Circulation Model. *Atmospheric Chemistry & Physics* **2005**, *5*, (7), 1931-1949.
<https://doi.org/10.5194/acp-5-1931-2005>.
41. Cross, E. S.; Onasch, T. B.; Ahern, A.; Wrobel, W.; Slowik, J. G.; Olfert, J., et al., Soot Particle Studies Instrument Inter-Comparison Project Overview. *Aerosol Science and Technology* **2010**, *44*, (8), 592-611.
<https://doi.org/10.1080/02786826.2010.482113>.
42. Crouzet, Y.; Marlow, W. H., Calculations of the Equilibrium Vapor Pressure of Water over Adhering 50–200-nm Spheres. *Aerosol Science and Technology* **1995**, *22*, (1), 43-59. <https://doi.org/10.1080/02786829408959727>.
43. Cundall, P. A.; Strack, O. D. L., A Discrete Numerical Model for Granular Assemblies. *Géotechnique* **1979**, *29*, (1), 47-65.
<https://doi.org/10.1680/geot.1979.29.1.47>.
44. Daubert, T. E.; Danner, R. P. (1989). *Physical and Thermodynamic Properties of Pure Chemicals : Data Compilation*. Washington, DC: Taylor & Francis.
45. Davis, E. J.; Ray, A. K., Submicron Droplet Evaporation in the Continuum and Non-Continuum Regimes. *Journal of Aerosol Science* **1978**, *9*, (5), 411-422.
[https://doi.org/10.1016/0021-8502\(78\)90003-4](https://doi.org/10.1016/0021-8502(78)90003-4).
46. DeCarlo, P. F.; Slowik, J. G.; Worsnop, D. R.; Davidovits, P.; Jimenez, J. L., Particle Morphology and Density Characterization by Combined Mobility and Aerodynamic Diameter Measurements. Part 1: Theory. *Aerosol Science and Technology* **2004**, *38*, (12), 1185-1205.
<https://doi.org/10.1080/027868290903907>.
47. Decesari, S.; Facchini, M. C.; Matta, E.; Mircea, M.; Fuzzi, S.; Chughtai, A. R.; Smith, D. M., Water Soluble Organic Compounds Formed by Oxidation of Soot. *Atmospheric Environment* **2002**, *36*, (11), 1827-1832.
[https://doi.org/10.1016/S1352-2310\(02\)00141-3](https://doi.org/10.1016/S1352-2310(02)00141-3).
48. DeMott, P. J.; Chen, Y.; Kreidenweis, S. M.; Rogers, D. C.; Sherman, D. E., Ice Formation by Black Carbon Particles. *Geophysical Research Letters* **1999**, *26*, (16), 2429-2432. <https://doi.org/10.1029/1999GL900580>.
49. Dixkens, J.; Fissan, H., Development of an Electrostatic Precipitator for Off-Line Particle Analysis. *Aerosol Science and Technology* **1999**, *30*, (5), 438-453.
<https://doi.org/10.1080/027868299304480>.

50. Dobbins, R. A.; Megaridis, C. M., Morphology of Flame-Generated Soot as Determined by Thermophoretic Sampling. *Langmuir* **1987**, *3*, (2), 254-259. <https://doi.org/10.1021/la00074a019>.
51. Donahue, N. M.; Trump, E. R.; Pierce, J. R.; Riipinen, I., Theoretical Constraints on Pure Vapor-Pressure Driven Condensation of Organics to Ultrafine Particles. *Geophysical Research Letters* **2011**, *38*, (16), L16801. <https://doi.org/10.1029/2011GL048115>.
52. Dong, J.; Zhao, J. M.; Liu, L. H., Morphological Effects on the Radiative Properties of Soot Aerosols in Different Internally Mixing States with Sulfate. *Journal of Quantitative Spectroscopy and Radiative Transfer* **2015**, *165*, 43-55. <https://doi.org/10.1016/j.jqsrt.2015.06.025>.
53. Draine, B. T.; Flatau, P. J., Discrete-Dipole Approximation For Scattering Calculations. *Journal of the Optical Society of America A* **1994**, *11*, (4), 1491-1499. <https://doi.org/10.1364/JOSAA.11.001491>.
54. Dusek, U.; Frank, G. P.; Hildebrandt, L.; Curtius, J.; Schneider, J.; Walter, S., et al., Size Matters More Than Chemistry for Cloud-Nucleating Ability of Aerosol Particles. *Science* **2006a**, *312*, (5778), 1375-1378. <https://doi.org/10.1126/science.1125261>.
55. Dusek, U.; Reischl, G. P.; Hitzenberger, R., CCN Activation of Pure and Coated Carbon Black Particles. *Environmental Science & Technology* **2006b**, *40*, (4), 1223-1230. <https://doi.org/10.1021/es0503478>.
56. Engelhart, G. J.; Moore, R. H.; Nenes, A.; Pandis, S. N., Cloud Condensation Nuclei Activity of Isoprene Secondary Organic Aerosol. *Journal of Geophysical Research: Atmospheres* **2011**, *116*, (D2). <https://doi.org/10.1029/2010JD014706>.
57. Felder, J. D.; Adams, W. J.; Saeger, V. W., Assessment of the Safety of Dioctyl Adipate in Freshwater Environments. *Environmental Toxicology and Chemistry* **1986**, *5*, (8), 777-784. <https://doi.org/10.1002/etc.5620050809>.
58. Feng, Y.; Ramanathan, V.; Kotamarthi, V. R., Brown Carbon: A Significant Atmospheric Absorber of Solar Radiation? *Atmospheric Chemistry & Physics* **2013**, *13*, (17), 8607-8621. <https://doi.org/10.5194/acp-13-8607-2013>.
59. Fierce, L.; Bond, T. C.; Bauer, S. E.; Mena, F.; Riemer, N., Black Carbon Absorption at the Global Scale is Affected by Particle-Scale Diversity in Composition. *Nature Communications* **2016**, *7*, (1), 12361. <https://doi.org/10.1038/ncomms12361>.

60. Filippov, A. V.; Zurita, M.; Rosner, D. E., Fractal-like Aggregates: Relation between Morphology and Physical Properties. *Journal of Colloid and Interface Science* **2000**, *229*, (1), 261-273. <https://doi.org/10.1006/jcis.2000.7027>.
61. Finlayson-Pitts, B. J.; Pitts, J. N. (2000). *Chemistry of the Upper and Lower Atmosphere: Theory, Experiments, and Applications*. San Diego, CA: Academic Press.
62. Flick, E. W. (1998). *Industrial Solvents Handbook* (5th ed.). Westwood, NJ: Noyes Data Corporation.
63. Forestieri, S. D.; Helgestad, T. M.; Lambe, A. T.; Renbaum-Wolff, L.; Lack, D. A.; Massoli, P., et al., Measurement and Modeling of the Multiwavelength Optical Properties of Uncoated Flame-Generated Soot. *Atmospheric Chemistry & Physics* **2018**, *18*, (16), 12141-12159. <https://doi.org/10.5194/acp-18-12141-2018>.
64. Fuller, E. N.; Schettler, P. D.; Giddings, J. C., A New Method for Prediction of Binary Gas-Phase Diffusion Coefficients. *Industrial and Engineering Chemistry* **1966**, *58*, (5), 18-27. <https://doi.org/10.1021/ie50677a007>.
65. Fuller, K. A., Scattering and Absorption Cross-Sections of Compounded Spheres. II. Calculations for External Aggregation. *Journal of the Optical Society of America A* **1995**, *12*, (5), 881-892. <https://doi.org/10.1364/JOSAA.12.000881>.
66. Fuller, K. A.; Malm, W. C.; Kreidenweis, S. M., Effects of Mixing on Extinction by Carbonaceous Particles. *Journal of Geophysical Research-Atmospheres* **1999**, *104*, (D13), 15941-15954. <https://doi.org/10.1029/1998JD100069>.
67. Gac, J.; Sosnowski, T. R.; Gradoń, L., Turbulent Flow Energy for Aerosolization of Powder Particles. *Journal of Aerosol Science* **2008**, *39*, (2), 113-126. <https://doi.org/10.1016/j.jaerosci.2007.10.006>.
68. Gao, C.; Bhushan, B., Tribological Performance of Magnetic Thin-Film Glass Disks: Its Relation to Surface Roughness and Lubricant Structure and Its Thickness. *Wear* **1995**, *190*, (1), 60-75. [https://doi.org/10.1016/0043-1648\(95\)06648-9](https://doi.org/10.1016/0043-1648(95)06648-9).
69. Ge, X.; Wexler, A. S.; Clegg, S. L., Atmospheric Amines - Part I. A Review. *Atmospheric Environment* **2011**, *45*, (3), 524-546. <https://doi.org/10.1016/j.atmosenv.2010.10.012>.
70. Ge, Y.; Liu, Y.; Chu, B.; He, H.; Chen, T.; Wang, S. X., et al., Ozonolysis of Trimethylamine Exchanged with Typical Ammonium Salts in the Particle Phase. *Environmental Science & Technology* **2016**, *50*, (20), 11076-11084. <https://doi.org/10.1021/acs.est.6b04375>.

71. Ghazi, R.; Olfert, J. S., Coating Mass Dependence of Soot Aggregate Restructuring due to Coatings of Oleic Acid and Dioctyl Sebacate. *Aerosol Science and Technology* **2013**, *47*, (2), 192-200. <https://doi.org/10.1080/02786826.2012.741273>.
72. Ghazi, R.; Tjong, H.; Soewono, A.; Rogak, S. N.; Olfert, J. S., Mass, Mobility, Volatility, and Morphology of Soot Particles Generated by a McKenna and Inverted Burner. *Aerosol Science and Technology* **2013**, *47*, (4), 395-405. <https://doi.org/10.1080/02786826.2012.755259>.
73. Grzybowski, K., Modeling of the Re-Entrainment of Particles from Powder Structures. *Advanced Powder Technology* **2005**, *16*, (2), 105-121. <https://doi.org/10.1163/1568552053621696>.
74. Guo, S.; Hu, M.; Lin, Y.; Gomez-Hernandez, M.; Zamora, M. L.; Peng, J., et al., OH-Initiated Oxidation of m-Xylene on Black Carbon Aging. *Environmental Science & Technology* **2016**, *50*, (16), 8605-8612. <https://doi.org/10.1021/acs.est.6b01272>.
75. Hallquist, M.; Wenger, J. C.; Baltensperger, U.; Rudich, Y.; Simpson, D.; Claeys, M., et al., The Formation, Properties and Impact of Secondary Organic Aerosol: Current and Emerging Issues. *Atmospheric Chemistry & Physics* **2009**, *9*, (14), 5155-5236. <https://doi.org/10.5194/acp-9-5155-2009>.
76. Hansen, J.; Nazarenko, L., Soot Climate Forcing Via Snow and Ice Albedos. *Proceedings of the National Academy of Sciences of the United States of America* **2004**, *101*, (2), 423. <https://doi.org/10.1073/pnas.2237157100>.
77. Hanson, D. R.; Eisele, F., Diffusion of H₂SO₄ in Humidified Nitrogen: Hydrated H₂SO₄. *Journal of Physical Chemistry A* **2000**, *104*, (8), 1715-1719. <https://doi.org/10.1021/jp993622j>.
78. Haynes, W. M. (2014). *CRC Handbook of Chemistry and Physics* (95th ed ed.). Hoboken, NJ: CRC Press.
79. Haywood, J.; Boucher, O., Estimates of the Direct and Indirect Radiative Forcing Due to Tropospheric Aerosols: A Review. *Reviews of Geophysics* **2000**, *38*, (4), 513-543. <https://doi.org/10.1029/1999RG000078>.
80. He, C.; Liou, K. N.; Takano, Y.; Zhang, R.; Levy Zamora, M.; Yang, P., et al., Variation of the Radiative Properties During Black Carbon Aging: Theoretical and Experimental Intercomparison. *Atmospheric Chemistry & Physics* **2015**, *15*, (20), 11967-11980. <https://doi.org/10.5194/acp-15-11967-2015>.

81. Heinson, W. R.; Liu, P.; Chakrabarty, R. K., Fractal Scaling of Coated Soot Aggregates. *Aerosol Science and Technology* **2017**, *51*, (1), 12-19. <https://doi.org/10.1080/02786826.2016.1249786>.
82. Hinckley, D. A.; Bidleman, T. F.; Foreman, W. T.; Tuschall, J. R., Determination of Vapor Pressures for Nonpolar and Semipolar Organic Compounds from Gas Chromatographic Retention Data. *Journal of Chemical & Engineering Data* **1990**, *35*, (3), 232-237. <https://doi.org/10.1021/jc00061a003>.
83. Hinds, W. C. (1999). *Aerosol Technology : Properties, Behavior, and Measurement of Airborne Particles* (2nd ed.). NY: John Wiley & Sons.
84. Huang, Y.; Su, C.; Yang, Y.; Lu, M., Degradation of Aniline Catalyzed by Heterogeneous Fenton-Like Reaction Using Iron Oxide/SiO₂. *Environmental Progress & Sustainable Energy* **2013**, *32*, (2), 187-192. <https://doi.org/10.1002/ep.10630>.
85. Hughes, M.; Kodros, J.; Pierce, J.; West, M.; Riemer, N., Machine Learning to Predict the Global Distribution of Aerosol Mixing State Metrics. *Atmosphere* **2018**, *9*, (1), 15. <https://doi.org/10.3390/atmos9010015>.
86. Jacobson, M. Z., A Physically-Based Treatment of Elemental Carbon Optics: Implications for Global Direct Forcing of Aerosols. *Geophysical Research Letters* **2000**, *27*, (2), 217-220. <https://doi.org/10.1029/1999GL010968>.
87. Jacobson, M. Z., Global Direct Radiative Forcing Due to Multicomponent Anthropogenic and Natural Aerosols. *Journal of Geophysical Research: Atmospheres* **2001a**, *106*, (D2), 1551-1568. <https://doi.org/10.1029/2000JD900514>.
88. Jacobson, M. Z., Strong Radiative Heating Due to the Mixing State of Black Carbon in Atmospheric Aerosols. *Nature* **2001b**, *409*, (6821), 695-697. <https://doi.org/10.1038/35055518>.
89. Jacobson, M. Z. (2012). *Air Pollution and Global Warming: History, Science, and Solutions* (2nd ed.). Cambridge, UK: Cambridge University Press.
90. Jacobson, M. Z.; Seinfeld, J. H., Evolution of Nanoparticle Size and Mixing State Near the Point of Emission. *Atmospheric Environment* **2004**, *38*, (13), 1839-1850. <https://doi.org/10.1016/j.atmosenv.2004.01.014>.
91. Jasper, J. J., The Surface Tension of Pure Liquid Compounds. *Journal of Physical and Chemical Reference Data* **1972**, *1*, (4), 841-1010. <https://doi.org/10.1063/1.3253106>.

92. Jimenez, J. L.; Canagaratna, M. R.; Donahue, N. M.; Prevot, A. S. H.; Zhang, Q.; Kroll, J. H., et al., Evolution of Organic Aerosols in the Atmosphere. *Science* **2009**, 326, (5959), 1525-1529. <https://doi.org/10.1126/science.1180353>.
93. Johnson, K. L.; Kendall, K.; Roberts, A. D.; Tabor, D., Surface Energy and the Contact of Elastic Solids. *Proceedings of the Royal Society of London. A. Mathematical and Physical Sciences* **1971**, 324, (1558), 301-313. <https://doi.org/10.1098/rspa.1971.0141>.
94. Kahnert, M., Modelling the Optical and Radiative Properties of Freshly Emitted Light Absorbing Carbon within an Atmospheric Chemical Transport Model. *Atmospheric Chemistry & Physics* **2010a**, 10, (3), 1403-1416. <https://doi.org/10.5194/acp-10-1403-2010>.
95. Kahnert, M., Numerically Exact Computation of the Optical Properties of Light Absorbing Carbon Aggregates for Wavelength of 200 nm–12.2 μm . *Atmospheric Chemistry and Physics* **2010b**, 10, (17), 8319-8329. <https://doi.org/10.5194/acp-10-8319-2010>.
96. Kahnert, M., On the Discrepancy between Modeled and Measured Mass Absorption Cross Sections of Light Absorbing Carbon Aerosols. *Aerosol Science and Technology* **2010c**, 44, (6), 453-460. <https://doi.org/10.1080/02786821003733834>.
97. Kahnert, M.; Devasthale, A., Black Carbon Fractal Morphology and Short-Wave Radiative Impact: A Modelling Study. *Atmospheric Chemistry & Physics* **2011**, 11, (22), 11745-11759. <https://doi.org/10.5194/acp-11-11745-2011>.
98. Kahnert, M.; Kanngießer, F., Modelling Optical Properties of Atmospheric Black Carbon Aerosols. *Journal of Quantitative Spectroscopy and Radiative Transfer* **2020**, 244, 106849. <https://doi.org/10.1016/j.jqsrt.2020.106849>.
99. Kahnert, M.; Nousiainen, T.; Lindqvist, H., Models for Integrated and Differential Scattering Optical Properties of Encapsulated Light Absorbing Carbon Aggregates. *Optics Express* **2013**, 21, (7), 7974-7993. <https://doi.org/10.1364/OE.21.007974>.
100. Kahnert, M.; Nousiainen, T.; Lindqvist, H.; Ebert, M., Optical Properties of Light Absorbing Carbon Aggregates Mixed with Sulfate: Assessment of Different Model Geometries for Climate Forcing Calculations. *Optics Express* **2012**, 20, (9), 10042-10058. <https://doi.org/10.1364/OE.20.010042>.
101. Kamm, S.; Möhler, O.; Naumann, K. H.; Saathoff, H.; Schurath, U., The Heterogeneous Reaction of Ozone with Soot Aerosol. *Atmospheric Environment* **1999**, 33, (28), 4651-4661. [https://doi.org/10.1016/S1352-2310\(99\)00235-6](https://doi.org/10.1016/S1352-2310(99)00235-6).

102. Khalizov, A. F.; Cruz-Quinones, M.; Zhang, R., Heterogeneous Reaction of NO₂ on Fresh and Coated Soot Surfaces. *The Journal of Physical Chemistry A* **2010**, *114*, (28), 7516-7524. <https://doi.org/10.1021/jp1021938>.
103. Khalizov, A. F.; Lin, Y.; Qiu, C.; Guo, S.; Collins, D.; Zhang, R., Role of OH-Initiated Oxidation of Isoprene in Aging of Combustion Soot. *Environmental Science & Technology* **2013**, *47*, (5), 2254-2263. <https://doi.org/10.1021/es3045339>.
104. Khalizov, A. F.; Xue, H.; Wang, L.; Zheng, J.; Zhang, R., Enhanced Light Absorption and Scattering by Carbon Soot Aerosol Internally Mixed with Sulfuric Acid. *Journal of Physical Chemistry A* **2009a**, *113*, (6), 1066-1074. <https://doi.org/10.1021/jp807531n>.
105. Khalizov, A. F.; Zhang, R.; Zhang, D.; Xue, H.; Pagels, J.; McMurry, P. H., Formation of Highly Hygroscopic Soot Aerosols Upon Internal Mixing with Sulfuric Acid Vapor. *Journal of Geophysical Research: Atmospheres* **2009b**, *114*, (D5). <https://doi.org/10.1029/2008JD010595>.
106. Khlebtsov, N. G., Orientational Averaging of Light-Scattering Observables in the T-Matrix Approach. *Applied Optics* **1992**, *31*, (25), 5359-5365. <https://doi.org/10.1364/AO.31.005359>.
107. Knox, A.; Evans, G. J.; Brook, J. R.; Yao, X.; Jeong, C. H.; Godri, K. J., et al., Mass Absorption Cross-Section of Ambient Black Carbon Aerosol in Relation to Chemical Age. *Aerosol Science and Technology* **2009**, *43*, (6), 522-532. <https://doi.org/10.1080/02786820902777207>.
108. Koch, D., Transport and Direct Radiative Forcing of Carbonaceous and Sulfate Aerosols in the GISS GCM. *Journal of Geophysical Research: Atmospheres* **2001**, *106*, (D17), 20311-20332. <https://doi.org/10.1029/2001JD900038>.
109. Kolb, M.; Botet, R.; Jullien, R., Scaling of Kinetically Growing Clusters. *Physical Review Letters* **1983**, *51*, (13), 1123-1126. <https://doi.org/10.1103/PhysRevLett.51.1123>.
110. Korosi, G.; Kovats, E. S., Density and Surface Tension of 83 Organic Liquids. *Journal of Chemical & Engineering Data* **1981**, *26*, (3), 323-332. <https://doi.org/10.1021/jc00025a032>.
111. Kousaka, Y.; Endo, Y.; Alonso, M.; Ichitsubo, H.; Fukui, A., Nanometer Coating on Aerosol Particles. *Advanced Powder Technology* **1995**, *6*, (1), 11-24. [https://doi.org/10.1016/S0921-8831\(08\)60544-0](https://doi.org/10.1016/S0921-8831(08)60544-0).

112. Köylü, Ü. Ö.; Faeth, G. M.; Farias, T. L.; Carvalho, M. G., Fractal and Projected Structure Properties of Soot Aggregates. *Combustion and Flame* **1995**, *100*, (4), 621-633. [https://doi.org/10.1016/0010-2180\(94\)00147-K](https://doi.org/10.1016/0010-2180(94)00147-K).
113. Kroll, J. H.; Donahue, N. M.; Jimenez, J. L.; Kessler, S. H.; Canagaratna, M. R.; Wilson, K. R., et al., Carbon Oxidation State as a Metric for Describing the Chemistry of Atmospheric Organic Aerosol. *Nature Chemistry* **2011**, *3*, (2), 133-139. <https://doi.org/10.1038/nchem.948>.
114. Kütz, S.; Schmidt-Ott, A., Characterization of Agglomerates by Condensation-Induced Restructuring. *Journal of Aerosol Science* **1992**, *23*, 357-360. [https://doi.org/10.1016/0021-8502\(92\)90423-S](https://doi.org/10.1016/0021-8502(92)90423-S).
115. Lee, S.; Jang, M.; Kamens, R. M., SOA Formation from the Photooxidation of α -Pinene in the Presence of Freshly Emitted Diesel Soot Exhaust. *Atmospheric Environment* **2004**, *38*, (16), 2597-2605. <https://doi.org/10.1016/j.atmosenv.2003.12.041>.
116. Leung, K. K.; Schnitzler, E. G.; Dastanpour, R.; Rogak, S. N.; Jäger, W.; Olfert, J. S., Relationship between Coating-Induced Soot Aggregate Restructuring and Primary Particle Number. *Environmental Science & Technology* **2017a**, *51*, (15), 8376-8383. <https://doi.org/10.1021/acs.est.7b01140>.
117. Leung, K. K.; Schnitzler, E. G.; Jaeger, W.; Olfert, J. S., Relative Humidity Dependence of Soot Aggregate Restructuring Induced by Secondary Organic Aerosol: Effects of Water on Coating Viscosity and Surface Tension. *Environmental Science & Technology Letters* **2017b**, *4*, (9), 386-390. <https://doi.org/10.1021/acs.estlett.7b00298>.
118. Li, H.; Liu, C.; Bi, L.; Yang, P.; Kattawar, G. W., Numerical Accuracy of “Equivalent” Spherical Approximations for Computing Ensemble-Averaged Scattering Properties of Fractal Soot Aggregates. *Journal of Quantitative Spectroscopy and Radiative Transfer* **2010**, *111*, (14), 2127-2132. <https://doi.org/10.1016/j.jqsrt.2010.05.009>.
119. Li, K.; Chen, L.; Han, K.; Lv, B.; Bao, K.; Wu, X., et al., Smog Chamber Study on Aging of Combustion Soot in Isoprene/SO₂/NO_x System: Changes of Mass, Size, Effective Density, Morphology and Mixing State. *Atmospheric Research* **2017**, *184*, 139-148. <https://doi.org/10.1016/j.atmosres.2016.10.011>.
120. Liu, C.; Teng, S.; Zhu, Y.; Yurkin, M. A.; Yung, Y. L., Performance of the Discrete Dipole Approximation for Optical Properties of Black Carbon Aggregates. *Journal of Quantitative Spectroscopy and Radiative Transfer* **2018**, *221*, 98-109. <https://doi.org/10.1016/j.jqsrt.2018.09.030>.

121. Liu, D.; Whitehead, J.; Alfarra, M. R.; Reyes-Villegas, E.; Spracklen, D. V.; Reddington, C. L., et al., Black-Carbon Absorption Enhancement in the Atmosphere Determined by Particle Mixing State. *Nature Geoscience* **2017**, *10*, (3), 184-188. <https://doi.org/10.1038/ngeo2901>.
122. Liu, F.; Yon, J.; Bescond, A., On the Radiative Properties of Soot Aggregates – Part 2: Effects of Coating. *Journal of Quantitative Spectroscopy and Radiative Transfer* **2016**, *172*, 134-145. <https://doi.org/10.1016/j.jqsrt.2015.08.005>.
123. Liu, L.; Mishchenko, M. I., Effects of Aggregation on Scattering and Radiative Properties of Soot Aerosols. *Journal of Geophysical Research: Atmospheres* **2005**, *110*, (D11), n/a-n/a. <https://doi.org/10.1029/2004JD005649>.
124. Liu, L.; Mishchenko, M. I., Scattering and Radiative Properties of Complex Soot and Soot-Containing Aggregate Particles. *Journal of Quantitative Spectroscopy and Radiative Transfer* **2007**, *106*, (1), 262-273. <https://doi.org/10.1016/j.jqsrt.2007.01.020>.
125. Liu, L.; Mishchenko, M. I., Scattering and Radiative Properties of Morphologically Complex Carbonaceous Aerosols: A Systematic Modeling Study. *Remote Sensing* **2018**, *10*, (10), 1634. <https://doi.org/10.3390/rs10101634>.
126. Liu, L.; Mishchenko, M. I.; Patrick Arnott, W., A Study of Radiative Properties of Fractal soot Aggregates Using the Superposition T-Matrix method. *Journal of Quantitative Spectroscopy and Radiative Transfer* **2008**, *109*, (15), 2656-2663. <https://doi.org/10.1016/j.jqsrt.2008.05.001>.
127. Liu, S.; Aiken, A. C.; Gorkowski, K.; Dubey, M. K.; Cappa, C. D.; Williams, L. R., et al., Enhanced Light Absorption by Mixed Source Black and Brown Carbon Particles in UK Winter. *Nature Communications* **2015**, *6*, 8435. <https://doi.org/10.1038/ncomms9435>.
128. Lohmann, U.; Feichter, J., Global Indirect Aerosol Effects: A Review. *Atmospheric Chemistry & Physics* **2005**, *5*, (3), 715-737. <https://doi.org/10.5194/acp-5-715-2005>.
129. Lu, Z.; Hao, J.; Hu, L.; Takekawa, H., The Compaction of Soot Particles Generated by Spark Discharge in the Propene Ozonolysis System. *Journal of Aerosol Science* **2008**, *39*, (10), 897-903. <https://doi.org/10.1016/j.jaerosci.2008.06.001>.
130. Luo, J.; Zhang, Y.; Wang, F.; Zhang, Q., Effects of Brown Coatings on the Absorption Enhancement of Black Carbon: A Numerical Investigation. *Atmospheric Chemistry & Physics* **2018**, *18*, (23), 16897-16914. <https://doi.org/10.5194/acp-18-16897-2018>.

131. Ma, X.; Zangmeister, C. D.; Gigault, J.; Mulholland, G. W.; Zachariah, M. R., Soot Aggregate Restructuring During Water Processing. *Journal of Aerosol Science* **2013a**, *66*, 209-219. <https://doi.org/10.1016/j.jaerosci.2013.08.001>.
132. Ma, Y.; Brooks, S. D.; Vidaurre, G.; Khalizov, A. F.; Wang, L.; Zhang, R., Rapid Modification of Cloud-Nucleating Ability of Aerosols by Biogenic Emissions. *Geophysical Research Letters* **2013b**, *40*, (23), 6293-6297. <https://doi.org/10.1002/2013GL057895>.
133. Mackowski, D. W., Electrostatics Analysis of Radiative Absorption by Sphere Clusters in the Rayleigh Limit: Application to Soot Particles. *Applied Optics* **1995**, *34*, (18), 3535-3545. <https://doi.org/10.1364/AO.34.003535>.
134. Mackowski, D. W.; Mishchenko, M. I., A Multiple Sphere T-Matrix Fortran Code for Use on Parallel Computer Clusters. *Journal of Quantitative Spectroscopy and Radiative Transfer* **2011**, *112*, (13), 2182-2192. <https://doi.org/10.1016/j.jqsrt.2011.02.019>.
135. Mätzler, C. *MATLAB Functions for Mie Scattering and Absorption*; Institut für Angewandte Physik, Research Report No. 2002-08: 2002.
136. Maugis, D., Adherence of Elastomers: Fracture Mechanics Aspects. *Journal of Adhesion Science and Technology* **1987**, *1*, (1), 105-134. <https://doi.org/10.1163/156856187X00120>.
137. Meakin, P., Formation of Fractal Clusters and Networks by Irreversible Diffusion-Limited Aggregation. *Physical Review Letters* **1983**, *51*, (13), 1119-1122. <https://doi.org/10.1103/PhysRevLett.51.1119>.
138. Megaridis, C. M.; Dobbins, R. A., Morphological Description of Flame-Generated Materials. *Combustion Science and Technology* **1990**, *71*, (1-3), 95-109. <https://doi.org/10.1080/00102209008951626>.
139. Mikhailov, E. F.; Vlasenko, S. S.; Kiselev, A. A.; Ryshkevich, T. I., Restructuring Factors of Soot Particles. *Izvestiya Atmospheric and Oceanic Physics* **1998**, *34*, 307-317.
140. Mikhailov, E. F.; Vlasenko, S. S.; Podgorny, I. A.; Ramanathan, V.; Corrigan, C. E., Optical Properties of Soot-Water Drop Agglomerates: An Experimental Study. *Journal of Geophysical Research: Atmospheres* **2006**, *111*, (D7). <https://doi.org/10.1029/2005JD006389>.
141. Miljevic, B.; Surawski, N. C.; Bostrom, T.; Ristovski, Z. D., Restructuring of Carbonaceous Particles Upon Exposure to Organic and Water Vapours. *Journal of Aerosol Science* **2012**, *47*, 48-57. <https://doi.org/10.1016/j.jaerosci.2011.12.005>.

142. Mishchenko, M. I., Light Scattering by Randomly Oriented Axially Symmetric Particles. *Journal of the Optical Society of America A* **1991**, *8*, (6), 871-882. <https://doi.org/10.1364/JOSAA.8.000871>.
143. Mishchenko, M. I.; Travis, L. D.; Mackowski, D. W., T-matrix Computations of Light Scattering by Nonspherical Particles: A Review. *Journal of Quantitative Spectroscopy and Radiative Transfer* **1996**, *55*, (5), 535-575. [https://doi.org/10.1016/0022-4073\(96\)00002-7](https://doi.org/10.1016/0022-4073(96)00002-7).
144. Moffet, R. C.; Prather, K. A., In-situ Measurements of the Mixing State and Optical Properties of Soot with Implications for Radiative Forcing Estimates. *Proceedings of the National Academy of Sciences* **2009**, *106*, (29), 11872. <https://doi.org/10.1073/pnas.0900040106>.
145. Monge, M. E.; D'Anna, B.; Mazri, L.; Giroir-Fendler, A.; Ammann, M.; Donaldson, D. J.; George, C., Light Changes the Atmospheric Reactivity of Soot. *Proceedings of the National Academy of Sciences* **2010**, *107*, (15), 6605-6609. <https://doi.org/10.1073/pnas.0908341107>.
146. Morse, P. M., Diatomic Molecules According to the Wave Mechanics. II. Vibrational Levels. *Physical Review* **1929**, *34*, (1), 57-64. <https://doi.org/10.1103/PhysRev.34.57>.
147. Moteki, N.; Kondo, Y.; Miyazaki, Y.; Takegawa, N.; Komazaki, Y.; Kurata, G., et al., Evolution of Mixing State of Black Carbon Particles: Aircraft Measurements Over the Western Pacific in March 2004. *Geophysical Research Letters* **2007**, *34*, (11). <https://doi.org/10.1029/2006GL028943>.
148. Murphy, S. M.; Sorooshian, A.; Kroll, J. H.; Ng, N. L.; Chhabra, P. S.; Tong, C., et al., Secondary Aerosol Formation from Atmospheric Reactions of Aliphatic Amines. *Atmospheric Chemistry and Physics* **2007**, *7*, (9), 2313-2337. <https://doi.org/10.5194/acp-7-2313-2007>.
149. Myhre, G.; Shindell, D.; Bréon, F.-M.; Collins, W.; Fuglestedt, J.; Huang, J., et al. (2013). Anthropogenic and Natural Radiative Forcing. In Stocker, T. F.; Qin, D.; Plattner, G.-K.; Tignor, M.; Allen, S. K.; Boschung, J.; Nauels, A.; Xia, Y.; Bex, V.; Midgley, P. M. (Eds.), *Climate Change 2013: The Physical Science Basis. Contribution of Working Group I to the Fifth Assessment Report of the Intergovernmental Panel on Climate Change* (pp. 659–740). Cambridge, United Kingdom and New York, NY, USA: Cambridge University Press.
150. Nakao, S.; Shrivastava, M. B.; Nguyen, A.; Jung, H.; Cocker, D. R., Interpretation of Secondary Organic Aerosol Formation from Diesel Exhaust Photooxidation in an Environmental Chamber. *Aerosol Science and Technology* **2011**, *45*, (8), 964-972. <https://doi.org/10.1080/02786826.2011.573510>.

151. Nenes, A.; Seinfeld, J. H., Parameterization of Cloud Droplet Formation in Global Climate Models. *Journal of Geophysical Research: Atmospheres* **2003**, *108*, (D14). <https://doi.org/10.1029/2002JD002911>.
152. Nielsen, C. J.; Anna, B. D.; Dye, C.; Graus, M.; Karl, M.; King, S. M., et al., Atmospheric Chemistry of 2-Aminoethanol (MEA). *Energy Procedia* **2011**, *4*, 2245-2252. <https://doi.org/10.1016/j.egypro.2011.02.113>.
153. Nielsen, C. J.; Bossi, R.; Bunkan, A. J. C.; Dithmer, L.; Glasius, M.; Hallquist, M., et al. *Atmospheric Degradation of Amines (ADA): Summary Report from Atmospheric Chemistry Studies of Amines, Nitrosamines, Nitramines and Amides*; University of Oslo: Oslo, Norway, 2012.
154. Nienow, A. M.; Roberts, J. T., Heterogeneous Chemistry of Carbon Aerosols. *Annual Review of Physical Chemistry* **2006**, *57*, (1), 105-128. <https://doi.org/10.1146/annurev.physchem.57.032905.104525>.
155. Ohe, S. (1976). *Computer Aided Data Book of Vapor Pressure*. Tokyo, Japan: Data Book Publishing Company.
156. Olfert, J.; Rogak, S., Universal Relations between Soot Effective Density and Primary Particle Size for Common Combustion Sources. *Aerosol Science and Technology* **2019**, 1-8. <https://doi.org/10.1080/02786826.2019.1577949>.
157. Olfert, J. S.; Symonds, J. P. R.; Collings, N., The Effective Density and Fractal Dimension of Particles Emitted from a Light-Duty Diesel Vehicle with a Diesel Oxidation Catalyst. *Journal of Aerosol Science* **2007**, *38*, (1), 69-82. <https://doi.org/10.1016/j.jaerosci.2006.10.002>.
158. Ovadnevaite, J.; Zuend, A.; Laaksonen, A.; Sanchez, K. J.; Roberts, G.; Ceburnis, D., et al., Surface Tension Prevails Over Solute Effect in Organic-Influenced Cloud Droplet Activation. *Nature* **2017**, *546*, (7660), 637-641. <https://doi.org/10.1038/nature22806>.
159. Pagels, J.; Khalizov, A. F.; McMurry, P. H.; Zhang, R. Y., Processing of Soot by Controlled Sulphuric Acid and Water Condensation—Mass and Mobility Relationship. *Aerosol Science and Technology* **2009**, *43*, (7), 629-640. <https://doi.org/10.1080/02786820902810685>.
160. Park, K.; Cao, F.; Kittelson, D. B.; McMurry, P. H., Relationship between Particle Mass and Mobility for Diesel Exhaust Particles. *Environmental Science and Technology* **2003**, *37*, (3), 577-583. <https://doi.org/10.1021/es025960v>.

161. Park, K.; Kittelson, D. B.; Zachariah, M. R.; McMurry, P. H., Measurement of Inherent Material Density of Nanoparticle Agglomerates. *Journal of Nanoparticle Research* **2004**, *6*, (2), 267-272. <https://doi.org/10.1023/B:NANO.0000034657.71309.e6>.
162. Pei, X.; Hallquist, M.; Eriksson, A. C.; Pagels, J.; Donahue, N. M.; Mentel, T., et al., Morphological Transformation of Soot: Investigation of Microphysical Processes During the Condensation of Sulfuric Acid and Limonene Ozonolysis Product Vapors. *Atmospheric Chemistry and Physics* **2018**, *18*, (13), 9845-9860. <https://doi.org/10.5194/acp-18-9845-2018>.
163. Petters, M. D.; Kreidenweis, S. M., A Single Parameter Representation of Hygroscopic Growth and Cloud Condensation Nucleus Activity. *Atmospheric Chemistry and Physics* **2007**, *7*, (8), 1961-1971. <https://doi.org/10.5194/acp-7-1961-2007>.
164. Popovicheva, O.; Persiantseva, N. M.; Shonija, N. K.; DeMott, P.; Koehler, K.; Petters, M., et al., Water Interaction with Hydrophobic and Hydrophilic Soot Particles. *Physical Chemistry Chemical Physics* **2008**, *10*, (17), 2332-2344. <https://doi.org/10.1039/B718944N>.
165. Pöschl, U., Atmospheric Aerosols: Composition, Transformation, Climate and Health Effects. *Cheminform* **2005**, *44*, (46), 7520. <https://doi.org/10.1002/anie.200501122>.
166. Prenni Anthony, J.; Petters Markus, D.; Kreidenweis Sonia, M.; DeMott Paul, J.; Ziemann Paul, J., Cloud Droplet Activation of Secondary Organic Aerosol. *Journal of Geophysical Research: Atmospheres* **2007**, *112*, (D10). <https://doi.org/10.1029/2006JD007963>.
167. Price, D.; Kacarab, M.; Cocker, D. R.; Purvisroberts, K. L.; Silva, P. J., Effects of Temperature on the Formation of Secondary Organic Aerosol from Amine Precursors. *Aerosol Science and Technology* **2016**, *50*, (11), 1216-1226. <https://doi.org/10.1080/02786826.2016.1236182>.
168. Qiu, C.; Khalizov, A. F.; Zhang, R., Soot Aging from OH-Initiated Oxidation of Toluene. *Environmental Science & Technology* **2012**, *46*, (17), 9464. <https://doi.org/10.1021/es301883y>.
169. Qiu, C.; Wang, L.; Lal, V.; Khalizov, A. F.; Zhang, R. Y., Heterogeneous Reactions of Alkylamines with Ammonium Sulfate and Ammonium Bisulfate. *Environmental Science & Technology* **2011**, *45*, (11), 4748-4755. <https://doi.org/10.1021/es1043112>.

170. Qiu, C.; Zhang, R., Multiphase Chemistry of Atmospheric Amines. *Physical Chemistry Chemical Physics* **2013**, *15*, (16), 5738-5752. <https://doi.org/10.1039/C3CP43446J>.
171. Radney, J. G.; You, R.; Ma, X.; Conny, J. M.; Zachariah, M. R.; Hodges, J. T.; Zangmeister, C. D., Dependence of Soot Optical Properties on Particle Morphology: Measurements and Model Comparisons. *Environmental Science & Technology* **2014**, *48*, (6), 3169-3176. <https://doi.org/10.1021/es4041804>.
172. Ramana, M. V.; Ramanathan, V.; Feng, Y.; Yoon, S. C.; Kim, S. W.; Carmichael, G. R.; Schauer, J. J., Warming Influenced by the Ratio of Black Carbon to Sulphate and the Black-Carbon Source. *Nature Geoscience* **2010**, *3*, (8), 542-545. <https://doi.org/10.1038/ngeo918>.
173. Ramanathan, V.; Carmichael, G., Global and Regional Climate Changes Due to Black Carbon. *Nature Geoscience* **2008**, *1*, (4), 221-227. <https://doi.org/10.1038/ngeo156>.
174. Reeks, M. W.; Reed, J.; Hall, D., On the Resuspension of Small Particles by a Turbulent Flow. *Journal of Physics D: Applied Physics* **1988**, *21*, (4), 574-589. <https://doi.org/10.1088/0022-3727/21/4/006>.
175. Reist, P. C. (1993). *Aerosol Science and Technology* (2nd ed.). NY: McGraw-Hill.
176. Riddick, J. A.; Bunger, W. B.; Sakano, T. K. (1985). *Techniques of Chemistry - Organic solvents* (4th ed. Vol. 2). New York, NY: John Wiley and Sons.
177. Riemer, N.; Vogel, H.; Vogel, B., Soot Aging Time Scales in Polluted Regions During Day and Night. *Atmospheric Chemistry & Physics* **2004**, *4*, (7), 1885-1893. <https://doi.org/10.5194/acp-4-1885-2004>.
178. Riemer, N.; West, M.; Zaveri, R.; Easter, R., Estimating Black Carbon Aging Time-Scales with a Particle-Resolved Aerosol Model. *Journal of Aerosol Science* **2010**, *41*, (1), 143-158. <https://doi.org/10.1016/j.jaerosci.2009.08.009>.
179. Riemer, N.; West, M.; Zaveri, R. A.; Easter, R. C., Simulating the Evolution of Soot Mixing State with a Particle-Resolved Aerosol Model. *Journal of Geophysical Research* **2009**, *114*, D09202. <https://doi.org/10.1029/2008jd011073>.
180. Riipinen, I.; Pierce, J. R.; Donahue, N. M.; Pandis, S. N., Equilibration Time Scales of Organic Aerosol Inside Thermodenuders: Evaporation Kinetics Versus Thermodynamics. *Atmospheric Environment* **2010**, *44*, (5), 597-607. <https://doi.org/10.1016/j.atmosenv.2009.11.022>.

181. Rose, W., Volumes and Surface Areas of Pendular Rings. *Journal of Applied Physics* **1958**, 29, (4), 687-691. <https://doi.org/10.1063/1.1723251>.
182. Saathoff, H.; Naumann, K. H.; Schnaiter, M.; Schöck, W.; Möhler, O.; Schurath, U., et al., Coating of Soot and (NH₄)₂SO₄ Particles by Ozonolysis Products of α -Pinene. *Journal of Aerosol Science* **2003**, 34, (10), 1297-1321. [https://doi.org/10.1016/S0021-8502\(03\)00364-1](https://doi.org/10.1016/S0021-8502(03)00364-1).
183. Saliba, G.; Subramanian, R.; Saleh, R.; Ahern, A. T.; Lipsky, E. M.; Tasoglou, A., et al., Optical Properties of Black Carbon in Cookstove Emissions Coated with Secondary Organic Aerosols: Measurements and Modeling. *Aerosol Science and Technology* **2016**, 50, (11), 1264-1276. <https://doi.org/10.1080/02786826.2016.1225947>.
184. Scarnato, B. V.; Vahidinia, S.; Richard, D. T.; Kirchstetter, T. W., Effects of Internal Mixing and Aggregate Morphology on Optical Properties of Black Carbon Using a Discrete Dipole Approximation Model. *Atmospheric Chemistry & Physics* **2013**, 13, (10), 5089-5101. <https://doi.org/10.5194/acp-13-5089-2013>.
185. Schell, B.; Ackermann, I. J.; Hass, H.; Binkowski, F. S.; Ebel, A., Modeling the Formation of Secondary Organic Aerosol within a Comprehensive Air Quality Model System. *Journal of Geophysical Research: Atmospheres* **2001**, 106, (D22), 28275-28293. <https://doi.org/10.1029/2001JD000384>.
186. Schnaiter, M.; Horvath, H.; Mohler, O.; Naumann, K. H.; Saathoff, H.; Schöck, O. W., UV-VIS-NIR Spectral Optical Properties of Soot and Soot-Containing Aerosols. *Journal of Aerosol Science* **2003**, 34, (10), 1421-1444. [https://doi.org/10.1016/s0021-8502\(03\)00361-6](https://doi.org/10.1016/s0021-8502(03)00361-6).
187. Schnitzler, E. G.; Dutt, A.; Charbonneau, A. M.; Olfert, J. S.; Jäger, W., Soot Aggregate Restructuring Due to Coatings of Secondary Organic Aerosol Derived from Aromatic Precursors. *Environmental Science & Technology* **2014**, 48, (24), 14309-14316. <https://doi.org/10.1021/es503699b>.
188. Schnitzler, E. G.; Gac, J. M.; Jäger, W., Coating Surface Tension Dependence of Soot Aggregate Restructuring. *Journal of Aerosol Science* **2017**, 106, 43-55. <https://doi.org/10.1016/j.jaerosci.2017.01.005>.
189. Sedlacek, A. J.; Lewis, E. R.; Kleinman, L.; Xu, J.; Zhang, Q., Determination of and Evidence for Non-Core-Shell Structure of Particles Containing Black Carbon Using the Single-Particle Soot Photometer (SP2). *Geophysical Research Letters* **2012**, 39, (6). <https://doi.org/10.1029/2012GL050905>.

190. Seinfeld, J. H.; Pandis, S. N. (2006). *Atmospheric Chemistry and Physics: From Air Pollution to Climate Change* (2nd ed.). Hoboken, NJ: John Wiley & Sons.
191. Shiraiwa, M.; Kondo, Y.; Iwamoto, T.; Kita, K., Amplification of Light Absorption of Black Carbon by Organic Coating. *Aerosol Science and Technology* **2010**, *44*, (1), 46 - 54. <https://doi.org/10.1080/02786820903357686>.
192. Shiraiwa, M.; Kondo, Y.; Moteki, N.; Takegawa, N.; Sahu, L. K.; Takami, A., et al., Radiative Impact of Mixing State of Black Carbon Aerosol in Asian Outflow. *Journal of Geophysical Research: Atmospheres* **2008**, *113*, (D24). <https://doi.org/10.1029/2008JD010546>.
193. Slowik, J. G.; Cross, E. S.; Han, J.-H.; Kolucki, J.; Davidovits, P.; Williams, L. R., et al., Measurements of Morphology Changes of Fractal Soot Particles using Coating and Denuding Experiments: Implications for Optical Absorption and Atmospheric Lifetime. *Aerosol Science and Technology* **2007**, *41*, (8), 734-750. <https://doi.org/10.1080/02786820701432632>.
194. Small, P. A.; Small, K. W.; Cowley, P., The Vapour Pressures of Some High Boiling Esters. *Transactions of the Faraday Society* **1948**, *44*, (0), 810-816. <https://doi.org/10.1039/TF9484400810>.
195. Soewono, A.; Rogak, S. N., Morphology and Optical Properties of Numerically Simulated Soot Aggregates. *Aerosol Science and Technology* **2013**, *47*, (3), 267-274. <https://doi.org/10.1080/02786826.2012.749972>.
196. Sorensen, C. M., Light Scattering by Fractal Aggregates: A Review. *Aerosol Science and Technology* **2001**, *35*, (2), 648-687. <https://doi.org/10.1080/02786820117868>.
197. Sorensen, C. M., The Mobility of Fractal Aggregates: A Review. *Aerosol Science and Technology* **2011**, *45*, (7), 765-779. <https://doi.org/10.1080/02786826.2011.560909>.
198. Sorensen, C. M.; Yon, J.; Liu, F.; Maughan, J.; Heinson, W. R.; Berg, M. J., Light Scattering and Absorption by Fractal Aggregates Including Soot. *Journal of Quantitative Spectroscopy and Radiative Transfer* **2018**, *217*, 459-473. <https://doi.org/10.1016/j.jqsrt.2018.05.016>.
199. Stier, P.; Feichter, J.; Kinne, S.; Kloster, S.; Vignati, E.; Wilson, J., et al., The Aerosol-Climate Model ECHAM5-HAM. *Atmospheric Chemistry & Physics* **2005**, *5*, (4), 1125-1156. <https://doi.org/10.5194/acp-5-1125-2005>.

200. Stipe, C. B.; Higgins, B. S.; Lucas, D.; Koshland, C. P.; Sawyer, R. F., Inverted Co-Flow Diffusion Flame for Producing Soot. *Review of Scientific Instruments* **2005**, *76*, (2), 023908. <https://doi.org/10.1063/1.1851492>.
201. Topping, D.; Connolly, P.; McFiggans, G., Cloud Droplet Number Enhanced by Co-Condensation of Organic Vapours. *Nature Geoscience* **2013**, *6*, (6), 443-446. <https://doi.org/10.1038/ngeo1809>.
202. Tritscher, T.; Jurányi, Z.; Martin, M.; Chirico, R.; Gysel, M.; Heringa, M. F., et al., Changes of Hygroscopicity and Morphology During Ageing of Diesel Soot. *Environmental Research Letters* **2011**, *6*. <https://doi.org/10.1088/1748-9326/6/3/034026>.
203. Videen, G.; Pinnick, R. G.; Ngo, D.; Fu, Q.; Chýlek, P., Asymmetry Parameter and Aggregate Particles. *Applied Optics* **1998**, *37*, (6), 1104-1109. <https://doi.org/10.1364/AO.37.001104>.
204. Wang, J.; Cubison, M. J.; Aiken, A. C.; Jimenez, J. L.; Collins, D. R., The Importance of Aerosol Mixing State and Size-Resolved Composition on CCN Concentration and the Variation of the Importance with Atmospheric Aging of Aerosols. *Atmospheric Chemistry & Physics* **2010a**, *10*, (15), 7267-7283. <https://doi.org/10.5194/acp-10-7267-2010>.
205. Wang, L.; Khalizov, A. F.; Zheng, J.; Xu, W.; Ma, Y.; Lal, V.; Zhang, R. Y., Atmospheric Nanoparticles Formed from Heterogeneous Reactions of Organics. *Nature Geoscience* **2010b**, *3*, (4), 238-242. <https://doi.org/10.1038/ngeo778>.
206. Wang, L.; Lal, V.; Khalizov, A. F.; Zhang, R. Y., Heterogeneous Chemistry of Alkylamines with Sulfuric Acid: Implications for Atmospheric Formation of Alkylammonium Sulfates. *Environmental Science & Technology* **2010c**, *44*, (7), 2461-2465. <https://doi.org/10.1021/es9036868>.
207. Wang, X. F.; Gao, S.; Yang, X.; Chen, H.; Chen, J. M.; Zhuang, G. S., et al., Evidence for High Molecular Weight Nitrogen-Containing Organic Salts in Urban Aerosols. *Environmental Science & Technology* **2010d**, *44*, (12), 4441-4446. <https://doi.org/10.1021/es1001117>.
208. Watson, J. G., Visibility: Science and Regulation. *Journal of the Air & Waste Management Association* **2002**, *52*, (6), 628-713. <https://doi.org/10.1080/10473289.2002.10470813>.
209. Weingartner, E.; Baltensperger, U.; Burtscher, H., Growth and Structural Change of Combustion Aerosols at High Relative Humidity. *Environmental Science & Technology* **1995**, *29*, (12), 2982-2986. <https://doi.org/10.1021/es00012a014>.

210. Weingartner, E.; Burtscher, H.; Baltensperger, U., Hygroscopic Properties of Carbon and Diesel Soot Particles. *Atmospheric Environment* **1997**, *31*, (15), 2311-2327. [https://doi.org/10.1016/S1352-2310\(97\)00023-X](https://doi.org/10.1016/S1352-2310(97)00023-X).
211. Wentzel, M.; Gorzawski, H.; Naumann, K. H.; Saathoff, H.; Weinbruch, S., Transmission Electron Microscopical and Aerosol Dynamical Characterization of Soot Aerosols. *Journal of Aerosol Science* **2003**, *34*, (10), 1347-1370. [https://doi.org/10.1016/S0021-8502\(03\)00360-4](https://doi.org/10.1016/S0021-8502(03)00360-4).
212. Wiedensohler, A., An Approximation of the Bipolar Charge Distribution for Particles in the Submicron Size Range. *Journal of Aerosol Science* **1988**, *19*, (3), 387-389. [https://doi.org/10.1016/0021-8502\(88\)90278-9](https://doi.org/10.1016/0021-8502(88)90278-9).
213. Willis, M. D.; Healy, R. M.; Riemer, N.; West, M.; Wang, J. M.; Jeong, C. H., et al., Quantification of Black Carbon Mixing State from Traffic: Implications for Aerosol Optical Properties. *Atmospheric Chemistry & Physics* **2016**, *16*, (7), 4693-4706. <https://doi.org/10.5194/acp-16-4693-2016>.
214. Wilson, J.; Cuvelier, C.; Raes, F., A Modeling Study of Global Mixed Aerosol Fields. *Journal of Geophysical Research: Atmospheres* **2001**, *106*, (D24), 34081-34108. <https://doi.org/10.1029/2000JD000198>.
215. Wittbom, C.; Eriksson, A. C.; Rissler, J.; Carlsson, J. E.; Roldin, P.; Nordin, E. Z., et al., Cloud Droplet Activity Changes of Soot Aerosol Upon Smog Chamber Ageing. *Atmospheric Chemistry & Physics* **2014**, *14*, (18), 9831-9854. <https://doi.org/10.5194/acp-14-9831-2014>.
216. Wu, Y.; Cheng, T.; Zheng, L.; Chen, H., Models for the Optical Simulations of Fractal Aggregated Soot Particles Thinly Coated with Non-Absorbing Aerosols. *Journal of Quantitative Spectroscopy and Radiative Transfer* **2016**, *182*, 1-11. <https://doi.org/10.1016/j.jqsrt.2016.05.011>.
217. Wypych, A. (2013). Chapter 3.2 - Adipates. In Wypych, A. (Ed.), *Plasticizers Databook* (pp. 22-65). Oxford: Elsevier.
218. Xie, J.; Marlow, W. H., Water Vapor Pressure over Complex Particles, I: Sulfuric Acid Solution Effect. *Aerosol Science and Technology* **1997**, *27*, (5), 591-603. <https://doi.org/10.1080/02786829708965499>.
219. Xue, H.; Khalizov, A. F.; Wang, L.; Zheng, J.; Zhang, R., Effects of Coating of Dicarboxylic Acids on the Mass–Mobility Relationship of Soot Particles. *Environmental Science & Technology* **2009a**, *43*, (8), 2787-2792. <https://doi.org/10.1021/es803287v>.

220. Xue, H.; Khalizov, A. F.; Wang, L.; Zheng, J.; Zhang, R., Effects of Dicarboxylic Acid Coating on the Optical Properties of Soot. *Physical Chemistry Chemical Physics* **2009b**, *11*, (36), 7869-7875. <https://doi.org/10.1039/B904129J>.
221. Yaws, C. L., Yaws' Handbook of Thermodynamic and Physical Properties of Chemical Compounds : Physical, Thermodynamic and Transport Properties for 5,000 Organic Chemical Compounds. **2003**.
<http://app.knovel.com/hotlink/toc/id:kpYHTPPCC4/yaws-handbook-of>.
222. Yaws, C. L.; Richmond, P. C. (2009). Chapter 21 - Surface Tension—Organic Compounds. In Yaws, C. L. (Ed.), *Thermophysical Properties of Chemicals and Hydrocarbons* (pp. 686-781). Norwich, NY: William Andrew Publishing.
223. Yon, J.; Bescond, A.; Liu, F., On the Radiative Properties of Soot Aggregates Part 1: Necking and Overlapping. *Journal of Quantitative Spectroscopy and Radiative Transfer* **2015**, *162*, 197-206. <https://doi.org/10.1016/j.jqsrt.2015.03.027>.
224. Yon, J.; Rozé, C.; Girasole, T.; Coppalle, A.; Méès, L., Extension of RDG-FA for Scattering Prediction of Aggregates of Soot Taking into Account Interactions of Large Monomers. *Particle & Particle Systems Characterization* **2008**, *25*, (1), 54-67. <https://doi.org/10.1002/ppsc.200700011>.
225. Young, T. F.; Grinstead, S. R., The Surface Tensions of Aqueous Sulfuric Acid Solutions. *Annals of the New York Academy of Sciences* **1949**, *51*, (4), 765-780. <https://doi.org/10.1111/j.1749-6632.1949.tb27304.x>.
226. Yurkin, M. A.; Hoekstra, A. G., The Discrete-Dipole-Approximation Code ADDA: Capabilities and Known Limitations. *Journal of Quantitative Spectroscopy and Radiative Transfer* **2011**, *112*, (13), 2234-2247. <https://doi.org/10.1016/j.jqsrt.2011.01.031>.
227. Yurkin, M. A.; Kahnert, M., Light Scattering by a Cube: Accuracy Limits of the Discrete Dipole Approximation and the T-Matrix Method. *Journal of Quantitative Spectroscopy and Radiative Transfer* **2013**, *123*, 176-183. <https://doi.org/10.1016/j.jqsrt.2012.10.001>.
228. Zangmeister, C. D.; You, R.; Lunny, E. M.; Jacobson, A. E.; Okumura, M.; Zachariah, M. R.; Radney, J. G., Measured In-Situ Mass Absorption Spectra for Nine Forms of Highly-Absorbing Carbonaceous Aerosol. *Carbon* **2018**, *136*, 85-93. <https://doi.org/10.1016/j.carbon.2018.04.057>.
229. Zaveri, R. A.; Easter, R. C.; Fast, J. D.; Peters, L. K., Model for Simulating Aerosol Interactions and Chemistry (MOSAIC). *Journal of Geophysical Research-Atmospheres* **2008**, *113*, (D13). <https://doi.org/10.1029/2007JD008782>.

230. Zaveri, R. A.; Easter, R. C.; Peters, L. K., A Computationally Efficient Multicomponent Equilibrium Solver for Aerosols (MESA). *Journal of Geophysical Research: Atmospheres* **2005**, *110*, (D24). <https://doi.org/10.1029/2004JD005618>.
231. Zaveri, R. A.; Peters, L. K., A New Lumped Structure Photochemical Mechanism for Large-Scale Applications. *Journal of Geophysical Research: Atmospheres* **1999**, *104*, (D23), 30387-30415. <https://doi.org/10.1029/1999JD900876>.
232. Zeng, C.; Liu, C.; Li, J.; Zhu, B.; Yin, Y.; Wang, Y., Optical Properties and Radiative Forcing of Aged BC due to Hygroscopic Growth: Effects of the Aggregate Structure. *Journal of Geophysical Research: Atmospheres* **2019**, *124*, (8), 4620-4633. <https://doi.org/10.1029/2018JD029809>.
233. Zhang, R.; Khalizov, A. F.; Pagels, J.; Zhang, D.; Xue, H.; McMurry, P. H., Variability in Morphology, Hygroscopicity, and Optical Properties of Soot Aerosols During Atmospheric Processing. *Proceedings of the National Academy of Sciences* **2008**, *105*, (30), 10291. <https://doi.org/10.1073/pnas.0804860105>.
234. Zhang, X.; Mao, M.; Yin, Y.; Wang, B., Absorption Enhancement of Aged Black Carbon Aerosols Affected by their Microphysics: A Numerical Investigation. *Journal of Quantitative Spectroscopy and Radiative Transfer* **2017**, *202*, 90-97. <https://doi.org/10.1016/j.jqsrt.2017.07.025>.
235. Zhao, G.; Bi, S.; Li, X.; Wu, J., Surface Tension of Diethyl Carbonate, 1,2-Dimethoxyethane and Diethyl Adipate. *Fluid Phase Equilibria* **2010**, *295*, (1), 46-49. <https://doi.org/10.1016/j.fluid.2010.03.040>.
236. Ziskind, G.; Fichman, M.; Gutfinger, C., Particle Behavior on Surfaces Subjected to External Excitations. *Journal of Aerosol Science* **2000**, *31*, (6), 703-719. [https://doi.org/10.1016/S0021-8502\(99\)00554-6](https://doi.org/10.1016/S0021-8502(99)00554-6).
237. Zuberi, B.; Johnson, K. S.; Aleks, G. K.; Molina, L. T.; Laskin, A., Hydrophilic Properties of Aged Soot. *Geophysical Research Letters* **2005**, *32*, (1), L01807. <https://doi.org/10.1029/2004GL021496>.